TOWARDS DIAMOND-BASED PHOTOCATALYSTS

Spectroscopic Investigations at the Diamond-Water Interface

SNEHA CHOUDHURY

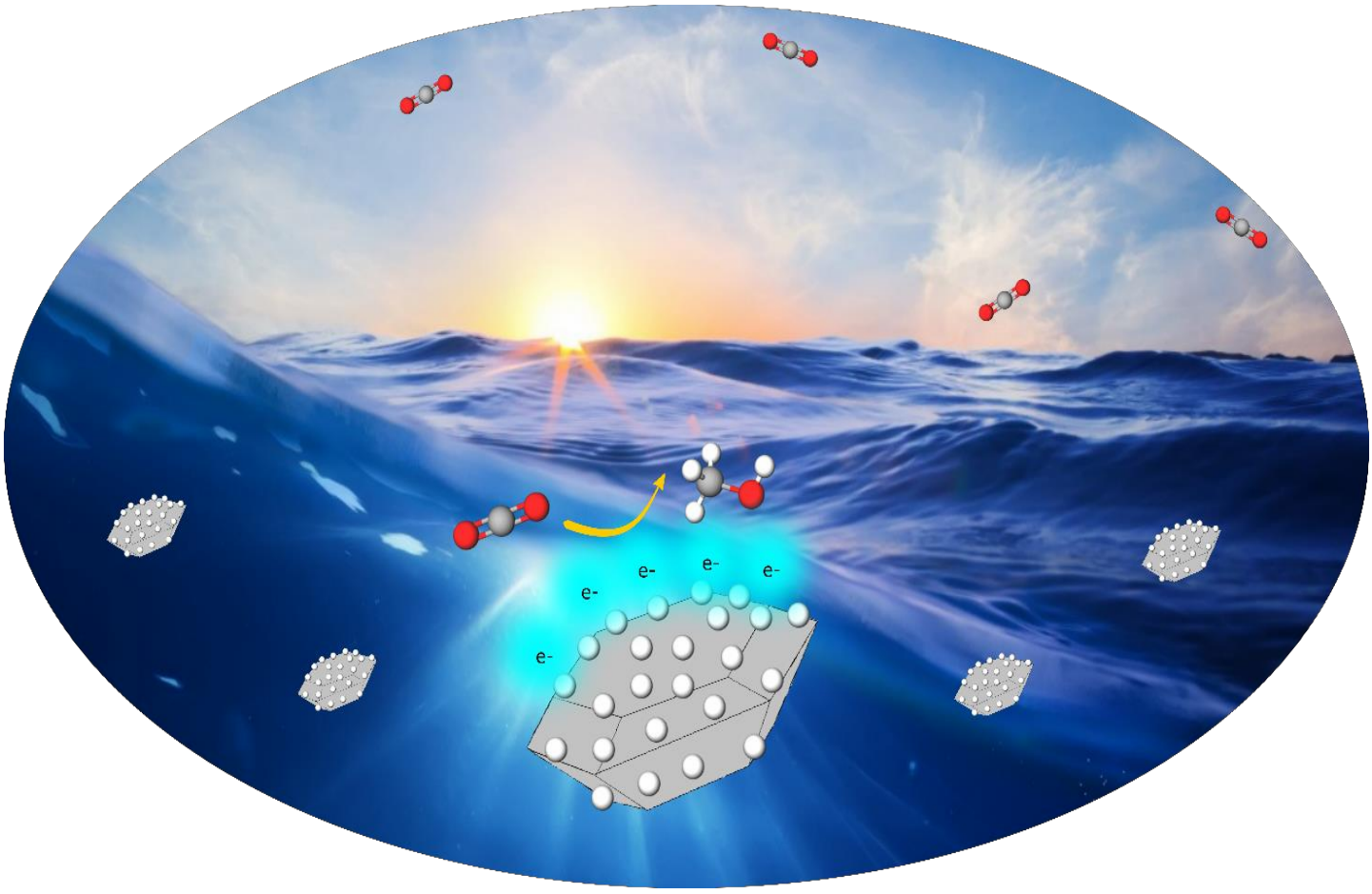

Towards Diamond-Based Photocatalysts: Spectroscopic Investigations at the Diamond-Water Interface

Inaugural-Dissertation

submitted in Partial Fulfillment of the Requirements
for the Degree of Doctor rerum naturalium (Dr. rer. nat)

to the Department of Biology, Chemistry and Pharmacy
of Freie Universität Berlin

by

Sneha Choudhury
Master of Science in Chemical Engineering, Technical University of Delft
from Burdwan, India

in

Berlin, Germany
January 2019

1. Reviewer: Prof. Dr. Anke Krueger
2. Reviewer: Prof. Dr. Ing. Christina Roth

Submission on: 31 January 2019
Date of Defense: 22 March 2019

The work described in this thesis was carried out within the Institute of Methods for Material Development at Helmholtz Zentrum Berlin für Materialien und Energie GmbH. This research was funded by the *DIACAT project* from European Union's H2020 Programme under Grant Agreement Nr. 665085

Science is a way of thinking much more than it is a body of knowledge

Carl Sagan

List of Abbreviations

CuOx	Copper Oxides
ATR	Attenuated Total Reflection
CBE	Conduction Band Edge
CBM	Conduction Band Minimum
CCD	Charge-Coupled-Device
CCS	Carbon Capture and Sequestration
Dfoam	Diamond Foam
DFT	Density Functional Theory
E_F	Fermi Energy
ECP	Effective Core Potentials
EELS	Electron Energy Loss Spectroscopy
EJ	Exajoule
ESR	Electron Spin Resonance
eV	electron Volts
EXAFS	Extended X-ray Absorption Fine Structure Spectroscopy
EXAFS	Near Edge X-ray Absorption Fine Structure Spectroscopy
EY	Electron Yield
FLR	Fullerene-like Reconstructions
FTIR	Fourier Transform Infrared Spectroscopy
FY	Fluorescence Yield
GeV	Giga electron Volt
GGA	Generalized Gradient Approximation
HOMO	Highest Occupied Molecular Orbital
HPHT	High Pressure High Temperature
HRTEM	High Resolution Transmission Electron Microscopy
IR	Infrared

kV	kilo Volt
LN_2	Liquid Nitrogen
LUMO	Lowest Unoccupied Molecular Orbital
mA	milli Ampere
MCP	Multi-Channel-Plate
MJ	Megajoule
MWCVD	Microwave Chemical Vapor Deposition
ND	Nanodiamond
NEA	Negative Electron Affinity
PBE	Perdew-Burke-Ernzerhof
PCD	Polycrystalline Diamond
PECVD	Plasma Enhanced Chemical Vapor Deposition
PES	Photoemission Spectroscopy
PFY	Partial Fluorescence Yield
ppm	parts per million
RIXS	Resonant Inelastic X-ray Scattering
Ru-ND	Ruthenium complex functionalized nanodiamond
SCD	Single Crystal Diamond
TDDFT	Time-dependent Density Functional Theory
TEY	Total Electron Yield
TFY	Total Fluorescence Yield
TW	Terawatt
UNCD	Ultra nanocrystalline Diamond
UV	Ultraviolet
VBE	Valence Band Edge
VBM	Valence Band Maximum
V	Volt
XAS	X-ray Absorption Spectroscopy
XES	X-ray Emission Spectroscopy

Chemical Formulae

Ag/AgCl	Silver/Silver Chloride
Au	Gold
CO_2	Carbon Dioxide
CO	Carbon Monoxide
Cu_2O	Copper (I) Oxide
CuO	Copper (II) Oxide
Cu	Copper
H_2O	Water
H_2	Hydrogen
N_2	Nitrogen
NH_3	Ammonia
O_2	Oxygen
Pt	Platinum
$Ru(bpy)_3$	Ruthenium tris-bipyridine
$Ru(tpy)_2$	Ruthenium terpyridine
$Ru(tpy)Cl_3$	Ruthenium terpyridine chloride
Si_3N_4	Silicon Nitride
TiO_2	Titanium dioxide/Titania
ZnO	Zinc Oxide

Contents

Abstract

Artificial Photosynthesis is a promising approach to tackle the increasing challenges of global warming. However, the direct conversion of CO_2 to other chemicals presents major kinetic challenges, evoking exploration of abundant, cost effective and sustainable photocatalysts.

Diamonds are promising candidates as H-terminated diamond surfaces exhibit excellent electron emission characteristics in water because of their negative electron affinity. However, due to their wide band gap of 5.4 eV, the generation of solvated electrons, requires the photoactivation of diamond using deep UV radiation which is scarcely available in the solar spectrum. In this thesis two strategies are investigated to enable visible light absorption and enhance electron emission from diamonds. Specifically, the effect of B, N and P doping on the electronic structure of diamonds were investigated using soft X-ray absorption spectroscopy at C K edge. The results of our study revealed that combining nanostructuration with B-doping leads to introduction of new electronic states close to both the valence band maximum and the conduction band minimum in B-doped diamonds. As an alternative strategy, the electronic structure of nanodiamonds sensitized with $Ru(bpy)_3$ was probed. These studies presented evidence of electronic coupling between the Ru complex and the nanodiamonds with the HOMO of $Ru(bpy)_3$ lying above the valence band minimum of the diamonds. As a result of this band alignment, the dye acts as an electron donor and can potentially refill the photogenerated holes in the valence band of diamonds.

Since photoactivation of diamonds generates solvated electrons in water, it is also important to understand the diamond-water interface. To this aim, infrared spectroscopy was used to elucidate the influence of different pH conditions on the surface interactions of ND-OH surfaces at the diamond-water interface. This study provided insights that could help to determine the optimal environment that would enhance electron emission from these surfaces. Based on the results, a possible formation of oxonium ions on an ND-OH surface in acidic conditions could be deduced. These oxonium ions could potentially form a charge stabilization layer with water molecules, thereby enhancing electron emission which could be advantageous for photocatalytic reductions. The results further suggested a possible aging mechanism of ND-H surfaces under long term UV irradiation. For efficient photoelectrocatalytic CO_2 reduction, diamonds were also co-promoted by Cu_2O to form a hybrid photocatalyst. The electronic structure of this hybrid material was probed at the Cu L edge to explain the role of diamond in this hybrid material. It was found out that diamond indeed acts as a very stable support for Cu_2O thereby decelerating the process of aging and subsequent deactivation of the catalyst.

With this work, we thus, aim to highlight some of the characteristics of diamonds that would enable the development of diamond based photocatalysts in the future.

Zusammenfassung

Die künstliche Photosynthese ist ein vielversprechender Ansatz, um den wachsenden Herausforderungen der globalen Erwärmung zu begegnen. Die direkte Umwandlung von CO_2 in andere Chemikalien stellt jedoch eine große Herausforderung dar, die zur Erforschung zahlreicher, kostengünstiger und nachhaltiger Photokatalysatoren führt.

Aufgrund ihrer großen Bandlücke von 5,4 eV sind Diamanten vielversprechende Kandidaten. Denn H-terminierte Diamantoberflächen weisen aufgrund ihrer negativen Elektronenaffinität in Wasser hervorragende Elektronenemissionseigenschaften auf. Die Erzeugung von solvatisierten Elektronen erfordert jedoch die Photoaktivierung von Diamanten mit tiefer UV-Strahlung, die im Sonnenspektrum kaum verfügbar ist. In der vorliegenden Arbeit wurden zwei Strategien untersucht, um die Absorption des sichtbaren Lichts zu ermöglichen und die Elektronenemission von Diamanten zu verbessern. Insbesondere wurden die elektronischen Strukturen von p- und n-Diamanten mit B-, N- bzw. P-Dotierung mittels weicher Röntgenabsorptionsspektroskopie an der C-K-Kante untersucht. Diese Untersuchungen zeigten, dass die Kombination von Nanostrukturierung mit B-Dotierung neue elektronische Zustände erzeugt, die sowohl dem Valenzbandmaximum als auch dem Leitungsbandminimum in B-dotierten Diamanten nahe kommen. Als alternative Strategie wurde die elektronische Struktur von Nanodiamanten untersucht, die mit $Ru(bpy)_3$ sensibilisiert sind. Diese Studien zeigten eine elektronische Kopplung zwischen dem Ru-Komplex und den Nanodiamanten, wobei das HOMO von $Ru(bpy)_3$ über dem Valenzband Minimum der Diamanten lag. Durch diese Bandausrichtung wirkt der Farbstoff als Elektronendonor und kann die photogenerierten Löcher im Valenzband der Diamanten potenziell wieder auffüllen.

Da die Photoaktivierung von Diamanten im Wasser solvatisierte Elektronen erzeugt, ist es auch wichtig, die Grenzfläche zwischen Diamant und Wasser zu verstehen. Wir untersuchten die Interaktion von OH-terminierten Diamant-Oberflächen mit Wasser bei unterschiedlichen pH-Werten, um die Elektronenemission von diesen Oberflächen zu verbessern. Es stellte sich heraus, dass unter sauren Bedingungen auf einer ND-OH-Oberfläche möglicherweise Oxoniumionen gebildet werden, die mit Wassermolekülen eine ladungsstabilisierende Schicht bilden könnten. Diese wiederum könnte die Elektronenemission erhöhen und die photokatalytische Reduktion von CO_2 begünstigen.

Einen hybriden Photokatalysator mit Cu_2O Schichten auf der Diamantenoberfläche wurde auch gebildet, als alternativen Weg für eine effiziente CO_2-Photoreduktion. Die elektronische Struktur dieses Hybridmaterials wurde an der Cu-L-Kante untersucht, um die Rolle des Diamanten in diesem Hybridmaterial zu erklären. Es wurde herausgefunden, dass Diamant tatsächlich als sehr stabiler Träger für Cu_2O wirkt, wodurch der Alterungsprozess und die daraus folgende Deaktivierung des Katalysators verzögert werden.

Mit dieser Arbeit wollen wir daher die Eigenschaften von Diamanten beleuchten, um künftig die Entwicklung von einem diamantbasierten Photokatalysator zu ermöglichen.

1

Diamonds for a Carbon Neutral Future

Global warming and climate change have become the harsh reality of today. To be able to deal with the drastic impact, countries across the globe have pledged to keep the emission of CO_2 as low as possible in order to limit the temperature rise to less than 2° C. As a result carbon capture and sequestration (CCS) has gained significant interest and developing new technologies for the same has become imperative. Within the scientific community a major focus is the development of new materials for artificial photosynthesis, a process by which CO_2 can directly be converted to other hydrocarbons in the presence of sunlight. To this aim, we discuss our motivation behind investigating diamond based photocatalysts in this chapter. Having laid the context of this research, this chapter gives an insight into the fundamentals of artificial photosynthesis followed by a concise discussion of the literature that forms the basis of the work described in this thesis. Additionally, the primary research questions and an outline of this thesis are also presented.

1

1.1. The global energy and environmental concerns

The world today is faced with an economic problem concerning its energy resources namely the fossil fuels viz. coal, oil and natural gas. Such an economic problem arises because there is a disparity between the limited availability of these resources and the increasing energy demands of the rising global population. The world population currently stands at 7.4 billion. This figure is expected to reach 8 billion by 2024 according to estimates of the United Nations.[1] The existing population already consumes more than 15TW of power at present and the consumption is anticipated to increase to 30 TW by 2050. One thing that is certain is that fossil fuels which provide currently about 80% of the energy supply will be unable to keep up with this demand. This is primarily because of their limited available reserves. According to the BP Statistical Review of World Energy, the total reserves of fossil fuels are: 1,139 billion tons of coal, 187 trillion cubic meters of natural gas and 1,707 billion barrels of crude oil.[2] These numbers seem pretty large but at the current rate of extraction, coal would be exhausted in another 134 years, natural gas by the end of 2068 and crude oil by 2066.[2] However, as extraction and recovery of the reserves get more and more difficult with passing time, the effect of these dwindling reserves are likely to be felt much earlier. This is because the peak in production will occur long before the supplies run out.

Several predictions have been made since 1956 to determine the timing of peak oil. Peak oil is that point in time when the maximum rate of crude oil extraction is reached after the rate of extraction is expected to encounter an indefinite decline.[3] Usually this is a combination of both geological and economic factors. In 1956, M. King Hubbert used models to, for the first time, predict that oil production in the United States would peak between 1965 and 1971.[4] His repeated predictions about the world peak oil did not concede to the real scenario back then. In the recent years, the International Energy Agency claimed that conventional oil has already peaked in 2006. Going by this claim and according to the definition, the rate of extraction then is on a decline since 2006. This could be a plausible explanation for the high oil prices because extraction of the resources from their reserves is not only more expensive but also requires a lot of effort. In fact, price of oil has been on a rise since 2001 and it is highly unlikely that it will return to its original low levels (pre 2001).

Apart from the rising oil prices and the limited fossil fuel reserves, what seems to be a perhaps bigger concern is the impact that fossil fuels have on our environment. The central concern in this regard is the emission of CO_2 and consequently their contribution to global warming. Since the beginning of the industrial revolution, the CO_2 level in the atmosphere has increased from 280 ppm to 408 ppm and is currently increasing at the rate of 2.9 ppm/year.[5] If the atmospheric CO_2 concentration rises

to 450 ppm, there exists a high risk of global warming by more than 2°C. Effects of global warming are already being felt through adverse changes on the global ecosystem in the form of temperature and climate changes, ocean acidification etc. It is possible to adapt to the changes if the temperature can be restricted to less than 2°C. This makes it imperative to reduce our dependence on fossil fuels and curb CO_2 exhausts. Therefore, we must gradually transition towards sustainable sources of energy.

1.2. A step towards sustainability with renewables

Our energy choices affect our health, environment and economy. For a more sustainable future, we must curb the use of fossil fuels such as coal, oil and natural gas as they are substantially more harmful to the environment. A better way to meet the increasing energy demands is to use renewable sources of energy such as wind, solar, hydroelectric etc.

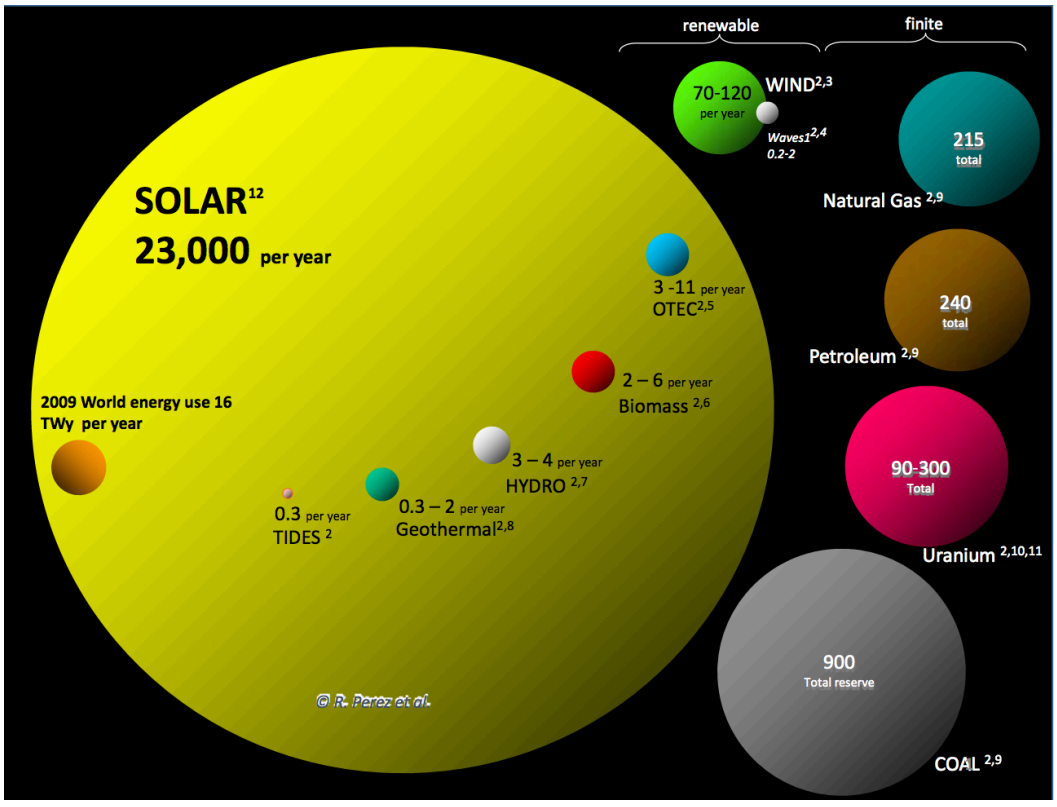

Figure 1.1: *Global Energy Potential of all renewable energy sources. This picture illustrates the outstanding potential of solar energy compared to all other sources.[6]*

Figure 1.1 shows the annual global potential for power generation of the various renewable energy sources. It is evident from the figure that, of all the renewable sources available, solar energy is the only source that has the potential to meet our energy needs. In fact the total solar energy absorbed by the earth's atmosphere, oceans and land masses is approximately 3,850,000 EJ/year which is more

in one hour than the world consumes in a year. Thus, sunlight is a compelling solution to our need for clean and abundant source of energy in the future. It is not only readily available to us, but is also secure from geopolitical tension and poses no threat to our environment through pollution or global warming emissions. In order to harness the energy from the sun to produce about 30 TW of power to meet the global energy demand, only 0.8% of the earth's surface must be covered with 10% efficient solar cells.

However, the potential solar energy that we can harness differs from the actual amount of energy present near the surface due to factors such as geography, time variation, cloud cover and the amount of land available to us. Geography affects solar energy potential because areas closer to the equator receive more solar radiation thus making it advantageous to install solar panels in such locations. Then again, the land available for the installations in such locations may also be limited as only a small portion may be unowned and suitable for solar panels. Additionally, time variation affects the solar energy potential as the sun is not available during the night as a result of which the solar panels can hardly absorb any radiation. Furthermore, clouds block the incoming sunlight and reduce the amount of solar energy available for solar cells. Due to this intermittent nature of solar energy, the amount of energy that can be absorbed by solar panels in a day is limited. In order to have access to the energy at all points of time, electricity network operators will have to cope up with the intermittent nature of solar power. [7] Although, a possible solution to this could be implementation of grid-based energy storage in the form of 'smart grids', yet, at some point in time, the grid capacity will be exceeded and large scale energy storage solutions would be necessary. Several options for alternative energy storage techniques are listed in Table 1.1.

In comparison to the mechanical –based energy storage systems or capacitors and batteries, evidently, fuels are a more effective way of storing energy with almost 2-3 order of magnitude higher energy density.[8] This is due to the fact that energy is stored in the chemical bonds that compose the fuels. Thus, storing solar energy in the form of chemical fuels is an attractive option.

Among all the chemical fuels listed in Table 1.1, hydrogen has the highest gravimetric energy density. However, its volumetric energy density is quite low (only 0.011 MJ/L which is about 3 orders of magnitude lower than gasoline), which can be increased by storing H_2 in high pressure containers (5.6 MJ/L at 700 bar) but this comes with the cost of ~10% energy penalty for H_2 compression.[8] An alternative option to store hydrogen would be in metal hydrides such as MgH_2, which at present have appreciable energy capacity of 7 wt.%.[10] Although solar hydrogen is a clean and carbon neutral energy technology and can be easily produced by water splitting with reported state-of-the-art efficiencies of 14.2%,[11] the challenges pertaining to its storage need to be addressed in order to make it a viable option. Further-

Table 1.1: *Gravimetric and Volumetric energy densities of various energy storage systems. All values are at 1 bar unless specified, adapted from [8]*

Energy Storage	Energy Density	
	Gravimetric (MJ/kg)	Volumetric (MJ/L)
Mechanical		
Compressed Air	0.512	0.16 (300 bar)
Pump Water Uphill	0.001	0.001
Capacitors		
Supercapacitor	0.306[9]	-
Batteries		
Pb	0.14-0.17	-
NiCd	0.14-0.22	-
Li-ion	0.54-0.72	-
Fuels		
Coal	24	-
Wood	16	-
Gasoline	44	35
Diesel	46	37
Methanol	20	18
Natural Gas	54	0.036
Hydrogen	143	0.011 | 5.6(700 bar)

more, solar hydrogen generation as a technology alone is not sufficient to address the environmental concerns related to global warming as a result of increased CO_2 concentrations in the atmosphere. Thus, efforts need to also be directed towards developing carbon capture and sequestration technologies to capture and utilize the existing and emitted CO_2 in the atmosphere.

One possibility is the solar conversion of CO_2 to hydrocarbon fuels. Such a carbon capture technology, if developed, will help to limit global warming to less than 2°C by recycling the carbon in the atmosphere in the form of usable fuels. The direct solar conversion of CO_2 and water vapor into hydrocarbon using sunlight would be carbon neutral while providing on a renewable basis an energy dense portable fuel that is compatible with our current energy infrastructure.

1

1.3. Storage of solar energy and CO_2 in the form of chemicals– Artificial Photosynthesis

Artificial Photosynthesis is the use of fundamental science underlying the natural photosynthetic energy conversion observed in plants to design synthetic systems for converting sunlight into chemical fuels.[12] Photosynthesis is the best method for large scale solar energy harvesting on the planet which is not only responsible for the energy stored in the fossil fuels that we are so heavily dependent on but also powers most of the biological world.[12] In the process of photosynthesis, we know that plants convert CO_2 and H_2O in the presence of sunlight to carbohydrates and oxygen. A synthetic system which could in a similar way convert CO_2 and H_2O to useful chemicals in the presence of sunlight would therefore be an ideal solution to our energy problem on the planet. The ideal system would be one, where water is oxidized at a photoanode and CO_2 is simultaneously reduced at the photocathode resulting in products that would be valuable as fuels and/or chemical feedstocks for the industry as shown in Figure 1.2. Although, water splitting has been widely researched and is a rather simple electrochemical reaction, CO_2 reduction is far more complex and challenging.

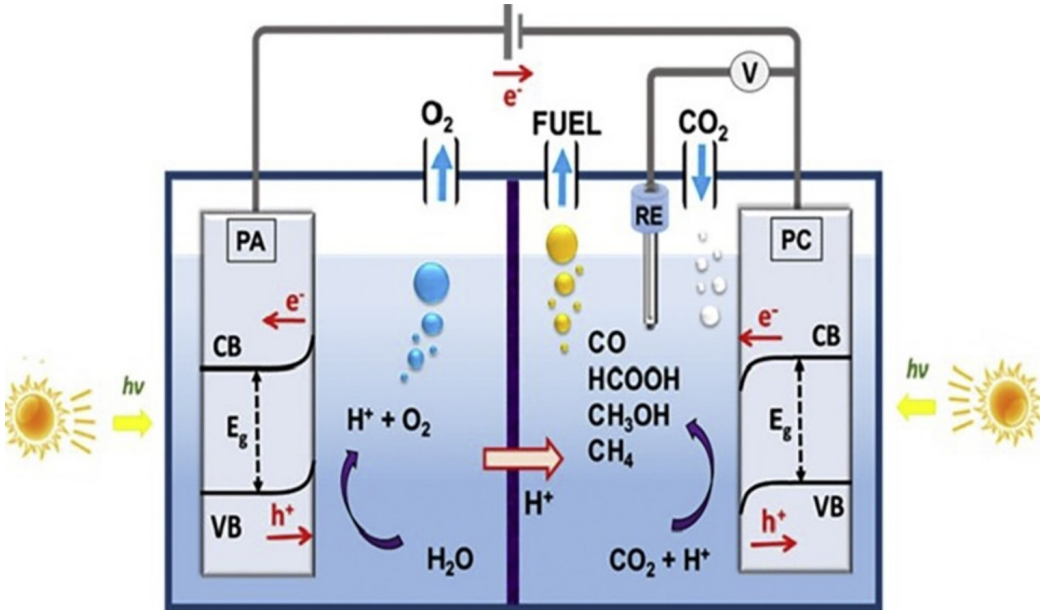

Figure 1.2: *Schematic of a photoelectrochemical cell with simultaneous CO_2 reduction at the photocathode and H_2O oxidation at the photoanode.[13]*

In the past few decades, research in the field of photochemical and photoelectrochemical CO_2 reduction has shown a tremendous increase. The catalytic conversion of CO_2 to liquid fuels is a goal that will positively impact the global carbon balance by recycling CO_2 into usable fuels. Despite the great challenges associated with the reaction, there are enormous potential rewards. CO_2 is an extremely stable

molecule produced by fossil fuel combustion and respiration. Returning CO_2 to a useful state by activation/reduction is a scientifically challenging problem which requires appropriate catalysts and energy input.[14] One of the main challenges is with respect to thermodynamic considerations.

With respect to CO_2 reduction to liquid fuels or fuel precursors such as synthesis gas (CO_2/H_2), proton coupled multiple electron transfer steps are generally more favorable than single electron reductions. This is because thermodynamically more stable molecules are produced. The reactions are summarized below. As is evident from the reactions, in a single electron reduction step the $CO_2^{\bullet-}$ has a far more negative redox potential of -1.9V due to a large reorganizational energy between the linear molecule and the bent radical anion. [15]

$$CO_2 + 2H^+ + 2e^- \longrightarrow CO + H_2O \qquad E° = -0.53V$$

$$CO_2 + 2H^+ + 2e^- \longrightarrow HCO_2H \qquad E° = -0.61V$$

$$CO_2 + 6H^+ + 6e^- \longrightarrow CH_3OH + H_2O \qquad E° = -0.38V$$

$$CO_2 + 8H^+ + 8e^- \longrightarrow CH_4 + 2H_2O \qquad E° = -0.24V$$

$$CO_2 + e^- \longrightarrow CO_2^{\bullet-} \qquad E° = -1.9V$$

Another key problem with conversion of CO_2 to liquid fuels is the assembly of the nuclei and formation of the chemical bonds to convert a simple molecule into complex and more energetic molecules. While CO_2 can be easily converted to CO followed by conversion of H_2O to H_2 resulting in synthesis gas that can be used in the Fischer Tropsch process, the actual challenge is associated with the direct electrocatalytic conversion of CO_2 to liquid fuels.[15] Here the challenge is kinetic in the sense that one catalyst must be identified which would directly complete the sequence of steps all with low energy barriers.[15] Alternatively, multiple catalysts maybe used where each catalyst is optimal for a single step in the whole conversion process.[15] This will then allow optimization of the individual catalysts for each step of the reaction.

Several semiconductor materials have been investigated over the past few decades for photochemical CO_2 reduction. For the photochemical conversion to take place, photogenerated electrons and holes must take part in the catalyzing the reactions on the surface of the catalysts. For the electron transfer or hole transfer to be successful, the band edge positions of the semiconductors with respect to the electrochemical potential of the different CO_2 redox reactions are very crucial. For the photogenerated electrons to be able to reduce CO_2 the conduction band edge should be more negative as compared

to the redox potential of CO_2. Figure1.3 below shows a schematic of the conduction and valence band potentials of semiconductor photocatalysts with respect to the redox potentials of different chemical species. Thus, from the conduction band potentials relative to those of the redox species the activity of a particular semiconductor photocatalyst with respect to formation of a particular reduction product maybe explained.

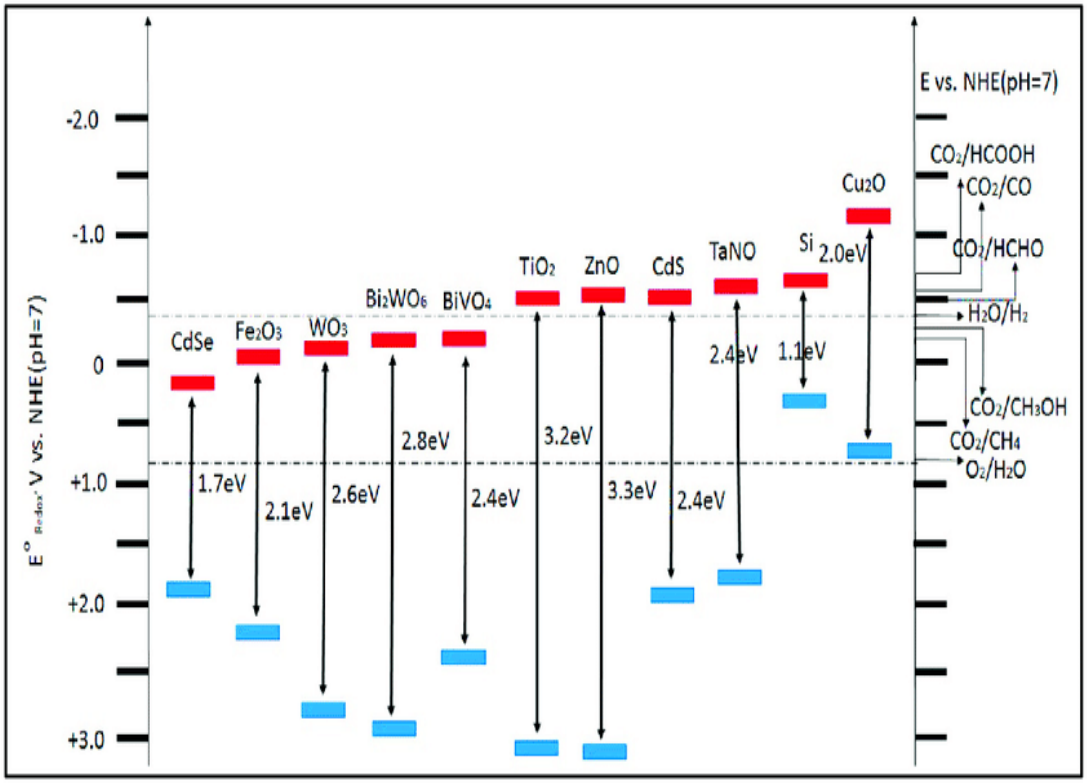

Figure 1.3: *Conduction and valence band potentials of semiconductor photocatalysts relative to the energy levels of the redox couples related to CO_2 reduction in water.[16]*

For most of the semiconductors reported for photocatalytic and photoelectrocatalytic CO_2 reduction, the reaction happens on the surface of the catalyst/electrode. Thus, adsorption of the reactant species and subsequent desorption of the product species plays a major role in the reaction. Consequently there are several phenomena that could potentially affect the catalytic activity such as competitive adsorption, mass transport limitations and structural deformations and deactivation of the catalyst.[17] In addition to this, a majority of the catalysts investigated so far for CO_2 reduction involve transition metals,[18] the cost and abundance of which are of major concern.[19, 20] To circumvent these potential issues, the search for new photocatalytic materials was extended to diamonds, when a few years ago Zhang *et al.* demonstrated the possibility of reducing CO_2 to CO directly using diamonds in the presence of UV radiation.[21] In the following section we discuss diamonds as promising materials for

artificial photosynthesis while highlighting some of the challenges associated with the material.

1.4. Diamonds for Artificial Photosynthesis

Diamonds are an allotrope of carbon containing sp^3 carbon atoms unlike other allotropes such as fullerene, carbon nanotubes and graphene which contain sp^2 carbon. Over time it has gained widespread attention as a wide band-gap semiconductor for a variety of applications due to properties such as high charge carrier mobility, thermal conductivity, chemical stability and hardness and the ability to produce it using benign starting materials in the laboratory.[22] Available in diverse morphologies such as single, poly-, nano- and ultranano- crystalline films as well as powders, diamonds can be artificially synthesized in the labs using primarily high pressure high temperature (HPHT),[23–25] plasma enhanced and microwave chemical vapour deposition (PE and MW CVD), [26–28] and detonation[29] methods. The starting material used in most of these preparation methods are benign in nature making the production processes highly sustainable. Of particular interest are nanodiamonds due to their large surface area which makes it easy to functionalize their surfaces with a wide range of atoms and functional groups.[30] This makes the material versatile for a wide range of applications such as biology, medicine, photocatalysis and environmental science.

Here, we focus on the photocatalytic applications of diamonds and specifically on CO_2 reduction. After the group of Hamers demonstrated the generation of solvated electrons by diamonds for photocatalytic reduction of N_2 to NH_3 in 2013,[31] Zhang *et al.* extended this work to demonstrate that these solvated electrons generated upon UV irradiation of diamonds are also capable of reducing CO_2 to CO as shown in Figure 1.4 .[21, 32] Specifically, the group of Hamers in both their works gave evidence of the fact that the negative electron affinity of diamonds[33] can be used to emit highly energetic solvated electrons in water more efficiently from the material. Himpsel *et al.* first showed that although diamonds have a wide band gap of 5.4 eV, in H terminated NDs the conduction band minimum (CBM) lies above the vacuum level.[33] This allows highly energetic electrons that have been photoexcited to the conduction band edge to be released into the solution spontaneously, thus making them available to catalyze reactions in solution.[31] This certainly makes diamonds promising materials for artificial photosynthesis along with the fact that it is also chemically stable in comparison to many other semiconductors that have been investigated for this application so far.

However, for the generation of solvated electrons, diamonds have to be photoactivated with deep UV radiation, which is only a very small part of the solar spectrum. For commercial applications this process must work with solar light, which therefore, presents a major challenge for the use of diamonds, which

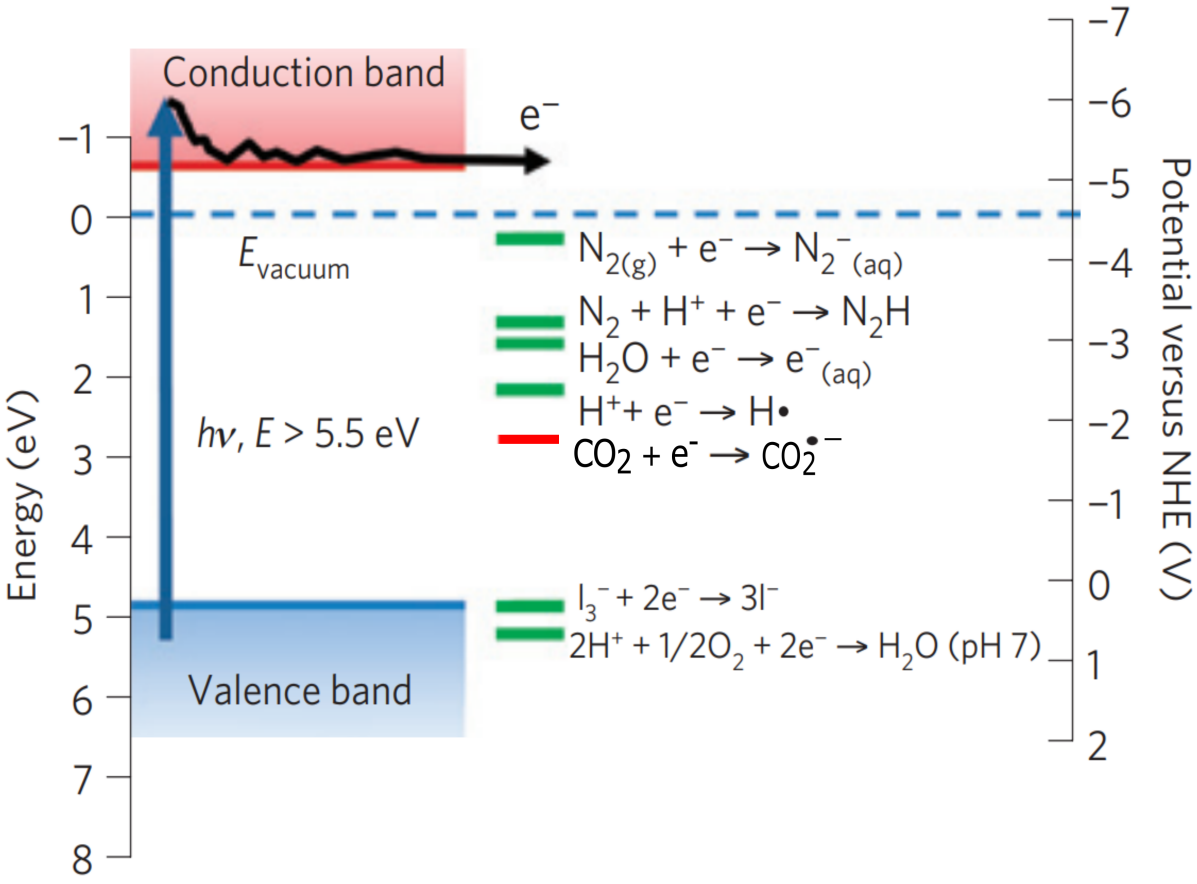

Figure 1.4: *Illustration of the band structure of H-diamond showing its negative electron affinity. Highly energetic electrons called solvated electrons can be emitted directly into the solution which can catalyze CO_2 and N_2 reduction reactions. Taken and adapted from [31]*

have a wide band gap, for photocatalytic CO_2 reduction.

Within the DIACAT project, we proposed to address this challenge following several approaches. Particularly, we will focus our investigations on three different approaches as shown in Figure 1.5, namely, doping, sensitization with visible light active complexes, and coupling with co-catalyst nanoparticles and films, which will be introduced in the following subsections.

1.4.1. Achieving visible light absorption in diamonds

Doping diamonds with B, N and P atoms

One of the most widely investigated approach in the photocatalysis community to enable visible light absorption in wide band gap semiconductors is to introduce surface states within the band gap of the material by doping. Doping is typically used in semiconductors to enhance the conductive properties of

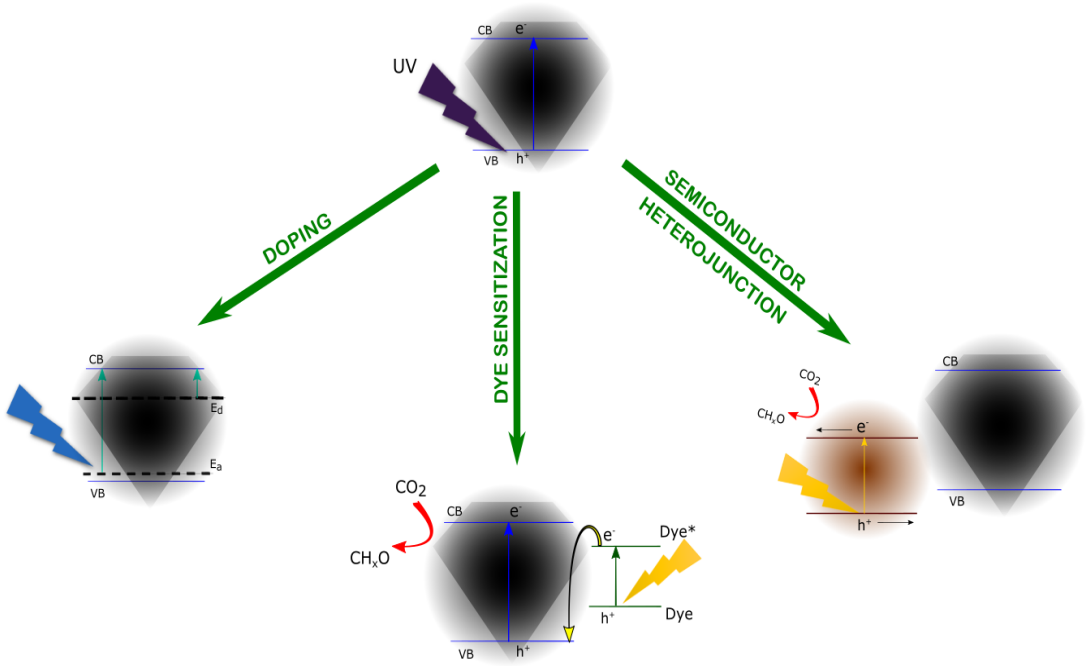

Figure 1.5: *Schematic of different approaches to address the challenge of photoexcitation of diamonds. Taken and adapted from [31]*

the material. Introducing a dopant atom in the material increases the number of available charge carriers in the material thereby increasing its conductivity. Depending on whether the dopant is a donor or an acceptor, electronic states are introduced within the band gap close to the conduction band or valence band. In the photocatalysis community, it is a well-known fact that to carry out the reactions under visible light ($\lambda > 380$ nm), the semiconductor material should ideally be optically active in this region of the solar spectrum and hence possess a band gap less than 3.1 eV.[34] The most widely investigated wide band gap semiconductor photocatalyst TiO_2 has therefore, been doped with elements such as N, C, P, S[35–37] and F[38] to make it visible light active by introducing localized dopant states within its band gap. In ultrawide band gap semiconductors such as diamonds, such defect states introduced by dopant atoms within the band gap could facilitate defect-based transitions in the material.[39–42] This would open a potential pathway by which photons of low energy could be harnessed to excite electrons from the conduction to the valence band. To this aim, B doping has been investigated in addition to n-type doping in diamond with N and P atoms. B doping is known to introduce acceptor states 0.39 eV above the valence band edge[43] and is therefore a shallow p-type dopant. Boron doping in diamonds has therefore, gained significant interest in power electronics due to its ability to reduce the series and contact resistance of the device. Additionally, there has been growing interest in N- and P doping of diamonds for electronic application, which introduce donor levels at 0.75 eV and 1.09 eV

below the conduction band edge respectively.[44] However, for most electronic applications, typically single crystal diamond films are investigated. The question that therefore, remains open is whether the acceptor and donor levels remain localized within the band gap at the positions reported in literature even for other morphologies of diamonds such as polycrystalline and nanocrystalline films and diamond nanoparticles. Furthermore, although X-ray spectroscopy experiments provide a means to directly observe these states[45] and HR-TEM experiments conducted on B-doped diamonds indicate the distribution of the dopant atoms in the material,[46, 47] the origin of the states and how they change in other morphologies of diamonds still remains unclear, which we address in this dissertation.

Sensitization of diamond surfaces with Ru complexes

Another approach to address the challenge of UV photoexcitation in diamonds is to graft visible light active transition metal complexes on its surface. Since the end goal is to have a photo(electro)catalytically active surface for CO_2 reduction, this approach could be beneficial whereby the molecular complex when covalently attached to the diamond surface could introduce states within the band gap of diamond which could facilitate charge transfer between the diamond and the complex to enhance photocatalytic activity of the system. A popular choice of molecular complex for this purpose is a Ruthenium based complex. Ru polypyridine complexes have been employed successfully in dye-sensitized solar cells [48] due to their small HOMO-LUMO gap which makes them very attractive materials for efficient harnessing of the solar energy. Furthermore, due to the stability of their oxidized and reduced forms they are especially interesting as mediators of photo-induced electron transfer reactions.[49] Hamers demonstrated a means to tether such electrochemically active molecular complexes to diamond surfaces to form redox-active surfaces which lie at the heart of photo(electro)catalysis.[50] Since then Ruthenium complexes have been attached to conductive boron doped diamond surfaces to demonstrate improved photoelectrochemical performance of the system.[51] The implications to photocatalysis were discussed based on investigations of the electronic structure of the functionalized materials with soft X-ray absorption spectroscopy techniques.[45] All of these investigations established the role of diamonds as an electron donor to the Ruthenium complex. However, in these studies the surfaces under consideration were B-doped polycrystalline diamond films. For enhanced catalytic activity it is well known that a high surface area of the catalyst is required. As a result, diamond nanoparticles were more interesting within the scope of this project. Yet, it remains to be clarified, what role is played by the Ruthenium complex when grafted on the surface of nanodiamonds and what are its implications to photocatalytic reactions.

1.4.2. Possible pathways for photocatalytic CO_2 reduction

Solvated Electron Emission: Effect of doping and surface chemistry at the diamond-water interface

In contrast to other photocatalysts for CO_2 reduction, with diamonds we hope to be able to catalyse the reaction directly in water with the help of highly energetic solvated electrons that can be generated from the material. This would essentially eliminate the need for activation of the CO_2 molecule on the catalyst surface. In order to have an efficient solvated electron generation, understanding of the diamond-water interface is absolutely imperative. In particular, the effect of surface chemistry, which is very diverse on diamond is known to have an impact and is shortly reviewed here. The diamond surface has been shown to be responsible for imparting surface conductivity to diamonds. Despite the large band gap of 5.4 eV, undoped high quality diamonds when exposed to air or liquid solutions exhibit pronounced surface conductivity [52]. Chakrapani et al. have shown in their study that electrons from the diamond transfer into redox electronic states of the liquid electrolyte leaving behind a highly conductive surface which originates from the holes [52]. Such a mechanism is referred to as 'transfer doping'. It is believed that these transfer doped holes in the nanodiamond are confined to a fairly deep yet narrow energy well where they can propagate contributing to the conductivity of the diamond surface [53]. This surface conductivity can increase or decrease depending on the properties of the surrounding liquid [53]. This makes it imperative to study the electronic structure of the interface via techniques that are non-electrochemical in nature.

For this purpose, core level spectroscopy at the K edge of oxygen and carbon was used to characterize the electronic properties of NDs in water. Soft X-ray absorption and emission spectroscopy techniques were used to study the electronic structure of diamonds deposited on a substrate and nanodiamonds in water (using a microjet). X-ray absorption spectroscopy (XAS) measurements revealed the presence of holes in the valence band of nanodiamonds in water. The absence of any signal from holes in the valence band of the nanodiamonds on the substrate confirms that the valence holes observed in the NDs in water is due to surface transfer doping. This hole doping is induced by an electron transfer between the diamond and O_2/H_2O redox couple. It was proposed that such charge transfer mechanism is possible even if the ND surface is not hydrogen or oxygen terminated. This is due to the fact that on detonated NDs other surface structures such as fullerene-like reconstructions (FLRs) may exist. A spontaneous polarization at the diamond-FLR interface may also induce migration of electrons to the graphene surface layer making it more sensitive to hole doping. [54]

Core level spectroscopy was further used by Petit *et al.* to shed light on the molecular and electronic

structure of the interfacial water on nanodiamond surfaces. It was found that the orientation of water molecules in the first solvation shell depended on the surface chemistry of the NDs. Particularly, more presence of C-H groups on the surface of NDs strongly impact the H-bonds between water molecules around the NDs. This could explain the different behaviour of the solvated electrons generated from NDs-H. At high concentrations of nanodiamonds there is a stronger contribution of the interfacial water layers which makes the electronic structure of water molecules very different from that of the bulk. Furthermore, it was suggested that the structure of the ordered water layers may resemble that of high density amorphous ice. [54]

Apart from core level spectroscopy, infrared spectroscopy techniques have also been employed to understand ND-water interactions as it impacts the chemical and catalytic activity of the nanoparticles. It is quite challenging to conduct IR measurements in liquid phase due to strong response from the solvent molecules. Therefore, most of the measurements are reported in vacuum and under a gaseous atmosphere. The first infrared spectroscopy results in vacuum revealed the presence of hydroxyl groups on the surface of diamonds as a result of water dissociation on carbon dimers. Such carbon dimers are known to result from FLRs that are formed due to surface reconstruction of diamonds upon annealing in vacuum.[55] In a gaseous atmosphere primarily composed of humid air, a strong adsorption of water molecules were observed on detonation NDs even at relative humidities < 35%. [56]Such a strong adsorption was evidenced by an increase in the intensities of the OH stretching and bending modes. On the other hand, a shift in the OH stretching mode alone indicated OH adsorption at acidic and basic sites on the ND surfaces.[55] Additionally it was also reported that the ND surfaces act as nucleation sites for water molecules that are H-bonded to neighbouring water molecules thus forming a multi-layered water structure.[55]

The study of diamond-water interface continues to be of interest for the development of an optimum diamond based photocatalyst with desired properties for CO_2 reduction. Particularly, H-terminated surfaces are readily hydroxylated under prolonged exposure to UV irradiation in water. The resulting OH-terminated surfaces also possess negative electron affinity (NEA). An understanding of their surface interactions in water could therefore be interesting to gain useful insights into electron emission from these surfaces in water.

Formation of heterojunctions with transition metal oxides

While doping and surface functionalization with molecular complexes are potential means to address the challenge of photoactivation of diamonds for catalysis, by co-promoting diamonds with a catalytically active species, a new photocatalyst system could be developed which exhibit enhanced activity

as well as stability towards CO_2 reduction reactions. For this purpose, diamond NPs were coated with metallic Cu NPs and thin film diamond electrodes were coated with electrodeposited Cu_2O to investigate the changes in oxidation state of Cu during the course of the electrochemical reactions. The choice of Cu based co-catalysts was motivated by the extensive research conducted on the high catalytic activity and selectivity towards CO_2 reduction. Research has shown that the selectivity of Cu based electrodes towards different reduction products originated in the different adsorption of CO_2 on the different facets of the catalyst.[57] This combined with the direct band gaps of 1.2 eV and 2.2 eV for CuO and Cu_2O respectively,[58] makes copper oxides an attractive material of choice. However, due to fast recombination of electron-hole pairs in the material it is quite unstable.[59] For commercial application of artificial photosynthesis, therefore, developing a stable photocatalyst is essential. In most cases this can be achieved by combining Cu based catalysts with wide band gap semiconductors which tend to be more stable. Traditionally, wide band gap semiconductors such as TiO_2[60]and ZnO[61] have been coupled to CuOx to form stable photocatalysts with enhanced activity, where TiO_2 and ZnO served as a support for the catalyst facilitating charge separation in the material. In addition, organic nanomaterials such as graphene and carbon nitrides have also been used to form composite catalysts with CuOx for enhanced activity.[59] While diamonds have a wide band gap, they are robust and chemically stable. Therefore, they can serve as an excellent support material for copper based catalysts. In fact, literature reports have shown boron-doped diamond to be a promising support material in fuel cells.[62, 63] Thus, a composite catalyst combining diamonds and CuOx could be beneficial in synergistically improving the stability as well as the catalytic activity of the material towards CO_2 reduction reactions.

1.5. Aim and Outline of the thesis

The main focus of this dissertation is the investigation of the electronic structure of diamonds either modified by doping or by surface functionalization with catalytically active metals and visible light active metal complexes. In addition, this thesis aims to lay the foundation of certain proof-of-concept investigations at the diamond-water interface, that would be essential to understand the potential application of diamond as a photocatalyst or as a photoelectrode in reactors and photoelectrochemical cells respectively. As this research project was a part of the EU Project DIACAT, all materials studied in the experiments were obtained from partners in the consortium. During the course of these investigations, the research was primarily focussed on answering two main questions,

- How to enable visible light absorption in diamonds? - This question was addressed using the following two approaches,

  - Doping of diamonds with B, N and P - [Chapter 3]
  - Sensitization with visible light active Ruthenium complexes - [Chapter 4]

- How to make diamonds viable for efficient CO_2 photoreduction? - In an effort towards developing diamond based photocatalysts the following investigations were conducted,
  - Direct electron emission from diamonds into water - Investigation of the diamond surface chemistry in water [Chapter 5]
  - Coupling diamonds with Cu based co-catalyst nanoparticles - *In-situ* X-ray spectroscopy to monitor changes in Cu oxidation state [Chapter 5]

To this aim, two different types of spectroscopy techniques were used in conducting the investigations, soft X-ray based spectroscopy and infrared spectroscopy. The first question was answered by performing XAS and XES measurements in the solid state at the Lixedrom endstation. The experimental results of the investigations were supported further by theoretical studies conducted by collaborators at Uppsala University and in HZB. The electronic structure of diamond at the solid-liquid interface was probed using XAS on the samples after annealing and after air exposure at the PEAXIS end station. Additionally, some first ambient pressure PES measurements were also conducted at the Sol3PES end station. XAS measurements conducted in an electrochemical flow cell at the Lixedrom end station provided further insights into the electronic properties of the transition metal coated nanodiamonds. In order to understand the role of pH, diamond nanoparticles with two different surface terminations, H and OH, in different pH solutions were exposed to humid air and probed with FTIR in the attenuated total reflection mode. Our investigations revealed some interesting results that will be discussed in the following chapters.

To begin with, chapter 2 will introduce the theoretical concepts behind the different spectroscopy techniques in order to provide an understanding of the fundamental principles behind the measurements and the kind of information that can be obtained from them. This will be followed by a brief description of the experimental setups that were used to conduct the measurements.

In chapter 3 experimental results obtained from soft X-ray absorption spectroscopy on B, N and P-doped diamonds will be discussed with its potential implications on photocatalysis. Section 3.1 will discuss published results on both experimental and theoretical studies conducted on B-doped diamonds which show that sub-band gap states in the material can be altered by combining nanostructuration and boron doping. A brief discussion on n-type diamonds, namely N- and P-doped diamonds in section 3.2 will be presented to demonstrate the presence of electron emission states in these materials close to the

conduction band minimum which could be promising for the generation of solvated electrons to carry out photocatalysis as described in section 3.3 of this chapter.

Results on Ruthenium complex functionalized nanodiamonds will be presented in chapter 4 of this dissertation. As a first step, XAS investigations will be presented to demonstrate electronic coupling between the complex and nanodiamonds in section 4.2. This discussion will be extended with the help of theoretical investigations to focus on $Ru(bpy)_3$ functionalized nanodiamonds with different linkers in section 4.3 to understand the effect of linkers on sub-band gap states in the diamond. Understanding the influence of linker on the electronic structure of the material would be an essential step towards understanding the charge carrier dynamics in these materials at a later stage, which is currently out of the scope of this thesis. With further investigations of the valence band of the functionalized diamonds, section 4.4 will present insights into the role of the Ru complex in the hybrid system.

Chapter 5 will present different proof-of-concept investigations conducted at the diamond-water interface using different experimental techniques. With a brief investigation of the electronic structure at the diamond-water interface XAS techniques, section 5.1 will provide first insights into the influence of moisture under ambient conditions on the surface electronic properties of the diamonds. The influence of pH on different diamond surfaces will be discussed in section 5.2 followed by a detailed investigation of metal coated nanodiamonds that will be presented in 5.3. This section will exclusively focus on understanding the role of diamonds in this hybrid photocatalyst thereby establishing a fundamental understanding of enhanced photocatalytic performance demonstrated by this material.

The last chapter of this thesis will summarize the most important results and present an outlook for future research in this direction.

References

[1] *World Population Today,* http://www.worldometers.info/world-population/.

[2] *World Reserves of Fossil Fuels,* https://knoema.com/smsfgud/bp-world-reserves-of-fossil-fuels.

[3] *Predicting the Time of Peak Oil,* https://en.wikipedia.org/wiki/Predicting_the_timing_of_peak_oil.

[4] M. K. Hubbert, *Nuclear Energy and the Fossil Fuels,* (1956), spring Meeting of the Southern District, American Petroleum Institute, Plaza Hotel, San Antonio, Texas.

[5] *Trends in Atmospheric Carbon Dioxide,* https://www.esrl.noaa.gov/gmd/ccgg/trends/index.html.

[6] *Solar Energy,* https://cleantechnica.com/solar-power/.

[7] R. van de Krol and M. Grätzel, *Photoelectrochemical Hydrogen Production* (Springer Science and Business Media, New York, 1993).

[8] F. F. Abdi, *Towards Highly Efficient Bias Free Solar Water Splitting*, Ph.D. thesis, Technical University of Delft (2013).

[9] C. Liu, Z. Yu, D. Neff, A. Zhamu, and B. Z. Jang, *Graphene-Based Supercapacitor with an Ultrahigh Energy Density,* Nano Letters **10**, 4863 (2010).

[10] M. Fellet, *Research on Metal Hydrides revived for Next-Generation Solutions to Renewable Energy Storage,* MRS Bulletin **38**, 1012 (2013).

[11] J.-W. Schüttauf, M. A. Modestino, E. Chinello, D. Lambelet, A. Delfino, D. Dominé, A. Faes, M. Despeisse, J. Bailat, D. Psaltis, C. Moser, and C. Ballif, *Solar-to-Hydrogen Production at 14.2% Efficiency with Silicon Pho-*

tovoltaics and Earth-Abundant Electrocatalysts, Journal of The Electrochemical Society **163**, F1177 (2016).
[12] D. Gust, T. A. Moore, and A. L. Moore, *Solar Fuels via Artificial Photosynthesis,* Accounts of Chemical Research **42**, 1890 (2009).
[13] E. Kalamaras, M. M. Maroto-Valer, M. Shao, J. Xuan, and H. Wang, *Solar carbon fuel via photoelectrochemistry,* Catalysis Today **317**, 56 (2018).
[14] B. Kumar, M. Llorente, J. Froehlich, T. Dang, A. Sathrum, and C. P. Kubiak, *Photochemical and Photoelectrochemical Reduction of CO_2,* Annual Review of Physical Chemistry **63**, 541 (2012).
[15] E. E. Benson, C. P. Kubiak, A. J. Sathrum, and J. M. Smieja, *Electrocatalytic and homogeneous approaches to conversion of CO_2 to liquid fuels,* Chem. Soc. Rev. **38**, 89 (2009).
[16] S. Nahar, M. F. M. Zain, A. A. H. Kadhum, H. A. Hasan, and M. R. Hasan, *Advances in Photocatalytic CO_2 Reduction with Water: A Review,* Materials **10** (2017), 10.3390/ma10060629.
[17] C. Sievers, Y. Noda, L. Qi, E. M. Albuquerque, R. M. Rioux, and S. L. Scott, *Phenomena Affecting Catalytic Reactions at Solid–Liquid interfaces,* ACS Catalysis **6**, 8286 (2016).
[18] K. P. Kuhl, T. Hatsukade, E. R. Cave, D. N. Abram, J. Kibsgaard, and T. F. Jaramillo, *Electrocatalytic Conversion of Carbon Dioxide to Methane and Methanol on Transition Metal Surfaces,* Journal of the American Chemical Society **136**, 14107 (2014).
[19] M. Ming, T. B. J., X. Jie, and S. W. A., *Selective and Efficient Reduction of Carbon Dioxide to Carbon Monoxide on Oxide-Derived Nanostructured Silver Electrocatalysts,* Angewandte Chemie **128**, 9900 (2016).
[20] X. Zhang, Z. Wu, X. Zhang, L. Li, Y. Li, H. Xu, X. Li, X. Yu, Z. Zhang, Y. Liang, and H. Wang, *Highly selective and active CO_2 reduction electrocatalysts based on cobalt phthalocyanine/carbon nanotube hybrid structures,* Nature Communications **8**, 14675 (2017).
[21] L. Zhang, D. Zhu, G. M. Nathanson, and R. J. Hamers, *Selective Photoelectrochemical Reduction of Aqueous CO_2 to CO by Solvated Electrons,* Angewandte Chemie International Edition **53**, 9746 (2014).
[22] C. Nebel, *General Properties of Diamonds,* in *Nanodiamonds-Advanced Materials Analysis, Properties and Applications*, edited by J.-C. Arnault (Elsevier, 2017) Chap. 1, pp. 1–21.
[23] E. A. Ekimov, V. A. Sidorov, E. D. Bauer, N. N. Mel'nik, N. J. Curro, J. D. Thompson, and S. M. Stishov, *Superconductivity in diamond,* Nature **428**, 542 (2004).
[24] E. A. Ekimov, V. A. Sidorov, A. Zoteev, Y. Lebed', J. D. Thompson, E. D. Bauer, and S. M. Stishov, *Superconductivity in diamond induced by boron doping at high pressure,* physica status solidi (b) **246**, 667 (2009).
[25] E. A. Ekimov, O. S. Kudryavtsev, A. A. Khomich, O. I. Lebedev, T. A. Dolenko, and I. I. Vlasov, *High-Pressure Synthesis of Boron-Doped Ultrasmall Diamonds from an Organic Compound,* Advanced Materials **27**, 5518 (2015).
[26] K. Nishimura, K. Das, and J. T. Glass, *Material and electrical characterization of polycrystalline boron-doped diamond films grown by microwave plasma chemical vapor deposition,* Journal of Applied Physics **69**, 3142 (1991).
[27] R. Zhang, S. Lee, and Y. Lam, *Characterization of heavily boron-doped diamond films,* Diamond and Related Materials **5**, 1288 (1996).
[28] P. May, W. Ludlow, M. Hannaway, P. Heard, J. Smith, and K. Rosser, *Raman and conductivity studies of boron-doped microcrystalline diamond, facetted nanocrystalline diamond and cauliflower diamond films,* Diamond and Related Materials **17**, 105 (2008).
[29] V. Yu. Dolmatov, *Detonation synthesis ultradispersed diamonds: properties and applications,* Russ. Chem. Rev. **70**, 607 (2001).
[30] A. Krueger and D. Lang, *Functionality is Key: Recent Progress in the Surface Modification of Nanodiamond,* Advanced Functional Materials **22**, 890 (2012).
[31] D. Zhu, L. Zhang, R. E. Ruther, and R. J. Hamers, *Photo-illuminated diamond as a solid-state source of solvated electrons in water for nitrogen reduction,* Nature Materials **12**, 836 (2013).
[32] L. Zhang and R. J. Hamers, *Photocatalytic reduction of CO_2 to CO by diamond nanoparticles,* Diamond and Related Materials **78**, 24 (2017).
[33] F. J. Himpsel, J. A. Knapp, J. A. VanVechten, and D. E. Eastman, *Quantum photoyield of diamond(111)—A stable negative-affinity emitter,* Phys. Rev. B **20**, 624 (1979).
[34] *Optical Properties of Semiconductors,* `http://www.ndhu.edu.tw/ezfiles/29/1029/img/2481/Chapter21-OpticalProperties.pdf`.
[35] T. Umebayashi, T. Yamaki, H. Itoh, and K. Asai, *Analysis of electronic structures of 3d transition metal-doped TiO_2 based on band calculations,* Journal of Physics and Chemistry of Solids **63**, 1909 (2002).
[36] R. Asahi, T. Morikawa, T. Ohwaki, K. Aoki, and Y. Taga, *Visible-Light Photocatalysis in Nitrogen-Doped Titanium Oxides,* Science **293**, 269 (2001).
[37] J. H. Park, S. Kim, and A. J. Bard, *Novel Carbon-Doped TiO_2 Nanotube Arrays with High Aspect Ratios for Efficient Solar Water Splitting,* Nano Letters **6**, 24 (2006).
[38] D. Li, H. Haneda, N. K. Labhsetwar, S. Hishita, and N. Ohashi, *Visible-light-driven photocatalysis on fluorine-doped TiO_2 powders by the creation of surface oxygen vacancies,* Chemical Physics Letters **401**, 579 (2005).
[39] J. Wang, D. N. Tafen, J. Lewis, Z. Hong, A. Manivannan, M. Zhi, M. Li, and N. Wu, *Origin of Photocatalytic Activity of Nitrogen-Doped TiO_2 Nanobelts,* Journal of the American Chemical Society **131**, 12290 (2009).
[40] S. Baruah, S. S. Sinha, B. Ghosh, S. K. Pal, A. K. Raychaudhuri, and J. Dutta, *Photoreactivity of Zno nanoparticles in visible light: Effect of surface states on electron transfer reaction,* Journal of Applied Physics **105**,

074308 (2009).
[41] D. Wang, G. Xing, M. Gao, L. Yang, J. Yang, and T. Wu, *Defects-Mediated Energy Transfer in Red-Light-Emitting Eu-Doped Zno Nanowire Arrays,* The Journal of Physical Chemistry C **115**, 22729 (2011).
[42] M. Mahboub, P. Xia, J. Van Baren, X. Li, C. H. Lui, and M. L. Tang, *Midgap States in PbS Quantum Dots Induced by Cd and Zn Enhance Photon Upconversion,* ACS Energy Letters **3**, 767 (2018).
[43] V. V. S. S. Srikanth, P. Sampath Kumar, and V. B. Kumar, *A Brief Review on the In Situ Synthesis of Boron-Doped Diamond Thin Films,* International Journal of Electrochemistry **2012**, 7 (2011).
[44] K. Jackson, M. R. Pederson, and J. G. Harrison, *Donor levels and impurity-atom relaxation in nitrogen- and phosphorus-doped diamond,* Phys. Rev. B **41**, 12641 (1990).
[45] I. Zegkinoglou, P. L. Cook, P. S. Johnson, W. Yang, J. Guo, D. Pickup, R. González-Moreno, C. Rogero, R. E. Ruther, M. L. Rigsby, J. E. Ortega, R. J. Hamers, and F. J. Himpsel, *Electronic Structure of Diamond Surfaces Functionalized by Ru(tpy)$_2$,* The Journal of Physical Chemistry C **116**, 13877 (2012).
[46] N. Dubrovinskaia, R. Wirth, J. Wosnitza, T. Papageorgiou, H. F. Braun, N. Miyajima, and L. Dubrovinsky, *An insight into what superconducts in polycrystalline boron-doped diamonds based on investigations of microstructure,* Proceedings of the National Academy of Sciences **105**, 11619 (2008).
[47] J. T. Huang, C. S. Hu, J. Hwang, H. Chang, and L. J. Lee, *Desegregation of boron at the grain boundaries of the in situ boron doped diamond films,* Applied Physics Letters **67**, 2382 (1995).
[48] C.-Y. Chen, S.-J. Wu, C.-G. Wu, J.-G. Chen, and K.-C. Ho, *A Ruthenium Complex with Superhigh Light-Harvesting Capacity for Dye-Sensitized Solar Cells,* Angewandte Chemie **118**, 5954 (2006).
[49] A. Juris, V. Balzani, F. Barigelletti, S. Campagna, P. Belser, and A. von Zelewsky, *Ru(II) polypyridine complexes: photophysics, photochemistry, eletrochemistry, and chemiluminescence,* Coordination Chemistry Reviews **84**, 85 (1988).
[50] R. E. Ruther, M. L. Rigsby, J. B. Gerken, S. R. Hogendoorn, E. C. Landis, S. S. Stahl, and R. J. Hamers, *Highly Stable Redox-Active Molecular Layers by Covalent Grafting to Conductive Diamond,* Journal of the American Chemical Society **133**, 5692 (2011).
[51] W. S. Yeap, X. Liu, D. Bevk, A. Pasquarelli, L. Lutsen, M. Fahlman, W. Maes, and K. Haenen, *Functionalization of Boron-Doped Nanocrystalline Diamond with N3 Dye Molecules,* ACS Applied Materials & Interfaces **6**, 10322 (2014).
[52] V. Chakrapani, J. C. Angus, A. B. Anderson, S. D. Wolter, B. R. Stoner, and G. U. Sumanasekera, *Charge Transfer Equilibria Between Diamond and an Aqueous Oxygen Electrochemical Redox Couple,* Science **318**, 1424 (2007).
[53] C. E. Nebel, *Surface-Conducting Diamond,* Science **318**, 1391 (2007).
[54] T. Petit, M. Pflüger, D. Tolksdorf, J. Xiao, and E. F. Aziz, *Valence holes observed in nanodiamonds dispersed in water,* Nanoscale **7**, 2987 (2015).
[55] T. Petit, *Interactions with Solvent,* in *Nanodiamonds-Advanced Materials Analysis, Properties and Applications*, edited by J.-C. Arnault (Elsevier, 2017) Chap. 11, pp. 301–318.
[56] T. Petit, L. Puskar, T. Dolenko, S. Choudhury, E. Ritter, S. Burikov, K. Laptinskiy, Q. Brzustowski, U. Schade, H. Yuzawa, M. Nagasaka, N. Kosugi, M. Kurzyp, A. Venerosy, H. Girard, J.-C. Arnault, E. Osawa, N. Nunn, O. Shenderova, and E. F. Aziz, *Unusual Water Hydrogen Bond Network around Hydrogenated Nanodiamonds,* The Journal of Physical Chemistry C **121**, 5185 (2017).
[57] W. Luo, X. Nie, M. J. Janik, and A. Asthagiri, *Facet Dependence of CO_2 Reduction Paths on Cu Electrodes,* ACS Catalysis **6**, 219 (2016).
[58] D. Tahir and S. Tougaard, *Electronic and optical properties of Cu, Cuo and Cu_2O studied by electron spectroscopy,* Journal of Physics: Condensed Matter **24**, 175002 (2012).
[59] K. C. Christoforidis and P. Fornasiero, *Photocatalysis for Hydrogen Production and CO_2 Reduction: The Case of Copper-Catalysts,* ChemCatChem **0** (2018), 10.1002/cctc.201801198.
[60] W. Siripala, A. Ivanovskaya, T. F. Jaramillo, S.-H. Baeck, and E. W. McFarland, *A Cu_2O/TiO_2 heterojunction thin film cathode for photoelectrocatalysis,* Solar Energy Materials and Solar Cells **77**, 229 (2003).
[61] Y. Cui, C. Wang, G. Liu, H. Yang, S. Wu, and T. Wang, *Fabrication and photocatalytic property of Zno nanorod arrays on Cu_2O thin film,* Materials Letters **65**, 2284 (2011).
[62] G. R. Salazar-Banda, K. I. Eguiluz, and L. A. Avaca, *Boron-doped diamond powder as catalyst support for fuel cell applications,* Electrochemistry Communications **9**, 59 (2007).
[63] J. Kim, Y.-S. Chun, S.-K. Lee, and D.-S. Lim, *Improved electrode durability using a boron-doped diamond catalyst support for proton exchange membrane fuel cells,* RSC Adv. **5**, 1103 (2015).

2

Experimental and Theoretical Methods

Different experimental techniques have been used in this work to investigate different properties of diamond materials. Soft X-ray spectroscopy techniques, which are element-sensitive are powerful tools to probe the electronic structure of materials. These techniques which encompass XAS, XES and XPS can provide insights into the unoccupied, occupied and valence states in a material, respectively. In this dissertation they were used to probe the electronic structure of diamonds at the C K edge. This chapter presents a theoretical background of all the experimental methods used in this work starting with a description of X-ray interaction with matter and X-ray absorption, emission and photoemission spectroscopies. Additionally, chemical interactions at the diamond-water interface were also studied using infrared spectroscopy on diamonds with different surface terminations. After discussing some fundamentals of vibrational spectroscopy, the Fourier Transform IR spectroscopy technique is described. The subsequent sections of the chapter describe the instrumentation including the synchrotron facility BESSY II, where the experiments presented in this work were conducted. The chapter is concluded with description of the theoretical methods used to interpret some of the experimental data that are presented in the subsequent chapters of this thesis.

2.1. X-ray spectroscopies

X-ray radiation, discovered by Wilhelm Conrad Röntgen in 1895 while performing high voltage discharge tube experiments in a dark room,[1] is a type of electromagnetic radiation whose wavelength ranges from a few Angstroms to a few nanometers. Several experiments conducted shortly after the discovery of X-rays eventually led to the observation of sharp or diffuse lines and bands on a photographic plate when X-rays impinged a metal sheet.[2] These lines and bands, referred to as a spectrum, later helped in the determination of different absorption edges of the elements in the periodic table.[2] Today, this continues to form a fundamental basis of our X-ray spectroscopy experiments thus enabling us to study the structure and properties of matter.

The two complementary techniques X-ray Absorption Spectroscopy (XAS) and X-ray Emission Spectroscopy (XES) together with Photoemission Spectroscopy (PES), generally referred to as X-ray spectroscopy provide an insight into the local partial density of unoccupied and occupied states in a material. The method involves production and monitoring of electronic transitions between ground and excited states. Since the method is based on photoexcitation of a core level electron in an atom to a higher unoccupied state or its ejection into the continuum, it is quite element-sensitive. In the following subsections, the fundamental absorption and emission processes upon X-ray excitation will be discussed followed by a description of the XAS, XES and PES techniques.

2.1.1. X-ray interaction with matter

Following the works of Planck, Einstein and de Broglie, the wave-particle duality of electromagnetic radiation has been an established fact since the 1900's. Thus, the energy of X-rays can also be given by the following equation,

$$E = h\nu = \frac{hc}{\lambda} \tag{2.1}$$

where E is the energy of the incident photon, h is the Planck's constant, c is the speed of light, ν and λ denote the frequency and wavelength of the wave, respectively. Upon interaction with matter, the intensity of X-rays is attenuated as a result of interaction of individual photons in the beam with atoms of the material. In this process of interaction, the X-ray photons are either absorbed or scattered. An X-ray photon is said to be scattered when it is deflected from its original direction upon interacting with the electron in the atom. A simple schematic of the different events upon X-ray interaction with matter is shown in Figure 2.1

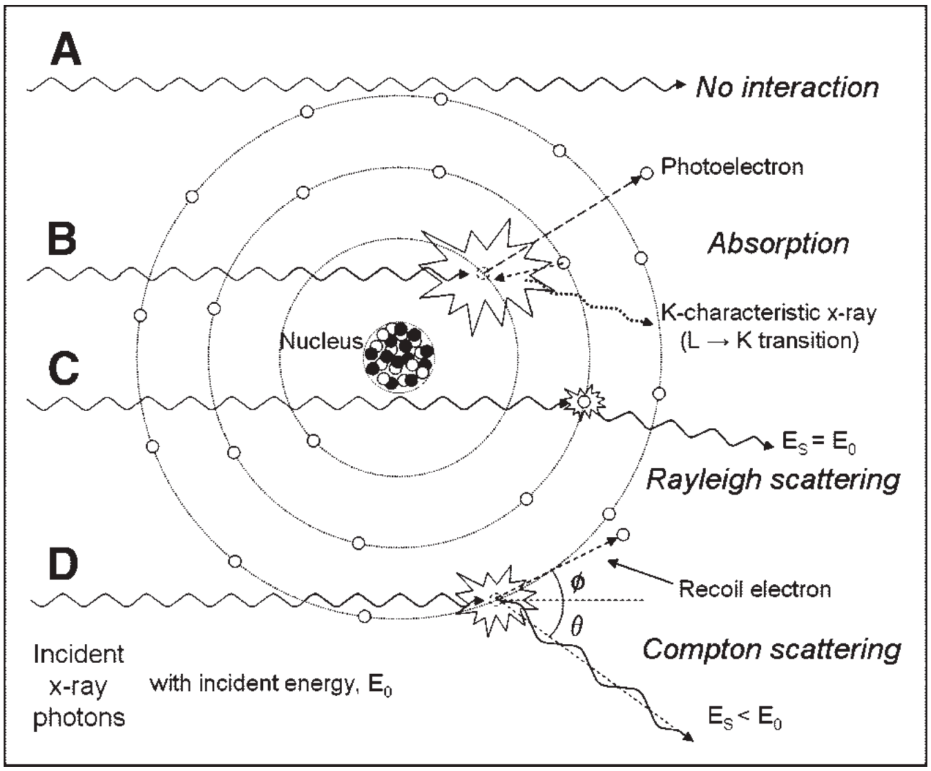

Figure 2.1: *Schematic of different processes upon interaction of an electromagnetic wave with an atomic target, taken from [3]. The incident photons can pass through the material without any interaction (A). Upon interaction with an atom, the photons can get absorbed (B), also known as photoelectric absorption or scattered either elastically (C), known as Thomson scattering or inelastically (D).*

As shown in Figure 2.1, interaction of incident X-ray photons with the electrons could result in elastic scattering of the photon, also known as *Thomson scattering*. Here the energy of the outgoing photon is the same as that of the incoming photon. In case of inelastic scattering the energy of the photon emitted after the scattering event is typically lower than that of the incident photon and the energy difference is transferred to the material for excitation of electrons in the material. In addition to scattering, another process that occurs when an X-ray photon collides with an atom is its absorption. Also known as *photoelectric absorption*, in this process an incident photon interacts with the core electron of an atom and excites it to the valence level or higher. When the energy of the incident photon is higher than the energy of the core electron but not enough to ionize the atom, the electron is excited to an unoccupied state above the Fermi level in the material. This is the underlying process in X-ray Absorption Spectroscopy (XAS) to probe the local density of unoccupied states in a material, that will be discussed in section 2.1.2. In the case where the incident photon energy is higher than the ionization energy of the material, an electron will be ejected with a kinetic energy that is given by,

$$K.E = h\nu_i - E_B - \phi \tag{2.2}$$

2

where $K.E$ denotes the kinetic energy of the outgoing photoelectron, ν_i the frequency of the incident X-ray, E_B the binding energy of the core electron and ϕ the work function of the material. Together $E_B + \phi$ denote the ionization energy of the material. This is the process behind photoemission spectroscopy, as discussed briefly in section 2.1.3 The absorption of an X-ray photon gives rise to two subsequent processes: X-ray fluorescence and non-radiative Auger electron emission. In the former process, the excited electron releases its excess energy upon relaxation which is carried away by an X-ray photon that is detected in a typical X-ray Emission Spectroscopy (XES) measurement. In Auger electron emission, the excess energy is carried away by an electron, unlike the case of X-ray fluorescence. These processes are depicted in Figure 2.2 and form the fundamental basis for the XAS, XES and PES techniques which will be described in the sections below.

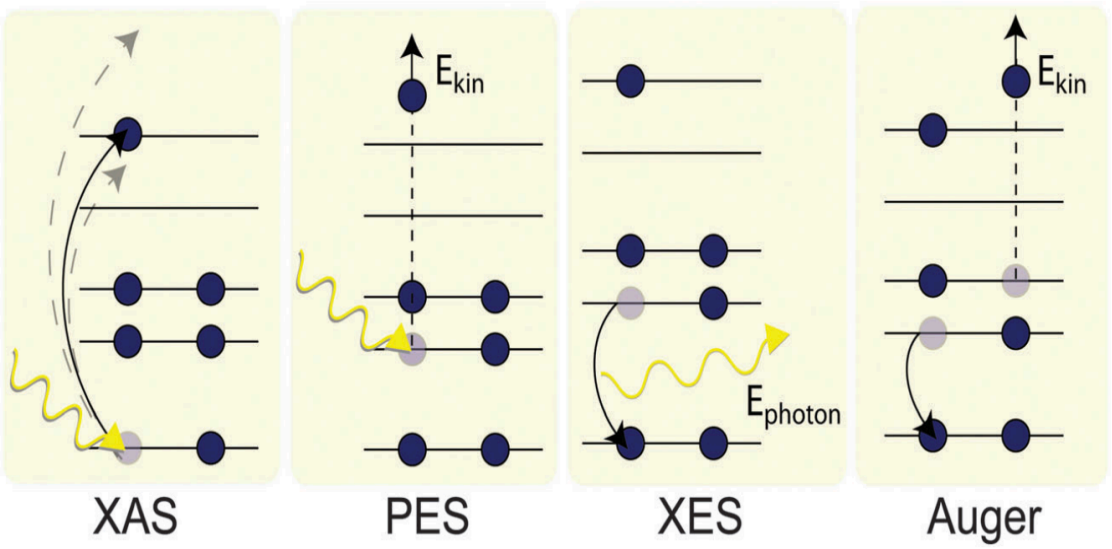

Figure 2.2: *Schematic of X-ray absorption process (XAS), photoexcitation of an electron into the continuum (PES), emission of an X-ray photon upon decay of a valence electron into the core hole (XES) and non-radiative relaxation of the core hole via Auger emission (Auger), taken from [4]*

2.1.2. X-ray absorption and emission spectroscopy

As pointed out in the previous section, in X-ray absorption spectroscopy a core electron is excited to an unoccupied state above the Fermi level. In a homogeneous isotropic material, absorption results in an attenuation of the transmitted beam intensity I upon passing through a sample of thickness D. This attenuation can be described by the Beer-Lambert law,

$$I = I_0 e^{-\mu D} \tag{2.3}$$

where I_0 is the incident intensity and μ is the total linear absorption coefficient. In a solid constituting of n different chemical species, this absorption coefficient is related to the absorption cross section σ_i and the atomic volume ρ_i of the constituent atoms,

$$\mu = \sum_{i=1}^{n} \mu_i = \sum_{i=1}^{n} \rho_i \sigma_i \tag{2.4}$$

The absorption cross section σ_i in this equation is usually expressed in square centimeters or mega barns (1 Mbarn = 10^{-18} cm^2). It is an intrinsic property of an element and can be experimentally measured by measuring the intensity of the transmitted beam as a function of incident photon energy as suggested by the Beer-Lambert law in Equation 2.3. This measurement forms the basis of X-ray absorption spectroscopy, which gives insights into the local partial density of the unoccupied states in the material. If the absorption coefficient is plotted as a function of energy, three primary features are observed as shown in Figure 2.3. Firstly, a general decreasing trend of the absorption coefficient is observed which indicates an overall decrease in X-ray absorption as the incident photon energy increases.[5] Secondly, sudden rises are observed at specific positions which are called edges and are characteristic to a material.[5] Finally, a series of oscillatory structures are observed above the edges which correspond to the extended X-ray absorption fine structure (EXAFS) and mainly reveals structural information of the material[5] which is out of scope of this thesis.

Here, we specifically focus on the edges observed in Figure 2.3 which appear due to the excitation of inner shell electrons. When the energy of the incoming photon is greater than or equal to the binding energy of the core electron, the photon is absorbed and this results in the excitation of the core electron. Now, electrons in quantum mechanics occupy discrete energy levels which are denoted by a series of quantum numbers which specify an electronic state. The principal quantum number **n** can take only positive integral values 1, 2, 3 and so on and is often denoted by the alphabets K, L, M and so on, corresponding to the shells in an atom. The value of **n** determines the size of the shell. Higher the value of **n**, the bigger is the shell and the farther away it is located from the nucleus. Each shell in an atom comprises of a smaller group of subshells called orbitals, denoted by the secondary quantum number *l* which determine the shape of the orbital. For any given shell, the quantum number *l* can take integral values from 0 to **n-1** and is denoted by the letters s, p, d, f, g and so on. According to the Sommerfeld notation, when an electron is ejected from the 1s, 2s, $2p_{1/2}$, $2p_{3/2}$ levels, the edge is denoted as K, L_1,

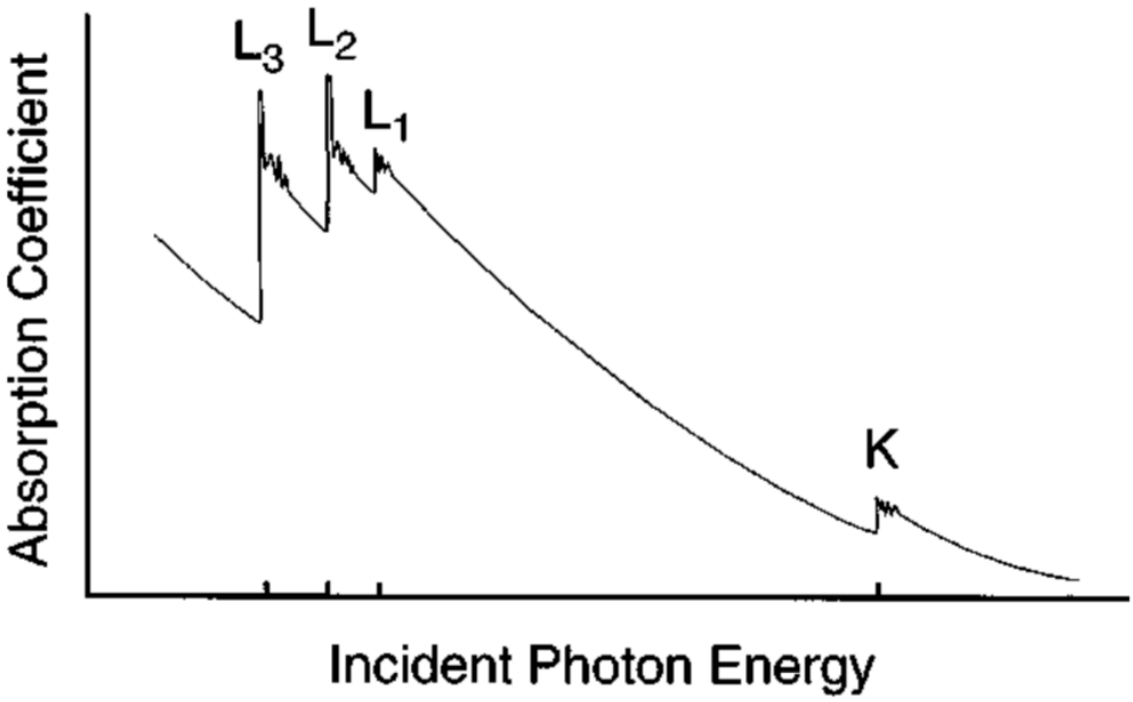

Figure 2.3: *Schematic of the variation of absorption coefficient with incident photon energy, taken from [5]. The absorption edges are observed at specific positions that are characteristic to an element.*

L_2, L_3 respectively. A schematic of the electronic states with their corresponding notations are shown in Figure 2.4

As pointed out above, X-ray absorption spectroscopy is based on the measurement of the absorption coefficient as a function of incident photon energy. Therefore, an accurate measurement of the attenuation in intensity of the incident photon according to the Beer-Lambert law is necessary. However, transmission measurements are extremely challenging especially in the soft X-ray regime. This is because soft X-rays are attenuated very strongly by any material within a few micrometers. In case of diamond, which is primarily carbon, the attenuation length is indeed in the sub micron range as shown in Figure 2.5 This makes the intensity of the transmitted photons too weak to detect, which calls for extremely thin samples. A caveat around this would be to detect one of the emitted particles as a result of subsequent relaxation processes such as fluorescence or Auger decay after X-ray absorption as mentioned in the previous section.[6] As depicted in Figure 2.2, when an inner shell electron is excited to a higher unoccupied state or to the continuum upon X-ray absorption, the core hole is subsequently filled by an outer shell electron, thus producing X-ray fluorescence. The energy of this outgoing photon is equal to the difference in energy between the outer shell from which the electron refills the core

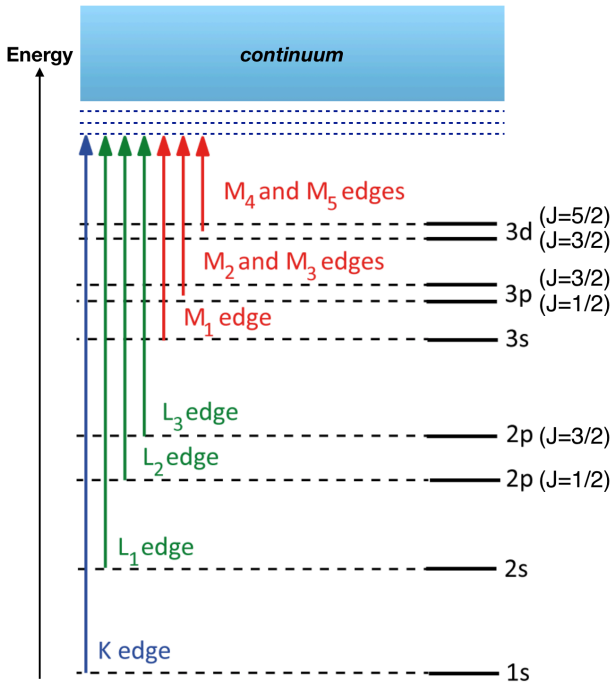

Figure 2.4: *Schematic of the electronic energy levels and corresponding notations for X-ray absorption edges. Redrawn and adapted from[6]*

hole and the core shell. The fluorescence yield is the ratio of X-ray photons emitted to the number of primary vacancies created.[6] Intensity of the fluorescence yield is dependent on the incident X-ray intensity, fluorescence yield probability and the absorption coefficient. The probability of fluorescence yield increases with increase in atomic number Z and is typically higher for K than L and higher edges, as shown in Figure 2.6.[6] Additionally, electrons emitted as a result of Auger process may also be detected. The two modes of detection are known as the Fluorescence Yield (FY) and Electron Yield (EY), respectively. In both of these modes, when the emitted particles of all energies are detected and added up to obtain the X-ray absorption measurement, they are known as Total Fluorescence Yield (TFY) and Total Electron Yielf (TEY), respectively. When electrons and photons of specific energies are discriminated, the detection mode is called a partial yield. In case of partial yield measurements, energy dispersion reduces the strength of the signal but enhances sensitivity by reducing background noise. Furthermore, any scattered light can also be distinguished from actual fluorescence in this detection mode.

Of primary interest for us is an understanding of the TEY and PFY modes of detection that have been used in the experiments described in Chapters 3 - 5. As pointed out before, the emission of primary Auger electrons due to non-radiative decay after X-ray excitation of an electron from the core level to empty states above the Fermi level makes the method strongly surface sensitive. The TEY intensity is

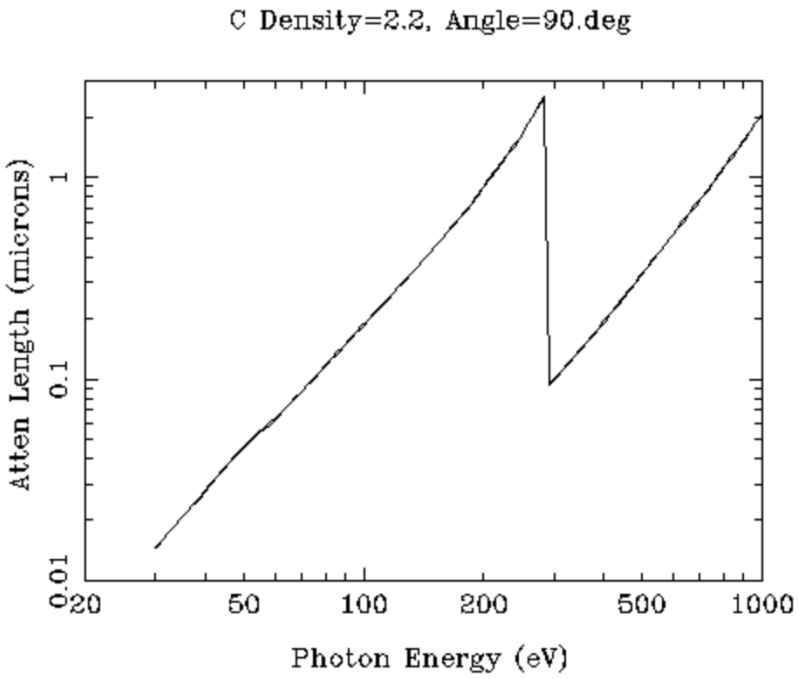

Figure 2.5: *X-ray attentuation length for carbon as a function of photon energy, taken from [7]*

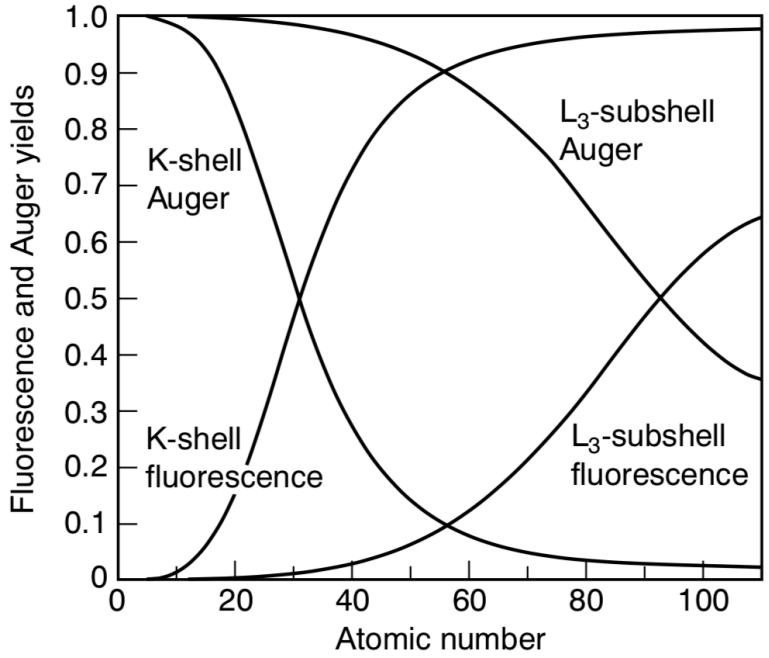

Figure 2.6: *Fluorescence and Auger yields as a function of atomic number Z, taken from [8]. In general, the Auger yield is higher for elements with lower atomic numbers while the fluorescence yield increases for elements with higher atomic numbers.*

however, dominated by secondary electrons created upon scattering as the Auger electrons leave the sample.[9] The typical depth sensitivity in case of electron yield measurement is given by the escape depth of electrons which lie within the range of 2-20 nm.[10] In contrast to electron yield, FY is a bulk sensitive technique with typical depth sensitivities in the order of 100 nm in the soft X-ray region.[10] In particular PFY uses energy sensitive detectors to select specific fluorescence emissions from a broad range of emitted photon energies. These specific emissions typically involve resonant de-excitations within a particular element of interest.

2.1.3. Photoemission spectroscopy

Based on the photoelectric effect first discovered by H.Hertz[11], photoemission spectroscopy is another X-ray based technique to study the electronic structure of a material. This technique was first developed by Kai Siegbahn and his co-workers at Uppsala University in Sweden where they discovered a high resolution spectrometer to accurately measure the binding energy of electrons, thus yielding the electronic structure of the material.[12] An electron is excited either to the continuum or to another unoccupied electronic state from a core level or valence level, depending on the energy of incident photons. Excitation of the electron to continuum is referred to as photoionization while the transition to another unoccupied state is called resonant photoexcitation. As a consequence of photoionization, electrons with various kinetic energies are ejected from the material which are then detected to yield the PE spectrum. The binding energy of the electrons can then be deduced from the relation between KE and BE of electron given by Equation 2.2. A schematic illustration of this process is presented in Figure 2.2. The PES is a photon-in electron-out technique and is element specific, allowing us to probe electrons in different orbitals and in different chemical environments. Since the particles detected in this technique are electrons, it is highly surface sensitive owing to the shorter mean free path of these electrons. Although soft X-ray penetration depths can be *ca.* 1 mm, electrons are typically detected only from a depth of upto *ca.* 10 nm in the sample. This corresponds to only a few atomic layers at the top of the sample.

The basic components of the PES instrument involve a light source, an electron analyzer and an electron detector as shown in Figure 2.7. The electron analyzer must be maintained in ultrahigh vacuum (UHV) in order to ensure that electrons reach the detector without getting scattered by other atoms and molecules. In a laboratory based XPS instrument a typical light source is a He gas discharge lamp and an X-ray tube with usually Al or Mg cathode. However, the development of synchrotron radiation has made possible to tune the excitation energies thereby changing the probe volume in the sample, in

addition to a higher photon flux and a smaller spot size.

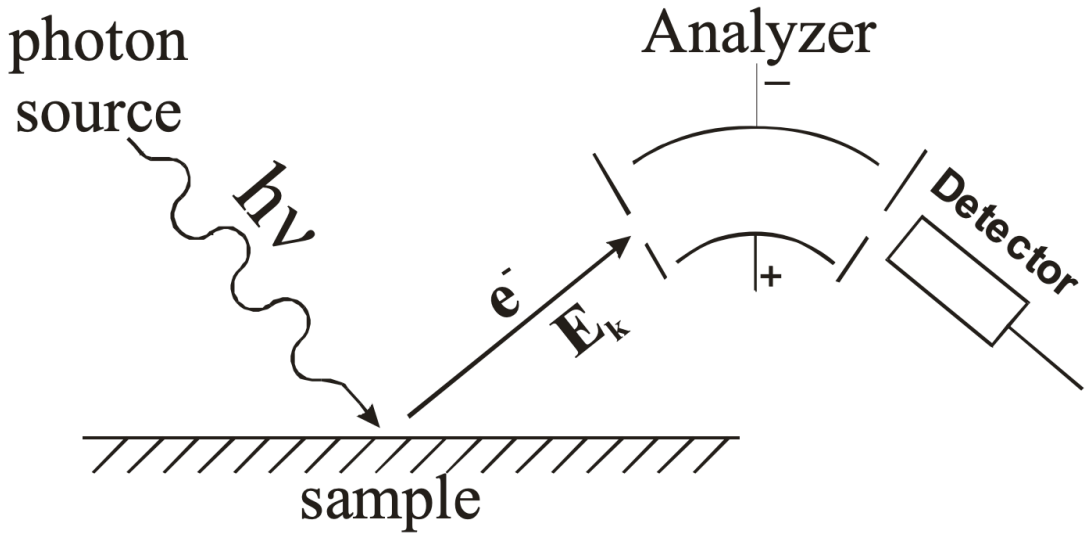

Figure 2.7: *Main components of a PES instrument, taken from [13]*

Since every chemical element has a characteristic XPS spectrum, the chemical composition of a material can be identified using this technique. Furthermore, the binding energy of a core electron depends on the chemical environment of the atom which can be identified based on the chemical shifts observed in the spectrum. Besides the chemical shift, the shape of the core level PES spectrum itself depends on the nature of the sample. Several components may be present in the peak due to the co-existence of a variety of chemical states in the sample. Thus, the shape of a peak corresponding to each chemical component, or in other words, a deconvolution of the core level spectrum is practical to obtain valuable information about the sample. For semiconductors, a Gaussian-Lorentzian or a Gaussian profile alone can be used to describe the shape of the peak. The PES spectrum also has a background which is primarily due to inelastically scattered electrons that escape the sample surface. This background can be corrected using a Shirley background correction.

2.2. Infrared Spectroscopy

Infrared was the first non-visible region of the electromagnetic spectrum that was discovered when the astronomer Sir William Herschley studied vibrational spectra in the form of absorption bands in this region.[14] The infrared radiations are electromagnetic waves with wavelengths longer than that of visible red light but shorter than microwaves (between 1 and 100 μ). This region of the spectrum is further divided into three regions, namely, far infrared (wavenumbers between 400-100 cm^{-1}), mid-infrared

(wavenumbers between 4000-400 cm^{-1}) and near infrared (wavenumbers between 14825-4000 cm^{-1}).

The measurement of a spectrum in the infrared region was made possible with the design of a two-beam interferometer developed by A.A.Michelson in 1891 which forms an essential part of all FTIR spectrometers even today. Although molecular spectra were observed in the IR region of the electromagnetic spectrum, a reasonable interpretation of these spectra was achieved only when the quantum theory was established towards the beginning of the twentieth century. With further development of the quantum theory, the Schrödinger wave equation could be applied to account for the different features in different regions of the IR spectrum. In the investigations presented in this thesis, the mid-IR is the primary region of interest. Quantum theory attributes the features in the mid-IR region to transitions between the different vibrational energy levels with the fine structure originating from the more closely spaced rotational energy levels. These fundamentals are further discussed with a focus on IR spectroscopy in the following section on vibrational spectroscopy. Following that, more specifically, the Attenuated Total Reflection(ATR) mode of FTIR spectroscopy is discussed, which was used in this thesis, to investigate the surface interactions at the diamond-water interface.

2.2.1. Fundamentals of vibrational spectroscopy

The chemical bonds in matter can be pictured as a harmonic oscillator implying that molecules held together by these chemical bonds can vibrate and have a certain natural vibrational frequency. Molecular vibrations range from very simple coupled motion of two atoms in a diatomic molecule to much complex motion of every individual atom in a polyatomic molecule. Molecules with N atoms have 3N degrees of freedom, of which there are 3N-6 vibrational modes, 3 rotational and 3 translational modes of motion.[15] In the vibrational mode, it can be assumed that each atom undergoes a harmonic displacement from its equilibrium position and therefore obeys Hooke's law. The vibrational energy levels in this case are given by the following expression,

$$V_{iv} = h\nu_i(v_i + 1/2) \tag{2.1}$$

where h is the Planck's constant, ν_i is the *fundamental frequency* of the particular mode, and v_i is the *vibrational quantum number* of the ith mode (v_i = 0,1,2,...). As is evident from the expression, the vibrational energy levels are quantized as shown in Figure 2.8. It is the transition between these quantized vibrational energy levels that gives rise to the IR spectrum. The vibrational frequencies are given in units of wavenumber (cm^{-1}) and the energy of radiation in the MIR region is primarily the difference between the energies of the ground state (v_i=0) and the first excited state (v_i=1) of the vibrational mode.

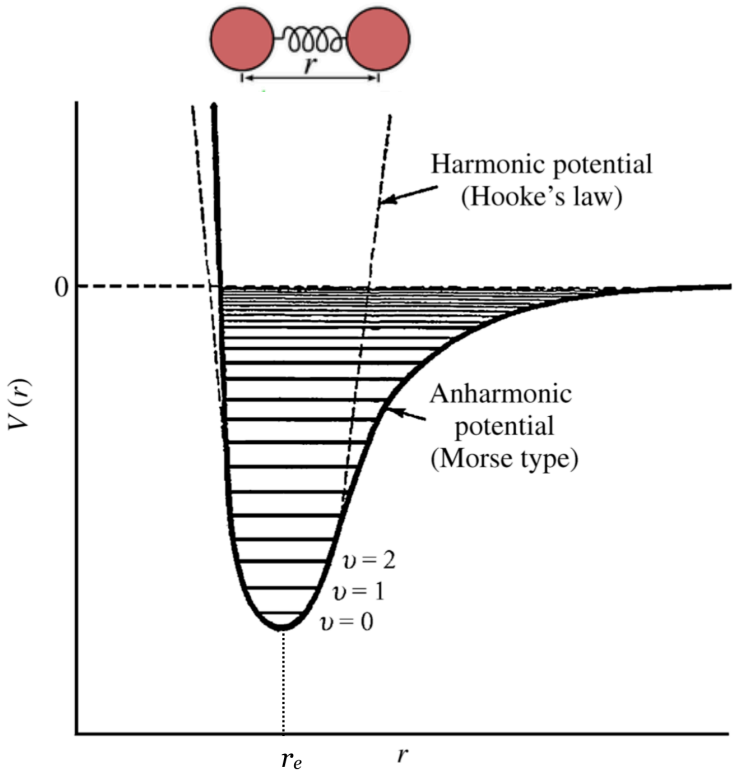

Figure 2.8: *Schematic of the vibrational energy levels.* $V(r)$ *denotes the potential energy and* r *is the internuclear distance. The equilibrium nuclear distance or the bond length is denoted as* r_e*. The harmonic potential holds true at shorter distances while at larger distances the anharmonic potential helps to explain potential dissociation of a molecule. Adapted from[16]*

For a change in vibrational state as a consequence of absorption or emission of radiation, the selection rule states that when the atoms are displaced relative to one another the electric dipole moment of the molecule must change. Such a vibration is said to be infrared active. If vibrations do not affect the molecule's dipole moment, it is said to be infrared inactive. Additionally, there are specific selection rules that allow transitions upon absorption and emission of radiation. Transitions for which $\Delta v_i = +1$ are allowed for absorption while $\Delta v_i = -1$ are allowed for emission.

The assumption of harmonic displacement results in a parabolic approximation of the potential energy curve which no longer holds true at higher vibrational excitations. In such a case, the motion becomes *anharmonic* where the restoring force is no longer potential to the displacement. This effect allows the selection rules to become more relaxed and transitions for which $\Delta v_i \neq \pm 1$ become allowed, resulting in the weak appearance of overtone ($\Delta v_i = 2, 3, 4, ..$) and combination ($\Delta v_i = +1, \Delta v_j = +1$, where j represents a different mode) bands in the mid-IR region of a spectrum.

Vibrational transitions in a molecule are also accompanied by rotational transitions for gas-phase molecules, which appear in the spectrum with separations less than 10 cm^{-1}. As the molecule swells or shrinks,

its moment of inertia changes along with it. As a result its rotational state also changes. This leads to categorization of the absorption into three different branches of the spectrum, P, Q and R, with $\Delta v_j =$ -1, 0 and +1 respectively for a fundamental vibrational transition with $\Delta v_i = +1$. These transitions are shown in Figure 2.9

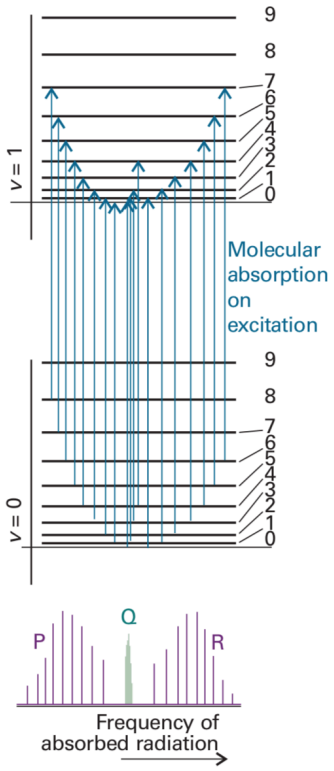

Figure 2.9: *Schematic of the vibrational and rotational energy levels in gas phase molecules, taken from[15]. The transitions give rise to very sharp line like features in the IR spectrum.*

In contrast to the gas-phase where molecules are very far apart from each other, in liquids, molecules are closely packed. They are held together by interactions between nearest neighbour molecules, also known as *intermolecular interactions* such as H-bonds and van der Waals forces. Such intermolecular interactions affect the force constant of the molecule thereby influencing its vibration frequency. The number of nearest neighbour molecules and the strength of intermolecular interactions vary within a liquid sample thereby giving rise to different chemical environments. This variation of chemical environment gives rise to variations in the vibration frequency and hence the wavenumber at which the molecules absorb infrared light. Samples which have stronger intermolecular interactions will have many different chemical environments in comparison to those with weaker interactions. The more chemical environments a sample would have, the more different wavenumbers of infrared light it will absorb, thus giving rise to a broad IR band, as is typically observed in water which exhibits strong inter-

molecular H-bonding due to the polar nature of the O-H bond.[17, 18] At the solid-liquid or solid-vapor interface, the adsorbed molecules on the surfaces form a few closely packed monolayers and therefore exhibit a situation similar to that of liquid samples, giving rise to broad IR bands.[19]

2.2.2. Attenuated Total Reflection-Fourier Transform Infrared Spectroscopy

Fourier Transform Infrared (FTIR) Spectroscopy is a very reliable and well-established fingerprinting technique, especially in the mid-IR region. Previously used to characterize organic molecules, FTIR spectroscopy has been used for over 20 years to characterize NDs due to its high sensitivity to functional groups on the diamond surface, non-destructive nature and easy sample preparation methods. In a typical FTIR spectrum, the absorption of IR radiation is plotted as a function of wavelength, described in units of wavenumbers or cm^{-1}. To record this spectrum, an FTIR spectrometer is used at the heart of which is a Michelson interferometer as pointed out previously. The Michelson interferometer is a two-beam interferometer comprising of two mirrors, one of which is fixed while the other is movable and a beam splitter. An infrared beam created by a source such as the synchrotron or a metal wire is split by the beam splitter into two portions which are reflected by the mirrors and finally recombine back at the beamsplitter with a phase difference due to their different path lengths. This beam then travels to the sample compartment where it is focussed on the sample and subsequently reaches the detector. The signal that is detected is an interferogram which is then subsequently Fourier transformed to yield a spectrum. The intensity of the detected signal depends on the absorption of IR radiation by the sample which is once again given by the Beer-Lambert law mentioned at the beginning of this chapter.

There are several methods of measuring the IR spectrum, an overview of which has been presented by Petit *et al.*[21] Here we briefly describe the principle governing the attenuated total reflection (ATR) mode of FTIR spectroscopy. The ATR mode is based on the total internal reflection of the IR beam at the interface of two materials with different refractive indices. Typically such an interface is formed by the ATR crystal and the sample of interest. The ATR crystal must have a higher refractive index (n_1) as compared to the sample (n_2) and total internal reflection can occur only if the angle of incidence is higher than the critical angle which is given by,

$$\theta_{\text{critical}} = sin^{-1}(n_2/n_1) \tag{2.2}$$

At the Ge-water interface, as in our measurements described in Chapter 5 of this dissertation, θ_{critical} is *ca.* 18°. At a 45° angle of incidence the IR beam is totally internally reflected generating an evanescent

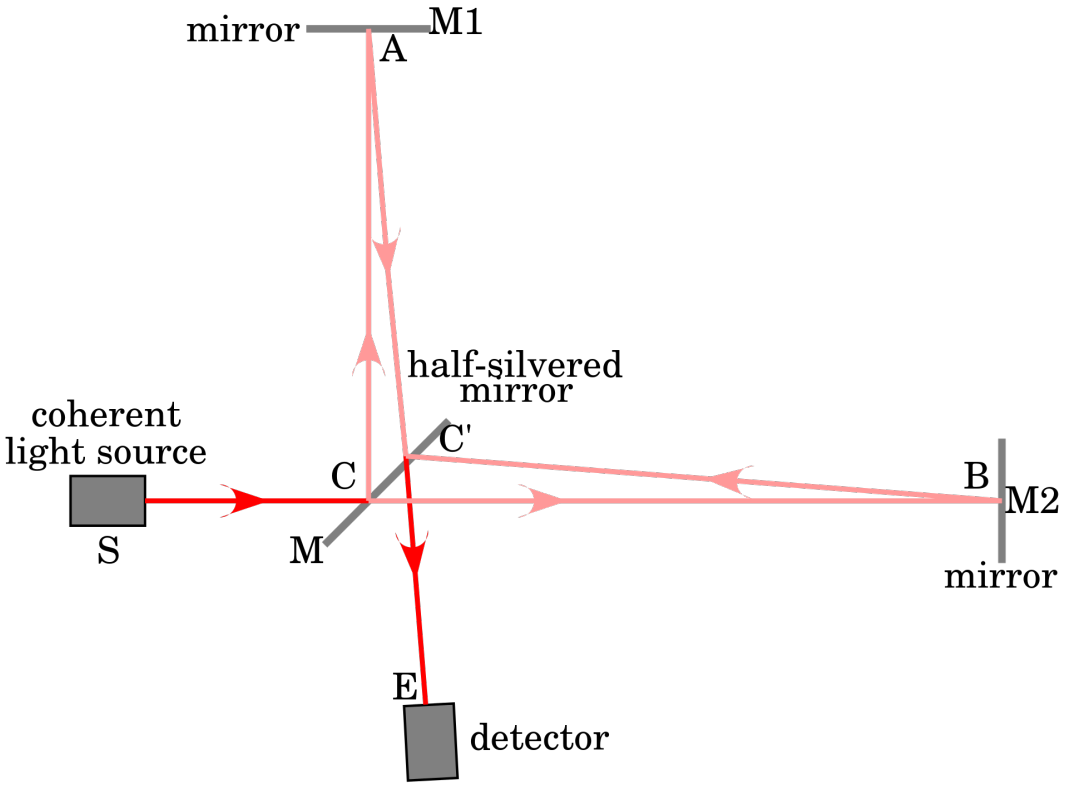

Figure 2.10: *Schematic of the Michelson interferometer. Taken from[20]*

wave perpendicular to the surface of the crystal at every point of reflection. The electric field of this wave interacts with the sample on the ATR crystal and a part of this field is absorbed, thus attenuating the intensity of the reflected beam. The amplitude of the electric field undergoes an exponential decline with the distance z from the surface of the ATR crystal which is expressed as,

$$E = E_0 \exp(-z/d_p) \tag{2.3}$$

where E and E_0 are the electric field after and before the exponential decline and d_p is the penetration depth of the electric field of the evanescent wave, indicating how far the wave can reach from the surface. The penetration depth d_p is generally given by,

$$d_p = \frac{\lambda}{2\pi n_1 \sqrt{(sin^2\theta - (n_2/n_1)^2)}} \tag{2.4}$$

where λ is the wavelength of the incident beam, θ is the angle of incidence and n_1 and n_2 are the refractive indices of the ATR crystal and the sample respectively. From this, it could be estimated that the penetration depth of the IR beam at the Ge-water interface at *ca.* 1650 cm^{-1} is *ca.* 0.38 μm. Hence, clearly, the ATR-IR is interface sensitive but not as much as X-ray spectroscopy. Furthermore, it is quite

clear that for ATR measurements the absorption is independent of the sample thickness, which makes this technique particularly interesting for investigating the interactions at the diamond-liquid interface. Different ATR crystals can be used depending on the spectral region of interest and sample environment.

2.3. Experimental Setup

2.3.1. Synchrotron Facility-BESSY II

A synchrotron is a cyclic particle accelerator in which a sub atomic particle is accelerated in a fixed closed loop path. It is the fundamental component in a synchrotron radiation source, a schematic of which is shown in Figure 2.11. Typically, electrons are produced in an electron gun which is a device similar to cathode ray tubes. These electrons are packed in bunches and accelerated in the linear accelerator or a microtron before being injected into the booster synchrotron where it is accelerated to relativistic speeds and finally injected into the storage ring. The storage ring comprises of several insertion devices such as bending magnets, undulators and wigglers which help to keep the electron bunches in a confined trajectory along which they circle at speeds close to that of light. In the process they produce X-rays that are then directed to beamlines where the beam is then focussed through various optical mirrors and lenses and the energy is tuned with the help of gratings and monochromators for use in a specific experiment.

The magnetic field in a storage ring can be generated by three different magnetic structures or insertion devices, namely, bending magnets, undulators and wigglers. Bending magnets produce a fan of radiation around the bend due to a single curved trajectory of the charged particle. Undulators comprise of periodic magnetic structures with weak magnetic fields that result in a harmonic osciallation of the charged particle. The weak magnetic field causes small angular excursions called undulations which produce a narrow cone of radiation due to its small amplitude. A tightly confined electron beam passing through undulators result in radiation with small angular divergence and narrow spectral width. Wigglers are similar to undulators but with stronger magnetic fields giving rise to a radiation cone that is both broad in space and angle. The radiation has a much higher photon flux. Further details on characteristics of the radiation produced by each of these magnetic structures can be found in Ref [8].

All experiments presented in thesis were performed in BESSY II which is a synchrotron facility located in Berlin, Germany. A 70 kV electron beam is produced from a hot cathode which is subsequently accelerated in a microtron before being injected into the booster synchrotron before reaching a final energy of 1.7 GeV. It takes 50 ms to accelerate the electrons and inject them into the storage ring. The electron

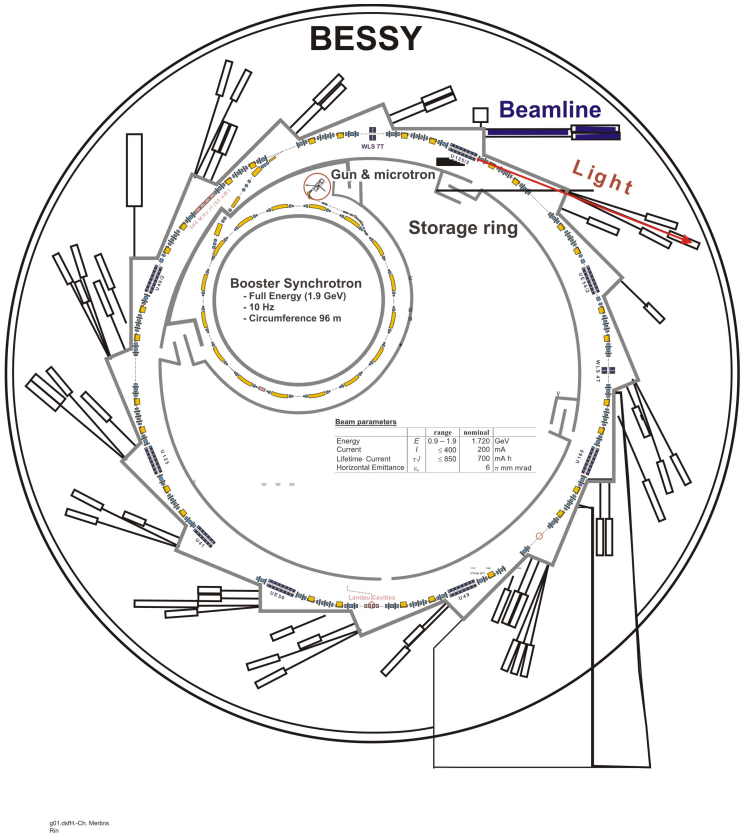

Figure 2.11: *Schematic of the synchrotron showing the electron gun, microtron, booster synchrotron, storage ring and beamlines, taken from [22]*

bunches are injected every 2-3 minutes in the *top-up* mode which ensures that a constant current between 250 - 300 mA is maintained in the ring. The storage ring has a circumference of 240 m and about 50 beamlines. Most of the X-ray spectrosopy experiments presented in this thesis, including those for liquids, were performed at the U49-2 PGM I beamline. Some solid state measurements on single crystal doped diamonds were also performed at the U41-PEAXIS beamline.

U49-2 PGM I Beamline

The U49-2 PGM I beamline at BESSY II is an undulator beamline with plane grating monochromator that delivers linearly polarized soft X-ray radiation with a high photon flux combined with a high stability and a small spot size. A schematic of this beamline is presented in Figure A.2 in Appendix A. In particular, a spot size of 100 μm $\times$ 22 μm with a photon flux of *ca.* 10^{13} photons/s can be achieved at the experiment from this beamline. It can deliver soft X-rays with energies in the range of 84 - 1600 eV which makes it a suitable choice for probing the C and O K edges and Cu L edges as presented in this thesis. The exit slit size of this beamline is also variable, which allows for tuning of the photon flux at the experiment. For

TEY and PFY measurements, slit sizes of 50 and 100 μm were used, respectively. The beamline has no fixed station. For X-ray spectroscopy measurements in this thesis, LiXedrom[23] and Sol3PES[24] end stations were attached to this beamline.

U41-PEAXIS Beamline

For detecting strong electron and photon emissions from materials, high brilliance photon sources are necessary. Additionally, to obtain high energy resolution, a highly focussed beam becomes imperative. These characteristics are fulfilled by the new U41-PEAXIS beamline at BESSY II, a schematic of which is shown in Figure A.1 in Appendix A. Similar to the U49-2 PGM I beamline, the beam from the storage ring is monochromatized and focussed on the exit slit and subsequently at the experiment in the fixed end station PEAXIS. A spot size of 3.8 μm $\times$ 12.4 μm with a photon flux of *ca.* 10^{13} photons/s can be achieved at the experiment from this beamline. This beamline can deliver photons of energy within 180-1600 eV and is therefore suitable for the measurement of X-ray spectra at the C, O and N K edges.

2.3.2. Experimental End Stations

2.3.2.1. LiXedrom end station - XAS and XES in solids and liquids

In order to conduct X-ray absorption and emission spectroscopy measurements under vacuum conditions for both solid state samples as well as in liquids, the LiXedrom end station was used at the U49-2 PGM I Beamline at BESSY II, a picture of which can be seen in Figure A.3 in Appendix A. Although this setup was developed for liquid jet and emission measurements, it can also be used for solid state measurements as well as liquid measurements in a flow cell. It consists of primarily two chambers, a main chamber, where the sample of interest can be studied either in solid state or in a liquid, typically in a flow cell or in a liquid microjet, and a grating chamber with a detector structure in a Rowland circle geometry. The Rowland circle geometry is a spherical grating that can be employed to achieve the desired decomposition of the emitted radiation for X-ray emission studies. The spherical grating in this geometry has a radius of $2R$. When the photon source lies on the Rowland circle which has a radius R, the emitted photons are energetically resolved and focussed along this specific circle as shown in Figure 2.12. More detailed discussions on the Rowland Circle geometry as well as a detailed description of the LiXedrom setup can be found in the literature.[23] (See Figure A.3 in Appendix A)

In the main chamber of LiXedrom, solid samples are introduced from the top, typically placed on a solid sample holder made out of copper with electrical connections to the metallic holder that would enable recording of the photocurrent for electron yield measurements, as shown in Figure 2.13. For electro-

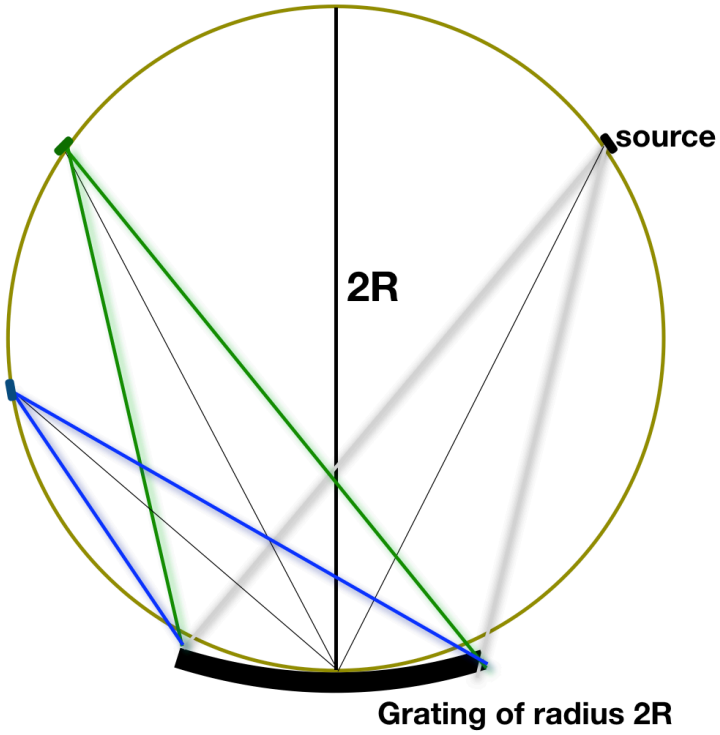

Figure 2.12: *Illustration of the Rowland circle geometry, adapted from [6]. A light source on the circle of radius R is dispersed by the spherical grating of radius 2R into components of different wavelength spatially on the circle.*

chemical investigations involving the solid-liquid interface, an electrochemical flow cell,[25] developed by Schwanke *et al.* was introduced into the main chamber (see Figure A.7 in Appendix A). The sample was deposited on a Si_3N_4 membrane, which is transparent to X-rays and separates the liquid in the flow cell, which was flown with the help of a syringe pump, from the vacuum conditions in the main chamber. The membrane was coated with Au and served as the working electrode for the *in-situ* electrochemical measurements. A Pt wire was used as the counter electrode and Ag/AgCl was the reference electrode. To ensure a stable vacuum of *ca.* 10^{-6} mbar in the main chamber several pumps are attached to the LiXedrom setup. A vacuum of 10^{-9} mbar is maintained in the grating chamber for the photon detector which consists of a microchannel plate/phosphorescent screen/CCD camera stack. Photons emitted from the sample upon X-ray excitation are collected at this photon detector for the PFY measurements.

2.3.2.2. PEAXIS end station - XAS in solids

The soft X-ray end station PEAXIS, a picture of which is shown in Figure A.4 in Appendix A, enables Resonant Inelastic X-ray Scattering (RIXS) as well Photoemission Spectroscopic (PES) studies on materials within the same experimental setup. With a rotating arm, it essentially allows for angle dependent RIXS

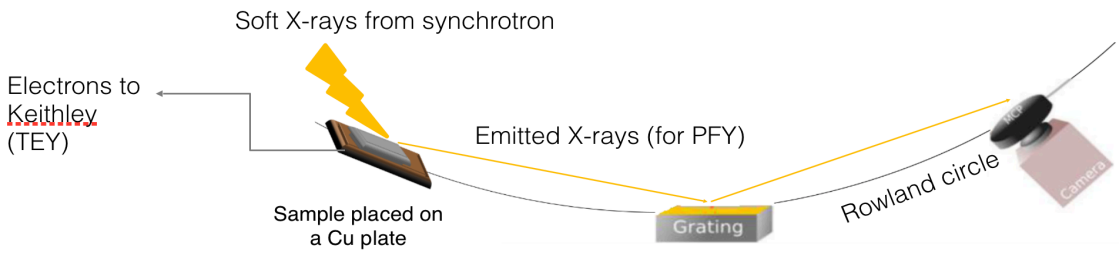

Figure 2.13: *Illustration of the sample geometry for TEY and PFY measurements.*

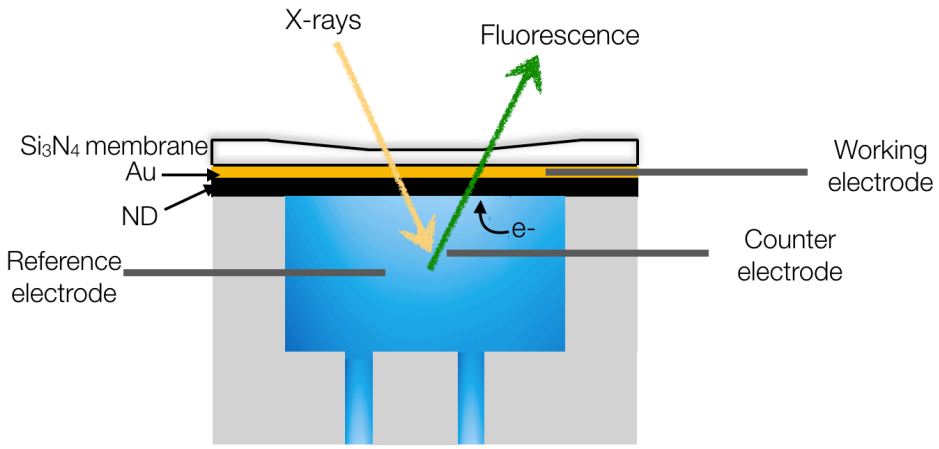

Figure 2.14: *Illustration of the electrochemical flow cell. X-rays pass through the Au coated Si_3N_4 membrane into the liquid chamber where the interaction takes place at the ND-liquid interface. Samples may either be deposited as a solid film on the membrane itself with the electrolyte flown in the liquid chamber through the liquid inlet and outlet or directly studied in solution. A Pt wire is used as the counter electrode while Ag/AgCl is the reference electrode.*

and PES measurements, which were however, not used for the experiments presented in this thesis. The PEAXIS end station has a sample chamber which is connected to the interaction chamber with a load lock which is used to transport the samples (see Figure A.4 in Appendix A). The sample chamber, load lock as well as the interaction chamber are kept under ultra high vacuum of 10^{-8} - 10^{-9} mbar. A commercial hemispherical electron analyzer from SPECS is used for electron detection during the PES measurements. The RIXS spectrometer comprises of a grating chamber, a 5 m long moveable arm for angle dependent RIXS and a CCD detector. For measurements presented in this thesis a solid sample manipulator was introduced into the sample chamber with heating capabilities enabling annealing of the samples in vacuum prior to the measurements. All samples were annealed to 300°C for 3 hours prior to measurements. X-ray absorption spectra were recorded primarily in the TEY mode.

2.3.2.3. IRIS end station - FTIR Spectroscopy

The FTIR spectra for nanodiamonds were measured in the ATR mode in a Bruker Vertex 66/v spectrometer equipped with a KBr beamsplitter, a liquid nitrogen (LN_2) cooled detector. A spectral resolution of 4 cm^{-1} was set and the spectra were recorded with ZnSe and Ge ATR crystals. An environmental cell was built in-house to facilitate *in-situ* surface chemistry investigations. It consists of a small chamber above the ATR crystal with an inlet and outlet that allows the sample under consideration to be exposed to gas or liquid. During the measurements the sample chamber and infrared path was maintained in vacuum while the environmental cell was subjected to ambient conditions by flowing dry air, humid air and liquid water through it. While liquid water was directly injected through the inlet using a syringe, humid air was prepared by bubbling dry air through deionized water. For all samples, a reference spectrum (1024 scans) was measured on the clean ATR crystal following which the spectra (128 scans) were first collected for the dry sample and then subsequently for the sample exposed to humid air and liquid water. After each sample, the crystal was cleaned with ethanol, acetone and water and a new reference spectrum was measured each time before drop casting in order to ensure the removal of the previous ND sample.

2.3.2.4. Sol3 end station - Near Ambient Pressure Photoemission Spectroscopy

The electronic structure at the diamond-water interface of differently terminated diamond surfaces were studied with ambient pressure photoemission spectroscopy (AP-PES) in the Sol^3 end station (see Figure A.6 in Appendix A) at U49-2 PGM I beamline at BESSY II.[24] The setup comprises of three primary components, namely, the interaction chamber, electron analyzer and a differential pumping unit. In order to probe the solid-liquid interface, a liquid nitrogen (LN_2) cooled sample holder was introduced into the interaction chamber to which a heating element as well as a PT-100 temperature sensor was attached in order to first anneal the sample in vacuum at 250°C. The thin film diamond samples were clamped on to the metallic copper sample holder. This sample holder is typically mounted on an x-y-z manipulator as it is introduced in the interaction chamber. A thin layer of liquid water was deposited on the sample by introducing water into the interaction chamber via a leak valve. Before introducing water into the chamber, it was outgassed using a freeze-pump-thaw cycle. Pressures between 1-5 mbar was maintained in the chamber to increase relative humidity and the sample temperature was constantly reduced in order to enable condensation of the water vapor on the sample surface.[26, 27] Photoelectrons were detected in a direction perpendicular to the X-ray beam with a Scienta Omicron R4000 HiPP-2 high-resolution hemispherical electron energy analyzer. The spectrometer consists of electrostatic lenses for

imaging of the electrons that are then guided into a section containing two electrostatic hemispheres. Here the electrons with a given pass energy are detected on a 2D detector comprised of two MCPs, a 40 mm diameter phosphor screen and a CCD camera that records the image. Multi-stage pumping of the analyzer ensures its operation at ambient pressures during the experiment. The interaction chamber of the end station is connected to the refocussing chamber of the beamline through a differential pumping unit. This unit ensures that the pressure in the refocussing chamber is always maintained below 10^{-9} mbar for any operating pressure in the interaction chamber.

2.4. Theoretical Modelling

In order to interpret the experimental data obtained using some of the aforementioned techniques and generate useful insights about the properties of diamonds, additional theoretical investigations were needed. These theoretical studies were performed by Prof. Karin Larsson in the Uppsala University and Dr. Kaan Atak in HZB. The results obtained from the investigations were used in this dissertation to gain a better understanding of the electronic structure of B-doped diamonds and $Ru(bpy)_3$-ND together with the XAS data as explained in Chapters 3 and 4, respectively. Here we will briefly present the two different theoretical modelling packages used by the colleagues, both of which are based on Density Functional Theory (DFT).

2.4.1. B doped diamonds - DFT using CASTEP and Dmol

The calculations performed on B-doped diamonds in this work were performed using the CASTEP and Dmol programs from BIOVIA, Inc. The CASTEP program was used for the geometry optimization of the model structures, in addition to calculations of the partial Density of State (pDOS) spectra. The Dmol program was used for the calculation of the valence band edge energies of the various surfaces. The optimized structures were used for these latter calculations. An ultrasoft pseudopotential density functional theory (DFT) method was used in all calculations, and performed under periodic boundary conditions.[28] More specifically, the spin-polarized general gradient approximation (GGSA) was used, which is based on the PBE functional (Perdew-Burke-Ernzerhof[28]) for electron exchange correlations. Moreover, a plane wave approach,[29] with a cutoff energy of 326.5 eV, was used in the CASTEP calculations. The Monkhorst-Pack scheme[30] was used for the k-point sampling of the Brillouin zone, which generated a uniform mesh of k points in reciprocal space. Moreover, the Dmol calculations included all electrons in the models and were furthermore based on the double numeric bases set with polarization functions (dnp). Three different super cells, modelling the H-terminated, non-terminated and Pandey

Chain-reconstructed diamond (111) surface planes, respectively, have been constructed in the present investigation. The corresponding models for the H-terminated and Pandey Chain-reconstructed surfaces are shown in Figure 3.2, together with the different ways B is incorporated in the surface region. The model for the non-terminated surface is presented in the Appendix. Boron atoms in the first diamond atomic layers are relevant to reflect surface effects on nanostructured diamond as well as at grain boundaries in polycrystalline diamond that are observed experimentally as explained later in Chapter 3. The bottom of the diamond slabs was terminated by H to saturate the dangling bonds and to mimic a bulk continuation. All atoms, with an exception for the bottom hydrogen and carbon layer, were allowed to freely relax during the optimization procedure. This geometry optimization procedure was based on the BFGS algorithm.[31]

2.4.2. $Ru(bpy)_3$-ND - DFT using CASTEP and ORCA

The most stable geometrical structure of the Ru-containing complexes were calculated by using Density Functional Theory (DFT). More specifically, an ultrasoft pseudopotential plane-wave approach was used, based on the PBE generalized gradient approximation (GGA) of the exchange-correlation functional.[32] The GGA takes into account the gradient of the electron density, which gives a high-quality energy evaluation. Moreover, the value of the energy cutoff for the plane wave basis sets was set to 420.00 eV. In addition, the Monkhorst-Pack scheme was used for the k-point sampling of the Brillouin zone, which generated a uniform mesh of k points in reciprocal space.[33] All atoms in the Ru-containing complexes were allowed to move freely in the calculations by using a BFGS approach (Broyden-FletcherGoldfarb-Sharmo).[34] The calculations in the present work were carried out using the Cambridge Sequential Total Energy Package(CASTEP) program from BIOVIA, Inc. [35]

The calculations for XA spectra were carried out with the ORCA program package.[36] Molecular geometry optimizations were performed with the B3LYP[37, 38] density functional with the def2-TZVP basis set.[39] Transition energies and moments for the carbon K edge were calculated with time-dependent density functional theory (TDDFT) using the same basis set and B3LYP functional.[40–46] During the calculations, the resolution of identity (RI) approximation was used utilizing the ”Autoaux” basis-set generation procedure.[47] Numerical integrations during the DFT calculations were performed on a dense grid (ORCA grid 4). K-edge absorption spectra were obtained by applying a 0.4 eV Lorentzian-type broadening on each transition moment respectively. The geometry calculations had no symmetry constraint. In all calculations, the relativistic effects were taken into account using effective core potentials (ECPs).[48] Visualizations of molecules and orbitals were created using Avogadro software.[49]

Having discussed the fundamentals of the experimental techniques used in this thesis along with the theoretical methods, the next chapters will discuss the results obtained on different diamond materials studied in the course of this project.

References

[1] W. C. Röntgen, *Ueber eine neue Art von Strahlen,* Annalen der Physik **300**, 12 (1898).
[2] A. Mottana and A. Marcelli, *The historical development of X-ray Absorption Fine Spectroscopy and of its applications to Materials Science,* Unpublished.
[3] J. A. Seibert and J. M. Boone, *X-ray Imaging Physics for Nuclear Medicine Technologists. Part 2: X-Ray Interactions and Image Formation,* Journal of Nuclear Medicine Technology **33**, 3 (2005).
[4] K. M. Lange and E. F. Aziz, *Electronic structure of ions and molecules in solution: a view from modern soft X-ray spectroscopies,* Chem. Soc. Rev. **42**, 6840 (2013).
[5] J. J. Rehr and R. C. Albers, *Theoretical approaches to x-ray absorption fine structure,* Rev. Mod. Phys. **72**, 621 (2000).
[6] R. Golnak, *Investigation of the Electronic Structure of Transition Metal-Ions in Solution from Aqua-Complexes to Porphyrins*, Ph.D. thesis, Freie Universität Berlin, Germany (2015).
[7] *X-ray Attenuation Length,* `http://henke.lbl.gov/optical_constants/atten2.html`.
[8] D. Attwood, *Soft X-rays and Extreme Ultraviolete Radiation* (Cambridge University Press, 2007).
[9] *Characterisation - X-ray Absorption Spectroscopy,* `https://www.nffa.eu/offer/characterisation/installation-5/xas/`.
[10] A. J. Achkar, T. Z. Regier, H. Wadati, Y.-J. Kim, H. Zhang, and D. G. Hawthorn, *Bulk sensitive X-ray absorption spectroscopy free of self-absorption effects,* Phys. Rev. B **83**, 081106 (2011).
[11] H. Hertz, *Ueber einen Einfluss des ultravioletten Lichtes auf die electrische entladung,* Annalen der Physik **267**, 983 (1887).
[12] K. Siegbahn, *Electron spectroscopy for atoms, molecules, and condensed matter,* Rev. Mod. Phys. **54**, 709 (1982).
[13] E. Kleimenov, *High Pressure X-ray Photoelectron Spectroscopy applied to Vanadium Phosphorus Oxide Catalysts under Reaction Conditions*, Ph.D. thesis, Technische Universität Berlin, Germany (2005).
[14] N. Sheppard, *The Historical Development of Experimental Techniques in Vibrational Spectroscopy,* in *Handbook of Vibrational Spectroscopy*, edited by J. M. Chalmers and P. R. Griffiths (John Wiley & Sons, 2002) Chap. 1, pp. 1–30.
[15] P. Atkins, J. d. Paula, and J. Keeler, *Atkins' Physical Chemistry* (Oxford University Press, 2006).
[16] P. R. Griffiths and J. A. d. Haseth, *Fourier Transform Infrared Spectroscopy* (John Wiley & Sons, 2007).
[17] J.-B. Brubach, A. Mermet, A. Filabozzi, A. Gerschel, and P. Roy, *Signatures of the hydrogen bonding in the infrared bands of water,* The Journal of Chemical Physics **122**, 184509 (2005).
[18] J. M. Headrick, E. G. Diken, R. S. Walters, N. I. Hammer, R. A. Christie, J. Cui, E. M. Myshakin, M. A. Duncan, M. A. Johnson, and K. D. Jordan, *Spectral Signatures of Hydrated Proton Vibrations in Water Clusters,* Science **308**, 1765 (2005).
[19] T. Petit, L. Puskar, T. Dolenko, S. Choudhury, E. Ritter, S. Burikov, K. Laptinskiy, Q. Brzustowski, U. Schade, H. Yuzawa, M. Nagasaka, N. Kosugi, M. Kurzyp, A. Venerosy, H. Girard, J.-C. Arnault, E. Osawa, N. Nunn, O. Shenderova, and E. F. Aziz, *Unusual Water Hydrogen Bond Network around Hydrogenated Nanodiamonds,* The Journal of Physical Chemistry C **121**, 5185 (2017).
[20] *Michelson Interferometer,* `https://en.wikipedia.org/wiki/Michelson_interferometer`.
[21] T. Petit and L. Puskar, *FTIR spectroscopy of nanodiamonds: Methods and interpretation,* Diamond and Related Materials **89**, 52 (2018).
[22] *Wie funktioniert BESSY II,* `https://www.helmholtz-berlin.de/quellen/bessy/elektronenspeicherring/wie-funktioniert-bessy_en.html`.
[23] Helmholtz Zentrum Berlin für Materialien und Energie, *Lixedrom: High Energy Resolution RIXS Station dedicated to Liquid Investigation at BESSY II,* Journal of large-scale research facilities **2**, A80 (2016).
[24] R. Seidel, M. N. Pohl, H. Ali, B. Winter, and E. F. Aziz, *Advances in liquid phase soft-x-ray photoemission spectroscopy: A new experimental setup at BESSY II,* Review of Scientific Instruments **88**, 073107 (2017).
[25] C. Schwanke, R. Golnak, J. Xiao, and K. M. Lange, *Electrochemical flowcell for in-situ investigations*

by soft x-ray absorption and emission spectroscopy, Review of Scientific Instruments **85**, 103120 (2014).
[26] K. Andersson, G. Ketteler, H. Bluhm, S. Yamamoto, H. Ogasawara, L. G. M. Pettersson, M. Salmeron, and A. Nilsson, *Autocatalytic Water Dissociation on Cu(110) at Near Ambient Conditions,* Journal of the American Chemical Society **130**, 2793 (2008).
[27] S. Kaya, D. Schlesinger, S. Yamamoto, J. T. Newberg, H. Bluhm, H. Ogasawara, T. Kendelewicz, G. E. Brown Jr., L. G. M. Pettersson, and A. Nilsson, *Highly Compressed Two-Dimensional Form of Water at Ambient Conditions,* Scientific Reports **3**, 1074 EP (2013).
[28] J. P. Perdew, K. Burke, and M. Ernzerhof, *Generalized Gradient Approximation Made Simple,* Phys. Rev. Lett. **77**, 3865 (1996).
[29] M. D. Segall, R. Shah, C. J. Pickard, and M. C. Payne, *Population analysis of plane-wave electronic structure calculations of bulk materials,* Phys. Rev. B **54**, 16317 (1996).
[30] H. J. Monkhorst and J. D. Pack, *Special points for Brillouin-zone integrations,* Phys. Rev. B **13**, 5188 (1976).
[31] B. G. Pfrommer, M. Côté, S. G. Louie, and M. L. Cohen, *Relaxation of Crystals with the Quasi-Newton Method,* Journal of Computational Physics **131**, 233 (1997).
[32] J. P. Perdew, K. Burke, and M. Ernzerhof, *Generalized Gradient Approximation Made Simple,* Phys. Rev. Lett. **77**, 3865 (1996).
[33] H. J. Monkhorst and J. D. Pack, *Special points for Brillouin-zone integrations,* Phys. Rev. B **13**, 5188 (1976).
[34] S. Antman, J. E. Marsden, and L. Sirovich, *Molecular Modeling and Simulation* (Springer-Verlag, 2002) p. 331.
[35] S. J. Clark, M. D. Segall, C. J. Pickard, P. J. Hasnip, M. I. J. Probert, K. Refson, and M. C. Payne, *First Principles Methods using CASTEP,* Zeitschrift für Kristallographie - Crystalline Materials **220**, 567 (2005).
[36] F. Neese, *The ORCA program system,* Wiley Interdisciplinary Reviews: Computational Molecular Science **2**, 73 (2012).
[37] A. D. Becke, *Density-functional exchange-energy approximation with correct asymptotic behavior,* Phys. Rev. A **38**, 3098 (1988).
[38] A. D. Becke, *Density-functional thermochemistry. III. the role of exact exchange,* The Journal of Chemical Physics **98**, 5648 (1993).
[39] F. Weigend and R. Ahlrichs, *Balanced basis sets of split valence, triple zeta valence and quadruple zeta valence quality for h to rn: Design and assessment of accuracy,* Phys. Chem. Chem. Phys. **7**, 3297 (2005).
[40] E. Baerends, D. Ellis, and P. Ros, *Self-consistent molecular Hartree—Fock—Slater calculations i. The computational procedure,* Chemical Physics **2**, 41 (1973).
[41] C. Van Alsenoy, *Ab initio calculations on large molecules: The multiplicative integral approximation,* Journal of Computational Chemistry **9**, 620 (1988).
[42] R. A. Kendall and H. A. Früchtl, *The impact of the resolution of the identity approximate integral method on modern ab initio algorithm development,* Theoretical Chemistry Accounts **97**, 158 (1997).
[43] K. Eichkorn, O. Treutler, H. Öhm, M. Häser, and R. Ahlrichs, *Auxiliary basis sets to approximate Coulomb potentials,* Chemical Physics Letters **240**, 283 (1995).
[44] K. Eichkorn, F. Weigend, O. Treutler, and R. Ahlrichs, *Auxiliary basis sets for main row atoms and transition metals and their use to approximate Coulomb potentials,* Theoretical Chemistry Accounts **97**, 119 (1997).
[45] J. L. Whitten, *Coulombic potential energy integrals and approximations,* The Journal of Chemical Physics **58**, 4496 (1973).
[46] B. I. Dunlap, J. W. D. Connolly, and J. R. Sabin, *On some approximations in applications of Xα theory,* The Journal of Chemical Physics **71**, 3396 (1979).
[47] G. L. Stoychev, A. A. Auer, and F. Neese, *Automatic Generation of Auxiliary Basis Sets,* Journal of Chemical Theory and Computation **13**, 554 (2017).
[48] D. Andrae, U. Häußermann, M. Dolg, H. Stoll, and H. Preuß, *Energy-adjusted ab initio pseudopotentials for the second and third row transition elements,* Theoretica chimica acta **77**, 123 (1990).
[49] M. D. Hanwell, D. E. Curtis, D. C. Lonie, T. Vandermeersch, E. Zurek, and G. R. Hutchison, *Avogadro: an advanced semantic chemical editor, visualization, and analysis platform,* Journal of Cheminformatics **4**, 17 (2012).

3

Tuning Band Structure by Doping of Diamonds

The wide band gap of diamond necessitates the use of deep UV radiation for photoexcitation of electrons from the valence to the conduction band in order to trigger a photochemical reaction. To enable practical applications, new electronic states in the band gap should be introduced in order to facilitate visible-light absorption. Doping has been a widely explored means to tune band gap of semiconductors in order to facilitate strong light absorption in the material that could result in enhanced photocatalytic activity. In particular, for diamond, boron, nitrogen and phosphorus dopings have been explored as a possible means to introduce electronic states in the band gap. Their electronic structures have been investigated in this chapter using soft X-ray spectroscopy techniques to probe the sub-bandgap states. Specifically, an extensive study has been conducted to understand the synergistic effect of nanostructuration and boron doping on the sub-bandgap states of p-type diamond and its potential implications on photocatalysis.

Parts of this chapter have been included in [1].

3

3.1. p-type Diamonds

In order to introduce new states within the large band gap of diamond, boron-doping has been investigated as boron is a trivalent atom with a smaller atomic radius which enables its easy incorporation in the diamond lattice.[2, 3] XAS studies conducted on boron doped diamonds previously showed the technique to be sensitive to boron acceptor states that are formed due to electronic interactions between B and C atoms.[4–8] These acceptor states, which appear in the pre-edge region of the C K edge XAS spectra of diamond materials, directly evidence the possibility of introducing electronic states in the band gap of the material by doping at or very close to the surface although the origin of these states remain unclear. As a material, diamond is known to be chemically inert and stable and can be prepared in various morphologies.[9–14] From a catalysis point of view, however, it would be essential to select a morphology that combines a large surface area with the desired electronic structure properties needed for photocatalytic reduction of CO_2. Therefore, different morphologies of boron-doped diamonds such as polycrystalline (**B:PCD**), single crystal (**B:SCD**), diamond foams (**B:Dfoam**) and nanodiamonds (**B:ND**) as shown in Figure 3.1 were investigated using soft X-ray spectroscopy technique, described in Chapter 2. The experimental results were further supported by theoretical calculations on the lattice models shown in Figure 3.2 performed by collaborators at Uppsala University.

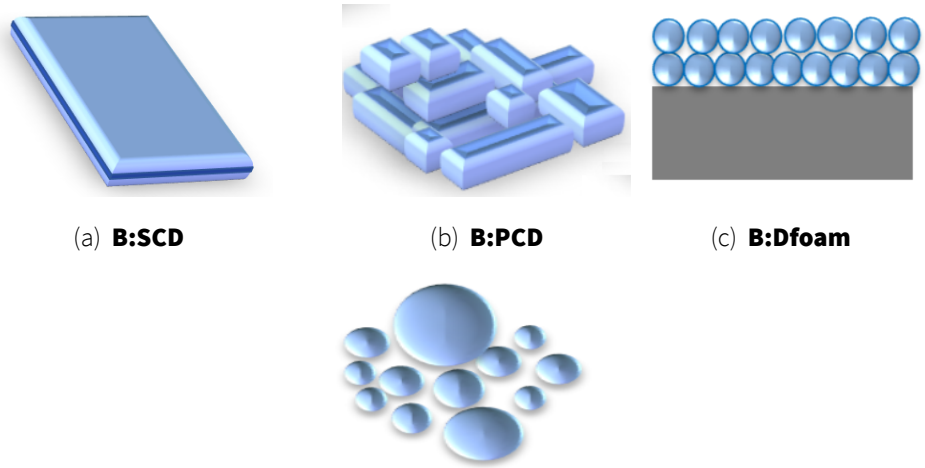

(a) **B:SCD** (b) **B:PCD** (c) **B:Dfoam**

(d) **B:ND**

Figure 3.1: *Illustrations of the different morphologies of B-doped diamonds investigated in this work.*

The different morphologies of boron-doped diamond were obtained from collaborators in the DIACAT consortium. Particularly, **B:ND**, which was prepared by milling a CVD boron-doped diamond electrode from *Element Six*, was obtained from Universität Würzburg. The starting material had a boron concentration of 1250 ppm which after milling resulted in a boron concentration of 1020 ppm in the nanodia-

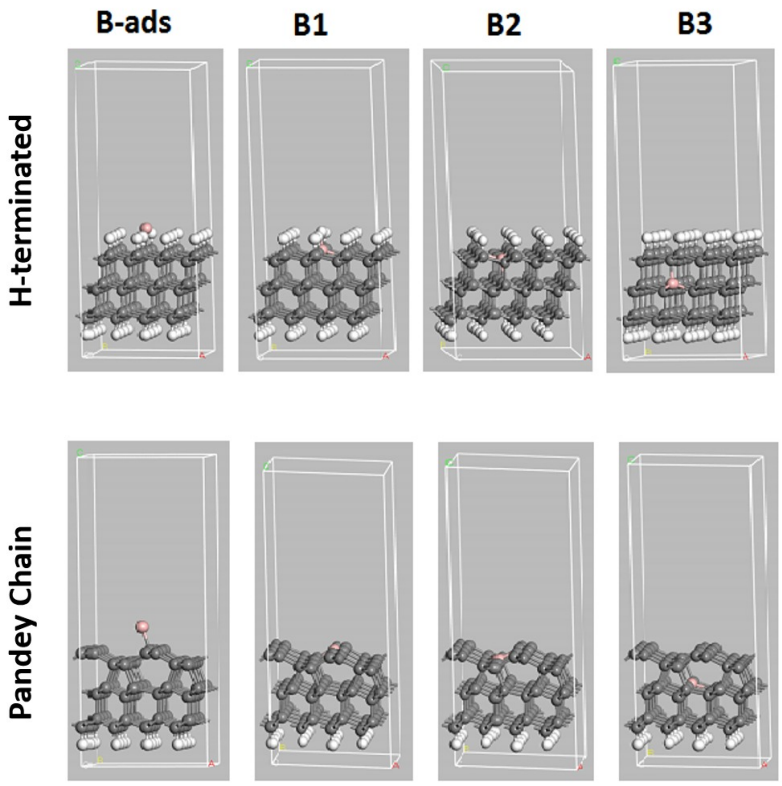

Figure 3.2: *Supercells showing the H-terminated and Pandey-Chain reconstructed diamond (111) surfaces, with B positioned as adsorbed (B-ads) or in atomic layer 1 (B1), 2 (B2) or 3 (B3), respectively. C, H and B are shown in grey, white and pink, respectively. Taken from [1]*

monds. The doped nanodiamonds were subsequently hydrogenated in a H_2 plasma at CEA in France and later drop casted on a Si wafer for the XAS studies. Undoped and boron-doped polycrystalline diamond as well as the diamond foam were prepared and subsequently hydrogenated at Fraunhofer IAF, Freiburg. The **PCD** and **B:PCD** film with boron concentration of 5670 ppm were prepared using a microwave plasma CVD reactor with CH_4, H_2 and $B(CH_3)_3$ in the gas mixture while **B:Dfoam** was prepared according to a method reported previously and contained 2835 ppm boron as determined by Raman scattering.[13] **B:SCD** was purchased from TISNCM (Moscow, Russia) with a boron content of 300 ppm and a <111> crystal orientation and subsequent H-termination was conducted using a H_2-plasma. All samples were measured in vacuum without prior annealing during the soft X-ray spectroscopic investigation. In the following sections the experimental results are presented which are supported by DFT calculations that were used to interpret the experimental observations.

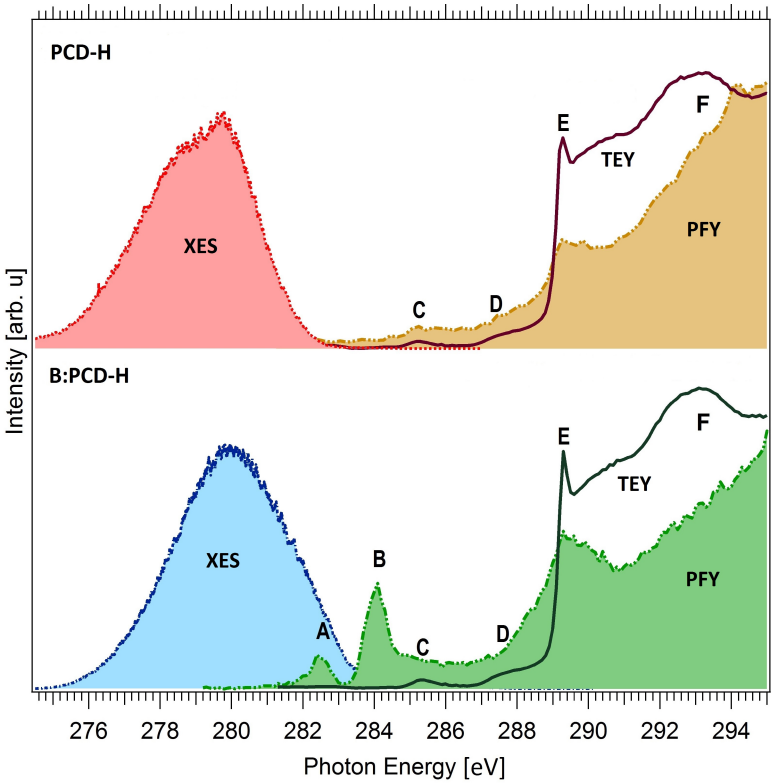

Figure 3.3: *C K edge XA (right) and XE (left) spectra of undoped and boron-doped H-terminated **PCD**. XA spectra on the right recorded in TEY (green and brown solid lines) and PFY (green and brown shaded regions) modes probe the unoccupied states. XE spectra on the left (red and blue shaded regions) represent the occupied states probed by non-resonant excitation at 320 eV. Taken from [1]*

3.1.1. Electronic structure of boron-doped diamonds

3.1.1.1. Soft X-ray spectroscopies

The density of unoccupied and occupied states in diamond are evidenced by XA and XE spectra respectively that are presented in Figure 3.3. The XA spectra were recorded in surface sensitive TEY mode which records the photocurrent resulting from X-ray absorption and bulk sensitive PFY mode which detects the emitted X-rays. In Figure 3.3, the XA and XE spectra of boron-doped and un-doped H terminated polycrystalline diamond (**B:PCD-H** and **PCD-H**) are presented. The XE spectra probes the occupied states corresponding to the carbon contribution to the valence band of diamonds. The XA spectra at the C K edge probe the unoccupied states corresponding to the carbon contribution to the conduction band in diamond, shown on the right of Figure 3.3. Both the TEY (solid lines) and PFY (shaded) XA spectra are presented.

No significant difference is observed between the TEY XA spectra of **B:PCD-H** and **PCD-H**. In the PFY spectra, three electronic states can be observed for both the undoped and doped polycrystalline dia-

monds as reported previously.[15] These are the characteristic features in diamond that appear at 285.4 eV (**C**), 289.3 eV (**E**) and 293.1 eV (**F**) and can be attributed to 1s to π^* transition, bulk excitons and 1s to σ^* transition in diamonds respectively.[15] An additional feature also appears at 287.5 eV (**D**) which is attributed to C-H bonds on the surface.[15] Two new unoccupied states at 282.5 eV (**A**) and 284.1 eV (**B**) close to the valence band edge of the diamonds are visible. These states do not appear in case of the un-doped diamond indicating that they result from the interaction of C with the dopant atoms.[4, 8] Furthermore, the absence of these two states in the TEY spectra of the B-doped diamond as seen in Figure 3.3 can be explained by the capture of electrons by the boron atom to form bound excitons which cannot be emitted, resulting in the absence of any signature in the TEY spectrum. [6]

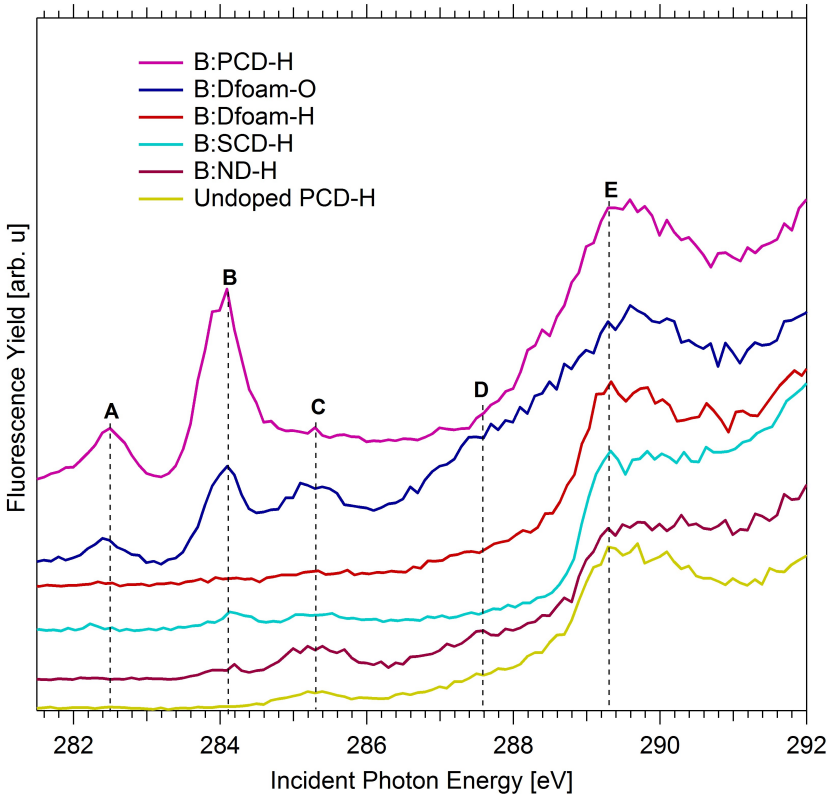

Figure 3.4: *C K edge XA spectra for different morphologies of boron-doped diamond. All spectra are recorded in the PFY mode. The figure highlights the difference in the pre-edge features of nanostructured diamond materials such as* ***B:Dfoam*** *and* ***B:ND****. Taken from [1]*

Analyzing the XA spectra of the different morphologies of diamonds as shown in Figure 3.4 resulted in a few interesting observations. The characteristic bulk excitonic peak **E** is observed for all diamond morphologies at *ca.* 289.3 eV. However, notable differences exist in the pre-edge region of the XA spectra of the different diamond samples. It can be noted that, in case of **B:SCD-H**, the resonance **A** almost vanishes and **B** is very weak. A similar trend is also observed for the resonances **A** and **B** in case of **B:ND-H**. The peaks **A** and **B** have a much higher intensity in **B:PCD-H** and **B:Dfoam-O** indicating a higher

probability of surface excitonic transitions in these two samples as compared to **B:SCD-H** and **B:ND-H**. A high relative intensity of peaks **A** and **B** with respect to the bulk excitonic peak **E**, in case of **B:Dfoam-O** and **B:PCD-H**, further suggests the possibility of a higher concentration of boron induced defects at the surface of the foam and at surfaces close to the grain boundaries in the PCD samples as compared to the other samples. Interestingly, these surface states vanish completely when the foam surface is hydrogenated (**B:Dfoam-H**) as shown in Figure 3.4 which is an indication of a possible saturation of the dangling bonds upon H termination and hydrogenation of π bonds. This is however, not the case for **B:PCD-H**.

On **B:ND-H** and **B:Dfoam-O**, an increased intensity of peak **C** is also observed (Figure 3.4), which is related to π^* transition due to amorphous carbon (a-C) present at the surface and at grain boundaries of the samples respectively and also those present around sites of lattice defects induced by boron doping. Additionally, in both the samples a very broad shoulder with a threshold at 286.5 eV (**D**) appears very close to the conduction band minimum (CBM) just below the bulk excitonic peak **E**.

This shoulder is further clarified by studying the H-terminated NDs of smaller particle sizes 30 nm and 50 nm as shown in Figure 3.5. Consequently, **B:ND-H** of smaller particle sizes 30 nm and 50 nm, both obtained by milling of commercially obtained **B:PCD** and subsequent centrifugation were investigated after a plasma hydrogenation treatment to remove any oxidized groups and impurities present on the surface.

The two peaks **A** and **B** induced by boron doping, as seen previously in other doped samples are absent in these smaller NDs. The lower concentration of boron in these nanoparticles or surface state passivation after hydrogenation could possibly explain this observation.[14] As can be seen in Figure 3.5, the pre-edge region exhibits only a single peak (**C**) at 285.2 eV, related to π^* transition from sp^2 carbon, which is a direct result of high concentration of a-C at the surface and at defect sites within the NDs. The broad shoulder **D** is observed with a high intensity only in case of the nanostructured diamonds, such as **B:Dfoam-O** (Figure 3.4) and **B:ND-H**(Figure 3.4 and Figure 3.5). In case of **B:Dfoam-H** this shoulder has a relatively lower intensity. C-H bonds that result from H-terminated surface of the diamonds are expected to exhibit a π^* resonance at 287.5 eV. An additional contribution from C-B bonds present on the surface could appear at 286.8 eV, as previously reported by Katamune *et al.*[16] We consider that both these π^* resonances due to C-B and C-H bonds at 286.8 eV and 287.5 eV, respectively, superpose to contribute to such a broad shoulder.

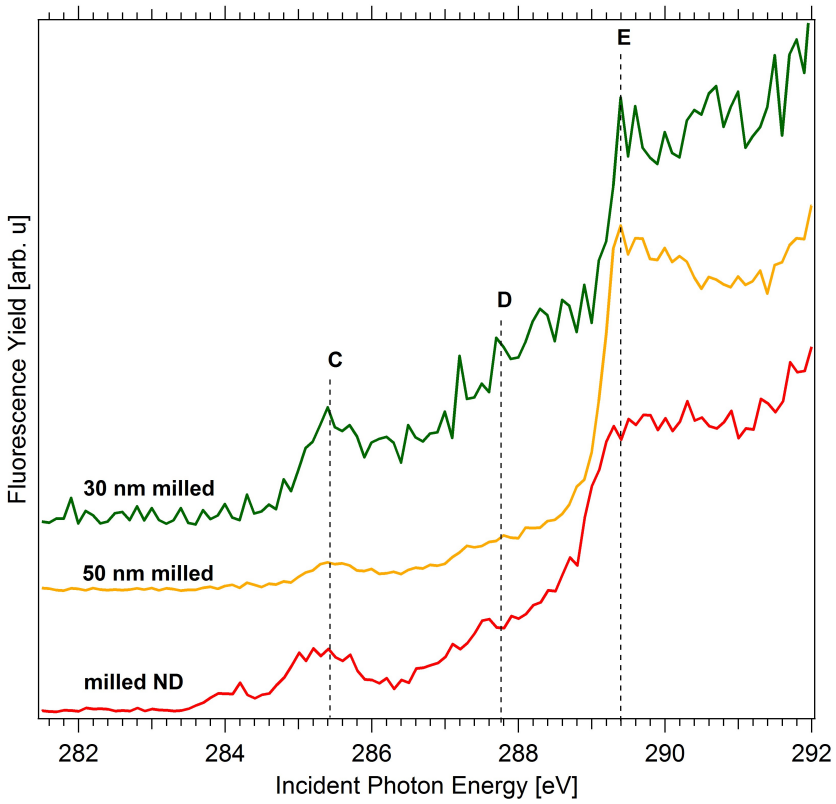

Figure 3.5: *C K edge XA spectra of boron-doped hydrogenated NDs with sizes 30 nm and 50 nm. The spectra are recorded in PFY mode and compared to that of the milled NDs with average particle size below 650 nm.[1]*

3.1.1.2. Density Functional Theory calculations

Theoretical calculations have been performed by Prof. Karin Larsson at Uppsala University to study the effect of substitutional boron doping on the formation of empty states above the valence-band edge of a diamond (111) surface. More specifically, pDOS spectra were calculated. To evaluate the accuracy of these calculations, the calculated band gap for bulk diamond was compared with the experimental one which resulted in very similar values; 5.40 eV vs. 5.47 eV.

Three different diamond surface models were used in the study; H-terminated (111), non-terminated (111), and Pandey-Chain reconstructed non-terminated (111). Figure 3.2 shows the super-cells of these specific surfaces. As a p-dopant species, the element B was, with one exception, substitutionally positioned at various levels in the diamond surface models. It was either adsorbed on the surface (B-ads) or positioned in the 1st (B1), 2nd (B2) or 3rd (B3) atomic C level (see Figure 3.2).

pDOS spectra of C atoms have been calculated with the purpose to investigate the boron-induced band gap-states just above the valence band edge of diamond. For comparison purposes, the density of states of the non-doped surfaces have also been calculated (see Figure 3.6). Since the Pandey-Chain

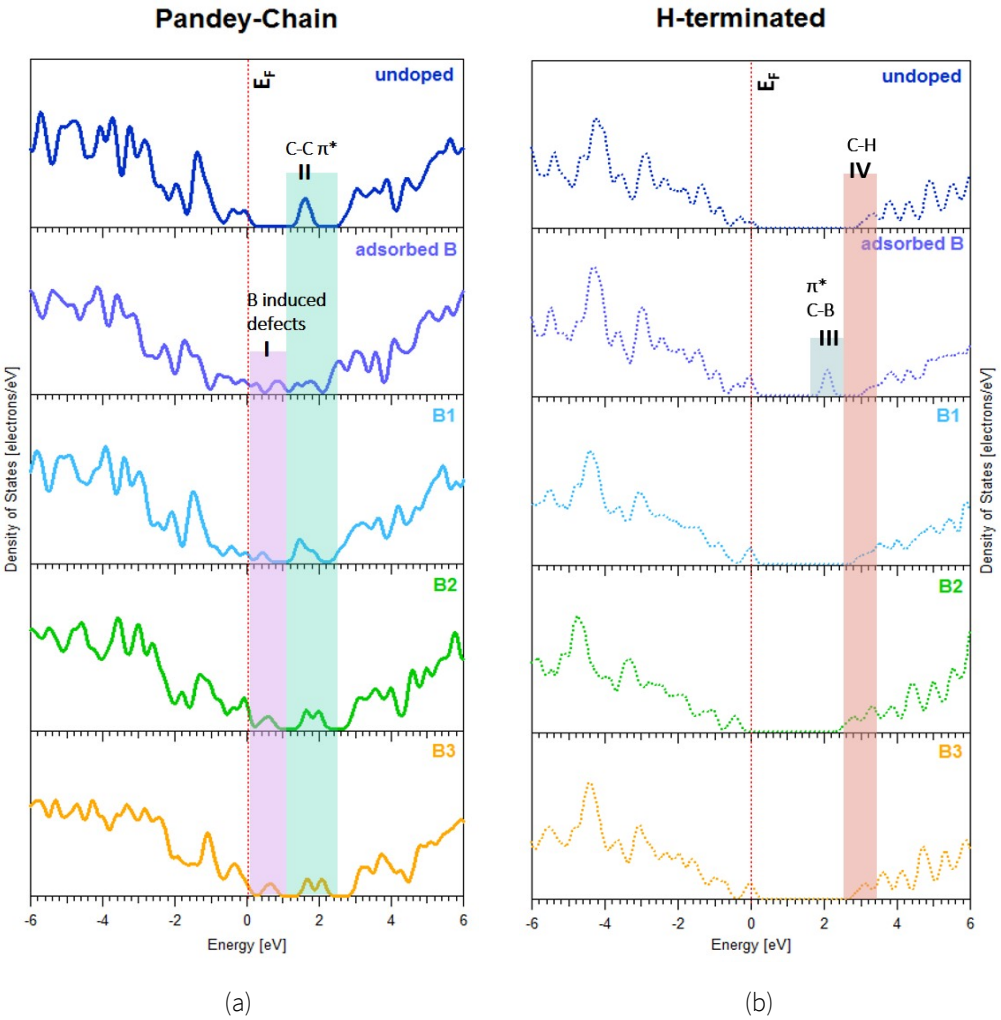

Figure 3.6: *pDOS spectra of carbon at (a) Pandey-chain reconstructed and (b) H-terminated surfaces. Both surfaces with boron atoms at different positions namely adsorbed B (in purple), boron in first atomic layer-B1 (in cyan), boron in second atomic layer-B2 (in green) and boron in third atomic layer-B3 (in yellow) have been compared with that of the undoped lattice (in blue). The Fermi level E_F is indicated as a dotted red line at 0 eV.*[1]

reconstructed surface is the most stable (111) surface at elevated temperatures, it is also the result for this specific surface that is interesting to compare with the experimental activities. As can be seen in Figure 3.6a and 3.6b, there are surface-induced band gap-states for diamond (111) surfaces, which are much lower positioned for the non-terminated Pandey-Chain reconstructed surface in comparison to the H-terminated one. The region I is induced by boron doping since it is not observed on the undoped diamond. The region II is related to π^* transitions due to surface reconstruction, but are also affected by the boron doping. The lowest positioned sub band gap state for the H-terminated surface is located in region III and is not observed on the undoped sample. The states in region IV are observed for all cases and are most likely related to C-H π^* transitions. The energy of this contribution varies slightly with boron doping.

Table 3.1: *Numerical values of the B-induced band gap peaks for various B and C positions in the diamond surface lattice as determined from DFT calculations. (All values provided are in eV with respect to the Fermi level)*

	C1[1]	C2[1]	C3[1]	C4[1]
H-terminated				
B-ads	2.1	2.1	2.1	2.1
B1	-	-	-	-
B2	-	-	-	-
B3	-	-	-	-
Non-terminated				
B-ads	0.9	0.9	0.9	0.8
B1	-	-	-	-
B2	0.8	0.8	0.8	0.8
B3	0.9	1.0	1.0	1.0
Pandey-Chain				
B-ads	0.3,0.9	0.2,0.9	0.2,0.9	0.2,0.9
B1	0.4	0.5	0.4	0.4
B2	0.6	0.6	0.5	0.6
B3	0.2	0.7	0.6	0.6

[1] C1, C2, C3 and C4 means that the choice of C for the pDOS calculations are within C layer 1, 2, 3 and 4, respectively. All of these specific C positions are as close as possible to the respective boron position.

An adsorbed boron did induce a surface state peak for the H-terminated surface at lower energy than the C-H bonds. The situation was completely different for the non-terminated and Pandey-Chain reconstructed diamond surfaces. All positions of boron (i.e., adsorbed, 1st, 2nd or 3rd atomic C layer) were found to induce a surface state peak for the Pandey-Chain reconstructed surface. It was only boron in layer 1 that did not render any surface peak for the non-reconstructed counterpart.

All numerical values of the boron induced mid-gap states in pDOS can be found in Table 3.1. More generally, it can be seen in Table 3.1 that boron incorporation affects the carbon atoms in the first four layers for the H-terminated and Pandey chain reconstructed diamond (111) surfaces. All C atoms sufficiently close to the B dopant will induce a surface state above the VBE for diamond 2.1 eV above the Fermi level

for H-terminated surface as opposed to 0.9 eV for other surfaces. The situation is very similar for the Pandey-Chain reconstructed diamond (111) surface. All C atoms sufficiently close to the B dopant will induce a surface state above the VBE for diamond. The numerical values as presented in Table 3.1 have been compared to experimental results in the discussion. Based on estimates from the experimental spectra, the Fermi level is placed at 283.8 eV in which case the relative positions of the sub-bandgap states in the boron-doped diamonds show good agreement with the theoretical estimates.

3.1.2. Discussions

Several studies have been conducted to determine the distribution of boron atoms within the diamond in order to establish a better correlation between the local environment of the boron atoms and its resulting electrical properties.[17–21] While these studies clarified the distribution of boron atoms in a polycrystalline or nanocrystalline diamond film, the impact of the local interaction of boron with C atoms at or close to the diamond surface and their impact on sub-bandgap defect states of carbon in nanostructured diamond materials remain unclear. Our experimental observations show that the local environment of boron induced defects may be different within the diamond lattice for different morphologies of the doped diamonds which could modify the energy of acceptor states within the band gap of diamond materials. The possible origin of the acceptor states close to the VBM and CBM will be discussed in the following sections.

3.1.2.1. Boron induced levels close to the valence band

We experimentally observe two new localized states **A** and **B** near the VBM of B-doped diamonds, below the Fermi level of the un-doped material. These states represent excitonic transitions from the C 1s core level to an empty surface state. In case of **B:PCD-H** and **B:Dfoam-OH**, the empty 2p orbitals of the boron atom hybridized with a C 2p orbital could contribute to a surface state to which a core electron from the C atom may be photoexcited. This conclusion has been supported by the theoretical calculations in the present study. All of the localized band gap states in region I of Figure 3.6a coincided with pDOS peaks for boron doped diamond. Previous microstructural investigations using HRTEM and EELS techniques on the local B environment in HPHT polycrystalline diamond films proposed that boron is present at the grain boundaries and in triangular shaped pockets at the grain junctions.[17, 20] However, using the same EELS technique, in case of CVD deposited boron doped polycrystalline diamond films, Huang *et al.* observed no signals from B at the grain boundaries and reported that the boron atoms are uniformly distributed inside each diamond grain.[18] FY intensity may vary depending on the

boron concentration as previously shown by Muramatsu *et al.*[7] In our case, the diamond materials have various boron concentrations between 300 and 6000ppm, which could explain partly the different FY intensities between the samples. Nevertheless, surface defects are also playing a role, especially on nanostructured diamonds, as seen by the disappearance of peaks **A** and **B** after H-termination of Dfoam.

All the diamond materials studied in the course of this investigation were hydrogenated at the surface. However, in case of **B:PCD-H** film and **B:Dfoam-O**, the surfaces at the grain boundaries may either contain carbon atoms with dangling bonds or C-C π bonded dimers which may be completely or partially H-terminated thus resulting in H atoms bonded to both sp^2 as well as sp^3 type C atoms.[22] Appearance of surface states due to dangling bonds on partially hydrogenated surfaces has already been reported by XAS investigations previously.[23] Incorporation of boron in the diamond lattice occurs predominantly by substitution of a tetrahedral coordinated C atom as it results in the least amount of distortion of the diamond lattice.[24] When the B atoms substitute C at the topmost layer of the lattice close to the grain boundaries, they could have two different environments. At the surfaces close to the grain boundaries, a substitutional B atom may result in C-C π bonded dimers, resulting in surface reconstruction of diamonds, thus reducing the number of dangling bonds. Glans et al. proposed that an excitonic transition to an empty state in this case should result in a resonance similar in character to the sp^2 peak **C**.[8] However, due to extensive hybridization between the B 2p and C 2p orbitals, the core level of carbon experiences a chemical shift to lower energy resulting in the surface excitonic state to appear at a lower incident photon energy of 284.1 eV (+0.3 eV vs. E_F as estimated from experiment). Theoretically, this hybridization is exhibited as a modification in the C-C π^* peak in the pDOS diagram as seen in region II of Figure 3.6a which is explained by an overlap between B and C orbitals. This implies that the feature **B** is due to surface states formed due to the sp^2 C-C bonds that are in close proximity to the B atoms at reconstructed surfaces. However some carbon atoms close to the B atoms do not undergo reconstruction. Such carbon atoms have dangling bonds and are predominantly found at partially or non hydrogenated surfaces typical to grain boundaries leading to unoccupied states within the valence band.[23] Glans et al. further proposed that localized states on these C atoms result in feature **A**.[8] This furthermore validates the observation of surface excitonic states in case of the **B:Dfoam-O**.

The experimental observations are complemented by DFT calculations which were presented in the previous section. According to the pDOS calculations, it is quite clear that the boron atoms at the Pandey-chain reconstructed surfaces contribute to the surface states closer to the valence band edge. As **B:PCD-H** and **B:Dfoam-O** contain numerous grain boundaries,[13] based on the theoretical calculations it is therefore reasonable to assert that presence of B atoms near the grain boundaries induce

defects at these non-terminated surfaces resulting in the high intensity peaks attributed to surface excitonic states. However, in case of **B:Dfoam-H** the defect states that are predominantly present at the surface of the crystallites are completely saturated upon hydrogenation[25–27] resulting in the absence of states **A** and **B** at the H-terminated surfaces as validated by theory calculations. Similar observation was reported by Barjon *et al.* based on cathodoluminescence measurements.[26, 27]

Such surface excitons were also observed by Graupner et al. on clean and hydrogen terminated (111) and (100) diamond surfaces at 284.6 eV and 284.15 eV respectively.[28] In case of **B:SCD-H** which has a (111) surface, the surface exciton peak appears very weakly at 284.1 eV. Such a red shift of 0.5 eV relative to the value reported in literature could be explained by the photoexcitation of C 1s electron from a C-C π bonded dimer into a boron 2p empty orbital, where the core level of C is also chemically shifted due to the presence of boron atoms. We can speculate that due to the absence of grain boundaries in the single crystal diamond, majority of the B atoms are present in the bulk of the crystal and hence do not induce a high concentration of defects near the surface. Since the possibility to dope a diamond (111) surface with boron is significantly higher than that of the (100) surface,[29] a higher concentration of boron can be achieved in case of (111) single crystal diamonds. However, in our study **B:SCD** has the least dopant concentration of all the materials investigated. The substitutional boron at the surface which is lesser in concentration than that in the bulk could result in defects such as dangling bonds which are completely passivated upon H termination.[26] Consequently, peak **A** which is attributed to dangling bond states vanishes. Reconstructions at the surface however are only weakly passivated resulting in a significantly reduced intensity of **B** as compared to **B:PCD-H** and **B:Dfoam-O**, in addition to the low concentration of boron in the sample.

In case of **B:ND-H** that is prepared by milling PC diamonds, bigger diamond crystallites are cleaved along the (111) planes.[14] During ball milling, crushing of the bigger crystallites along highly defective regions is preferred. In CVD PC diamonds, which is the starting material for preparation of the boron-doped NDs, defect rich regions have a high concentration of a-C.[14] Near these defect regions, boron is usually present as substitutional tetrahedral impurities in the diamond lattice. With defects diffusing away during the crushing process,[14] a significant amount of B would also be lost resulting in a lower concentration of B in the bulk of the resulting nanoparticles as was previously reported by Heyer *et al.*[14] The remaining boron centers at the surface of the produced nanoparticles contribute to the weakly observed surface excitonic state **B** at 284.1 eV as seen in Figure 3.4 which is attributed then to the surface states formed as a result of interaction between the residual sp^2 C atoms and tetrahedrally substituted boron atom. The appearance of peak **B** with an extremely weak intensity only suggests that the defect states are partially saturated upon hydrogenation. The π^* state due to the presence of sp^2 C

atoms on the nanoparticles further contribute towards the π^* resonance **C** at 285.2 eV. As proposed by Turner et al., such an amorphous shell of C also surrounds the nanocrystals[19] that compose diamond foams. Therefore a similar π^* resonance is also observed for **B-Dfoam:O**.

3.1.2.2. Boron induced levels close to the conduction band

What seems to differentiate the nanostructured morphologies of boron doped diamond from the other samples studied in this investigation is the additional broad shoulder near the conduction band edge extending from ca. 286.5 eV-288.7 eV. This additional feature is observed with a higher intensity for **B:Dfoam-O** as well as **B:ND-H** with sizes up to 10 nm. The presence of this peak is indicative of presence of C-B bonds at the surface of the nanostructured diamonds. [16] Our hypothesis here is that, in addition to the substitutional boron at the topmost layer of the diamond lattice, some of the carbon atoms at the surface with single dangling bonds bind to the B atoms which could originate from amorphous B_4C type inclusions[21] in nanocrystalline diamonds in order to reduce the surface energy during the doping process. Such inclusions were previously reported to be trapped in PC diamonds during their growth process.[20, 21] With a bond dissociation energy of ca. 448 kJ mol^{-1}, the C-B bond once formed is much stronger than a C-H bond. Hence hydrogenation treatment of the boron doped nanostructured diamonds cannot eliminate C-B bonds that are formed at the surface. The possibility of boron coordinated to the C atoms when not embedded in the diamond lattice is further confirmed by DFT calculations. The pDOS calculations for the adsorbed boron (B-ads) configuration in case of H terminated (111) diamond surface as shown in region III of Figure 3.6b evidences the appearance of a surface state closer to the conduction band, 2.1 eV above E_F which is in relative agreement with the experimentally estimated value of 3.0 eV vs E_F. The presence of such a bond results in a π^* resonance at 286.8 eV as was observed by Katamune et al. [16] For NDs smaller than 50 nm, the absence of surface excitonic peaks in the XA spectra indicates that most of the boron is present in the form of C-B bonds at the surface of the nanoparticles and that the defects induced upon surface reconstruction are milled away leaving the nanoparticle surfaces with surface defects that may have been completely saturated during the hydrogenation treatment. The concentration of substitutional boron at the surface is too low to be detected with our instrument. In case of **B:Dfoam-O**, besides the π^* resonance due to B adsorbed on the surface, additional contribution from C=O groups[15] at the oxidized surface leads to a higher intensity of the shoulder as observed in Figure 3.4.

3.2. n-type Diamonds

Surface states can also be introduced close to the CBM by doping diamond with donor atoms. This results in n-type doping of the material. Although boron doping in diamonds can be easily achieved by direct substitution of the carbon atom by boron atom, n-type doping in diamond is said to be extremely difficult.[30] Investigation of potential candidates for n-type dopants suggests nitrogen and phosphorus among others as potential substitutional donors in diamond. Nitrogen which is also present in natural types Ib and Ia diamonds have a negative formation energy of -3.4 eV, as shown by *ab initio* calculations and hence can be easily incorporated in the diamond lattice.[31] However, nitrogen substitution in the diamond lattice results in distortion of the diamond lattice due to antibonding interaction between the N lone pair orbitals and C dangling bond.[31]. Furthermore, the incorporation of nitrogen leads to the formation of deep donor levels, 1.7 eV below CBM, which makes it insulating at room temperature and therefore not useful for electronic applications. On the other hand, phosphorus, which is the next candidate in group V, although suitable as a donor atom due to its shallow donor level 0.6 eV below CBM, has a very high formation energy of 10.4 eV, leading to its small solubility, thus making it difficult to incorporate in the diamond lattice.[31] Despite these challenges, phosphorus has been incorporated in the diamond (111) layers at high concentrations.[32, 33] The suitability of these materials in electronic applications has been investigated using various experimental techniques such as cathodoluminescence, mobility measurements using Hall experiments etc.[34–36] Furthermore, it has also been suggested that n-type doping of H-terminated diamonds results in enhanced electron emission due to lowering of the effective work function.[37, 38] Sun *et al.* even evidenced sub band gap photo-induced electron emission which could be advantageous for a solar energy conversion device.[39] These reports suggest that n-type diamonds could be especially interesting for photocatalytic reactions in solution enabled via solvated electron generation. Investigation of their electronic structure is therefore, of great importance.

Literature suggests that theoretical models for N-doped UNCD have already predicted an increase in sp^2 carbon due to the presence of nitrogen in diamond.[40] Furthermore, it was reported that doping grain boundaries of diamond with nitrogen results in new electronic states within the band gap of diamond which are associated with carbon and nitrogen.[40] At the same time, however, the effect of phosphorus doping on the electronic structure of diamonds has remained largely unexplored till date. XAS as a technique can therefore, be employed to investigate the general effect of n-type doping on the electronic structure of diamond as it is an element-sensitive local probe for the partial density of unoccupied states in a material. In particular, it is sensitive to the π^* state of sp^2 carbon as also evi-

denced in the case of B-doped diamonds and other surface states which appear in the pre-edge of the C K edge XA spectrum. In this section, therefore, we present a short X-ray absorption study of the electronic structure of n-type diamonds doped with nitrogen and phosphorus. The studies were primarily conducted on H-terminated doped single crystal diamond (111) surfaces (**N:SCD** and **P:SCD**) obtained from collaborators at CEA in France and Fraunhofer IAF in Freiburg.

3.2.1. Electronic structure of Nitrogen- and Phosphorus-doped Diamonds

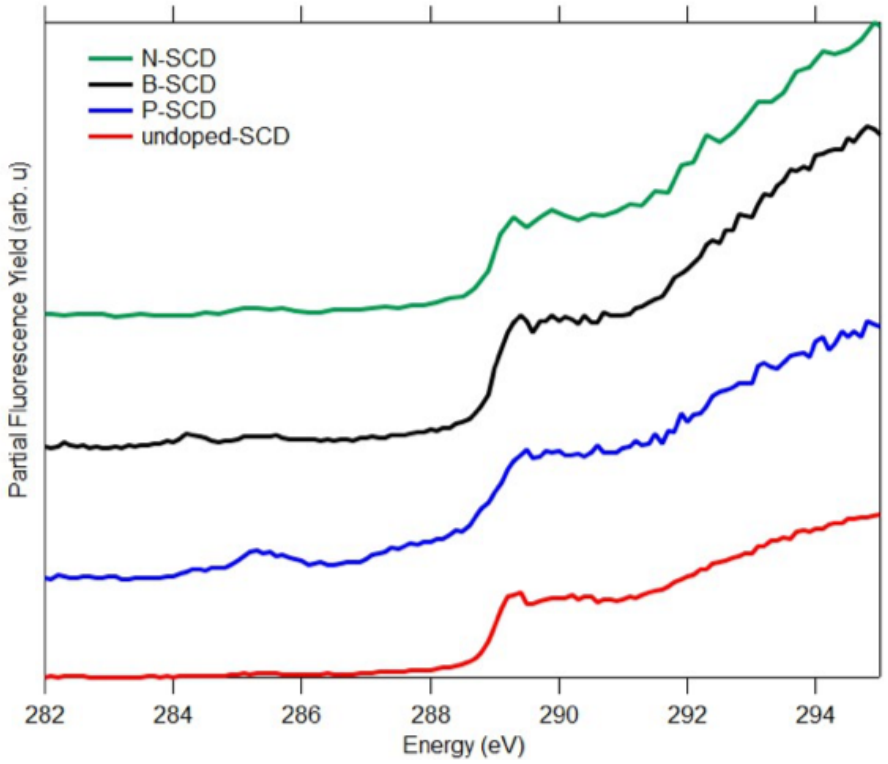

Figure 3.7: *C K edge PFY spectra for N- and P-doped single crystal diamonds (in green and red). The spectra have been compared with those of undoped (in blue) and B-doped (in black) single crystal diamond samples.*

Figures 3.7 and 3.8 present the density of unoccupied states in N- and P-doped SC diamonds (**N:SCD** and **P:SCD**) as evidenced by the PFY and TEY spectra, respectively. The TEY spectra exhibit four prominent features. On the undoped singe crystal diamond, a very sharp peak can be observed at 289.3 eV, corresponding to the core-exciton near the diamond surface.[15] This characteristic feature of diamond materials is also evident in the doped diamonds. However, the excitonic peak becomes very broad and shallow for the N doped and P doped diamond samples. The difference in the excitonic peak is not so clear in the PFY spectra. This is because in PFY, photons emitted from the bulk of the sample are detected while TEY detects the current resulting from emission of electrons from the surface of the sample.

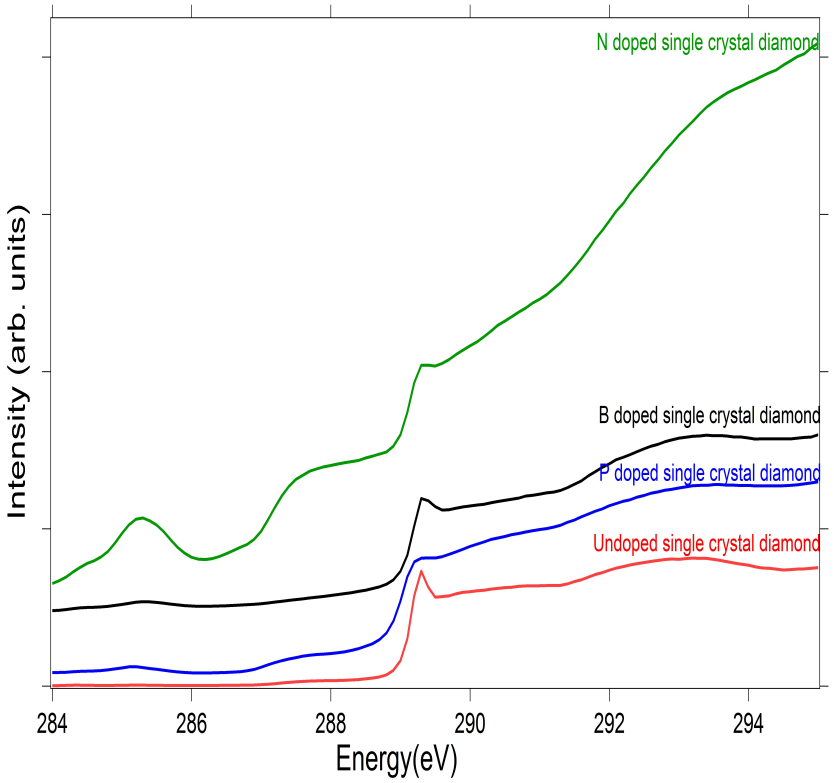

Figure 3.8: *C K edge TEY spectra for N- and P-doped single crystal diamonds (in green and blue). The TEY spectra have been compared with those of undoped (in red) and B-doped (in black) single crystal diamond samples.*

In addition to the excitonic peak, the σ^* transition is also observed in the **undoped-SCD** and **B:SCD** at 293.2 eV.[15] Once again, this transition becomes less pronounced in case of the N and P doped diamond samples. The feature due to C-H groups around 287.5 eV is very strong in case of the N and P doped samples as is evident from Figure 3.8. This shoulder is not evident in the bulk sensitive PFY spectrum which indicates that N and P dopant atoms induce an n-type doping in the diamond samples resulting in more available electrons that can be emitted, as will be explained in the following section. Also, the π^* transition at 285.3 eV becomes quite pronounced for the N doped diamond in the TEY spectrum. This is due to the presence of a significant amount of sp^2 carbon atoms on the surface. A comparison of the PFY spectra also shows a pronounced π^* feature at 285.3 eV and C-H shoulder at 287.3 eV for **P:SCD** alone.

3.2.2. Discussions

Unlike boron-doped diamonds, there have not been too many studies reported in literature elucidating the electronic structure of n-type diamonds doped with nitrogen and phosphorus atoms. In this section, therefore, we will briefly discuss our experimental observations, explaining the origin of the main features in the spectra.

The characteristic peak of diamonds at 289.3 eV as observed in the TEY spectrum corresponds to the core exciton formed close to the surface and is therefore said to be susceptible to changes due to surface groups.[41] This peak which is typically very sharp in the undoped and B-doped SC diamonds are broad and shallow for the N- and P- doped diamonds as seen in Figure 3.8. A study by Birrell *et al.* reported the disappearance of the diamond exciton in N-doped ultrananocrystalline diamond.[42] The authors of this study proposed that the excitonic peak in diamond is quite prominent for short range order of C atoms and incorporation of nitrogen leads to increase in the crystallite size resulting in more long-range order.[42] In CVD grown single crystal diamonds long range order has been evidenced by the appearance of a single peak in the X-ray diffractogram.[43] This could explain the shallow nature of the excitonic peak in the N- and P-doped SC diamonds as a result of the disappearance of the core exciton.

That the excitons disappear in SCD is further in agreement with the fact that NEXAFS is a technique sensitive to only short-range order[44] and hence not sensitive to the bulk excitons in SCD. In fact the diamond core excitonic peak is said to be the most sensitive feature in NEXAFS whereby the intensity of this peak reduces drastically upon formation of point defects in the diamond that affects the short-range crystalline order in the material.[44] In N-doped SCD N-V centers are the most commonly observed point defects formed during the CVD growth of the diamond.[45] Similar impurity-vacancy complex formation was theoretically investigated in P-doped SCD.[46] A CVD grown P-doped SCD film is also reported to contain point defects in the form of carbon dangling bonds as evidenced by ESR spectroscopy.[47] The presence of these point defects in our **N:SCD** and **P:SCD** films could further explain the broadened excitonic peak observed in our experimental spectra. Furthermore, this core-excitonic feature is highly susceptible to surface groups on diamond as pointed out by Stacey *et al.*[41] In particular, Koeck *et al.* reported that N- and P-doping reduces the effective work function of H-terminated diamonds thus allowing sub-band gap electron emission with a lower emission barrier.[37, 38]. Since the samples were H-terminated and not annealed before measurements, the electron emission to an adsorbed water layer on the surface of H-terminated **N:SCD** and **P:SCD**[48] could potentially explain the disappearance of the core-exciton. This role of surface adsorbates becomes further clear when the samples are measured in annealed and unannealed state at the PEAXIS end station, presented in section 5.1 of this dissertation.

Such an electron emission is possibly also evidenced in the TEY spectrum by the intense shoulder at 287 eV close to the conduction band minimum. This shoulder could be attributed to a transition from the core to a π^* orbital of a C-H bond, which is enhanced by the presence of donor levels of N and P located 1.7 eV [42] and 0.56 eV [49] below the CBM respectively. In addition to the broad and shallow excitonic peak, N-doped SC diamond exhibits a very intense peak at 285.4 eV compared to the other

single crystal samples. This high intensity may be attributed to possible reconstructions of the (111) surface at structural defects and dislocations formed during N incorporation in the films.

3.3. Implications to photocatalysis

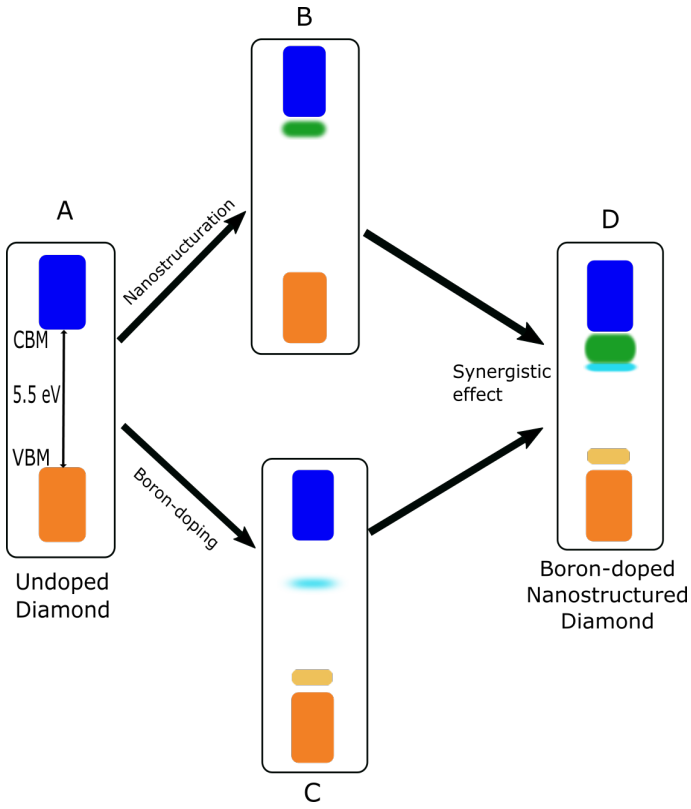

Figure 3.9: *Schematic illustration depicting the two ways of introducing surface states in the band gap of undoped diamond (A). One way is nanostructuration which introduces states close to the CBM due to surface groups on nanostructured diamond surfaces (B). Another means to introduces in-gap states is boron-doping which introduces surface states close to both the CBM and VBM (C). A synergistic effect results in a broad band of surface states close to the CBM and acceptor states close to the VBM in nanostructured B-doped diamond (D).*

In view of our discussions, nanostructuration along with boron doping can be proposed as a synergetic strategy that could potentially introduce defect states that are close to both the VBM and CBM of diamonds, as exhibited in Figure 3.4.

As shown in Figure 3.9, boron doping of diamonds result in acceptor states close to both the VBM and CBM of diamonds which is a surface dominated effect as these states are not so strongly observed for the single crystal B-doped diamond. These states are therefore further enhanced upon nanostructuration. Furthermore, H-termination introduces additional states below the CBM while saturating the acceptor states close to the VBM. A combination of these two steps produces boron doped nanostruc-

tured diamonds with enhanced surface areas which is an essential characteristic of an efficient catalyst. Furthermore, the introduction of defect states within the band gap of nanostructured diamonds, close to both the valence and conduction bands could potentially facilitate a pathway for defect-based transitions.[50–54] Energy upconversion based on related principle has been demonstrated in other materials.[54] In addition, the negative electron affinity of the diamond surface should also be preserved in order to generate solvated electrons. It has to be noted that other surface treatments such as ozone treatment and amination of the surface could also lead to complementary surface states close to the conduction band of diamonds.[55]

Our results show that a synergistic effect of nanostructuration and boron doping, coupled with a high surface area offered by the nanostructured diamond materials such as foam and NDs could potentially make them promising materials for application as membranes in photoelectrocatalytic cells or catalyst nanoparticles in slurry based photocatalaytic reactors respectively. However, boron-doping alone may not be sufficient to ensure visible light induced sub-band gap electron emission from the diamonds for a direct photocatalysis in solution. For the purpose of electron emission, n-type diamonds have been indeed shown to be more promising as they reduce the emission barrier in H-terminated diamonds.[37] Furthermore, in nanostructured diamonds, N-doping has been particularly predicted to introduce sp^2 carbon along the grain boundaries which impart conductivity to the diamond. Therefore, one might say that an acceptor and donor co-doped nanostructured diamond material could be a possible consideration for a potential catalyst, which may potentially open a new avenue of research on diamond-based photocatalytic materials. Such a doping scheme in diamonds would not only introduce more conductive surface states within the band gap of the material for defect-assisted transition, but also enable visible light sub-band gap electron emission in order to generate solvated electrons for photocatalytic reactions.

3.4. Conclusions

The electronic structure of p- and n-type diamonds have been investigated using soft X-ray absorption spectroscopy. In particular, boron doped diamond materials were investigated in detail to engineer solutions enabling eventual defect-based visible-light absorption. Different morphologies of diamonds ranging from polycrystalline to single crystals, foams and nanodiamonds were studied using soft X-ray absorption supported by density functional theory to understand the influence of morphology of the doped diamond materials on the electronic structure. Our observations show that B-dopants close to the surface of diamond crystallites introduces electronic states in the band gap of diamond which can

be altered by tuning the morphology of the diamond. Surface states localized close to the VBM were deduced to originate from boron doping induced surface reconstructions and dangling bonds which are likely to be found at surfaces of the crystallites. Additionally, boron doping in nanostructured diamonds such as foams and nanodiamonds was also found to introduce π^* states close to the conduction band of diamonds related to the C-B bond.

The most interesting results were obtained from the electronic structure investigation of the N and P doped diamonds. Our studies show that n-type doping in diamond with N and P atoms results in a broad and shallow excitonic peak which could originate from point defects in the samples along with long-range crystalline order in single crystal diamonds in the bulk of the material. Furthermore, an enhanced sub-band gap electron emission is observed from a continuous band below the conduction band minimum in the H-terminated diamond samples, which is well in agreement with literature reports on reduction in electron emission barrier upon n-type doping of H-terminated diamonds. This electron emission further helps to explain the disappearance of the core-exciton at the surface which is attributed to a transfer of the electron to an adsorbed water layer on the surface of the H-terminated material. Additionally, nitrogen doping enhances the intensity of the sub band gap sp^2 carbon state which is known to impart conductivity to nanostructured N-doped diamonds.

As diamonds have previously been demonstrated as promising photocatalysts due to their electron emission capabilities, it may be suggested that nanostructured diamonds co-doped with boron and an electron donor could be a promising solution for sustainable photocatalysts for direct visible light induced CO_2 reduction in solution.

References

[1] S. Choudhury, B. Kiendl, J. Ren, F. Gao, P. Knittel, C. Nebel, A. Venerosy, H. Girard, J.-C. Arnault, A. Krueger, K. Larsson, and T. Petit, *Combining nanostructuration with boron doping to alter sub band gap acceptor states in diamond materials,* J. Mater. Chem. A **6**, 16645 (2018).

[2] A. Deneuville, *Chapter 4 Boron doping of diamond films from the gas phase,* Semiconductors and Semimetals - SEMICOND SEMIMET **76**, 183 (2003).

[3] E. A. Ekimov, V. A. Sidorov, E. D. Bauer, N. N. Mel'nik, N. J. Curro, J. D. Thompson, and S. M. Stishov, *Superconductivity in diamond,* Nature **428**, 542 (2004).

[4] J. Nakamura, E. Kabasawa, N. Yamada, Y. Einaga, D. Saito, H. Isshiki, S. Yugo, and R. C. C. Perera, *Electronic structures of* $\mathrm{B}\ 2p$ *and* $\mathrm{C}\ 2p$ *levels in boron-doped diamond films studied using soft X-ray absorption and emission spectroscopy,* Phys. Rev. B **70**, 245111 (2004).

[5] Y. Muramatsu, T. Takebe, A. Sawamura, J. Iihara, A. Nanba, T. Imai, J. D. Denlinger, and R. C. C. Perera, *Two-acceptor levels in the band gap of boron-doped diamond semiconductors analyzed by soft X-ray absorption spectroscopy and DV-Xα calculations,* X-Ray Spectrometry **36**, 162 (2007).

[6] I. Zegkinoglou, P. L. Cook, P. S. Johnson, W. Yang, J. Guo, D. Pickup, R. González-Moreno, C. Rogero, R. E. Ruther, M. L. Rigsby, J. E. Ortega, R. J. Hamers, and F. J. Himpsel, *Electronic Structure of Diamond Surfaces Functionalized by Ru(tpy)$_2$,* The Journal of Physical Chemistry C **116**, 13877 (2012).

[7] Y. Muramatsu and Y. Yamamoto, *Local structure analysis of heavily boron-doped diamond by soft X-ray spectroscopy,* Diamond and Related Materials **39**, 53 (2013).

[8] P.-A. Glans, T. Learmonth, K. E. Smith, S. Ferro, A. D. Battisti, M. Mattesini, R. Ahuja, and J.-H. Guo, *Electronic structure of boron doped diamond: An x-ray spectroscopic study,* Applied Physics Letters **102**, 162103 (2013).

[9] O. A. Williams and M. Nesládek, *Growth and properties of nanocrystalline diamond films,* physica status solidi (a) **203**, 3375 (2006).

[10] M. Nesládek, D. Tromson, C. Mer, P. Bergonzo, P. Hubik, and J. J. Mares, *Superconductive B-doped nanocrystalline diamond thin films: Electrical transport and Raman spectra,* Applied Physics Letters **88**, 232111 (2006).

[11] W. Gajewski, P. Achatz, O. A. Williams, K. Haenen, E. Bustarret, M. Stutzmann, and J. A. Garrido, *Electronic and optical properties of boron-doped nanocrystalline diamond films,* Phys. Rev. B **79**, 045206 (2009).

[12] H. Kato, J. Hees, R. Hoffmann, M. Wolfer, N. Yang, S. Yamasaki, and C. E. Nebel, *Diamond foam electrodes for electrochemical applications,* Electrochemistry Communications **33**, 88 (2013).

[13] F. Gao, M. T. Wolfer, and C. E. Nebel, *Highly porous diamond foam as a thin-film micro-supercapacitor material,* Carbon **80**, 833 (2014).

[14] S. Heyer, W. Janssen, S. Turner, Y.-G. Lu, W. S. Yeap, J. Verbeeck, K. Haenen, and A. Krueger, *Toward Deep Blue Nano Hope Diamonds: Heavily Boron-Doped Diamond Nanoparticles,* ACS Nano **8**, 5757 (2014).

[15] Z. Shpilman, I. Gouzman, T. Minton, L. Shen, A. Stacey, J. Orwa, S. Prawer, B. Cowie, and A. Hoffman, *A Near Edge X-ray Absorption Fine Structure Study of Oxidized Single Crystal and Polycrystalline Diamond Surfaces,* Diamond and Related Materials **45**, 20 (2014).

[16] K. Yuki, T. Satoshi, O. Shinya, S. Hiroyuki, and Y. Tsuyoshi, *Near-Edge X-ray Absorption Fine-Structure Study on Hydrogenated Boron-Doped Ultrananocrystalline Diamond/Amorphous Carbon Composite Films Prepared by Coaxial Arc Plasma Deposition,* Transactions of the Materials Research Society of Japan **40**, 243 (2015).

[17] N. Dubrovinskaia, R. Wirth, J. Wosnitza, T. Papageorgiou, H. F. Braun, N. Miyajima, and L. Dubrovinsky, *An insight into what superconducts in polycrystalline boron-doped diamonds based on investigations of microstructure,* Proceedings of the National Academy of Sciences **105**, 11619 (2008).

[18] J. T. Huang, C. S. Hu, J. Hwang, H. Chang, and L. J. Lee, *Desegregation of boron at the grain boundaries of the in situ boron doped diamond films,* Applied Physics Letters **67**, 2382 (1995).

[19] S. Turner, Y.-G. Lu, S. D. Janssens, F. Da Pieve, D. Lamoen, J. Verbeeck, K. Haenen, P. Wagner, and G. Van Tendeloo, *Local boron environment in B-doped nanocrystalline diamond films,* Nanoscale **4**, 5960 (2012).

[20] G. Zhang, S. Turner, E. A. Ekimov, J. Vanacken, M. Timmermans, T. Samuely, V. A. Sidorov, S. M. Stishov, Y. Lu, B. Deloof, B. Goderis, G. V. Tendeloo, J. V. de Vondel, and V. V. Moshchalkov, *Global and Local Superconductivity in Boron‐Doped Granular Diamond,* Advanced Materials **26**, 2034 (2014).

[21] Y.-G. Lu, S. Turner, E. Ekimov, J. Verbeeck, and G. V. Tendeloo, *Boron-rich inclusions and boron distribution in HPHT polycrystalline superconducting diamond,* Carbon **86**, 156 (2015).

[22] M. Sh., T. O., A. R., W. O. A., G. D., and H. A., *Hydrogen concentration and bonding in nano-diamond films of varying grain sizes grown by different chemical vapor deposition methods,* physica status solidi (a) **204**, 2860 (2007).

[23] K. Bobrov, G. Comtet, G. Dujardin, L. Hellner, P. Bergonzo, and C. Mer, *Surface electronic states of the partially hydrogenated diamond* $\mathrm{C}(100)-(2\times1):\mathrm{H}$ *surface,* Phys. Rev. B **63**, 165421 (2001).

[24] X. Hu, Y. Dai, R. Li, H. Shen, and X. He, *A molecular dynamics study of interstitial boron in diamond,* Physica B: Condensed Matter **327**, 39 (2003).

[25] C. Fernández-Lorenzo, D. Araújo, J. Martín, R. Alcántara, J. Navas, M. Villar, M. Alegre, P. Volpe, F. Omnàs, and E. Bustarret, *Hydrogen passivation of boron acceptors in as-grown boron-doped CVD diamond epilayers,* Diamond and Related Materials **19**, 904 (2010).

[26] J. Barjon, N. Habka, J. Chevallier, F. Jomard, E. Chikoidze, C. Mer-Calfati, J. C. Arnault, P. Bergonzo, A. Kumar, J. Pernot, and F. Omnes, *Hydrogen-induced passivation of boron acceptors in monocrystalline and polycrystalline diamond,* Phys. Chem. Chem. Phys. **13**, 11511 (2011).

[27] J. Barjon, *Luminescence Spectroscopy of Bound Excitons in Diamond,* physica status solidi (a) **214**, 1700402 (2017).

[28] R. Graupner, J. Ristein, L. Ley, and C. Jung, *Surface-sensitive k-edge absorption spectroscopy on clean and hydrogen-terminated diamond (111) and (100) surfaces,* Phys. Rev. B **60**, 17023 (1999).

[29] A. Boussadi, A. Tallaire, O. Brinza, M. Pinault-Thaury, and J. Achard, *Thick heavily boron doped CVD diamond films homoepitaxially grown on (111)-oriented substrates,* Diamond and Related Materials **79**, 108 (2017).

[30] M.-A. Pinault, J. Barjon, T. Kociniewski, F. Jomard, and J. Chevallier, *The n-type doping of diamond: Present status and pending questions,* Physica B: Condensed Matter **401-402**, 51 (2007).

[31] S. A. Kajihara, A. Antonelli, J. Bernholc, and R. Car, *Nitrogen and potential n-type dopants in diamond,* Phys. Rev. Lett. **66**, 2010 (1991).

[32] T. Grotjohn, D. Tran, M. Yaran, S. Demlow, and T. Schuelke, *Heavy phosphorus doping by epitaxial growth on the (111) diamond surface,* Diamond and Related Materials **44**, 129 (2014).

[33] H. Kato, D. Takeuchi, M. Ogura, T. Yamada, M. Kataoka, Y. Kimura, S. Sobue, C. E. Nebel, and S. Yamasaki, *Heavily phosphorus-doped nano-crystalline diamond electrode for thermionic emission application,* Diamond and Related Materials **63**, 165 (2016), 9th International Conference on New Diamond and Nano Carbons – NDNC 2015.

[34] D. Araujo, A. Tajani, E. Gheeraert, and E. Bustarret, *Study of the phosphorus incorporation in n-doped diamond films by cathodoluminescence,* Journal of Physics: Condensed Matter **16**, S287 (2004).

[35] Z. Remes, C. Uzan-Saguy, E. Baskin, R. Kalish, Y. Avigal, M. Nesladek, and S. Koizumi, *Photo-Hall effect measurements in P, N and B-doped diamond at low temperatures,* Diamond and Related Materials **13**, 713 (2004), 14th European Conference on Diamond, Diamond-Like Materials, Carbon Nanotubes, Nitrides and Silicon Carbide.

[36] J. Barjon, M.-A. Pinault, T. Kociniewski, F. Jomard, and J. Chevallier, *Cathodoluminescence as a tool to determine the phosphorus concentration in diamond,* physica status solidi (a) **204**, 2965 (2007).

[37] F. A. Koeck and R. J. Nemanich, *Low temperature onset for thermionic emitters based on nitrogen incorporated UNCD films,* Diamond and Related Materials **18**, 232 (2009), nDNC 2008 Proceedings of the International Conference on New Diamond and Nano Carbons 2008.
[38] F. A. Koeck, R. J. Nemanich, A. Lazea, and K. Haenen, *Thermionic electron emission from low work-function phosphorus doped diamond films,* Diamond and Related Materials **18**, 789 (2009), proceedings of Diamond 2008, the 19th European Conference on Diamond, Diamond-Like Materials, Carbon Nanotubes, Nitrides and Silicon Carbide.
[39] T. Sun, F. A. M. Koeck, C. Zhu, and R. J. Nemanich, *Combined visible light photo-emission and low temperature thermionic emission from nitrogen doped diamond films,* Applied Physics Letters **99**, 202101 (2011).
[40] P. Zapol, M. Sternberg, L. A. Curtiss, T. Frauenheim, and D. M. Gruen, *Tight-binding molecular-dynamics simulation of impurities in ultrananocrystalline diamond grain boundaries,* Phys. Rev. B **65**, 045403 (2001).
[41] A. Stacey, B. C. C. Cowie, J. Orwa, S. Prawer, and A. Hoffman, *Diamond C 1s core-level excitons: Surface sensitivity,* Phys. Rev. B **82**, 125427 (2010).
[42] J. Birrell, J. E. Gerbi, O. Auciello, J. M. Gibson, D. M. Gruen, and J. A. Carlisle, *Bonding structure in nitrogen doped ultrananocrystalline diamond,* Journal of Applied Physics **93**, 5606 (2003).
[43] C.-s. Yan, Y. K. Vohra, H.-k. Mao, and R. J. Hemley, *Very high growth rate chemical vapor deposition of single-crystal diamond,* Proceedings of the National Academy of Sciences **99**, 12523 (2002).
[44] A. Laikhtman, I. Gouzman, A. Hoffman, G. Comtet, L. Hellner, and G. Dujardin, *Sensitivity of near-edge X-ray absorption fine structure spectroscopy to ion beam damage in diamond films,* Journal of Applied Physics **86**, 4192 (1999).
[45] A. Tallaire, M. Lesik, V. Jacques, S. Pezzagna, V. Mille, O. Brinza, J. Meijer, B. Abel, J. Roch, A. Gicquel, and J. Achard, *Temperature dependent creation of nitrogen-vacancy centers in single crystal CVD diamond layers,* Diamond and Related Materials **51**, 55 (2015).
[46] R. Jones, J. E. Lowther, and J. Goss, *Limitations to n□type doping in diamond: The phosphorus□vacancy complex,* Applied Physics Letters **69**, 2489 (1996).
[47] M. Katagiri, J. Isoya, S. Koizumi, and H. Kanda, *Electron spin resonance characterization of phosphorus-doped CVD diamond films,* physica status solidi (a) **201**, 2451 (2004).
[48] F. Maier, M. Riedel, B. Mantel, J. Ristein, and L. Ley, *Origin of Surface Conductivity in Diamond,* Phys. Rev. Lett. **85**, 3472 (2000).
[49] G. Alfieri, L. Kranz, and A. Mihaila, *Phosphorus-Related Complexes and Shallow Doping in Diamond,* physica status solidi (RRL) – Rapid Research Letters **12**, 1700409 (2018).
[50] D. Wang, G. Xing, M. Gao, L. Yang, J. Yang, and T. Wu, *Defects-Mediated Energy Transfer in Red-Light-Emitting Eu-Doped Zno Nanowire Arrays,* The Journal of Physical Chemistry C **115**, 22729 (2011).
[51] Z. Haibo, D. Guotao, L. Yue, Y. Shikuan, X. Xiaoxia, and C. Weiping, *Blue Luminescence of Zno Nanoparticles Based on Non□Equilibrium Processes: Defect Origins and Emission Controls,* Advanced Functional Materials **20**, 561 (2010).
[52] J. Wang, D. N. Tafen, J. Lewis, Z. Hong, A. Manivannan, M. Zhi, M. Li, and N. Wu, *Origin of Photocatalytic Activity of Nitrogen-Doped TiO_2 Nanobelts,* Journal of the American Chemical Society **131**, 12290 (2009).
[53] S. Baruah, S. S. Sinha, B. Ghosh, S. K. Pal, A. K. Raychaudhuri, and J. Dutta, *Photoreactivity of Zno nanoparticles in visible light: Effect of surface states on electron transfer reaction,* Journal of Applied Physics **105**, 074308 (2009).
[54] M. Mahboub, P. Xia, J. Van Baren, X. Li, C. H. Lui, and M. L. Tang, *Midgap States in PbS Quantum Dots Induced by Cd and Zn Enhance Photon Upconversion,* ACS Energy Letters **3**, 767 (2018).
[55] I. Boukahil, P. S. Johnson, F. J. Himpsel, R. Qiao, J. A. Bandy, and R. J. Hamers, *Unoccupied surface state induced by ozone and ammonia on h-terminated diamond electrodes for photocatalytic ammonia synthesis,* Journal of Vacuum Science & Technology A: Vacuum, Surfaces, and Films **35**, 04D102 (2017).

4

Surface Functionalization of Diamonds with Transition Metals

Surface functionalization with transition metals could be another means to introduce states within the band gap of diamonds. When metal atoms are electronically coupled to the diamond surface through organic moieties, new surface states are created which are coupled to the electronic structure of diamond. Depending on their band alignment, the metallic surface functional groups can either serve as an electron or hole donor. Ru polypyridine complexes have long been explored as preferred sensitizers for wide band-gap semiconductors. For diamond, which is known to be a promising photocatalyst owing to its ability to generate solvated electrons, Ru complex functionalization is studied in order to understand the possibility of refilling the photogenerated holes in the material. In this chapter we present the electronic structure of Ru-ND investigated using soft X-ray absorption spectroscopy at the C K edge which is explained with the help of additional DFT calculations. After a brief overview of the materials investigated, a detailed X-ray spectroscopic analysis is presented exhibiting the electronic coupling between the dye and diamond. In addition, the effect of linker on the sub-band gap dye states in the Ru-NDs has also been discussed with the help of theoretical calculations performed on the dye molecules. Furthermore, the band alignment in Ru-ND has also been presented which demonstrates the role of the Ru complex as a potential electron donor, thus paving way for a brief discussion on the potential implications of such a band alignment on photocatalytic applications.

4.1. Ruthenium complex functionalized nanodiamonds

Ru complex functionalized nanodiamonds (**Ru-ND**) were obtained in the form of colloidal solutions from our collaborators at the Universität Würzburg. The polypyridyl complexes of Ruthenium were of particular interest in the project because of two reasons. Ruthenium polypyridyl complexes are well established photosensitizers for wide-band gap semiconductors used in dye-sensitized solar cells with reported efficiencies of more than 10%.[1] In addition to that, these complexes are also widely investigated as catalysts for water oxidation reaction.[2] In view of these two characteristic properties of the Ru complexes, we hypothesized that the Ru complexes could potentially provide an electron to fill the photogenerated hole in the VB of the diamond. Therefore, we present here a spectroscopic study on the dye-functionalized NDs to investigate their electronic structures in order to confirm our hypothesis and get insights into their potential photocatalytic applications.

Three different dye systems were initially studied namely, tris-bipyridine (**$Ru(bpy)_3$**), terpyridine chloride(**$Ru(tpy)Cl_3$**) and bis-terpyridine(**$Ru(tpy)_2$**), to demonstrate the versatility of the synthesis method. All of these dyes were attached to the nanodiamonds with a non-conjugated linker, the structures for which are shown in Figures 4.1a, 4.1c and 4.1d, respectively. While the bis-terpyridine dye had potential applications in other photoorganocatalytic reactions investigated at Universität Würzburg, it was found out that the Cl ligand in the terpyridine chloride is unstable and undergoes exchange with water under UV radiation. Therefore, within the scope of the DIACAT Project, it was decided to focus further studies on the $Ru(bpy)_3$ system. In particular, Ruthenium trisbipyridine(**$Ru(bpy)_3$**) complex was attached to the nanodiamond surfaces with two different linker systems using click chemistry with a surface loading of 0.21 mmol g^{-1}, as shown in Figures 4.1a and 4.1b.

The NDs were subsequently dispersed in water to obtain a colloidal solution which was then dropcasted on a Si (100) wafer. The electronic structure was studied using XAS, primarily recorded in the TEY mode, at the C K edge at the diamond-vacuum interface in the LiXedrom endstation previously mentioned in Chapter 2. The experimental spectra were explained using theoretical calculations performed using the ORCA package described in Chapter 2.

For the Ru complex functionalized nanodiamonds, additional ultraviolet photoemission spectroscopy measurements were performed by dropcasting the samples on an FTO substrate. The pure trisbipyridine dye (**$Ru(bpy)_3$**) was also studied using X-ray absorption and photoemission spectroscopies as a reference.

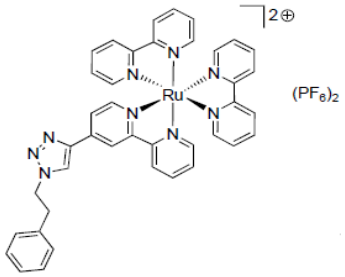

(a) **Ru(bpy)$_3$** with non-conjugated linker

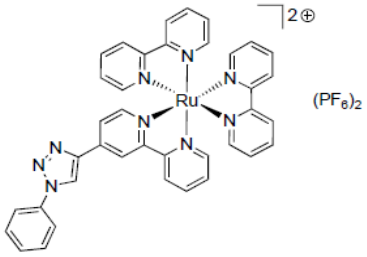

(b) **Ru(bpy)$_3$** with conjugated linker

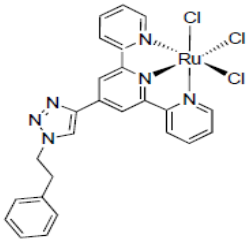

(c) **Ru(tpy)Cl$_3$**

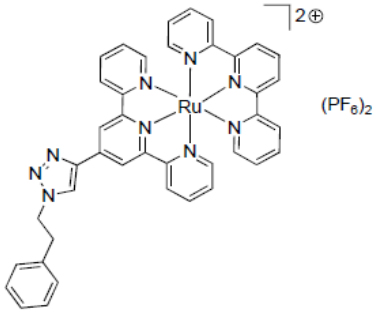

(d) **Ru(tpy)$_2$**

Figure 4.1: *Structures of Ru complexes.*

4.2. Electronic coupling between Ru complexes and nanodiamonds

For the Ru dye to function as a sensitizer that can facilitate charge transfer to or from the diamond, a good electronic coupling between the dye and diamond is essential. This electronic coupling can be evidenced by investigating the electronic structure of diamond using XAS at the C K edge, presented in Figure 4.2.

In Figure 4.2, the XA spectra of the functionalized nanodiamonds are compared to the pure Ru dye which is used as a reference. The XA spectrum of the Ru dye shows two peaks located 0.8 eV photon energies apart at 285 eV and 285.8 eV respectively.[3] These peaks result from C 1s to π^* transitions in the ligand molecule after X-ray absorption. In particular, the peak at 285 eV is attributed to a transition to the LUMO.[3] The second π^* transition is to the LUMO+1 state and is well in agreement with the literature report.[3]

Comparing the reference spectrum of the pure dye to the XA spectra of the functionalized nanodia-

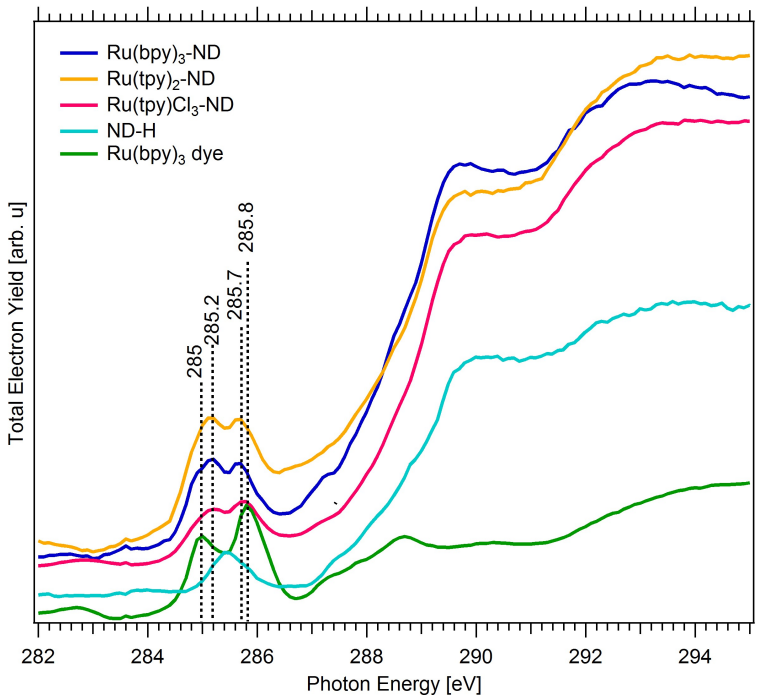

Figure 4.2: *C K edge XA spectra of* ***Ru(bpy)$_3$*** *dye (in green),* ***Ru(bpy)$_3$-ND*** *(in blue),* ***Ru(tpy)$_2$-ND*** *(in yellow) and* ***Ru(tpy)Cl$_3$-ND*** *(in pink) samples. The XA spectrum of non-functionalized diamond (in cyan) (****ND-H****) has been presented for reference. The pre-edge exhibits two strong peaks attributed to transitions to the LUMO and LUMO+1 of the dye respectively.*

mond, a clear difference is observed at the rising edge beyond 287 eV. The NDs exhibit a broad excitonic peak at 289.3 eV[4] which is absent in the pure dye reference. The pre-edge of the Ru functionalized NDs, however, show a double peak feature at around 285 eV similar to the pure dye. In particular the peaks appear 0.5 eV apart at 285.2 eV and 285.7 eV photon energies for the functionalized molecules. Interestingly, the characteristic feature of the sp^2 C atoms at 285.4 eV is not very evident in the spectra of the functionalized NDs. As a first interpretation based on existing literature, the first peak at the lower energy is attributed to a π^* transition to the LUMO orbital of the dye.[3, 5, 6] Yeap et al previously investigated polycrystalline boron doped diamond functionalized with N3 dye with XAS and a separation of 1 eV was observed between the LUMO and LUMO+1 levels for N3.[6] Based on literature reports, the second peak above the LUMO may therefore, be attributed to a π^* state resulting from transition from the C 1s core orbital to the LUMO+1 orbital of the dye. Furthermore, the LUMO is blue shifted by 0.2 eV and the LUMO+1 is red shifted in comparison to the pure dye, which is well in agreement with existing literature.[5, 6] The appearance of the LUMO and LUMO+1 orbitals of the dye in the pre-edge of the diamond electronic structure at different positions compared to the pure dye indicates an influence of the NDs on the functionalized dye.[6] More specifically, it may be said that the electronic states of the dye are coupled to the states of the NDs. Thus, XA spectroscopy provides a reliable means to characterize

the attachment of the dye on the ND surface.

Although the XA spectra presented in this section give evidence for electronic coupling between the dye and NDs, the literature provides only a naive interpretation of the pre-edge features. Therefore, in the following section we dive deeper into understanding the origin of the split peak pre-edge feature in the dye with the help of a combined experimental and theoretical study of linker effects on **Ru(bpy)$_3$-ND**.

4.3. Effect of linker on sub-band gap states in **Ru-ND**s

The overlap of p orbitals facilitates delocalization of electrons in conjugated molecules which results in lowering the energy of the system thereby increasing its stability. Due to the good charge transfer characteristics of conjugated systems, **Ru(bpy)$_3$-ND** was synthesized using both non-conjugated and conjugated linkers, as shown in Figures 4.1a and 4.1b. To better understand the possible origin of an enhanced charge transfer process in the conjugated system, the electronic structures of the molecules with different linker systems are compared in this section. Combined with DFT calculations, we investigate the difference in their pre-edge features and their respective origins in this section. The experimental XA spectra are presented in Figure 4.2.

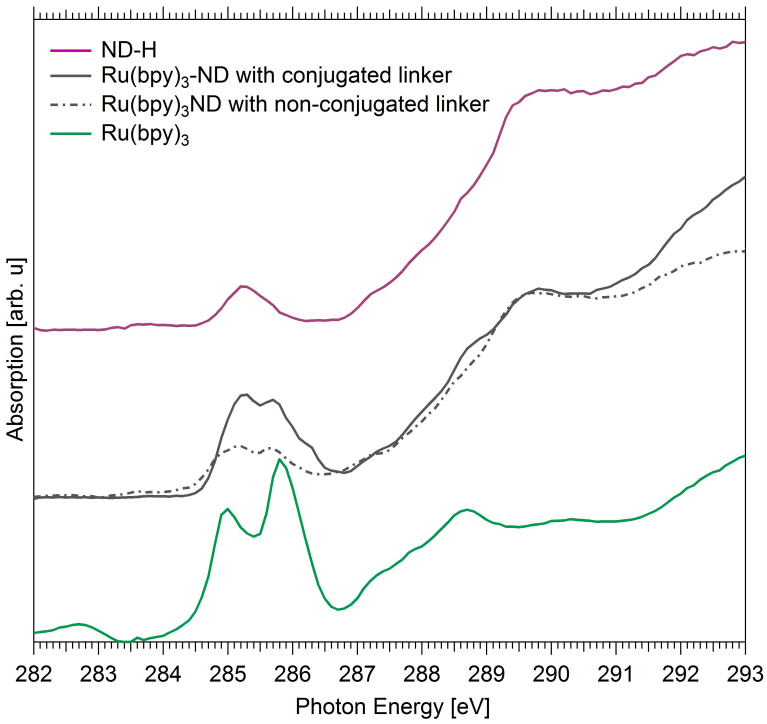

Figure 4.3: *C K edge XA spectra of **Ru(bpy)$_3$** dye (in green) and the **Ru(bpy)$_3$-ND** with non-conjugated and conjugated linkers compared to **ND-H**. Conjugation in the linker contributes to additional shoulder above the second peak in the pre-edge.*

As can be seen in the figure, the experimental spectra for the Ru-ND are compared to that of the non-

functionalized NDs (**ND-H**) and the pure Ru dye for reference. The nanodiamonds (in pink) as well as the **Ru(bpy)$_3$-ND** (in grey) exhibit a rising edge after 287 eV. The excitonic peak [4] at 289.5 eV is also present for the **ND-H** and **Ru(bpy)$_3$-ND** samples. This clearly evidences the fact that the presence of Ru complex on the surface of the nanodiamonds does not completely suppress the spectral features related to ND. The pre-edge of the **ND-H** exhibits only a single feature at 285.3 eV which is attributed to a transition from the core C 1s orbital to a π^* state of an sp^2 hybridized carbon.[4] In comparison to the NDs, the pre-edge of **Ru(bpy)$_3$-ND** exhibits a double peak feature for both the cases of conjugated and non-conjugated linker systems. For nanodiamond with conjugated linker, a split of 0.4 eV is observed with peak positions at 285.3 eV and 285.7 eV while that with the non-conjugated linker exhibits a split of 0.5 eV with the maxima appearing at 285.2 eV and 285.7 eV. These values are slightly lower than the energy difference of 0.8 eV reported for the pure dye in the previous section, which is also in close agreement with literature.[3] In addition to the positions of the maxima of the double peak pre-edge feature, it is also interesting to note that in the pure dye reference, the second peak is higher in intensity as compared to the first one which equalizes when the dye molecule is attached to the ND.

These experimental observations can be further explained with the help of theoretical XA spectra which were calculated using TD-DFT method explained in Chapter 2. Theoretical computations were performed only for the Ru complex molecule with the linker systems. Since the molecules contain carbon atoms with two different chemical environments, TD-DFT computations were performed to first obtain the core level spectra for each of the two different types of carbon atoms. The resultant XA spectrum which was then obtained by adding the two contributions is shown in Figure 4.4a for the non-conjugated and Figure 4.4b for the conjugated system.

The resultant theoretical spectra exhibit a double peak feature as is evident from the Figure 4.4, which is in agreement with our experimental observations. These calculations further suggest that the double peak feature originates from two different chemical environments of the C atoms in the complex molecules with linker systems. One type of C has another C atom as its nearest neighbour, referred to as **C1** while the second type of C atoms has a N atom as the nearest neighbour, referred to as **C2**. The atomic orbitals of **C1** and **C2** are shown in Figures 4.5a, 4.5b, 4.5c and 4.5d. Analysis of the theoretical XA spectra shows that the first peak that appears at 285.2 eV and 285.15 eV for the non-conjugated and conjugated linker systems respectively is due to transitions originating from a 1s orbital on a **C1** type C atom. The second peak located at 285.6 eV and 285.55 eV for the non-conjugated and conjugated linker systems respectively originates from transitions from the core of a **C2** type C atom.

The energy levels for the core 1s orbitals of **C1** and **C2** type carbon are different, in the sense that the

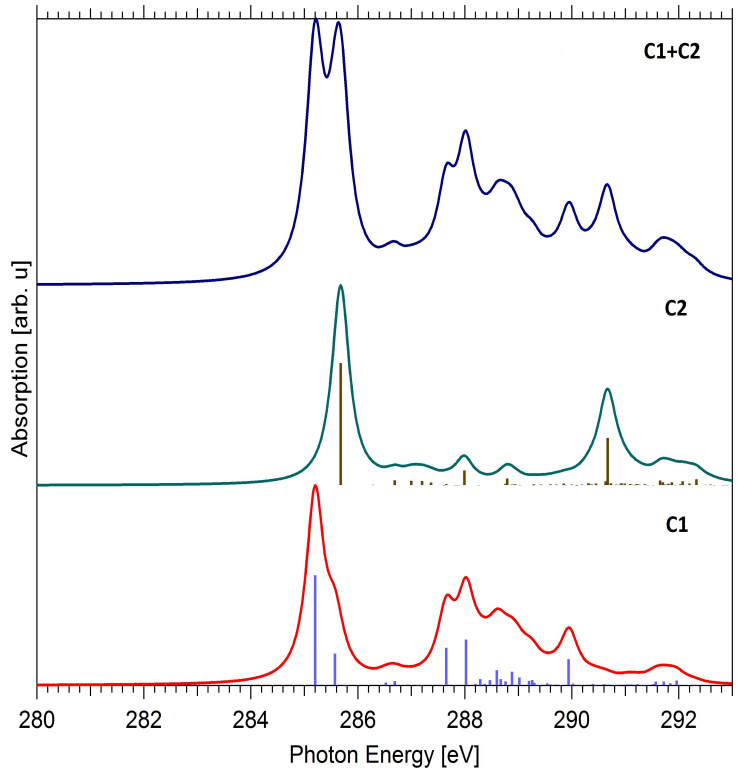

(a)

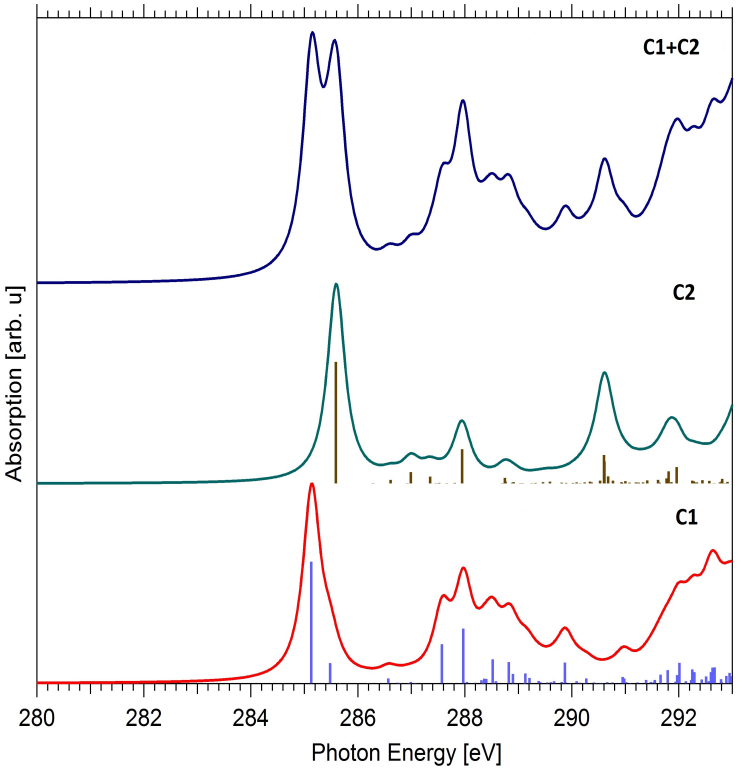

(b)

Figure 4.4: *Theoretical XA spectra of C computed for* ***Ru(bpy)$_2$-ND*** *with (a) non-conjugated and (b) conjugated linkers. The XA spectra for contributions from C atoms with C neighbours(**C1**) (in red) and from C atoms with N neighbours(**C2**) (in dark green) were computed and the resultant spectra (in dark blue) were obtained by summing the two contributions multiplied by the respective number of C atoms of each type. The dark brown and purple vertical lines show the transition probabilities.*

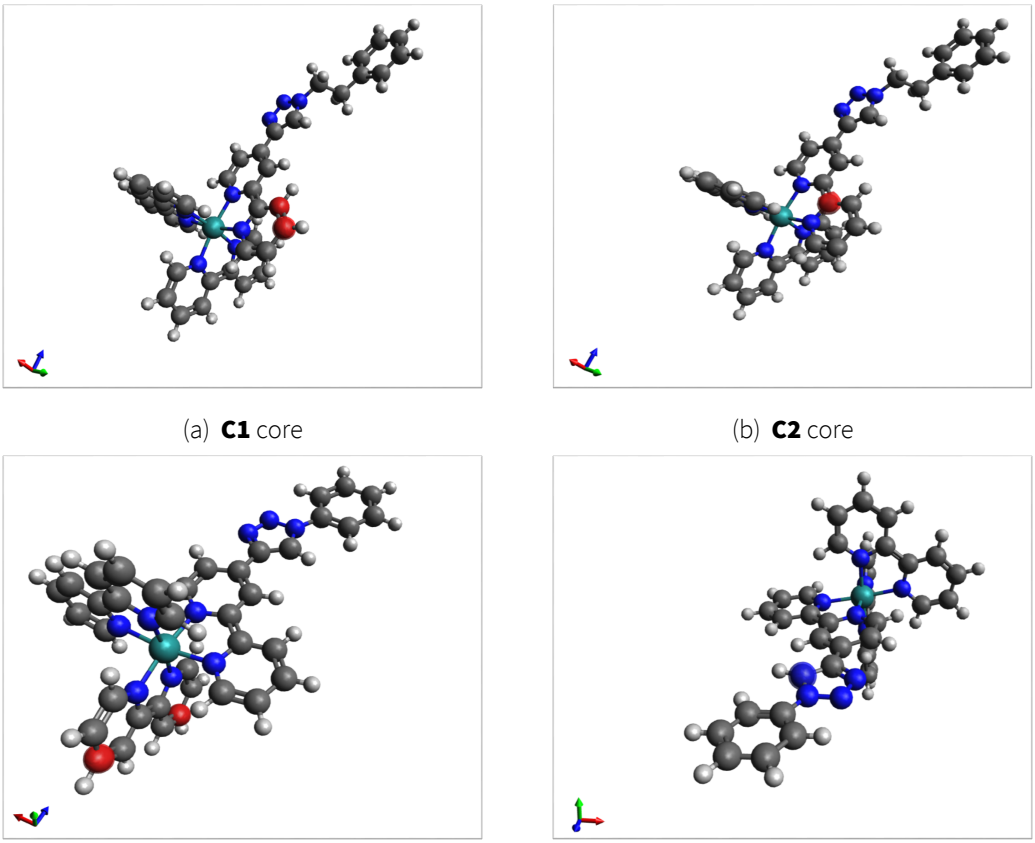

(a) **C1** core (b) **C2** core

(c) **C1** core (d) **C2** core

Figure 4.5: *C 1s core orbitals of **C1** and **C2** carbon atoms in Ru complex with (a,b) non-conjugated and (c,d) conjugated linker. The grey spheres in the figure indicate C atoms while the white spheres represent H atoms. Ru atom is represented in teal while the small blue spheres represent N atoms. The core level 1s orbitals for C atom is represented in red for both the cores of the non-conjugated system and **C1** core of the conjugated system. The **C2** core of the conjugated system (d) is represented as a blue sphere bonded to a C and a N atom in the pyridine ring of the linker*

core level of **C1** type C is located at a higher energy level as compared to the core level of **C2** type C. This is due to a higher electronegativity of the N atom as compared to the C atom which is responsible for shifting the core level to more negative values and consequently higher binding energies. Since the ground states are different for both these transitions, although the electrons are eventually excited to the same molecular orbitals, they would require photons of different energy for these transitions to occur which essentially results in two different electronic states. Having said this, for the non-conjugated linker system the first peak at a lower photon energy is a result of a transition from 1s core level of **C1** carbon to the LUMO while the second peak results from a transition from the core level of **C2** carbon to the LUMO+1 level. A similar analysis of the transitions for the conjugated system shows that the first peak is a result of a simultaneous transition to the LUMO and LUMO+1 from 1s orbital of **C1** carbon while the second peak is attributed to a similar transition from the 1s orbital of **C2** carbon. It is interesting

to observe that the highest probability of transition is either to the LUMO or LUMO+1 orbitals in the non-conjugated system and there is a mixed probability observed for the conjugated system as can be gauged from the values presented in Table 4.1

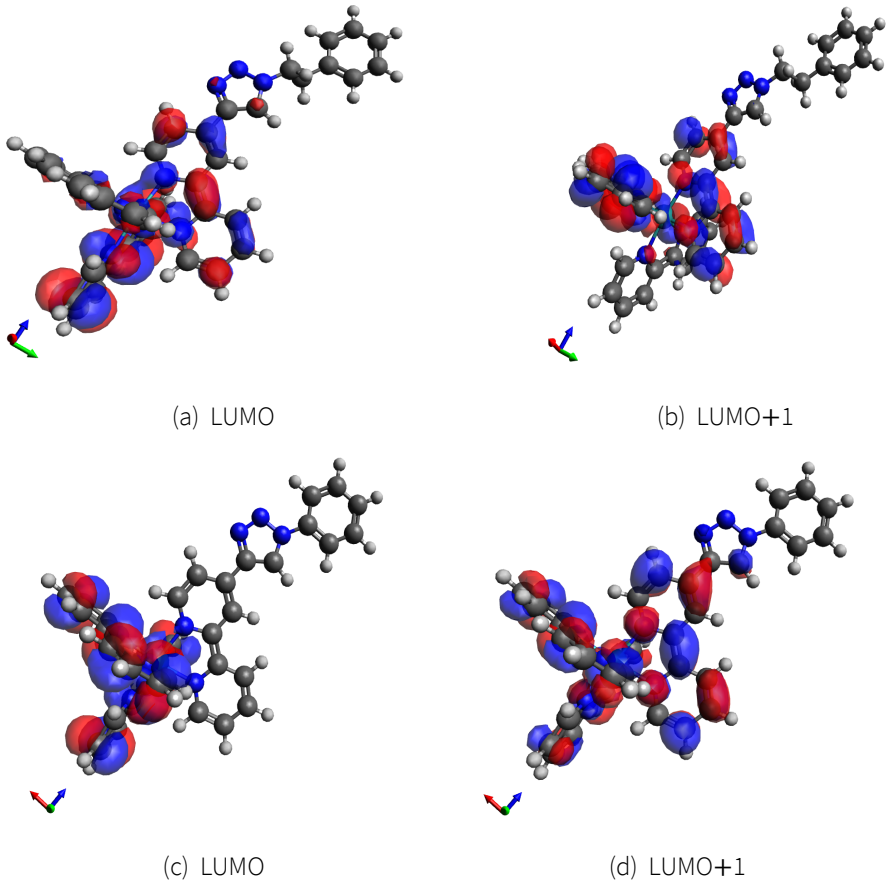

(a) LUMO (b) LUMO+1

(c) LUMO (d) LUMO+1

Figure 4.6: *Illustrations of LUMO and LUMO+1 molecular orbitals that have the highest contributions to the final excited state of the core electron in $Ru(bpy)_3$-ND with non-conjugated (a,b) and conjugated (c,d) linker systems.*

As can be seen from Figure 4.6 the LUMO and LUMO+1 orbitals for the non-conjugated system look significantly different from those of the conjugated system. Evidently, from Figures 4.6a and 4.6b it may be observed that the LUMO and LUMO+1 orbitals are predominantly distributed over two of the trisbipyridine rings. While the LUMO orbital has a smaller distribution over the third trisbipyridine ring that is out-of-plane with the other two, such a possibility is not observed for the LUMO+1 orbital in the non-conjugated system. In comparison, from Figures 4.6c and 4.6d, it is evident that although the LUMO orbital is predominantly distributed over just two trisbipyridine rings, that are located in planes perpendicular to each other, LUMO+1 exhibits almost equal distribution over all the three ligands. Such a distribution of molecular orbitals may be attributed to extensive conjugation in the entire molecule when the Ru complex is attached to a conjugated linker which is absent when the linker is non-conjugated.

Table 4.1: *Probability of transitions to the LUMO and LUMO+1 levels in $Ru(bpy)_3$ functionalized ND. For a transition from the **C1** core the transitions to LUMO and LUMO+1 orbitals gives rise to three states whereas transitions from the **C2** core can give rise to only two distinct states. The energy differences for each of the two consecutive electronic states are indicated in parantheses. The highlighted values indicate the most relevant transition probabilities for the experiments.*

Cores	States	Ru(bpy)3-conj			Ru(bpy)3-nonconj		
		LUMO	LUMO+1	Higher Orbitals	LUMO	LUMO+1	Higher Orbitals
C1(C-C)	1	**0.54**	**0.32**	0.14	**0.83**	**0.035**	0.135
	2 (+1 eV)	0.12	-	0.88	0.11	-	0.89
	3 (+0.3eV)	**0.30**	**0.66**	0.04	**0.029**	**0.96**	0.011
C2(C-N)	1	**0.80**	**0.16**	0.04	**0.084**	**0.895**	0.021
	2 (+1 eV)	**0.16**	**0.82**	0.02	**0.913**	**0.083**	0.004

Due to extensive conjugation and a higher electronegativity of the sp^2 carbon atoms there is a higher degree of polarization of the molecular orbitals over the ligands in the complex when the system contains a conjugated linker. This would in turn help to reduce the gap between the LUMO and LUMO+1 orbitals. The possibility of simultaneous transitions to LUMO and LUMO+1 that was previously mentioned may therefore be explained by this reduced gap between the LUMO and LUMO+1 for the conjugated linker system.

In addition to the double peak feature, an additional shoulder appears at 286.4 eV in the XA spectrum of the Ru-ND system with a conjugated linker. This is however, not evident in the system with the non-conjugated linker. This particular feature appears at a photon energy 0.7 eV higher than the double peak feature. One may hypothesize the presence of a possible charge transfer state arising due to conjugation in the functionalized nanodiamond. Theoretical calculations suggest the possibility of transitions to the LUMO+2 orbital from both C-C and C-N cores in the conjugated molecule, the probability for which is very low in the non-conjugated system. In addition to the two linkers presented here, an extended tolane linker system was also investigated, the data for which can be found in Figure A.9 in Appendix A.

4.4. Implications of band alignment of Ruthenium complex and nanodiamonds

Ultraviolet Photoemission Spectroscopy or UPS is a valuable tool to probe the electronic structure of the valence band of a material. This method measures the kinetic energy of the photoelectrons emitted upon absorption of UV photons by molecules, in order to determine the energies of their molecular

orbitals in the valence region. The binding energy of the molecular orbitals can be consequently determined using Einstein's photoelectric law, which helps us determine the energy of the valence band states. Here the alignment of the HOMO level of **Ru(bpy)$_3$** dye with respect to the valence band maximum (VBM) of the nanodiamonds was investigated by UPS. Such a band alignment study would help to illustrate the process of charge transfer between the dye and the ND with potential implications on photocatalytic applications of the system. Figure 4.7 presents the PE spectra of the bare **FTO** substrate (in grey), **ND** (in black), **Ru dye** (in green) and **Ru(bpy)$_3$-ND** (in blue) deposited on FTO substrate.

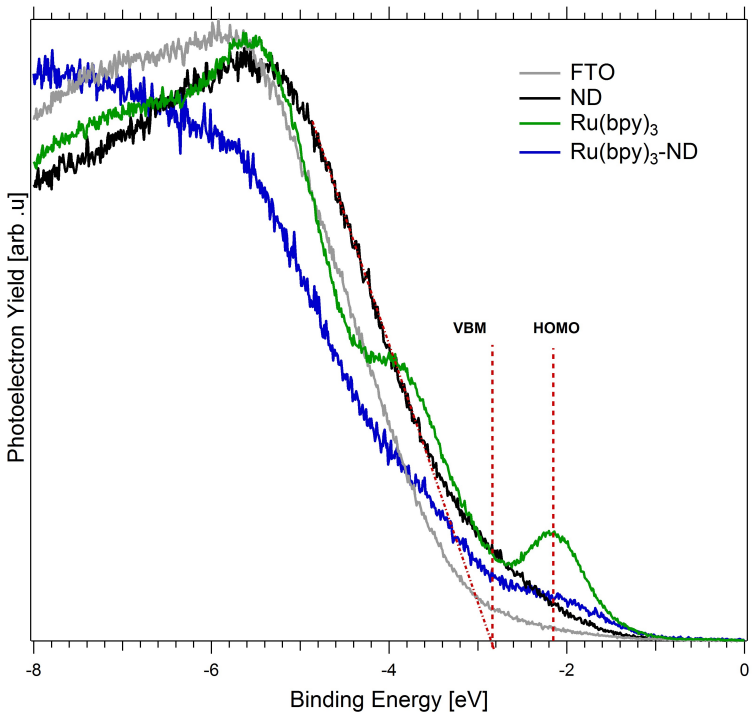

Figure 4.7: *Steady state photoemission spectrum of **Ru(bpy)$_3$-ND** is compared to that of the bare dye, bare ND and the bare FTO substrate. The HOMO of the dye is visible also upon functionalization of the ND and is blue shifted compared to the VBM of the ND.*

As is evident from the figure, the HOMO of the dye (in green) is clearly visible and appears at a binding energy of -2.16 eV. The position of the VBM of nanodiamonds is estimated by fitting a straight line at the absorption edge of the PE spectrum of the **ND**s. This places the VBM at a binding energy almost 0.9 eV higher than the HOMO of the dye. Comparing the functionalized NDs with the bare NDs and **Ru dye** reference suggests that the BE of the HOMO of the dye is lowered by 0.3 eV when the dye is attached to the diamond surface. Therefore it becomes quite evident that the VBM of the **ND**s lies lower than the HOMO of the dye. Such a band alignment has implications on the direction of charge transfer between the nanodiamond and the dye.

As shown in Figure 4.8, since the HOMO of the Ru dye lies almost 0.9 eV above the VBM of the diamonds,

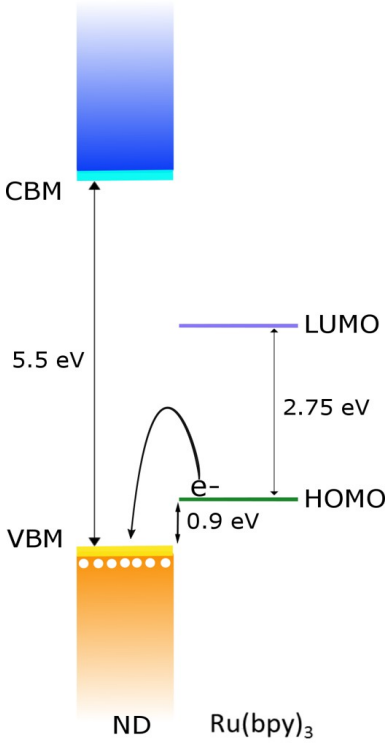

Figure 4.8: *Illustration of band alignment in Ru functionalized NDs showing a possible electron transfer from the dye to the diamonds in order to refill the photogenerated holes in NDs upon solvated electron generation.*

the Ru dye can act as an electron donor to the diamonds. Dye sensitized diamonds studied previously report hole donation from Ruthenium dye to the diamond in case of B-doped diamond films where the HOMO of the dye is located below the VBM of diamonds resulting in improved photocurrents through photochemical experiments.[5, 6] Similar improved performances were also reported in other semiconductor materials[7–12] functionalized with Ruthenium complexes. One of the widely studied oxide semiconductors is TiO_2 functionalized with Ru complex for enhanced performance in dye-sensitized solar cells [7] or photoelectrochemical reactions[8, 9]. Other transition metal oxide semiconductors such as $BiVO_4$[11] and Fe_2O_3[12] have also been functionalized with Ru complexes to catalyze water splitting and CO_2 reduction to observe improved catalytic performances. However, in all of these cases the catalytic center for photochemical reactions is the metal center Ru(II) in the complex.

Here, we demonstrate a nanodiamond based functionalized system which exhibits a switched position of the HOMO with respect to the VBM of diamonds. The use of nanodiamonds instead of bulk diamonds in this case may help to explain this observation. If the unique property of solvated electron generation in nanodiamonds is to be exploited for photocatalytic applications, a way to replenish the photogenerated holes has to be established. Based on the band alignment, it may therefore be proposed here that the donation of electrons to the diamond from **$Ru(bpy)_3$** dye would help to fill the holes which are cre-

ated in the valence band of the diamond upon solvated electron emission. Ongoing ultrafast transient absorption spectroscopy experiments have demonstrated initial signs of a possible charge transfer between the Ruthenium complex and NDs. This indicates that it may be possible to increase the yield of solvated electrons emitted upon photoactivation of the nanodiamonds thus, making diamonds a promising photocatalyst for CO_2 reduction.

4.5. Conclusions

The electronic structure of nanodiamonds functionalized with Ruthenium complexes were studied using XAS at the C K edge which evidences strong electronic coupling between the complex and the nanodiamonds. Furthermore, the effect of linker on the pre-edge features of the functionalized nanodiamonds was investigated by studying **Ru(bpy)$_3$-ND** with two different linker systems, non-conjugated and conjugated. A double peak feature, similar to that for the pure dye reference was observed in case of the functionalized NDs. This double peak is in agreement with theoretical XA spectra of the dye and the linker system, calculated using TD-DFT. The theoretical calculations suggest that each of the two features in the double peak originates from one of the two different types of carbon atoms, **C1** and **C2**, with C and N atoms as nearest neighbours respectively. Furthermore, comparison of the experimental spectra with the theory indicates a mixed probability of transition to both the LUMO and LUMO+1 in presence of the conjugated linker which could be explained by the relatively smaller gap between the two levels. In the presence of a non-conjugated linker distinct transitions from the **C1** and **C2** cores to the LUMO and LUMO+1 orbitals respectively was observed. An investigation of the band alignment showed that the HOMO of the dye lies 0.9 eV above the VBM of the nanodiamonds indicating the possibility of electron donation from the dye to the NDs. Such a band alignment scheme could potentially establish a mechanism to refill the photogenerated holes in the VB of NDs in order to increase the yield of solvated electrons, which needs to be further investigated.

References

[1] C.-Y. Chen, M. Wang, J.-Y. Li, N. Pootrakulchote, L. Alibabaei, C.-h. Ngoc-le, J.-D. Decoppet, J.-H. Tsai, C. Grätzel, C.-G. Wu, S. M. Zakeeruddin, and M. Grätzel, *Highly Efficient Light-Harvesting Ruthenium Sensitizer for Thin-Film Dye-Sensitized Solar Cells,* ACS Nano **3**, 3103 (2009).

[2] L. Tong, A. K. Inge, L. Duan, L. Wang, X. Zou, and L. Sun, *Catalytic Water Oxidation by Mononuclear Ru Complexes with an Anionic Ancillary Ligand,* Inorganic Chemistry **52**, 2505 (2013).

[3] P. Johnson, P. Cook, I. Zegkinoglou, J. M. García-Lastra, A. Rubio, R. E Ruther, R. Hamers, and F. J Himpsel, *Electronic Structure of Fe- vs. Ru-based Dye Molecules,* The Journal of chemical physics **138**, 044709 (2013).

[4] Z. Shpilman, I. Gouzman, T. Minton, L. Shen, A. Stacey, J. Orwa, S. Prawer, B. Cowie, and A. Hoffman, *A Near Edge X-ray Absorption Fine Structure Study of Oxidized Single Crystal and Polycrystalline Diamond Surfaces,* Diamond and Related Materials **45**, 20 (2014).

[5] I. Zegkinoglou, P. L. Cook, P. S. Johnson, W. Yang, J. Guo, D. Pickup, R. González-Moreno, C. Rogero, R. E. Ruther, M. L. Rigsby, J. E. Ortega, R. J. Hamers, and F. J. Himpsel, *Electronic Structure of Diamond Surfaces Functionalized by Ru(tpy)$_2$,* The Journal of Physical Chemistry C **116**, 13877 (2012).

[6] W. S. Yeap, X. Liu, D. Bevk, A. Pasquarelli, L. Lutsen, M. Fahlman, W. Maes, and K. Haenen, *Functionalization of Boron-Doped Nanocrystalline Diamond with N3 Dye Molecules,* ACS Applied Materials & Interfaces **6**, 10322 (2014).

[7] F. Gao, Y. Wang, D. Shi, J. Zhang, M. Wang, X. Jing, R. Humphry-Baker, P. Wang, S. M. Zakeeruddin, and M. Grätzel, *Enhance the Optical Absorptivity of Nanocrystalline TiO_2 Film with High Molar Extinction Coefficient Ruthenium Sensitizers for High Performance Dye-Sensitized Solar Cells,* Journal of the American Chemical Society **130**, 10720 (2008).

[8] C. Wang, X.-X. Ma, J. Li, L. Xu, and F. xing Zhang, *Reduction of CO_2 Aqueous Solution by using Photosensitized-TiO_2 Nanotube Catalysts Modified by Supramolecular Metalloporphyrins-Ruthenium(II) Polypyridyl Complexes,* Journal of Molecular Catalysis A: Chemical **363-364**, 108 (2012).

[9] Y. Gao, X. Ding, J. Liu, L. Wang, Z. Lu, L. Li, and L. Sun, *Visible Light Driven Water Splitting in a Molecular Device with Unprecedentedly High Photocurrent Density,* Journal of the American Chemical Society **135**, 4219 (2013).

[10] T. Baran, S. Wojtyła, A. Dibenedetto, M. Aresta, and W. Macyk, *Zinc Sulfide Functionalized with Ruthenium Nanoparticles for Photocatalytic Reduction of CO_2,* Applied Catalysis B: Environmental **178**, 170 (2015).

[11] M. de Respinis, K. S. Joya, H. J. M. De Groot, F. D'Souza, W. A. Smith, R. van de Krol, and B. Dam, *Solar Water Splitting Combining a $BiVO_4$ Light Absorber with a Ru-Based Molecular Cocatalyst,* The Journal of Physical Chemistry C **119**, 7275 (2015).

[12] K. Sekizawa, S. Sato, T. Arai, and T. Morikawa, *Solar-Driven Photocatalytic CO_2 Reduction in Water Utilizing a Ruthenium Complex Catalyst on p-type Fe_2O_3 with a Multiheterojunction,* ACS Catalysis **8**, 1405 (2018).

5

Understanding Diamonds in Water

Negative electron affinity of H-terminated diamond surfaces enables the emission of highly energetic solvated electrons in water to catalyze CO_2 and N_2 reduction under UV irradiation. This electron emission is known to be influenced by doping as well as surface chemistry of diamonds. Therefore, in order to develop photocatalytic applications of diamonds in aqueous electrolytes, understanding the behaviour of diamonds in water is important. In particular, this chapter discusses the electronic structure of different doped diamonds using soft X-ray absorption spectroscopy to shine light on the role of atmospheric adsorbates on the diamond surface in sub-band gap electron emission from the material. Furthermore, since the barrier for electron emission is influenced by surface chemistry and local environment of diamonds, an FTIR study of the surface interactions of diamonds in water under different pH conditions is also presented. Moreover, the need for deep UV illumination to photoactivate the diamonds, makes photocatalysis an inefficient process with bare diamonds. Therefore, hybrid photocatalysts can be developed by promoting diamonds with a co-catalyst that can absorb visible light and shows enhanced efficiencies towards CO_2 reduction. CuOx is a promising candidate for this purpose as it has been demonstrated to enhance the photocatalytic performance of H-BND under solar and UV irradiation. However, the material is also known to suffer from stability issues due to poisoning of its surface as a result of carbonate adsorption. Using in-situ soft X-ray spectroscopy at the Cu L edge, the last part of this chapter therefore elucidates the role of diamonds as a support material by progressively monitoring the change in Cu oxidation state at different applied potentials.

5.1. Interaction of Doped Diamonds with Adsorbates in Vacuum

In Chapter 3, X-ray spectroscopic investigations on p- and n-type diamonds conducted at the LiXedrom end station were presented. According to these investigations, new electronic states were introduced within the band gap of diamonds. Specifically, p-type doping of diamond with boron introduced two localized states close to the VBM of diamonds which were found to be dependent on the diamond morphology besides the dopant concentration.[1] The key insight from this study was however, the fact that nanostructuration of B-doped diamonds introduces not only localized states close to the VBM but also delocalized states close to the CBM of diamonds which could have special implications with respect to defect-assisted transitions that could possibly enable visible light absorption for photocatalytic applications.[1] In contrast to the p-type diamonds, nitrogen and phosphorus doping introduced delocalized electronic states close to the CBM. These states were found to be strongly electron emitting in nature as was evidenced by the electron yield spectrum.

Since the samples studied in LiXedrom could not be annealed, it can be said that all the samples had a few monolayers of adsorbate on its surface. To confirm the effect of adsorbate on the surface of doped diamonds, this investigation was further extended to compare the pre-edge features of the annealed diamond surfaces with that of unannealed surfaces, as this region of the spectrum is most sensitive to electronic states due to changes in adsorbed molecules on the surface. To this aim, soft X-ray absorption experiments on undoped, B, N and P doped single crystal diamonds were conducted at the PEAXIS end station. The diamond surfaces were annealed at 250°C for 3 hours before the measurements to remove any adsorbates on the surface, especially water and other oxygen containing molecules. After characterization, the annealed samples were exposed to air under ambient conditions, where the clean and annealed diamond surfaces now interacted with a thin monolayer of adsorbate molecules. They were then subsequently placed back in the chamber to record TEY-XA spectra after air exposure. Here we present the pre-edge region of the TEY-XA spectra for all the samples. These spectra have not been background corrected for the carbon contamination from the beamline. For details on the procedure for background correction of the TEY-XA spectra, refer to section A.2 in Appendix A.

As seen in Figure 5.1, the C K edge TEY-XA spectrum of the undoped single crystal diamond shows primarily two features. The characteristic feature at 289.3 eV corresponds to the core-excitonic peak of diamonds, in agreement with literature reports.[2] The other feature observed at *ca.* 282.4 eV corresponds to a surface state due to single dangling bonds on non-terminated or partially H-terminated surface of diamond.[3] Upon air exposure, the spectrum remains same with a slight increase in the intensity of the peak at 282.4 eV and a decrease in the core-excitonic peak at 289.3 eV. This is further evident from

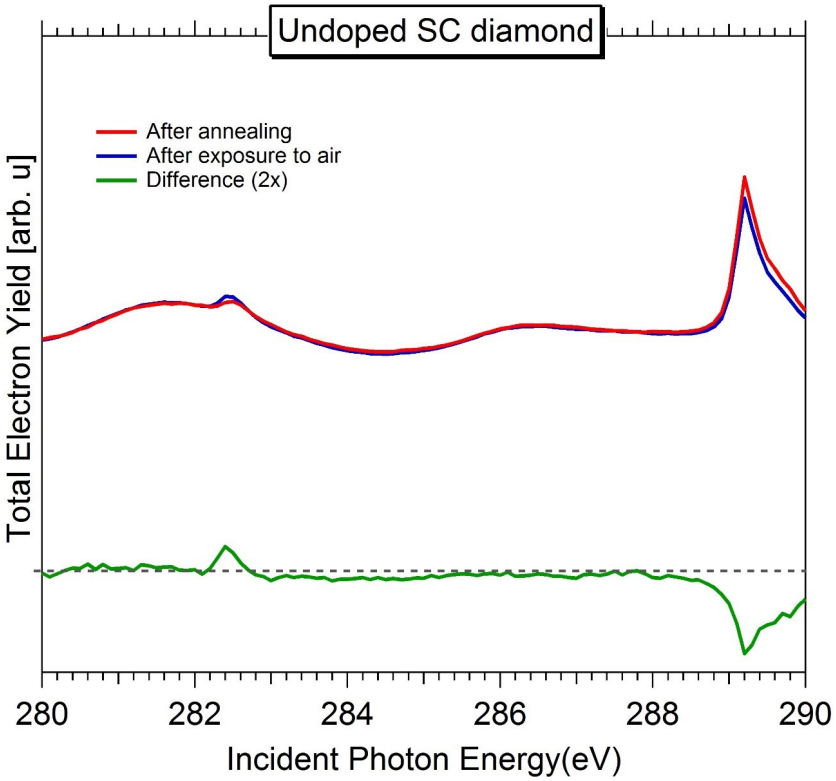

Figure 5.1: *C K edge XAS of undoped SC diamond films measured at the PEAXIS end station measured in TEY mode after annealing (in red) and after exposure to air (in blue) are shown alongside a difference spectrum (in green). The dotted line represents a reference that indicates that there is no difference between the two spectra.*

the difference spectrum which exhibits a positive peak at 282.4 eV and a negative one at 289.3 eV. The decrease in intensity of the core-excitonic peak could be attributed to a disappearance of excitons at the surface. Maier *et al.* have shown that exposure to air results in the formation of water adsorbate layer on the surface of H-terminated diamonds which acts as a sink for electrons, thereby imparting surface conductivity to the diamond.[4] Therefore, an electron transfer to the neighbouring adsorbate water and other oxygen containing molecules on the surface could serve as a possible explanation for the decreased intensity of the core-excitonic peak.

In case of B-doped diamond, which is a p-type semiconductor, the spectrum is blue shifted towards higher photon energies by 0.2 eV, as is evident from Figure 5.2. This shift is more prominent at the core-excitonic peak position at 289.3 eV. Since, the TEY-XA spectrum is surface sensitive, the core excitonic peak may be sensitive to surface termination. In particular, it has been reported by Stacey *et al.* that reconstructed surfaces and oxygen containing groups on the surface could result in a shift of the excitonic peak to higher energy positions,[5] which is well in agreement with our experimental observations. Stacey *et al.* attributed this shift to a possible band bending which is known to occur near the surface

of diamonds when exposed to air.[4, 5] In addition to this change, the other characteristic features of diamond are also evident in the spectra which include the surface states due to dangling C bonds on the surface and the electron emission states due to C-H interaction since the diamond is partially H-terminated. It may also be noted here than the feature due to the dangling bonds does not completely vanish upon air exposure. This is probably because the samples were exposed to air for *ca.* 10 minutes which may not be enough to saturate all the dangling bonds.

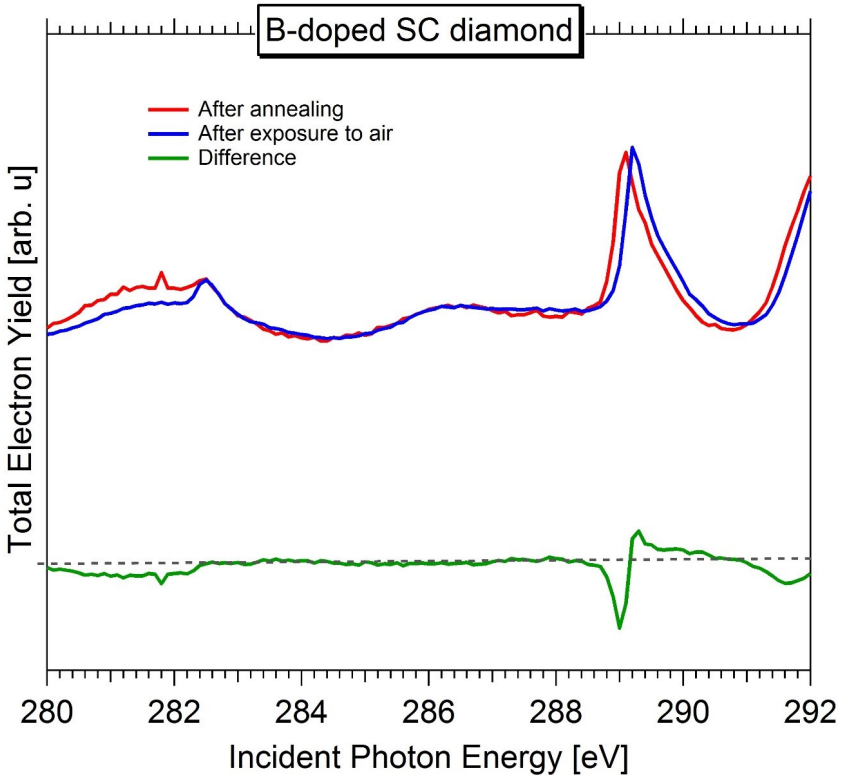

Figure 5.2: *C K edge XAS of B-doped single crystal diamond films measured at the PEAXIS end station in TEY mode after annealing (in red) and after exposure to air (in blue) are shown alongside the difference spectrum (in green). The dotted line represents a reference that indicates that there is no difference between the two spectra.*

Changes are observed upon air exposure in the N-doped SC diamond sample as shown in Figure 5.3. Besides the characteristic excitonic peak at 289.3 eV[2] and a surface state at 284.2 eV due to single C dangling bonds,[3] a prominent shoulder appears close to the conduction band edge below the excitonic peak with a threshold at 286 eV in the spectrum recorded on the annealed sample. This feature is said to originate from electron emission states arising as a result of N doping and C-H interactions due to H-termination of the diamond surface.[2] Since N is a deep donor, it introduces states *ca.* 1.7 eV below the conduction band edge. The electron emission states due to N and C-H interactions are delocalized in nature which result in the formation of a broad band of states below the conduction band minimum. Upon air exposure this shoulder increases significantly in intensity as is also evident from

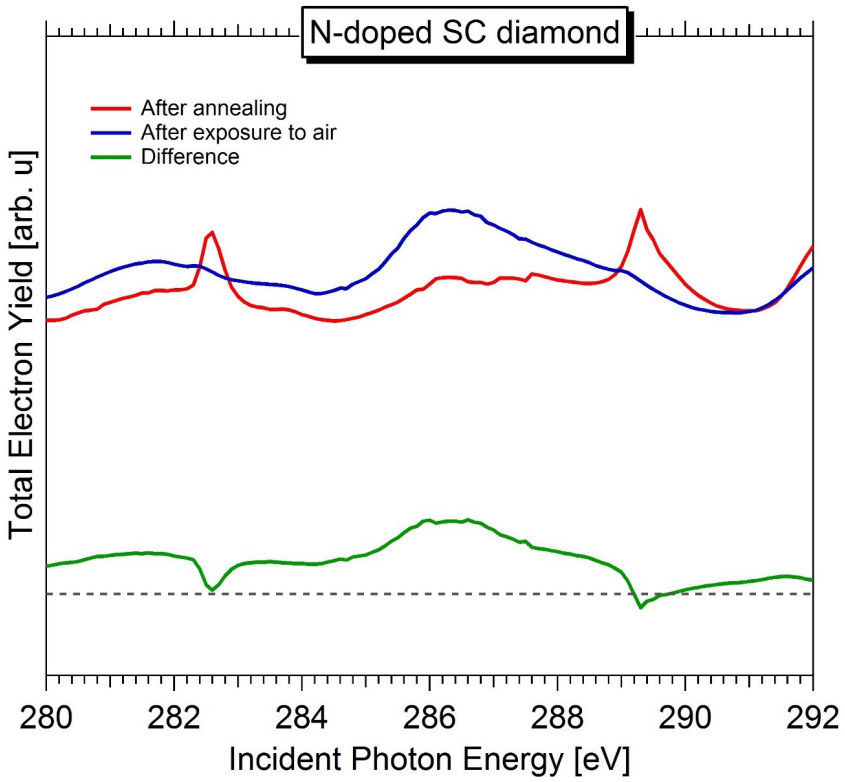

Figure 5.3: *C K edge XAS of N-doped single crystal diamond films measured at the PEAXIS end station in TEY mode after annealing (in red) and after exposure to air (in blue) are shown alongside a difference spectrum (in green). The dotted line represents a reference that indicates that there is no difference between the two spectra.*

the difference spectrum where a positive broad peak is observed starting at 286 eV and extending all the way to 289 eV. N-doping of diamonds makes more electrons available in the material and is also known to reduce the work function of NEA H-terminated diamonds.[6] Due to more electrons available close to the conduction band, it is expected that the Fermi level of N-doped diamonds would shift more towards the CBM. Maier *et al.* proposed that when the Fermi level of H-terminated diamond lies above the chemical potential of the water adsorbate layer, electron transfer from diamond to the adsorbate layer is facilitated by a water redox reaction.[4] Our knowledge of semiconductor physics tells us that the Fermi level of n-type diamond is expected to lie higher in energy than that of an undoped diamond. Therefore, based on the mechanism proposed by Maier *et al.* it can be said that the presence of N donor levels in H-terminated diamonds enhances sub band-gap electron emission to adsorbed water molecules on the surface upon air exposure. Additionally, it can also be observed from Figure 5.3 that the single C dangling bonds at 284.2 eV are completely saturated upon air exposure and the excitonic peak almost vanishes upon air exposure. The vanishing of the excitonic peak could be related to the enhanced electron emission from the diamond as a result of which excitons will no longer be formed in the material.

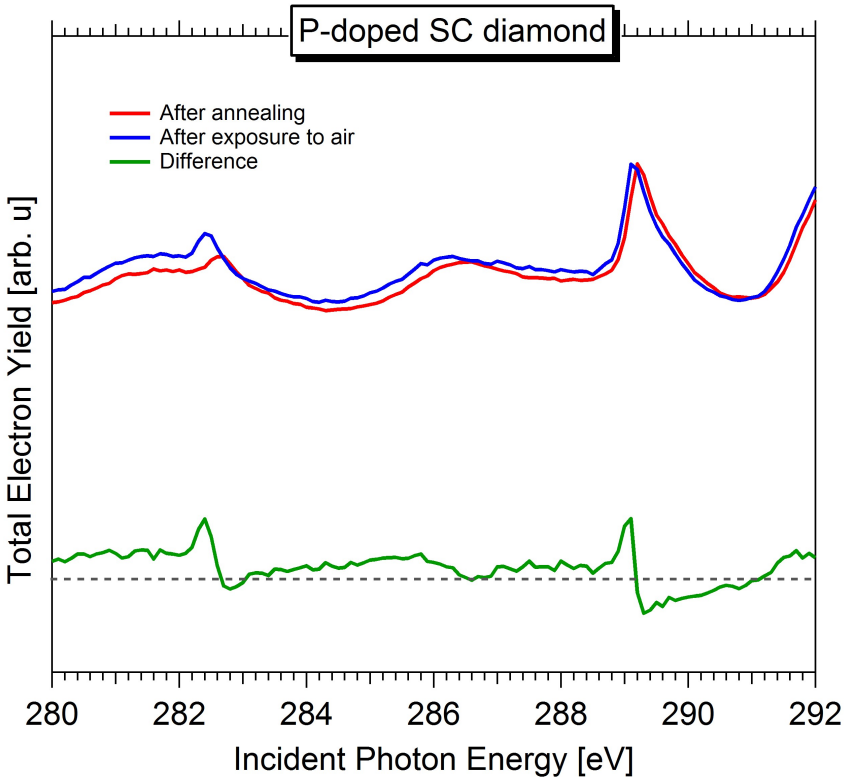

Figure 5.4: *C K edge XAS of P-doped single crystal diamond films measured at the PEAXIS end station. TEY-XA after annealing (in red) and after exposure to air (in blue) are shown alongside the difference spectrum (in green). The dotted line represents a reference that indicates that there is no difference between the two spectra.*

Again an n-type dopant, phosphorus is also expected to induce similar changes in diamonds as nitrogen, namely introduction of new donor states within the band gap of diamonds which could give rise to electron emission. This is evident in Figure 5.4 from the broad shoulder at ca. 286.5 eV in the red spectrum recorded on the annealed sample. In addition, the characteristic excitonic feature at 289.3 eV[2] as well as a small peak at 282.4 eV due to the single C dangling bonds[3] are also observed. Although an increased electron emission shoulder is also observed at around 286 eV in P-doped diamonds, the spectrum is shifted to lower photon energies by 0.2 eV, which could be attributed to an upward band bending evidenced on H-terminated (111) surface of P-doped diamond.[7]

Since TEY-XA is a surface sensitive detection method due to the shorter mean free path of electrons, it may be sensitive to surface band bending in materials. This band bending is also reflected as a shift in the core-excitonic peak which is known to be susceptible to surface termination related shifts.[5] From the TEY-XA spectra presented here, we can further conclude that in presence of water and other oxygen containing adsorbates, n-type diamonds exhibit photon-induced sub-band gap electron emission. Our experiments therefore, confirm the role of n-type dopants and adsorbates as presented in the hypoth-

esis in Chapter 3.

5.2. Influence of Water on the Surface Chemistry of Diamonds

5.2.1. FTIR Spectroscopy of the Diamond-Water Interface

In order to further develop photocatalytic applications of diamonds, it is equally important to understand the surface interactions of diamond with its environment. Specifically, a study of the diamond-water interface is essential since solvated electrons from H-terminated diamonds are emitted in water under UV irradiation for catalysis.[8] However, OH radicals may also be generated in water as a side product[9] which could potentially hydroxylate the H-terminated diamond surfaces that are known to be highly reactive under UV illumination.[10] These OH-terminated surfaces are interesting on their own as they are also known to possess NEA, albeit 0.2-0.3 eV lower than that of H-terminated NDs.[11] Depending on protonation of the OH groups under acidic pH conditions, these surfaces may exhibit enhanced electron emission characteristics. Such results were already demonstrated on protonated NH_2-terminated NDs by Hamers *et al.*[12] which motivates the study of pH effects on the surface interaction of OH-terminated diamonds with water. Fourier transform Infrared Spectroscopy (FTIR) has proven to be a powerful technique to reliably characterize the surface of diamonds in various environments. As a vibrational spectroscopy method, it is not only sensitive to the different surface functional groups on NDs but is also non-destructive in nature, versatile and involves easy sample preparation, as also previously pointed out in Chapter 2.[13] Therefore, this technique was used to characterize the surface interactions at the ND-OH-water interface in acidic as well as basic pH conditions.

For this study, H-termination of the detonation NDs was performed using a plasma hydrogenation technique developed by Girard *et al.* in CEA.[14] ND surfaces were terminated with OH groups using two different treatments, a Borane only reduction treatment and a successive Borane[15] and Fenton[16] treatment by Benjamin Kiendl from the group of Prof. Anke Krueger. The samples for FTIR measurements were prepared by drop casting 150 μL of the pH controlled ND dispersion on a Ge ATR crystal and drying the drop overnight to obtain a thin film. The pH was adjusted to 3.5 and 10 with HCl and NaOH, respectively while dispersions in deionized water were used for measurements under neutral pH conditions. FTIR scans were first recorded under a flow of dry air following which humid air was introduced in the measurement cell. The RH of the humid air was progressively varied from 0 to 80% before liquid water was introduced using a syringe.

NDs are susceptible to water adsorption upon exposure to ambient air. This could bring about changes

to their surface chemistry which become evident from the different H_2O related bands in the FTIR spectrum. In addition, the interactions with water molecules primarily through H-bonding also exhibit IR-active vibrational frequencies due to their polar nature.[13] These signatures can be observed in a full range spectrum as shown in Figure 5.5, which represents the FTIR spectrum of ND-OH in basic pH under varying humidity conditions. While the specific pH effect will be discussed in the next section, here we present a general discussion of the FTIR spectrum of diamonds upon exposure to humid air.

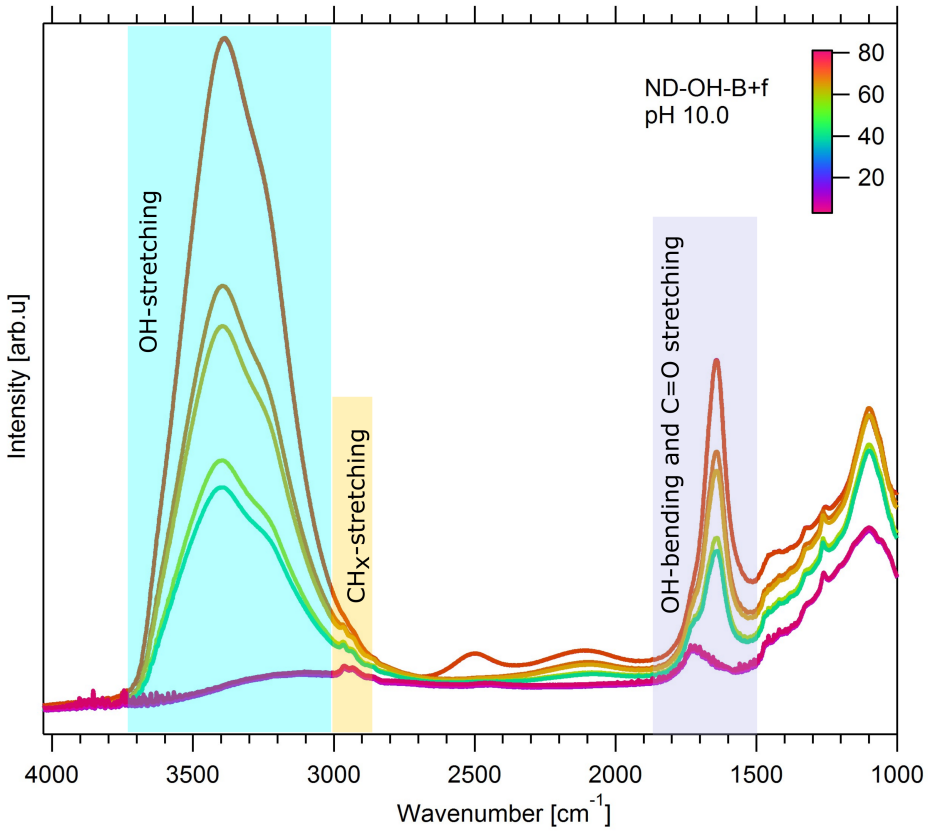

Figure 5.5: *Full range FTIR spectrum of ND-OH in humid air with varied levels of relative humidity as represented by the colour bar. In considering interaction with water molecules, three different regions are of primary interest as depicted by the coloured bands.*

In Figure 5.5, different peaks represent different vibrational modes of the surface groups on diamond, of which three are of primary interest to us in the study. These are OH stretching, CH_x stretching and the OH bending modes. As pointed out before, NDs are susceptible to water adsorption on the surface. This could result in a broad band appearing between 3200-3600 cm^{-1} introduced by OH-stretching modes, as shown in Figure 5.5 which could be attributed to ice-like water, liquid-like water or gas-like water close to the diamond surface.[13, 17] Such a band could also appear on OH terminated surfaces and is attributed to OH stretching vibrations from the hydroxyl groups. [13] Measurements conducted in D_2O

(see Figures A.11 and A.12 in Appendix A) showed that most of the bands came from water. Following OH stretching, the next region of interest is that of the CH_x stretching, which typically appears between 2830-2960 cm^{-1}.[13] This region is said to be greatly influenced from the crystallinity difference in differently sized nanodiamonds and synthesis methods.[13] However, since ND surfaces are highly susceptible to hydrocarbon contamination, this region of the IR spectrum is complicated to interpret[13], especially when the ND samples are not annealed in vacuum prior to the measurements. Therefore, this region will not be discussed further in the course of this study.

The final region of interest, which is also the primary focus of the results presented in this section of the dissertation, is the OH-bending region between 1540-1900 cm^{-1}. According to literature reports, different OH bending vibrations have been reported to occur on ND surfaces.[13] The OH bending from hydroxyl groups or water appear between 1620-1640 cm^{-1}, which is typical for oxidized and OH terminated ND surfaces.[13] Between 1650-1858 cm^{-1} different C=O stretching vibrations are visible due to presence of carbonyl groups originating from protonated or deprotonated carboxylic groups, aldehydes, ketones, esters and anhydrides.[13] In case of the ND-OH surface prepared by Borane+Fenton treatment, the C=O stretching vibrations are more likely to originate from the carbonyl groups on the surface which are formed due to the partial oxidation of the OH groups on the borane reduced ND surface. The OH bending due to a water molecule close to an excess electron on the surface appears between 1545-1589 cm^{-1} which was previously attributed to the formation of a charge stabilization layer on the hydrophobic H-terminated ND surfaces, upon interaction with water.[18] This region of the IR spectrum between 1540-1900 cm^{-1} is clearly, highly susceptible to changes due to the environment of the sample as well as its surface chemistry and therefore, shall be our main focus for further discussions in this study. With this general overview in mind, the following part will discuss the changes that are observed in the OH bending and C=O stretching modes on ND-OH surfaces with changes in pH of the surrounding environment.

5.2.2. pH Effects on the Surface Interactions of Nanodiamonds

Due to the formation of highly oxidizing hydroxyl radicals in water under UV illumination, H-terminated diamond surfaces could transform into OH-terminated surfaces. Since these ND-OH surfaces also possess NEA, understanding their surface interactions in water under varying pH conditions could be interesting to determine the optimal environment which could facilitate electron emission from these surfaces for photocatalysis. To this aim, we present here a study of the surface interactions under neutral pH conditions for ND-OH as well as ND-H surfaces. Thereafter, the effect of pH on ND-OH surfaces

will be discussed.

Surface Interactions under neutral pH conditions

While real-life applications are almost always realized in either acidic or basic pH conditions, a detailed understanding of the surface interactions of NDs with different surface chemistries in a neutral pH environment is essential. Hence, as a first step we shall try to establish the difference in their surface interactions when thin films of dispersions of NDs in deionized water (pH 7.0) are exposed to humid air, as mentioned in the previous section. Figure 5.6 exhibits the FTIR spectra of the dry surfaces as well as those exposed to humid air and also the corresponding difference spectra for ND-OH surfaces prepared by Borane (**ND-OH B**) and Borane+Fenton(**ND-OH B+f**) surface treatments and **ND-H**.

As is evident from Figure 5.6a, the dry **ND-H** and ND-OH samples exhibit a peak at 1715 cm^{-1} which is attributed to the C=O stretching mode due to aldehydic groups on the surface.[13] Specifically, the C=O vibration induces a broad peak for **ND-OH B+f** with a relatively lower intensity of the OH-bending induced shoulder at 1625 cm^{-1}. This indicates the presence of a higher number of carbonyl groups on the surface and relatively lesser OH coverage. In the case of borane reduced surface **ND-OH B**, some non-reduced carbonyl groups are present on the surface which give rise to the shoulder at 1715 cm^{-1}, since borane selectively reduces carboxylic acid groups to OH.[19] The broad shoulder centered at *ca.* 1625 cm^{-1} is therefore, attributed to the OH bending mode of the hydroxyl group.[13] Additionally, **ND-OH B** exhibits a peak at 1669 cm^{-1} which could be attributed to the C=O stretching vibration of a carbonyl group such as aldehyde or ketone[13] that is shifted in frequency, due to the H-bond formation with water molecules adsorbed on the diamond surface. Since OH-terminated surfaces are hydrophilic, it is possible that some water molecules remain adsorbed on the surface despite drying of the sample. Upon interaction with humid air while **ND-OH B+f** and **ND-H** exhibit a peak with maxima at 1637 cm^{-1} induced by OH-bending in water, **ND-OH B** exhibits a rather broad peak with maximum centered at around 1651 cm^{-1}. Such a broad peak possibly contains contributions from the OH bending of water molecules itself as well as the OH bending and C=O stretching vibrations of the surface groups on the ND that form H-bonds with the water molecules that are close to the surface. The difference spectra as shown in Figure 5.6b further evidence the enhancements in C=O stretching and O-H bending vibrations upon exposure of the ND surfaces to humid air.

Due to the hydrophobic nature of H-terminated ND surfaces, its interaction with water is unusual in comparison to the OH-terminated surfaces. In particular, Petit *et al.* reported the possibility of charge accumulation in the hydrophobic gap between ND-H and water which results in OH bending vibrations red shifted to 1545 cm^{-1} upon exposure to humid air.[18] It is surprising that we do not observe this

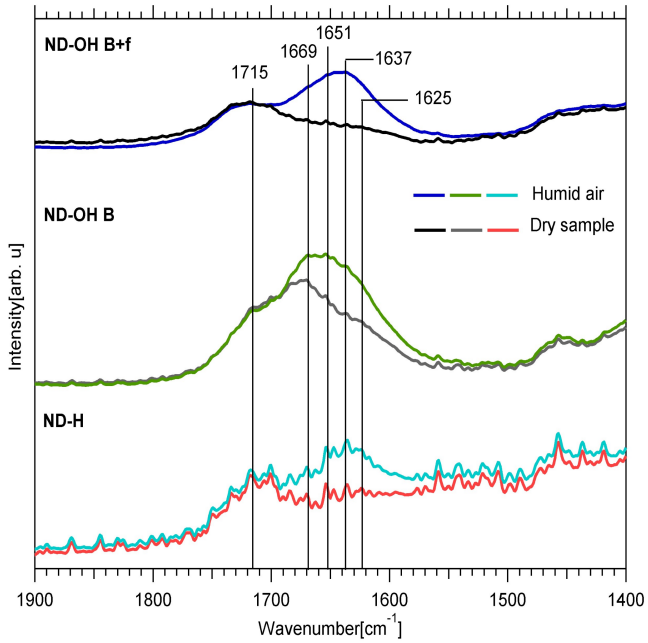

(a)

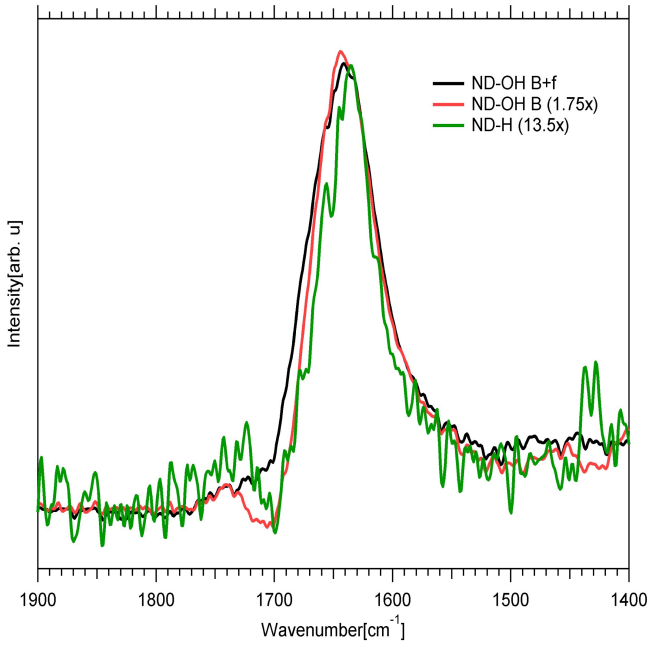

(b)

Figure 5.6: *(a) Comparison spectra of dry ND samples and after exposure to humid air under neutral pH conditions. (b) Difference FTIR spectra between dry ND surfaces with H (green) and OH surface terminations (black and red) and after exposure to humid air under neutral pH conditions.*

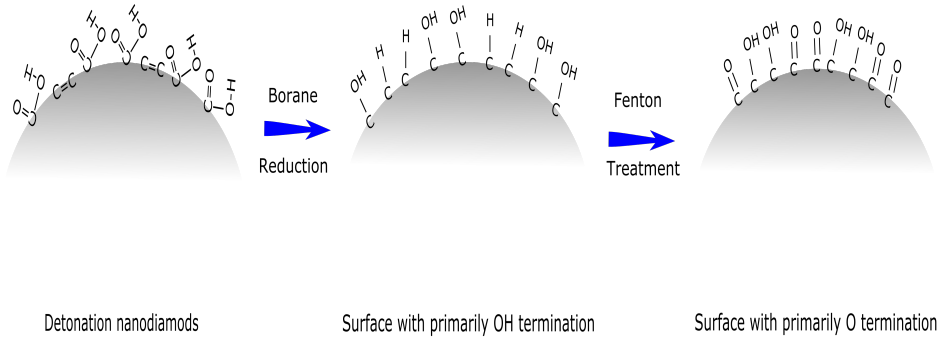

Figure 5.7: *Schematic showing surface groups on detonation NDs after Borane reduction and a successive Borane and Fenton treatment. Primarily a high amount of OH groups are expected as a result of the reduction of carboxylic acid groups by Borane on the detonation NDs, in addition to the conversion of sp^2 carbon to C-H groups. After a successive Fenton treatment, OH groups are introduced at sites with H termination, however the already exisiting hydroxyl groups are oxidized to C=O groups.*

feature which could possibly be explained by a high RH during the measurements and prolonged storage of the NDs-H in water. In our case, the vibration feature at 1637 cm^{-1} observed in **ND-H** could be attributed to the OH bending in bulk water. The fact that the feature at 1715 cm^{-1} on the dry ND samples has a significantly lower intensity upon exposure to humid air indicates a dominance of the signal by weakly H-bonded water molecules in the bulk. Another possible hypothesis to explain the deviation in our experimental observation from that of the reported value is an incomplete hydrogen termination of the diamond surface resulting in the presence of oxygen groups which interact with water molecules forming strong H-bonds. The FTIR spectrum of the dry sample already evidences the presence of C=O groups on the surface, due to possible oxidation of the surface in water. In a highly humid environment, these carbonyl groups could interact strongly with the water molecules which would lead to their adsorption on the surface of diamonds forming bulk water like H-bonded layers in close proximity to the diamond surface. The OH-bending mode in these H-bonded water layers adsorbed on the surface could then explain the feature at 1637 cm^{-1}.

The situation for the OH terminated surfaces is however, slightly different. For the **ND-OH B** sample, presence of C=O stretching bands with a lower intensity than that observed for **ND-OH B+f** indicates that a small amount of non-reduced carbonyl groups on the surface such as aldehydic and ketonic groups may be present in addition to OH and H. This is because borane reduction tends to selectively reduce carboxylic acid to alcohols. Furthermore, C=C bonds are also converted to sp^3 carbon by borane reduction. A Fenton treatment following a borane reduction is ideally supposed to homogeneously hydroxylate the diamond surface due to the strong oxidizing power of the $OH^{\bullet}$. However, the OH radicals

may only be effective in case of H-terminated carbon present on the surface. The strongly oxidizing $OH^{\bullet}$ would eventually also slightly oxidize the already present OH groups on the diamond surface to carbonyl groups such as aldehydes and ketones, which would help to explain the features at 1715 cm^{-1} and 1669 cm^{-1} on the dry ND surface. Upon interaction with humid air, the predominant C=O groups as well as the smaller number of OH groups interact with water via H-bonding resulting in the broad peak with increased intensity observed in Figure 5.6a.

Changes in the Surface Interactions under acidic and basic pH

As pointed out previously, long time exposure of ND-H surfaces to UV radiation in water could result in the formation of OH-terminated surfaces, which exhibit NEA similar to the H-terminated surfaces. Since ND-OH surfaces are hydrophilic as compared to ND-H, pH conditions are expected to influence their interactions with water molecules more strongly. In particular, it is expected that in an acidic environment the OH groups would likely be protonated and enhance electron emission characteristics of the ND-OH surfaces. Therefore, OH terminated NDs will be primarily investigated in this section (see Appendix A for FTIR spectrum of ND-H in acidic pH). To study the samples under acidic and basic pH conditions, solutions of NDs were prepared in HCl and NaOH with pH values adjusted to 3.5 and 10, respectively. The FTIR spectra of the dry samples were recorded following which they were exposed to a steady flow of humid air. Figures 5.8a and 5.9a show the FTIR spectra of the dry samples and after exposure to humid air in acidic and basic pH conditions, respectively. The corresponding difference spectra are presented in Figures 5.8b and 5.9b, respectively.

A comparison of Figures 5.8a and 5.9a does not reveal a significant difference in the peak positions. However, comparing with the spectra in neutral pH makes it clear that the C=O stretching band is shifted to higher frequencies of 1726 cm^{-1}. Upon exposure to humid air there is a peak at 1643 cm^{-1} which appears for both the samples under acidic as well as basic pH conditions which is expected from a strongly H-bonded water solvation shell. The difference becomes more evident, however, upon comparing the difference spectra for the ND-OH samples shown in Figures 5.8b and 5.9b for the acidic and basic pH, respectively. Particularly, in acidic pH, a shoulder is visible between 1710-1720 cm^{-1} for the **ND-OH B+f** sample. There could be two possible hypotheses to explain this feature. Since the OH groups on the borane reduced ND surface are likely to get oxidized after Fenton treatment, one possibility could be that this shoulder is due to the C=O stretching of the aldehydic and ketonic groups present on the surface. This feature increases in intensity at high RH since H-bonding of the C=O groups with water may induce stronger IR absorption of the bond. That the C=O stretching does not appear at higher frequencies allows us to rule out the possibility of any carboxylic groups on the surface. A second possibility

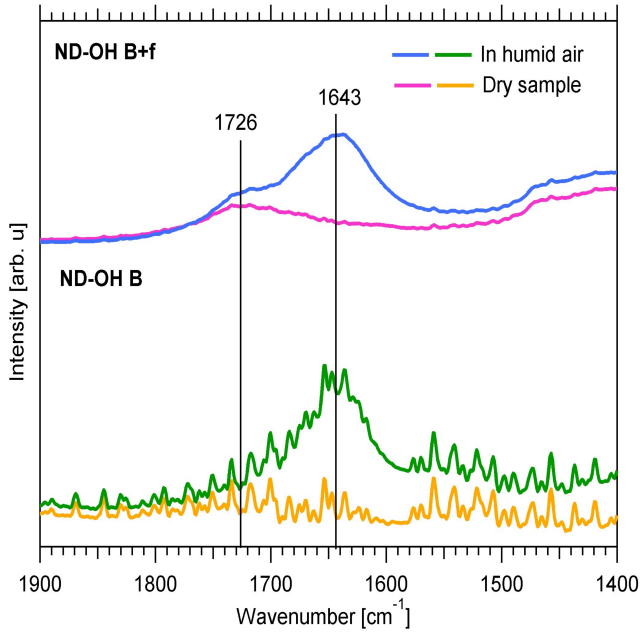

(a)

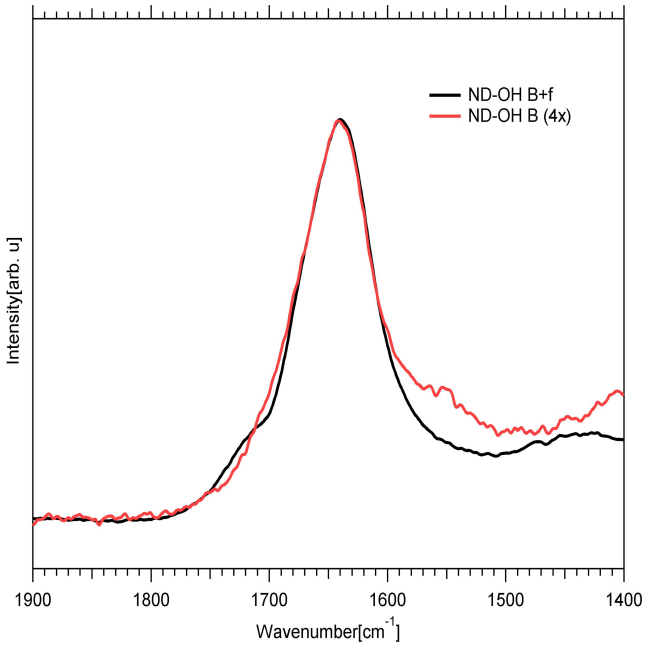

(b)

Figure 5.8: *(a) Comparison spectra of dry ND samples and after exposure to humid air under acidic pH conditions (pH 3.5). (b) Difference FTIR spectra of ND-OH B (red) and ND-OH B+f samples(black) before and after exposure to humid air under acidic pH conditions*

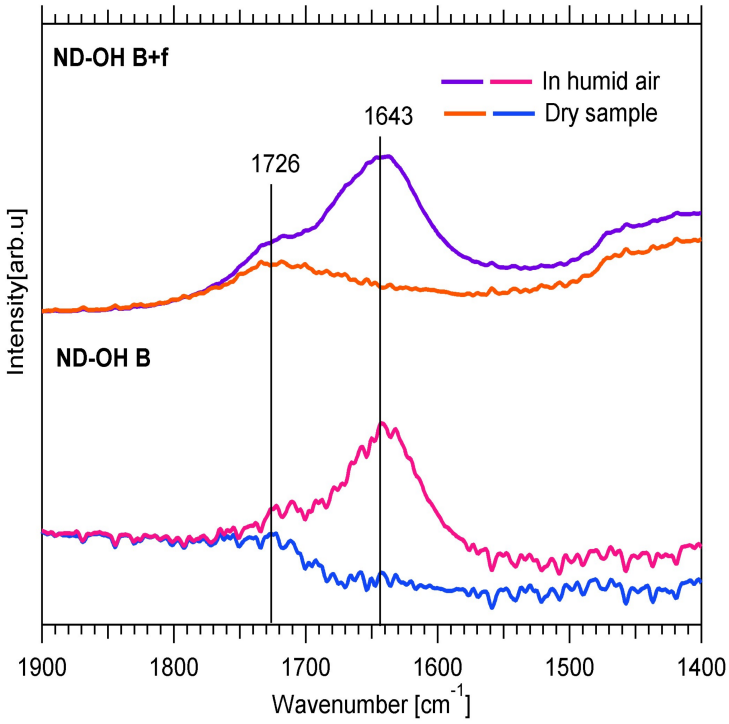

(a)

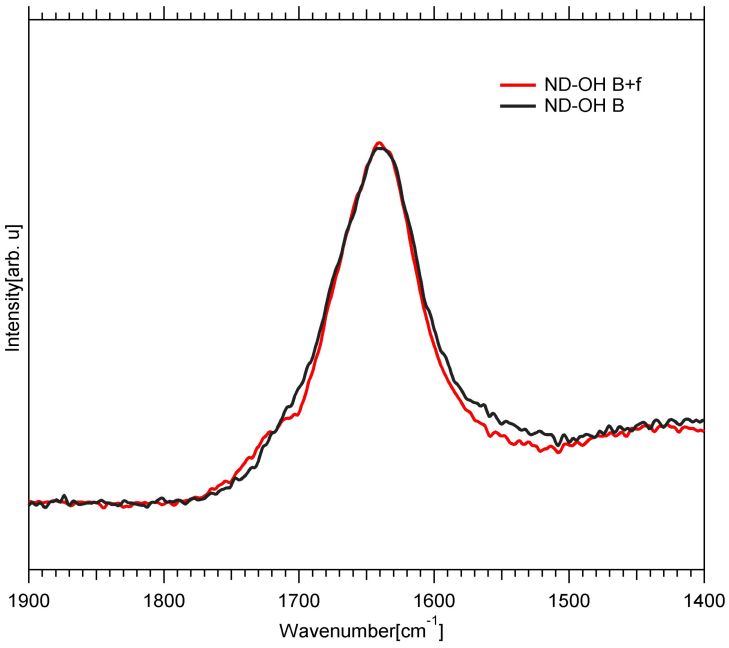

(b)

Figure 5.9: *(a) Comparison spectra of dry ND samples and after exposure to humid air under basic pH conditions (pH 10.0). (b) Difference FTIR spectra of ND-OH B (black) and ND-OH B+f samples(red) before and after exposure to humid air under basic pH conditions.*

could be the formation of hydronium ions in acidic solution and their subsequent adsorption on the diamond surface. The H-O-H asymmetric bending mode of the H_3O^+ ion is reported to also appear in the same region.[20] This H_3O^+ ion is oriented with its H atoms towards the diamond surface forming H-bonds with the oxygen atom of the carbonyl groups on the diamond surface. This shoulder between 1710-1720 cm^{-1} is however, not as strongly evident in the **ND-OH B** sample.

Instead, **ND-OH B** exhibits a strong shoulder at 1550 cm^{-1}. During borane reduction, predominantly carboxylic acids are reduced to OH groups[19] and C=C sp^2 carbon is converted to sp^3 carbon terminated by an H atom.[21] In acidic pH conditions, the OH group possibly gets protonated resulting in the formation of a -C-OH_2^+ group on the surface. Because of negative electron affinity, OH- as well as H-terminated diamonds can emit electrons in water. While it is known that H-terminated surfaces form a hydrophobic gap in water that can accomodate a charge accumulation layer,[22] OH-terminated surfaces are known to be hydrophilic. Therefore, our hypothesis here is that, the lack of electron density on the H atoms in -C-OH_2^+, formed upon protonation of the OH group in acidic pH conditions, helps to potentially stabilize the negatively charged electron cloud, emitted in water from OH-terminated surfaces, as shown in Figure 5.10a. This coupled with the charge accumulation layer close to H-terminated carbon atoms[18] on **ND-OH B** could give rise to the intense shoulder at 1550 cm^{-1}. Upon successive Fenton treatment the existing OH groups get oxidized back to carbonyl groups by the OH radicals. At the same time, C-H groups formed upon borane reduction of C=C sp^2 carbon are converted to -C-OH groups. Thus successive Fenton treatment possibly introduces lesser OH groups on the surface as compared to borane reduction while terminating the diamond surface with electron rich oxygen groups, as shown in Figure 5.10b. This may explain the absence of the peak at 1550 cm^{-1} in **ND-OH B+f**.

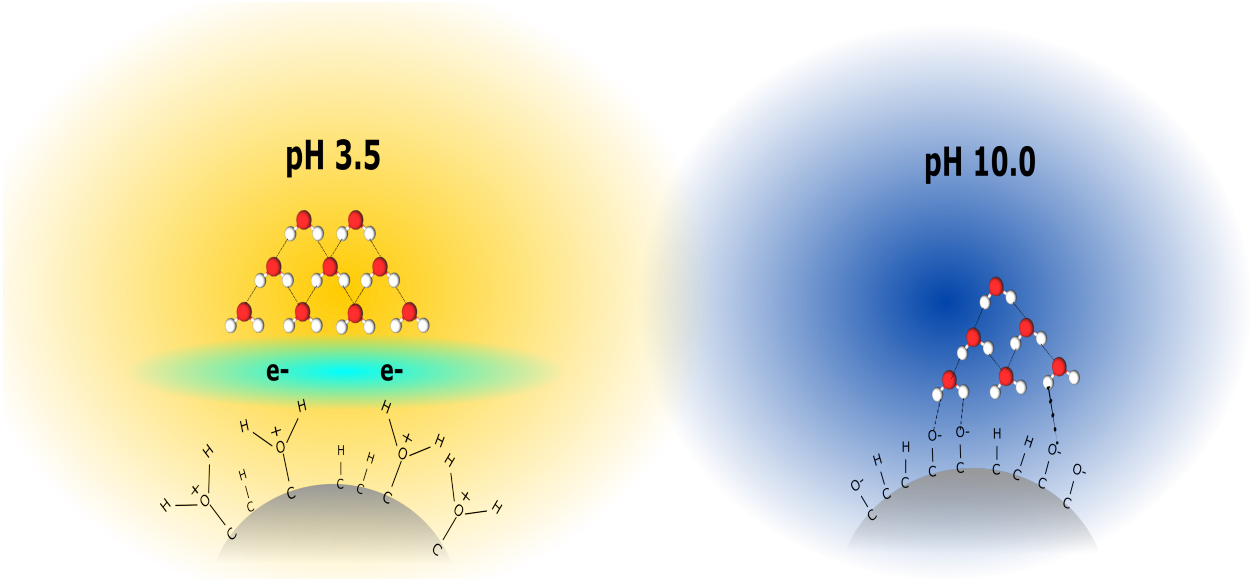

(a)

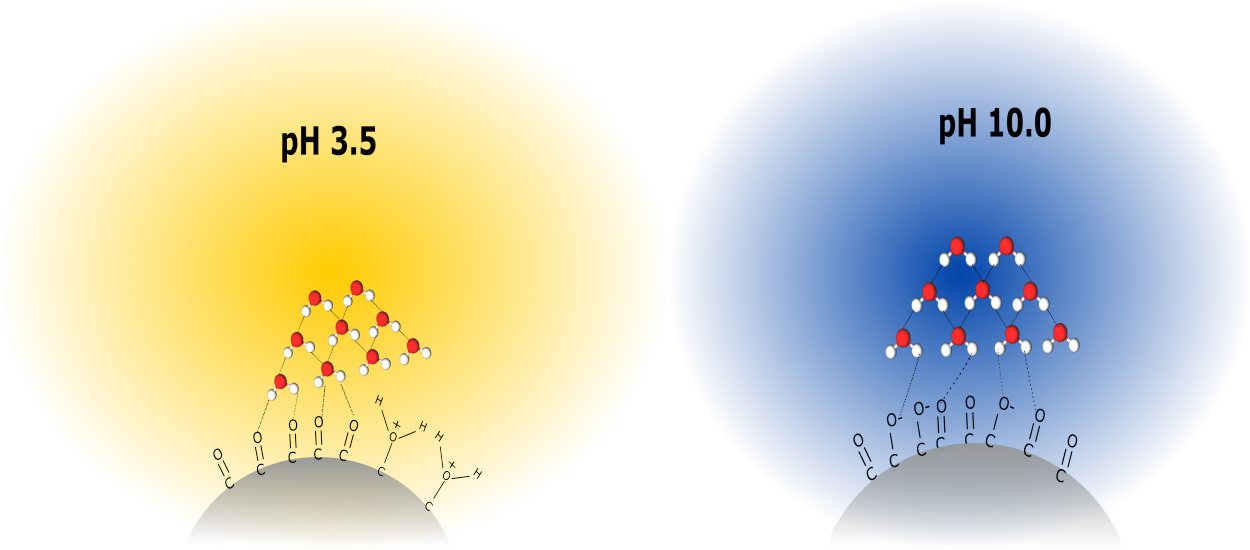

(b)

Figure 5.10: *Schematic illustrating surface interactions of (a)* ***ND-OH B*** *and (b)* ***ND-OH B+f*** *in acidic and basic pH.*

In a basic environment, however, the carbonyl groups formed on the surface of the **ND-OH B+f** remain unaffected and form H-bonds with water molecules upon exposure to humid air. This could explain the shoulder between 1726 cm^{-1} due to C=O stretching, in addition to the band due to OH-bending at 1643 cm^{-1}. The difference spectra as shown in Figure 5.9b, however, evidences a broader band induced by OH-bending on **ND-OH B** which could be due to more number of deprotonated OH groups on the surface interacting with water molecules via H-bonding. Additionally, a small shoulder is also observed at 1550 cm^{-1} for **ND-OH B** which is absent in **ND-OH B+f** and is much weaker in intensity than that

observed under acidic pH conditions. This shoulder could be due to a rather weak charge accumulation layer[22] due to smaller number of C-H groups on the surface of **ND-OH B**. A simple schematic to illustrate the different interactions are shown in Figure 5.10.

Implications on Photocatalysis with Diamonds

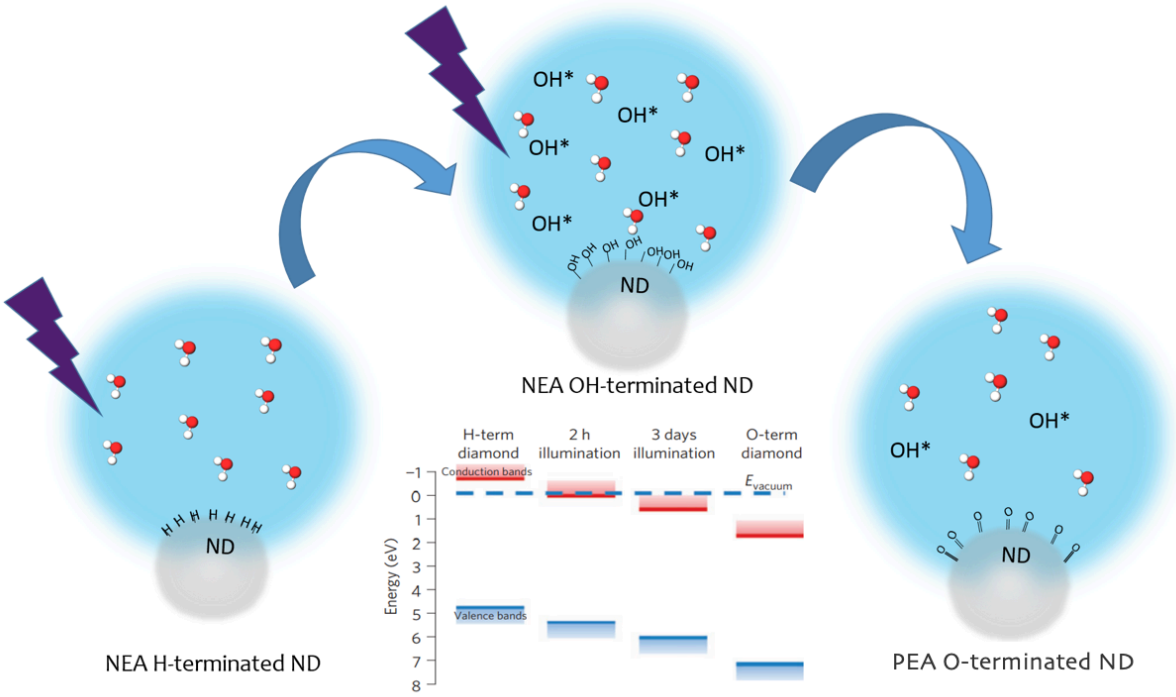

Figure 5.11: *Schematic showing potential oxidation of diamond surfaces under long exposure to UV irradiation in water. The H-terminated surfaces undergo photochemical hydroxylation under UV irradiation. Subsequent oxidation of the OH groups to carbonyl groups could result in an O-terminated surface which has a positive electron affinity thereby inhibiting the emission of solvated electrons. This oxidation mechanism is in further agreement with the progressive shift of the EA to positive values as shown in the band diagram taken from [8].*

OH-terminated diamond surfaces exhibit NEA and can therefore emit electrons like H-terminated surfaces. Our experiments here show the possible formation of oxonium ions due to the protonation of the OH groups on the surface in acidic pH conditions, which could potentially enhance electron emission from the material. Although this is advantageous for application of diamonds as a photocatalyst for CO_2 reduction, it must be noted that long term exposure to UV radiation in water may result in the oxidation of the diamond surface, resulting in the formation of carbonyl groups on the surface. The electron rich oxygen groups could eventually raise the electron emission barrier, thus hindering the generation of solvated electrons in a basic solution.[8] Interestingly, our experimental observations also point out a possible mechanism of aging of the ND surface promoted by $OH^{\bullet}$, as illustrated in Figure 5.11.

Based on the FTIR observations it may seem that the Fenton treatment potentially accelerates the aging process of the nanodiamonds. This may be helpful in gaining insights into changes in the surface chemistry of the ND surfaces in photo electrochemical applications under UV illumination. More specifically, Kurzyp et al. have shown that due to NEA of H-terminated ND surfaces, irradiation of ND-H in water with low energy X-rays results in emission of an electron which produces $OH^{\bullet}$ as a result of radiolysis of water molecules.[9] Production of $OH^{\bullet}$ may also be induced by deep UV irradiation,[23] which could oxidize the diamond surface resulting in aging of the material involving a mechanism that is analogous to a successive borane and Fenton treatment of detonation nano diamond surface. Under acidic or basic pH conditions, oxidation of diamonds changes the interactions of the diamond surface with its environment. This would therefore, make it challenging to use ND-H for photocatalytic applications in basic conditions. An alternative would be to use ND-OH in acidic pH conditions as the formation of oxonium ions may potentially enhance electron emission from diamonds as well as stabilize the electron cloud close to the diamond surface which could be beneficial for catalytic applications. At the same time, it would be useful to find a means to enable visible light absorption in the material as explained in Chapters 3 and 4. Additionally, for efficient photocatalysis with diamonds, hybrid materials with transition metals and metal oxides could be explored, as will be discussed in the next section.

5.3. Investigation of transition metal coated diamonds at the solid-liquid interface

5.3.1. Introduction

The study of surface interactions of diamond materials in water revealed a possibility of eventual oxidation of the diamond surfaces under long exposure to UV radiation in water. This could affect its capability of solvated electron generation for catalyzing CO_2 reduction under long-term irradiation. Furthermore, the energetically uphill process of CO_2 reduction calls for more efficient photocatalysts to drive the reaction. Copper has been demonstrated to be the most promising element to catalyze CO_2 reduction into hydrocarbons by the group of Hori.[24] Since then investigations in the electrocatalytic reduction of CO_2 on Cu based catalysts have followed[25–32]. Moreover, since CuOx based catalysts have a suitable band gap in the visible light region,[33] this idea was further extended to the area of photocatalysis and photoelectrocatalysis which triggered numerous studies on Cu and CuOx nanostructures as catalysts for enhancing the activity and selectivity of several semiconductors including those with wide band-gap.[34–38] However, the lack of long-term stability of copper containing catalysts has resulted

in extensive research on hybrid catalyst materials combining CuOx and Cu with stable photocatalysts which typically tend to have a wider band gap.[39–41] Hybrid structures not only enhance the stability of the catalyst but also the ability of the material to use a significantly large part of the available solar spectrum thus boosting its catalytic performance. Diamonds which are robust and chemically stable, wide band gap semiconductor materials with demonstrated activity towards CO_2 reduction under UV irradiation,[42] were therefore decorated with CuNP on the surface with the goal of studying the enhancement in their photocatalytic activity. CuNP/ND were synthesized within the framework of the DIACAT Project by collaborators at Universität Würzburg according to a well-established method previously reported by Turcheniuk *et al.*[43] This method involves adsorption of copper (II) acetate on the surface of the nanodiamonds followed by subsequent reduction yielding metallic Cu nanoparticles.

Experimental[44] and theoretical studies[25, 45] on copper surfaces have helped to propose reaction mechanisms for the electrocatalytic CO_2 reduction. However, the role of copper oxides in this reaction could only be elucidated using soft X-ray absorption spectroscopy. This is because XAS is an element-selective technique and is a local probe for the density of unoccupied states in a material that is largely influenced by the morphology of the material and chemical state of the sample. In particular, *operando* XAS at the K edge of Cu was shown to provide essential structural information obtained from EXAFS and chemical state information obtained from XANES that can be used to determine the oxide content of the CuOx catalyst and can be correlated to its catalytic activity.[46] However, it is the Cu L edge that has been shown to be more sensitive to changes in oxidation state of Cu and hence can be used as a direct unambiguous probe to monitor oxidation changes during an electrochemical process.[47–49] In particular the shape of the L_3 edge is shown to be very sensitive to the chemical state of the Cu atom.[47] Recently, Velasco-Velez *et al.* probed the nature of electrodeposited of CuOx[48] as well as demonstrated *in-situ* XAS at the Cu L edge to be sensitive to the changes in oxidation state at different stages of the CO_2 electroreduction.[49] Therefore by using XAS at the Cu L edge, we firstly intend to determine the chemical state of the Cu NP on the surface of the NDs in water. Moreover, by monitoring the changes in the oxidation state of Cu during electrochemistry, we would also like to specifically illuminate the role of B-doped nanodiamond in the diamond-electrodeposited CuOx hybrid catalyst by performing *in-situ* XAS at the Cu L edge under applied potentials.

5.3.2. X-ray absorption spectroscopy of metal-coated nanodiamonds in water

In this section we present a soft X-ray absorption study to characterize the electronic structure of the nanoparticles in water as a first step towards understanding the properties of the material that could

potentially shed light on its photocatalytic activity. To this aim, a colloidal solution of **CuNP/ND** was dropcasted on a Si (100) substrate as well as on a Si_3N_4 membrane to investigate the Cu L edge of the material in vacuum and directly in water, respectively using Partial Fluorescence Yield (PFY) mode, as mentioned in Chapter 2. The recorded spectra were compared to a reference spectrum for Cu foil, which is presented in Figure 5.12.

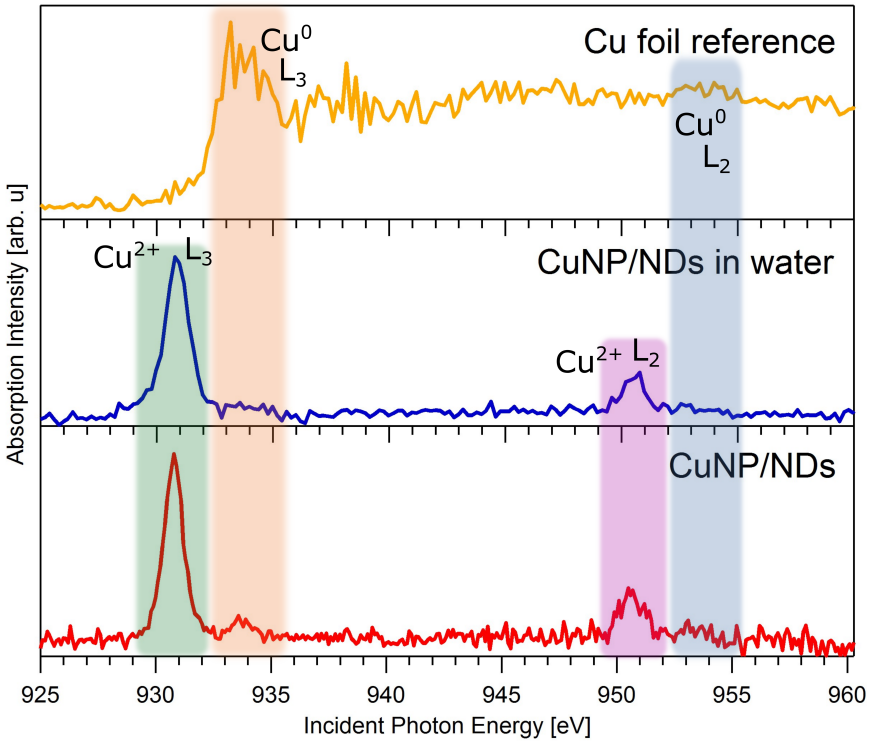

Figure 5.12: *Cu L edge PFY-XA spectra of **CuNP/NDs**. The **CuNP/NDs** were studied both under vacuum (in red) and in water (in blue) to observe changes in the electronic structure at the solid-water interface. Pure Cu foil (in yellow) was used as a reference for metallic copper.*

The Cu L edge spectra for **CuNP/ND** in vacuum and water are compared to that of a Cu foil reference in Figure 5.12. As is evident from the comparison in the figure, the composite nanoparticles exhibit a different oxidation state of Cu as compared to the Cu foil reference. The Cu foil reference which is known to be composed of pure metallic copper exhibits an oxidation state of Cu^0. The L_3 edge is observed in this case at 933.5 eV and the L_2 at around 953.3 eV, although the intensity of the latter is significantly reduced and can barely be distinguished from the noise level. The Cu NPs in the composite material however, exhibit Cu^{2+} oxidation state as is evident from the spectra, where sharp resonances are observed at L_3 and L_2 that are shifted to lower energies by about 2.5 eV and now appear at 931 eV and 950.8 eV respectively. The difference of 19.8 eV between the L_3 and L_2 resonances in the spectra is in close agreement with the spin-orbit splitting of 19.9 eV determined by XPS investigations reported pre-

viously in literature. In addition to Cu^{2+} a small amount of Cu^{+} is also present in the **CuNP/ND** as is evident from the small L_3 peak around 933.5 eV and a bump in the L_2 region at 953.3 eV when the measurements are conducted in vaccuum. This Cu^{+} eventually gets oxidized in aqueous environment to Cu^{2+} when measurements are conducted in water. Figure 5.13 illustrates what happens at the surface of the **CuNP/ND** that could explain our experimental observations.

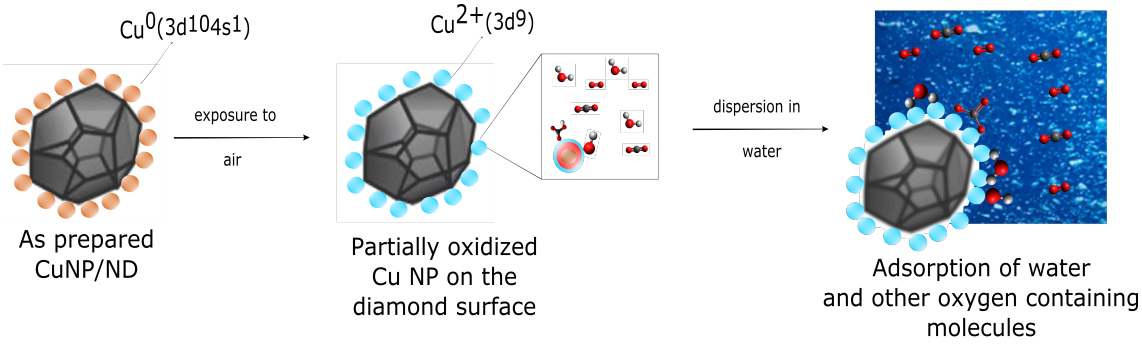

Figure 5.13: *Graphical illustration of oxidation of metallic Cu NPs in air. In the presence of moisture, oxygen and carbon dioxide in air the Cu NPs are covered with an oxide layer which comprises of CuO (blue layer) and Cu_2O (red layer). Subsequent dispersion in water results in adsorption of water molecules as well as other oxygen containing species such as hydroxyl groups and carbonates*

The reduction of copper (II) acetate salts on the surface of the nanodiamonds results in the formation of metallic Cu nanoparticles on the surface of the as-prepared **CuNP/ND** sample. Here the copper is in 0 oxidation state with a $3d^{10}4s^{1}$ configuration, containing completely filled *3d* states. Copper which is susceptible to oxidation in air even at room temperature forms a duplex type oxide layer with a CuO layer that is in direct contact with the atmosphere on the outside and a Cu_2O layer at the interface to the Cu metal as depicted in Figure 5.13. The presence of this double layer structure is evidenced in the X-ray absorption structure shown in Figure 5.12. Subsequent dispersion of the **CuNP/ND** in water could result in the adsorption of water as well as other oxygen containing molecules on the surface as shown in Figure 5.13. For the XAS measurements, a thin film of the sample was drop casted on a Si substrate from this liquid dispersion. Exposure to vacuum could result in the removal of some loosely adsorbed molecules from the Cu surface without essentially changing the chemical state of the surface. Therefore, the sample measured in vacuum exhibits sharp resonances at the L_3 and L_2 edges corresponding to transitions from *2p* to unoccupied *3d* levels in CuO and rather weak resonances arising from transition to empty *4s* levels in Cu_2O. Such sharp resonances, also known as white lines are typically not observed for metallic copper due to its filled *3d* states. Interestingly, the formation of CuO layer on the nanoparticle is further responsible for aging of the nanoparticle by modifying the surface properties of the same.

In presence of CO_2 in the atmosphere, hydroxyl groups attached to the surface of the oxide layer facilitate the formation of bicarbonates on the surface upon CO_2 adsorption. In water, the probability of water molecules interacting with the oxide surface is much higher due to the higher water to CO_2 molar ratio. The co-adsorbed water layer on the oxide surface facilitates formation of surface carbonates along with protonated hydroxyl groups on the surface. Additionally, in water the Cu_2O layer also gets oxidized to Cu^{2+} due to larger specific surface area and much higher surface energy of the nanoparticles. Moreover, since the Cu L edge lies above the O K edge, oxidation of the Cu NPs on the diamond surface due to X-ray induced $OH^{\bullet}$ formation as a result of non-resonant ionization of the water molecules also cannot be completely excluded. This could essentially explain the higher density of the Cu^{2+} states in water. In the following section we shall compare these results with the experimental observations on nanodiamonds electrochemically coated with Cu_2O.

5.3.3. *In-situ* electrochemical investigations on Cu_2O coated Nanodiamonds

Cuprous oxide decorated boron doped nanodiamonds (Cu_2O-B-ND) were investigated as photoelectrodes at the University of Oxford for its performance towards CO_2 reduction. The enhanced photoelectrocatalytic performance in comparison to bare diamond electrodes motivated the *in-situ* electrochemical investigations using soft X-ray absorption spectroscopy. Such a study was aimed at directly observing the changes in the oxidation states of copper during the electrochemical process under different bias conditions. Due to larger surface area of nanostructures, boron-doped nanodiamonds (B-ND) were chosen as the material for the working electrode on which Cu_2O was to be electrodeposited. Additionally, the results of the in-situ electrochemical investigations further made possible to understand the role of nanodiamonds in the promoted catalyst material.

B-ND synthesized by collaborators at Universität Würzburg was used in these *in-situ* investigations. The colloidal solution of B-ND was drop casted on a Au coated Si_3N_4 membrane to form a thin film working electrode. A Pt wire was used as the counter electrode while Ag/AgCl was the reference electrode. Cu_2O was electrodeposited on the B-ND film from a $CuSO_4$ electrolyte prepared using a procedure identical to that used in Oxford.[38] The electrodeposition was done at a constant current of 6.6 mA for 60s. During the subsequent electrochemical measurements, a $KHCO_3$ electrolyte solution with pH 12 was used which was first purged with N_2 gas and then subsequently saturated with CO_2 gas before introducing into the flow cell. All measurements presented here were conducted in the CO_2 saturated electrolyte. X-ray absorption spectra were recorded under three different conditions, without bias, with -1.2 V bias vs Ag/AgCl and +0.5V vs Ag/AgCl. The resultant spectra are presented in Figure 4 which have been com-

pared to the spectra presented in Figure 5 that was obtained from bare electrodeposited Cu_2O electrodes without B-ND.

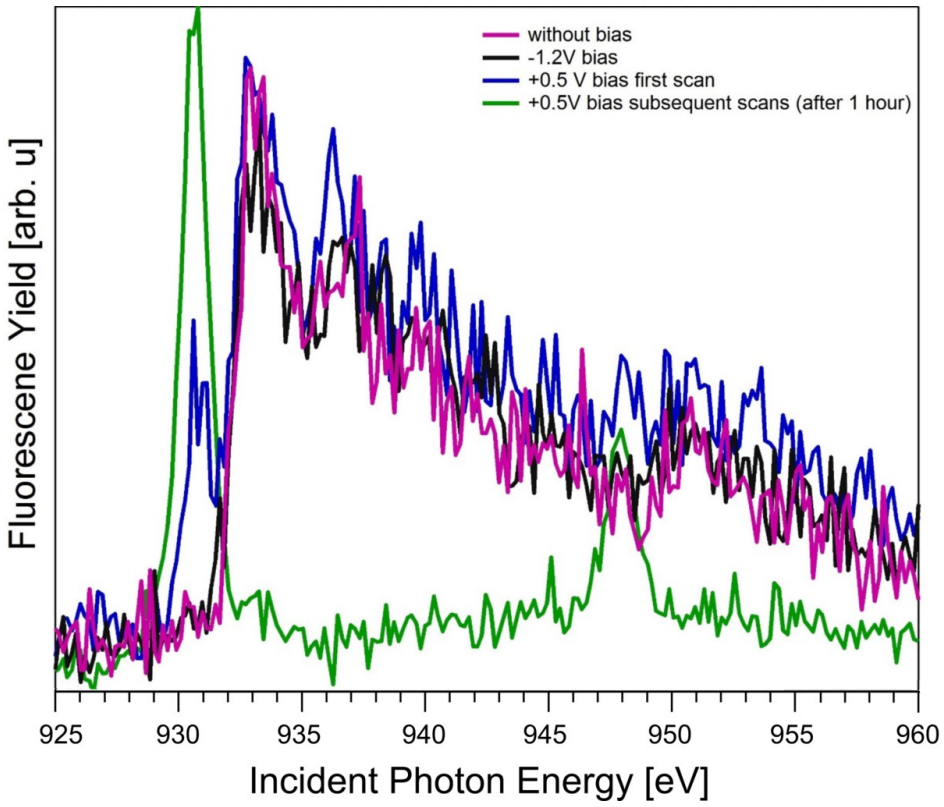

Figure 5.14: *Cu L edge in-situ PFY-XA spectra for Cu_2O deposited on a Si_3N_4 membrane coated with a film of B-ND. The spectra were recorded without bias, at -0.5 V vs Ag/AgCl and +1.2V vs Ag/AgCl. Upon electrodeposition CuOx is present in a +1 oxidation state.*

In Figure 5.14 the Cu L edge PFY-XA spectra have been presented for Cu_2O deposited on B-ND film. The first series of spectra were recorded without a bias and summed up to result in the spectrum represented in pink. The L_3 edge is evident as a sharp rising edge at 933.5 eV with a weaker feature appearing at 936 eV. A smaller rising edge is observed at *ca.* 951.5 eV which is the L_2 edge. Subsequent spectra were recorded first at a reduction potential of -1.2V vs Ag/AgCl where the reduction of CO_2 is expected to take place and thereafter at an oxidation potential of +0.5V vs Ag/AgCl to observe the oxidation of Cu and consequently its deactivation. At -1.2V bias the spectrum looks identical to that recorded without bias. Applying positive potential between the working and counter electrode results in the oxidation of Cu(I) to Cu(II) state which is irreversible. This is evidenced from the two sharp peaks, that are observed at the L_3 and L_2 edges at 930.5 and *ca.* 948.5 eV respectively. Furthermore, these peaks are also shifted by 3 eV towards lower energies compared to Cu(I) state. Interestingly a complete oxidation does not take place instantly upon applying +0.5V bias. Instead the first spectrum recorded after the bias, presented in blue in Figure 5.14, exhibits a co-existence of both Cu(I) and Cu(II) states, with the density of Cu(II) states

being relatively lower than Cu(I).

According to literature reports on the mechanism of CO_2 reduction, it has been proposed that Cu_2O is reduced to metallic copper which is the active species for the catalysis. In such a case one would expect to see a Cu(0) spectrum with L_3 and L_2 edge positions roughly similar to the Cu(I) spectrum but with different satellite structures.[32] However, in our case such a difference is hard to observe in order to be able to draw any specific conclusions about the mechanism. This is primarily because of the following experimental limitations. Firstly, despite saturating the solution with CO_2 there could be diffusion limitations to the working electrode since in the flow cell, we are operating in the microfluidic regime, with a laminar flow of the electrolyte in a micron sized channel.[50] Secondly, the uptake of CO_2 in aqueous electrolytes is much lesser in comparison to ionic liquids as already investigated in Oxford. Since all measurements presented here have been performed in CO_2 saturated electrolyte, this would imply that despite bubbling CO_2 through the electrolyte solution for more than 30 minutes, the concentration in the solution is very little. Finally, the PFY-XA spectra as shown in Figure 5.14 and also later in Figure 5.15 have a relatively low signal/noise ratio despite long measurements. This makes it difficult to distinguish and resolve the Cu(I) from that of Cu(0).

To better understand the role of B-ND in the catalytic activity of the Cu_2O promoted electrode, the electronic structure at the Cu L edge was measured without the ND film under similar bias conditions as with the ND film. The corresponding spectra are shown in Figure. 5.15.

As is evident from the spectrum recorded without an applied bias (in pink) shown in Figure 5.15, the electrodeposited film contains copper in a +1 oxidation state with characteristic L_3 and L_2 edges at ca. 933 eV and 951.5 eV respectively. A weaker L_3 feature also seems to appear at *ca.* 936 eV. This helps to confirm the electrodeposition of Cu_2O on the Au coated Si_3N_4 membrane. In the subsequent cases when reductive and oxidative potentials are applied, significant changes are observed which are different from the case when Cu_2O is deposited on a film of B-ND deposited on the membrane. At -1.2V bias vs Ag/AgCl the L_3 and L_2 edges appear at similar positions with the maximum of L_3 appearing to be shifted to lower energy by less than 0.5 eV. Additionally, it can be seen from the figure that the weak L_3 feature is also not very prominent in the spectrum. This differing satellite structure in the spectra may suggest the evidence of a possible reduction of Cu(I) to Cu(0) for the CO_2 reduction reaction which was not very apparent in the Cu_2O promoted B-ND electrode. However, the noisy character of the signals still make it difficult to draw further concrete conclusions about the mechanism. Applying +0.5V bias leads to dramatic changes in the spectrum. As it can be seen from the blue and green spectra in Figure 5.15, Cu(0) decreases in intensity and a sharp L_3 peak appears at ca. 930 eV alongside a peak at L_2 at ca.

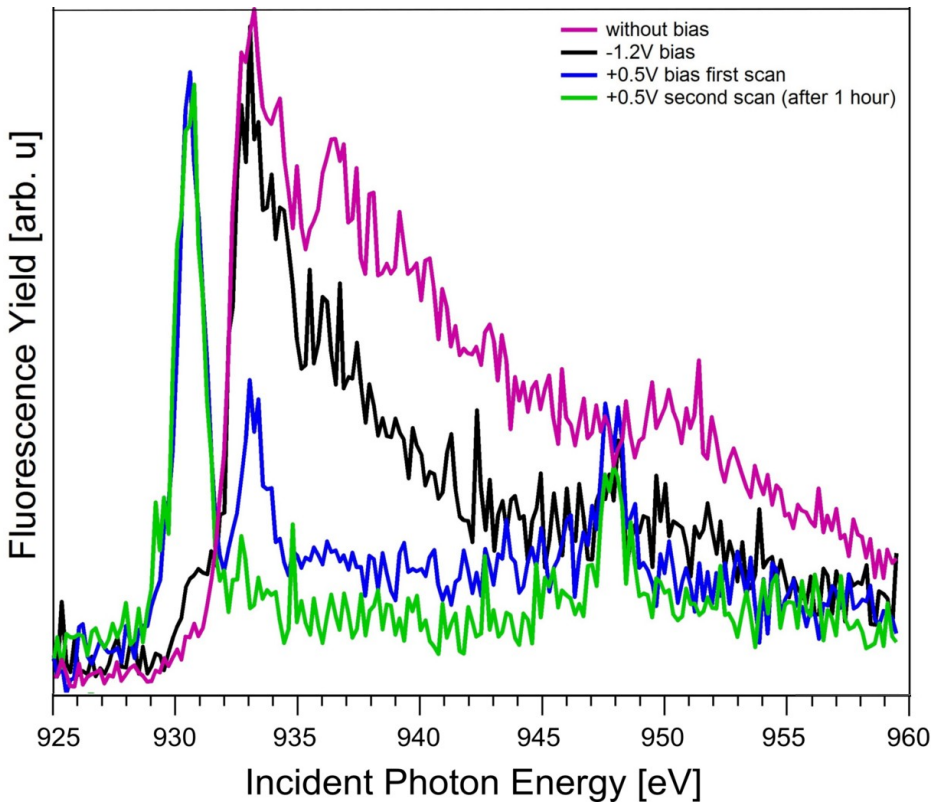

Figure 5.15: *In-situ XAS at the Cu L edge of Cu_2O deposited on a Au coated Si_3N_4 membrane. The deposited CuOx shows a +1 oxidation state as is evident from the spectrum recorded without bias (pink).*

948.5 eV. This appearance of two sharp peaks at L_3 and L_2 edges is characteristic of Cu(II). Hence, it may be concluded that on applying +0.5V bias vs Ag/AgCl the Cu species gets immediately partially oxidized to Cu(II). Subsequently a complete oxidation is evident from the disappearance of Cu(0).

The notable difference between the bare Cu_2O electrode and the Cu_2O promoted B-ND electrode appear both at -1.2V and +0.5V bias. Although in both cases the Cu species get eventually oxidized to Cu(II) at positive bias potentials which deactivates the catalyst, the first scan already tells us that this oxidation happens at a somewhat slower rate in the presence of B-ND, considering that one PFY-XAS scan takes around *ca.* 60 minutes to record. In order to explain these observations, we use the band structure of the components of the electrode shown in Figure 5.16 as a guide to understand the possible charge transport pathways that may influence the subsequent oxidation of Cu and therefore its deactivation as the catalytic species.

In Figure 5.16 the conduction and valence band edges (CBE and VBE) of H-terminated boron doped diamonds (H-BDD), Cu_2O and CuO have been represented in addition to the Fermi level of the Au layer on the membrane.[51, 52] The scheme shows that the VBE of Cu_2O and CuO lie ca. 1.4 eV and 1.1 eV below that of the diamond. The CBE of Cu_2O and CuO lie well below the CBM of diamond as well as the

EF of Au. From Figure 5.16, it is further evident that the redox levels for the two CO_2 reduction reactions of interest lie above the CBM of CuO but below that of diamond and Cu_2O.

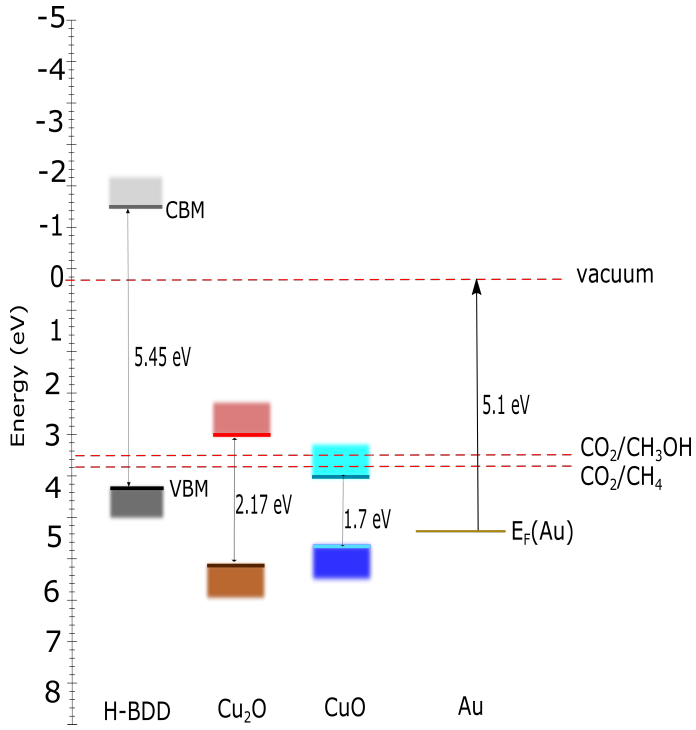

Figure 5.16: *Illustration of the band structure of the components of the working electrode. Cu_2O is electrodeposited on H-BDD and undergoes subsequent oxidation to CuO which is deactivated by a carbonate adsorption in the electrolyte. Au layer forms the electrical connection between the working electrode and Pt counter electrode. The energy scale represents absolute energy values relative to vacuum level. Redox levels of two likely CO_2 reduction reactions are represented in the illustration.*

Starting with an electrode system combining two p-type semiconductors, diamond and Cu_2O, it is expected that the Fermi levels of these two materials would lie below the redox levels of the species in solution. For simplicity, we consider this to be the redox level of the CO_2 reactions that are of interest to us. In order to maintain equilibrium, therefore, electrons would have to be transferred from the solution to the semiconductor material which would result in an upward band bending at the Cu_2O-electrolyte interface.[53] Application of a negative potential results in further depletion of holes from the material and accumulation of more electrons at the interface which can participate in catalyzing the CO_2 reduction reaction when the CO_2 molecule is adsorbed on to the catalyst surface.[53] When, however, a positive potential is applied, holes which are the majority charge carriers in the p-type Cu_2O tend to accumulate at the interface[53] thereby oxidizing the Cu(I) to Cu(II) species. In the presence of BDD or B-ND as a support material,as in our case, the higher position of the VBM relative to that of Cu_2O plays an important role. Electrons from the B-ND VBM can travel to the Cu_2O thereby filling the accumu-

lated holes and facilitating charge separation at the interface. This slows down the oxidation process and the consequent deactivation of Cu2O by formation of carbonates on the surface as described in the previous section. Therefore, it could be said that the hybrid electrode material B-ND/Cu_2O exhibits a synergistic effect, whereby B-ND provides a support and stability to the Cu_2O and the latter enhances the catalytic activity of the material due to its high reactivity towards CO_2 reduction reactions.

5.4. Conclusions

In conclusion, we have presented three preliminary studies in this chapter to understand the behaviour of diamonds in water. Specifically, XAS was conducted at the C K edge of B, N and P doped diamonds to elucidate the role of adsorbates on the electron yield from diamond surfaces. Our experiments have demonstrated photon-induced sub band gap electron emission in n-type diamonds doped with N and P due to the introduction of delocalized donor states close to the CBM of diamonds. These results are also in agreement with our observations presented in Chapter 3, where the XAS measurements were conducted without prior annealing of the samples. Having clarified the role of adsorbate layer on the surface of diamonds in vacuum, we were also able to throw light on the surface interaction of OH-terminated diamonds under different pH conditions in humid air environment.

From the FTIR results, we could hypothesize a possible oxonium ion formation in an acidic environment on the ND-OH surface prepared by borane reduction. This behaviour changes in the basic environment where the OH groups are likely to get deprotonated leaving electron rich negatively charged oxygen on the surface. Our results further hint towards a possible oxidation of ND-H that is likely to occur when diamonds are exposed to UV radiation in water. This could essentially raise the electron emission barrier for photocatalysis in solution. It could be therefore, hypothesized that ND-OH surfaces in acidic solution would be a better solution to enable electron emission for photocatalytic CO_2 reduction, in addition to enabling visible light absorption in the material. However, further investigations would be necessary to confirm this hypothesis.

In the final study of diamonds in water, we were able to propose the role of B-ND as a potentially good support material for Cu_2O catalyst, which slows down the deactivation of Cu thereby enhancing the stability of the hybrid catalyst which could result in enhanced photocatalytic performance of the material. Our results demonstrate only a proof-of-concept measurement to study the diamond-water interface, calling for further investigations in order to develop a better diamond-based photocatalyst for CO_2 reduction.

References

[1] S. Choudhury, B. Kiendl, J. Ren, F. Gao, P. Knittel, C. Nebel, A. Venerosy, H. Girard, J.-C. Arnault, A. Krueger, K. Larsson, and T. Petit, *Combining nanostructuration with boron doping to alter sub band gap acceptor states in diamond materials,* J. Mater. Chem. A **6**, 16645 (2018).

[2] Z. Shpilman, I. Gouzman, T. Minton, L. Shen, A. Stacey, J. Orwa, S. Prawer, B. Cowie, and A. Hoffman, *A Near Edge X-ray Absorption Fine Structure Study of Oxidized Single Crystal and Polycrystalline Diamond Surfaces,* Diamond and Related Materials **45**, 20 (2014).

[3] K. Bobrov, G. Comtet, G. Dujardin, L. Hellner, P. Bergonzo, and C. Mer, *Surface electronic states of the partially hydrogenated diamond* $\mathrm{C}(100)-(2\times1):\mathrm{H}$ *surface,* Phys. Rev. B **63**, 165421 (2001).

[4] F. Maier, M. Riedel, B. Mantel, J. Ristein, and L. Ley, *Origin of Surface Conductivity in Diamond,* Phys. Rev. Lett. **85**, 3472 (2000).

[5] A. Stacey, B. C. C. Cowie, J. Orwa, S. Prawer, and A. Hoffman, *Diamond C* $1s$ *core-level excitons: Surface sensitivity,* Phys. Rev. B **82**, 125427 (2010).

[6] F. A. Koeck and R. J. Nemanich, *Low temperature onset for thermionic emitters based on nitrogen incorporated UNCD films,* Diamond and Related Materials **18**, 232 (2009), nDNC 2008 Proceedings of the International Conference on New Diamond and Nano Carbons 2008.

[7] S. Kono, K. Mizuochi, G. Takyo, N. I. Plusnin, T. Aoyama, T. Goto, T. Abukawa, A. Namba, Y. Nishibayashi, and T. Imai, *Surface Energy Band and Electron Affinity of Highly Phosphorous-doped Epitaxial CVD Diamond,* e-Journal of Surface Science and Nanotechnology **5**, 33 (2007).

[8] D. Zhu, L. Zhang, R. E. Ruther, and R. J. Hamers, *Photo-illuminated diamond as a solid-state source of solvated electrons in water for nitrogen reduction,* Nature Materials **12**, 836 (2013).

[9] M. Kurzyp, H. A. Girard, Y. Cheref, E. Brun, C. Sicard-Roselli, S. Saada, and J.-C. Arnault, *Hydroxyl radical production induced by plasma hydrogenated nanodiamonds under X-ray irradiation,* Chem. Commun. **53**, 1237 (2017).

[10] H. A. Girard, T. Petit, S. Perruchas, T. Gacoin, C. Gesset, J. C. Arnault, and P. Bergonzo, *Surface properties of hydrogenated nanodiamonds: a chemical investigation,* Phys. Chem. Chem. Phys. **13**, 11517 (2011).

[11] M. J. Rutter and J. Robertson, *Ab initio calculation of electron affinities of diamond surfaces,* Phys. Rev. B **57**, 9241 (1998).

[12] R. J. Hamers and J. Bandy, *Atmospheric-pressure photoelectron emission from H-terminated and amino-terminated diamond,* physica status solidi (a) **213**, 2069 (2016).

[13] T. Petit and L. Puskar, *FTIR spectroscopy of nanodiamonds: Methods and interpretation,* Diamond and Related Materials **89**, 52 (2018).

[14] H. Girard, J. Arnault, S. Perruchas, S. Saada, T. Gacoin, J.-P. Boilot, and P. Bergonzo, *Hydrogenation of nanodiamonds using MPCVD: A new route toward organic functionalization,* Diamond and Related Materials **19**, 1117 (2010), proceedings of Diamond 2009, The 20th European Conference on Diamond, Diamond-Like Materials, Carbon Nanotubes and Nitrides, Part 2.

[15] A. Krüger, Y. Liang, G. Jarre, and J. Stegk, *Surface functionalisation of detonation diamond suitable for biological applications,* J. Mater. Chem. **16**, 2322 (2006).

[16] R. Martín, M. Álvaro, J. R. Herance, and H. García, *Fenton-Treated Functionalized Diamond Nanoparticles as Gene Delivery System,* ACS Nano **4**, 65 (2010).

[17] S. Ji, T. Jiang, K. Xu, and S. Li, *FTIR study of the adsorption of water on ultradispersed diamond powder surface,* Applied Surface Science **133**, 231 (1998).

[18] T. Petit, L. Puskar, T. Dolenko, S. Choudhury, E. Ritter, S. Burikov, K. Laptinskiy, Q. Brzustowski, U. Schade, H. Yuzawa, M. Nagasaka, N. Kosugi, M. Kurzyp, A. Venerosy, H. Girard, J.-C. Arnault, E. Osawa, N. Nunn, O. Shenderova, and E. F. Aziz, *Unusual Water Hydrogen Bond Network around Hydrogenated Nanodiamonds,* The Journal of Physical Chemistry C **121**, 5185 (2017).

[19] N. M. Yoon, C. S. Pak, B. H. C., S. Krishnamurthy, and T. P. Stocky, *Selective reductions. XIX. Rapid reaction of carboxylic acids with borane-tetrahydrofuran. Remarkably convenient procedure for the selective conversion of carboxylic acids to the corresponding alcohols in the presence of other functional groups,* The Journal of Organic Chemistry **38**, 2786 (1973).

[20] K.-i. Ataka, T. Yotsuyanagi, and M. Osawa, *Potential-Dependent Reorientation of Water Molecules at an Electrode/Electrolyte Interface Studied by Surface-Enhanced Infrared Absorption Spectroscopy,* The Journal of Physical Chemistry **100**, 10664 (1996).

[21] R. G. Ryan, A. Stacey, K. M. O'Donnell, T. Ohshima, B. C. Johnson, L. C. L. Hollenberg, P. Mulvaney, and D. A. Simpson, *Impact of Surface Functionalization on the Quantum Coherence of Nitrogen-Vacancy Centers in Nanodiamonds,* ACS Applied Materials & Interfaces **10**, 13143 (2018).

[22] M. Dankerl, A. Lippert, S. Birner, E. U. Stützel, M. Stutzmann, and J. A. Garrido, *Hydrophobic Interaction and Charge Accumulation at the Diamond-Electrolyte Interface,* Phys. Rev. Lett. **106**, 196103 (2011).

[23] S. Le Caër, *Water Radiolysis: Influence of Oxide Surfaces on* H_2 *Production under Ionizing Radiation,* Water **3**, 235 (2011).

[24] Y. Hori, *Electrochemical* CO_2 *Reduction on Metal Electrodes,* in *Modern Aspects of Electrochemistry*, edited by C. G. Vayenas, R. E. White, and M. E. Gamboa-Aldeco (Springer New York, New York, NY, 2008) pp. 89–189.

[25] A. A. Peterson, F. Abild-Pedersen, F. Studt, J. Rossmeisl, and J. K. Nørskov, *How copper catalyzes the elec-*

troreduction of carbon dioxide into hydrocarbon fuels, Energy Environ. Sci. **3**, 1311 (2010).
[26] M. Le, M. Ren, Z. Zhang, P. T. Sprunger, R. L. Kurtz, and J. C. Flake, *Electrochemical Reduction of CO_2 to CH_3OH at Copper Oxide Surfaces,* Journal of The Electrochemical Society **158**, E45 (2011).
[27] K. P. Kuhl, E. R. Cave, D. N. Abram, and T. F. Jaramillo, *New insights into the electrochemical reduction of carbon dioxide on metallic copper surfaces,* Energy Environ. Sci. **5**, 7050 (2012).
[28] C. W. Li and M. W. Kanan, *CO_2 Reduction at Low Overpotential on Cu Electrodes Resulting from the Reduction of Thick Cu_2O Films,* Journal of the American Chemical Society **134**, 7231 (2012).
[29] R. Kas, R. Kortlever, A. Milbrat, M. T. M. Koper, G. Mul, and J. Baltrusaitis, *Electrochemical CO_2 reduction on Cu_2O-derived copper nanoparticles: controlling the catalytic selectivity of hydrocarbons,* Phys. Chem. Chem. Phys. **16**, 12194 (2014).
[30] D. Ren, Y. Deng, A. D. Handoko, C. S. Chen, S. Malkhandi, and B. S. Yeo, *Selective Electrochemical Reduction of Carbon Dioxide to Ethylene and Ethanol on Copper(i) Oxide Catalysts,* ACS Catalysis **5**, 2814 (2015).
[31] F. S. Roberts, K. P. Kuhl, and A. Nilsson, *High Selectivity for Ethylene from Carbon Dioxide Reduction over Copper Nanocube Electrocatalysts,* Angewandte Chemie **127**, 5268 (2015).
[32] A. Engelbrecht, C. Uhlig, O. Stark, M. Hämmerle, G. Schmid, E. Magori, K. Wiesner-Fleischer, M. Fleischer, and R. Moos, *On the Electrochemical CO_2 Reduction at Copper Sheet Electrodes with Enhanced Long-Term Stability by Pulsed Electrolysis,* Journal of The Electrochemical Society **165**, J3059 (2018).
[33] B. K. Meyer, A. Polity, D. Reppin, M. Becker, P. Hering, P. J. Klar, T. Sander, C. Reindl, J. Benz, M. Eickhoff, C. Heiliger, M. Heinemann, J. Bläsing, A. Krost, S. Shokovets, C. Müller, and C. Ronning, *Binary copper oxide semiconductors: From materials towards devices,* physica status solidi (b) **249**, 1487 (2012).
[34] K. Adachi, K. Ohta, and T. Mizuno, *Photocatalytic reduction of carbon dioxide to hydrocarbon using copper-loaded titanium dioxide,* Solar Energy **53**, 187 (1994).
[35] Q. Zhai, S. Xie, W. Fan, Q. Zhang, Y. Wang, W. Deng, and Y. Wang, *Photocatalytic Conversion of Carbon Dioxide with Water into Methane: Platinum and Copper(I) Oxide Co-catalysts with a Core–Shell Structure,* Angewandte Chemie **125**, 5888 (2013).
[36] X. An, K. Li, and J. Tang, *Cu_2O/Reduced Graphene Oxide Composites for the Photocatalytic Conversion of CO_2,* ChemSusChem **7**, 1086 (2014).
[37] I. Shown, H.-C. Hsu, Y.-C. Chang, C.-H. Lin, P. K. Roy, A. Ganguly, C.-H. Wang, J.-K. Chang, C.-I. Wu, L.-C. Chen, and K.-H. Chen, *Highly Efficient Visible Light Photocatalytic Reduction of CO_2 to Hydrocarbon Fuels by Cu-Nanoparticle Decorated Graphene Oxide,* Nano Letters **14**, 6097 (2014).
[38] C. K. Mavrokefalos, M. Hasan, J. F. Rohan, R. G. Compton, and J. S. Foord, *Electrochemically deposited Cu_2O cubic particles on boron doped diamond substrate as efficient photocathode for solar hydrogen generation,* Applied Surface Science **408**, 125 (2017).
[39] W. Siripala, A. Ivanovskaya, T. F. Jaramillo, S.-H. Baeck, and E. W. McFarland, *A Cu_2O/TiO_2 heterojunction thin film cathode for photoelectrocatalysis,* Solar Energy Materials and Solar Cells **77**, 229 (2003).
[40] K. Lalitha, G. Sadanandam, V. D. Kumari, M. Subrahmanyam, B. Sreedhar, and N. Y. Hebalkar, *Highly Stabilized and Finely Dispersed Cu_2O/TiO_2: A Promising Visible Sensitive Photocatalyst for Continuous Production of Hydrogen from Glycerol:Water Mixtures,* The Journal of Physical Chemistry C **114**, 22181 (2010).
[41] Y. Liu, B. Zhang, L. Luo, X. Chen, Z. Wang, E. Wu, D. Su, and W. Huang, *TiO_2/Cu_2O Core/Ultrathin Shell Nanorods as Efficient and Stable Photocatalysts for Water Reduction,* Angewandte Chemie International Edition **54**, 15260 (2015).
[42] L. Zhang, D. Zhu, G. M. Nathanson, and R. J. Hamers, *Selective Photoelectrochemical Reduction of Aqueous CO_2 to CO by Solvated Electrons,* Angewandte Chemie International Edition **53**, 9746 (2014).
[43] K. Turcheniuk and V. Mochalin, *Adsorption behavior and reduction of copper (II) acetate on the surface of detonation nanodiamond with well defined surface chemistry,* Carbon **109**, 98 (2016).
[44] D. W. DeWulf, T. Jin, and A. J. Bard, *Electrochemical and Surface Studies of Carbon Dioxide Reduction to Methane and Ethylene at Copper Electrodes in Aqueous Solutions,* Journal of The Electrochemical Society **136**, 1686 (1989).
[45] A. J. Garza, A. T. Bell, and M. Head-Gordon, *Mechanism of CO_2 Reduction at Copper Surfaces: Pathways to C2 Products,* ACS Catalysis **8**, 1490 (2018).
[46] K. Klingan, T. Kottakkat, Z. P. Jovanov, S. Jiang, C. Pasquini, F. Scholten, P. Kubella, A. Bergmann, B. Roldan Cuenya, C. Roth, and H. Dau, *Reactivity Determinants in Electrodeposited Cu Foams for Electrochemical CO_2 Reduction,* ChemSusChem **11**, 3449 (2018).
[47] M. Grioni, J. B. Goedkoop, R. Schoorl, F. M. F. de Groot, J. C. Fuggle, F. Schäfers, E. E. Koch, G. Rossi, J.-M. Esteva, and R. C. Karnatak, *Studies of copper valence states with cu L_3 x-ray-absorption spectroscopy,* Phys. Rev. B **39**, 1541 (1989).
[48] J.-J. Velasco-Vélez, K. Skorupska, E. Frei, Y.-C. Huang, C.-L. Dong, B.-J. Su, C.-J. Hsu, H.-Y. Chou, J.-M. Chen, P. Strasser, R. Schlögl, A. Knop-Gericke, and C.-H. Chuang, *The Electro-Deposition/Dissolution of $CuSO_4$ Aqueous Electrolyte Investigated by In Situ Soft X-ray Absorption Spectroscopy,* The Journal of Physical Chemistry B **122**, 780 (2018).
[49] J.-J. Velasco-Vélez, T. Jones, D. Gao, E. Carbonio, R. Arrigo, C.-J. Hsu, Y.-C. Huang, C.-L. Dong, J.-M. Chen, J.-F. Lee, P. Strasser, B. Roldan Cuenya, R. Schlögl, A. Knop-Gericke, and C.-H. Chuang, *The Role of the Copper Oxidation State in the Electrocatalytic Reduction of CO_2 into Valuable Hydrocarbons,* ACS Sustainable Chemistry & Engineering **7**, 1485 (2019).

5

[50] C. Schwanke, R. Golnak, J. Xiao, and K. M. Lange, *Electrochemical flowcell for in-situ investigations by soft x-ray absorption and emission spectroscopy,* Review of Scientific Instruments **85**, 103120 (2014).
[51] V. Jeyalakshmi, R. Mahalakshmy, K. R. Krishnamurthy, and B. Vishwanathan, *Photocatalytic Reduction of Carbon Dioxide by Water: A Step Towards Sustainable Fuels and Chemicals,* Materials Science Forum **734**, 1 (2013).
[52] A. Kahn, *Fermi level, work function and vacuum level,* Mater. Horiz. **3**, 7 (2016).
[53] *Electrochemistry of Semiconductors,* http://www.currentseparations.com/issues/17-3/cs-17-3d.pdf/.

6

Summary and Future Outlook

6.1. Conclusion

Diamonds are wide band gap semiconductors having a band gap of 5.4 eV. When the surface is H-terminated, the material has a negative electron affinity, enabling the direct emission of electrons in water. This unique property of diamonds makes it promising for photocatalysis. However, photoactivation of diamonds require deep UV irradiation making the process extremely challenging and also inefficient with solar spectrum. The primary objective of this research was therefore to generate physical insights into efficient photoactivation of synthetic diamonds at the diamond-water interface in order to develop an abundant, low cost and sustainable photocatalyst for CO_2 reduction. To this aim, the research was conducted in two parts to answer two broad research questions, the results of which are summarized below.

How to enable visible light absorption in diamonds?

To make the photoactivation of diamonds more efficient, the material should be able to absorb the visible part of the available solar spectrum. Therefore, the first part of this research concerns understanding the electronic structure of diamonds in order to develop strategies to enable visible light absorption in the material. Here, we have investigated two different approaches namely, doping and photosensitization with visible light active dyes.

In the first approach, we investigated the electronic structure of different diamond materials doped with B, N and P, developed within the DIACAT consortium, using XAS at the C K edge. Such a study allowed us to directly probe the new electronic states introduced by the dopant atoms within the band gap of diamonds. Particularly, the study on B-doped diamonds revealed the possibility of tuning the sub band-gap states in diamond by tuning the morphology. More specifically, our results showed that

XAS is sensitive to acceptor states introduced close to VBM by B-doping. Furthermore, new acceptor states were also found to be introduced close to the CBM in nanostructured B-doped diamonds such as diamond foams and NDs. Based on our results we were able to propose a synergistic effect of nanostructuration and B-doping as a strategy to enable defect-assisted transitions in diamonds. The electron emission characteristics of diamond became more evident on further investigation of n-type diamonds formed by N and P doping. Here, the C K edge XA spectrum revealed the possibility of photo-induced sub-band gap electron emission from donor states close to the CBM. Furthermore, an increase in sp^2 states was also evidenced which is typically said to impart conductivity to the n-type diamonds. From the study of doped diamonds, we can therefore conclude that while B-doping introduces sub-band gap acceptor states close to both VBM and CBM, n-type doping with N and P helps to reduce the threshold for electron emission. Therefore, in order to facilitate visible light photoactivation for solvated electron generation, besides nanostructuration, co-doping with both p- and n-type dopant atoms may also be a strategy worth exploring.

The second approach involves sensitizing diamond surfaces with Ru complexes, primarily $Ru(bpy)_3$. The role of $Ru(bpy)_3$ on diamond NPs was meant to be twofold. On one hand the Ru complex could absorb visible light and subsequently oxidize water. On the other hand, the photogenerated electrons available in the dye could potentially fill the photogenerated holes in the VB of diamonds. This would make more electrons available in the diamonds, thereby increasing the efficiency of solvated electron generation. In our investigations of the electronic structure of $Ru(bpy)_3$-ND, we were able to evidence electronic coupling between the dye molecule and diamonds. With the help of theoretical calculations, we could also identify a difference in the transitions to the LUMO and LUMO+1 levels of the dye which was linker-dependent. Particularly, in presence of a conjugated linker, the gap between LUMO and LUMO+1 orbitals was found to be lower. Our experimental results also evidenced the possibility of an additional charge transfer state which was absent in case of the non-conjugated linker. A study of the valence band showed that the HOMO of the dye lies above the VBM of NDs indicating that the dye can potentially act as an electron donor to fill the photogenerated holes in the VB of diamond. The charge transfer mechanism and dynamics between the Ru dye and ND should be explored in the next step in order to further corroborate the results obtained from electronic structure investigations.

How to make diamonds viable for efficient CO_2 photoreduction?

Solvated electrons are at the heart of diamond-based photocatalysis, that sets diamonds apart from other catalysts explored so far for CO_2 photoreduction. Apart from doping, electron emission of diamonds in water is also influenced by the surface chemistry of diamonds. Therefore, an understanding

of the diamond-water interface formed the primary focus of the second part of the thesis. To begin with, we clarified the role of adsorbates on electron emission from diamonds in vacuum. To this aim, XAS experiments were conducted after annealing the different doped diamond samples and subsequently after exposing them to air. A comparison of the electronic structures before and after air exposure revealed enhanced sub-band gap electron emission from n-type diamonds doped with N and P due to the presence of water and other oxygen containing adsorbates on the air exposed surfaces. Furthermore, we also observed shifts of the excitonic peak in opposite directions in the B- and P-doped diamonds, indicating possible band bending in the presence of water molecules and other oxygen containing adsorbates on the surface of diamonds.

We also studied the influence of surface termination on the interactions at diamond-water interface. Here, our primary focus was on hydrophilic OH-terminated ND surfaces which are likely to form when H-terminated NDs are exposed to UV irradiation in water for a long time. With the help of FTIR investigations, we were able to show different behaviour of the OH- groups under acidic and basic conditions, which could help us understand the optimum conditions for enhanced electron emission from diamonds in water. In particular, we found out that borane reduction of detonation NDs could introduce more OH groups on the surface in comparison to successive borane and Fenton treatments. The Fenton treatment step after a borane reduction especially tends to oxidize the existing OH groups back to carbonyls leaving a predominantly O-terminated surface that would essentially raise the electron emission barrier. Based on our results, we therefore hypothesized that, for predominantly OH-terminated surfaces, as is the case after borane reduction, an oxonium ion is likely to be formed due to protonation under acidic conditions. This could enhance electron emission from the diamond surface and potentially stabilize this electron cloud at the diamond-water interface, like H-terminated diamonds. In basic conditions, deprotonation of the OH-group leaves electron-rich negatively charged oxygen groups on the surface which could potentially inhibit electron emission. Our results also hint towards a possible mechanism of aging of the diamond surface upon prolonged exposure to UV irradiation in water which is accelerated by the OH radicals. Thus, we may conclude that in order to enhance the efficiency of solvated electron emission in water, OH-terminated surfaces in acidic solutions maybe a promising alternative. The viability of this alternative needs to be investigated further in photocatalytic experiments.

Since the ultimate goal would be to develop an efficient diamond-based photocatalyst, formation of hybrid catalytic materials with transition metals and their oxides are also worth exploring. Especially CuOx have been proven to be very efficient photocatalysts for CO_2 reduction but have demonstrated very poor stabilities on their own. As a last strategy to make diamonds viable for efficient photocatalytic CO_2 reduction, they were co-promoted with Cu and Cu_2O. The study of Cu on diamond NP revealed the

existence of a duplex type oxide layer comprising of an inner Cu_2O layer and an outer CuO layer in direct contact with atmosphere and/or water. The diamond-Cu_2O hybrid electrode was further studied with *in-situ* XAS at the Cu L edge, which helped us monitor the change in Cu oxidation states with change in potential. Since the hybrid material exhibited a more than twofold increase in efficiency, this study was interesting to better understand the role of diamonds in this hybrid geometry. Our results on the bare Cu_2O electrode revealed that at positive potentials Cu_2O gets irreversibly oxidized and subsequently deactivated due to adsorption of carbonates and bicarbonates on the surface. This could be detrimental for photocatalysis applications, since Cu_2O acts as the catalytic center in the hybrid material. Comparing with the diamond-Cu_2O electrode configuration, our studies suggested that presence of a diamond layer in this hybrid material provides a stable support. This is because diamond facilitates better charge separation thereby preventing the accumulation of holes at the Cu_2O-electrolyte interface and consequently slowing down the oxidation process.

6.2. Future Outlook

The research on diamonds presented in this thesis provide fundamental insights into the properties of diamonds and how they can be tuned to make the material suitable for efficient photocatalysis with sunlight. The results summarized above lay the foundation but there is still a long way to go before diamonds can be established as efficient photocatalysts, in par with the existing and well known transition metals and their oxides. For the way forward, some of the hypotheses formed, based on the conclusions from our results, could motivate further research in this direction.

Study of n-type and co-doped diamonds

For doped diamonds, we were able to show in Chapter 3 that XAS is quite sensitive to the surface states introduced by dopants and also to the morphology dependent changes in these states. In case of N-doped diamonds, it is known that formation of nanocrystalline diamonds increases the sp^2 content in the material which makes the diamond highly conductive. We have already evidenced the sp^2 induced surface state in the XA spectrum of both N- and P-doped diamonds. Therefore, a morphology and size dependent study can also be extended to the n-type diamonds for a deeper investigation of the effect of nanostructuration on their electronic structures and consequently on electron emission characteristics. In addition, we could also probe the electronic structure of co-doped diamonds with p- and n-type dopants to understand the synergistic effects, if any. Furthermore, in Chapter 5, we also shed some light on the role of adsorbates on electronic structure and electron emission characteristics of doped

diamonds in vacuum. This study can be further deepened by conducting a study on the role of adsorbates in electron emission using near-ambient pressure PES. Combining the information on electronic structure of these materials with laser based time-resolved studies could be helpful in establishing the photoexcitation mechanism in p-type, n-type and co-doped diamonds.

Electronic structure and charge transfer mechanisms in dye sensitized diamonds

The study on electronic structure of transition-metal complex functionalized NDs in Chapter 4 suggested the role of the dye as an electron donor to refill the photogenerated holes in the diamond. Time-resolved laser spectroscopy based experiments could be useful in gaining further insights on this process. For this purpose, the diamonds would need to be photoactivated using deep UV laser pulses in order to generate holes in the VB. Alternatively, one could also consider doping the diamond with boron which introduces holes in the valence band of diamonds, that could possibly be filled by photogenerated electrons upon visible light excitation of the dye. Furthermore, in order to observe the process, as hypothesized, it may also be worthwhile to design the experiment in aqueous medium with a hole scavenger that would prevent recombination of the charge carriers in the dye. While we have primarily explored $Ru(bpy)_3$ in Chapter 4, other visible light active dyes with appropriate band edge positions may also be explored as potential electron donors to diamond in order to enhance the efficiency of solvated electron emission in water.

Direct observation of charge transfer processes at the diamond-water interface

In addition to doping, the surface chemistry of diamonds also influence its electron emission characteristics, as pointed out previously. Particularly Chakrapani *et al.* demonstrated surface transfer doping in undoped H-terminated diamonds which impart a surface conductivity to the diamonds. They reported an increase in conductivity under acidic conditions and a decrease thereof in basic pH. Our FTIR studies on undoped OH-terminated diamond surfaces also point towards a possible electron emission from the OH-terminated surfaces which is stabilized in acidic pH, similar to H-terminated surfaces. This hypothesis is however based on an investigation of the surface interactions in water alone. To confirm the same, further FTIR measurements would be necessary. Furthermore, these measurements can be complemented by probing the carbon and oxygen core levels at the diamond-water interface using near ambient pressure-PES. This is because surface transfer doping in diamonds in the presence of adsorbates on the surface is likely to cause band bending at the diamond-electrolyte interface which can be probed by a surface sensitive core level spectroscopy technique such as PES. To be able to conduct near ambient pressure PES measurements, we have therefore, developed a liquid nitrogen cooled sample

holder to enable condensation of water vapour on diamond surfaces at near ambient pressures ranging between 1-5 mbar. The first measurements were conducted on H, OH and F terminated B-doped PC diamond and undoped nanodiamond surfaces, the data for which can be found in Appendix A. From the first data, we were able to evidence deposition of water layers by condensation of water vapour on the diamond surfaces. By adjusting the experimental conditions to control the thickness of this water layer, band structure at the diamond-water interface could be probed to directly evidence surface transfer doping in diamonds.

To conclude, the path forward towards a possible commercial application of diamonds as photo(electro)catalysts is still too long as there is an essentially big question that remains to be addressed. This concerns the use of diamonds in a working device and subsequent quantification of the products formed from solar conversion of CO_2 to chemical fuels. Additionally, the economics of the process would also have to be considered for diamonds to be at par with other well-known photo(electro)catalysts for artificial photosynthesis.

List of Figures

List of Tables

Acknowledgements

Three years have flown by and from day one until today, this doctoral research has been a great learning experience for me. It is a work that has culminated out of the joint efforts of a large number of people who have all played an important role in my growth as a scientist, but also more importantly as a person.

To begin with, I would like to thank *Anke*, my doctoral advisor, for supervising my thesis and also more importantly, for giving me the opportunity to develop my scientific expertise as well as my soft skills within the framework of the DIACAT Project. This has essentially been the most challenging but at the same time a fun project experience in my life so far. I am equally thankful to *Tristan*, my mentor and doctoral supervisor, without whose day-to-day guidance and fruitful scientific discussions this thesis would not have been complete. Three and a half years ago when I started this work, little did I believe I would make it in time and also be able to dive into a topic that was absolutely new for me. Thank you very much for being so supportive and teaching me all about diamonds, how to work in a synchrotron and how to write scientific articles for publication. It was your patience and belief in me and the constant encouragement that made my doctoral study a memorable journey despite the challenges, that I would like to cherish all my life. Also, I would like to express my gratitude to *Christina*, for agreeing to be the second reviewer of my thesis, following up on my work from time to time and also giving me fruitful inputs.

For most part of my doctoral research, I collaborated closely with people from University of Würzburg, Fraunhofer IAF, CEA Paris, University of Oxford, Uppsala University. So a big thanks to all of you - *Benjamin, Amélie, Peter, Fang, Emina, Karin, Jean-Charles, Hugues, Christoph, John* and *Natalia*, for providing me samples (often on very short notice), inputs from your investigations and fruitful discussions at the monthly telcos and project meetings that helped me proceed with my research. There was a lot that I was able to learn from each one of you.

A special thanks to *Ronny, Marc* and *Jie* for their help during the LiXedrom beamtimes. In addition, I am greatly thankful to *Klaus* and *Christian* for their help during the PEAXIS beamtimes and for teaching me how to operate the machine. Thank you *Kaan* for the theoretical calculations and for patiently discussing the results with me multiple times. And ofcourse, thanks to you and *Sreeju*, I learnt to survive the night shifts at BESSY. It was always a pleasure to drop by you guys for a chat. Although the idea for XPS measurements on Sol3 was conceived almost towards the end of my doctoral study and I did not have too many beamtimes on it, thank you *Robert* and *Arno*, for helping with the planning and your support during the measurements. A big thanks to you *Florian*, for designing the complicated sample holder for the PES beamtime despite your busy schedule and to *Lili* and *Ulli*, for your support during the IR beamtimes.

In these three and a half years of my research I was fortunate to develop an amazing peer group at HZB. Thank you *Franziska*, for being such an amazing room mate. Especially for bearing with me during the days when I bothered you a lot with my numerous questions about German grammar. It has been a great pleasure sharing office space with you. Working in the laser lab with you has also been quite a fun learning experience. Thanks *Jian* for being such a great team mate at work. I really appreciate your social nature and have absolutely enjoyed working together with you during the beam time. *Mailis, Ameer,* and *Maryam*, thank you very much for your help during the experiments. Thanks to *Fabian, Karen, Dawei Annika, Axel, Daniela and Sabbir* for providing me with a lovely experience in the EM-IMM group. As I take the opportunity to thank all my peers, I would like to extend my heartfelt gratitude to

Heba, my partner-in-crime and best friend at work. Thank you for always having my back and for being there for me, for motivating me when I was low, and for knocking sense in to me, when I am an irrational child. I couldn't have imagined my life in Berlin and this journey without you.

Just like my peers at work, my friends outside the workplace have also been a great source of support during this journey. Thanks to *Aseem, Sulabh*, and *Sachi*, for spontaneously planning meetups and helping me keep my social life beyond work active. Thanks to *Debojit da*, for being the big brother I can always approach. Your advice on all aspects of life and work has always been very very helpful. A special thanks to *Christian, Jana* and *Anastasia (Nastja)* for believing in me more than I have ever believed in myself and for giving me the confidence to achieve great things in life. And ofcourse, thank you *Michael* for being the encouraging friend, that you are. Your enthusiasm about my work has always served as a huge motivation for me even during the most mundane phases of my research. You have always encouraged me to push my limits and inspired me to take chances with new things which I greatly appreciate.

Last but not the least, *Ma* and *Baba*, thank you so much for all the hard work and sacrifices that you have put in all your life. It is because of your unconditional love and constant faith, that your little girl has reached this stage in her life today. This doctorate would not have been possible without you.

Sneha Choudhury

January 2019

A

Appendix

A.1. Instrumentation

A.1.1. Beamlines

The schematics of the undulator beamlines U41-PEAXIS and U49-PGM1 are presented in Figures A.1 and A.2, respectively.

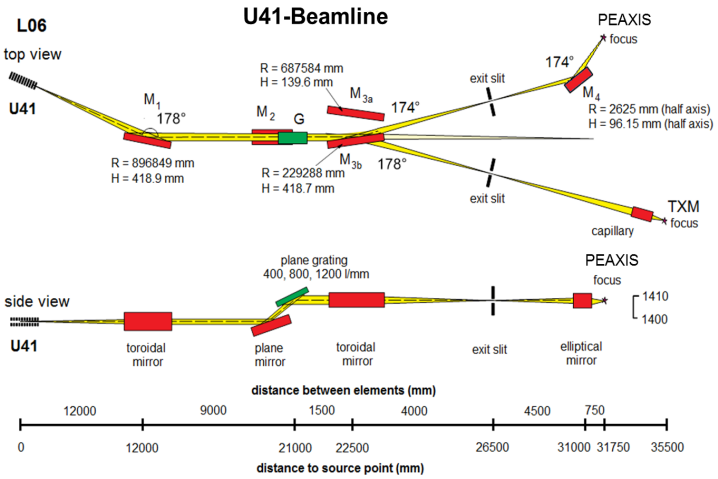

Figure A.1: *Schematic of the U-41 beamline with two fixed end stations. The end station PEAXIS enables the study of solid samples using XAS, RIXS and XPS, taken from [1].*

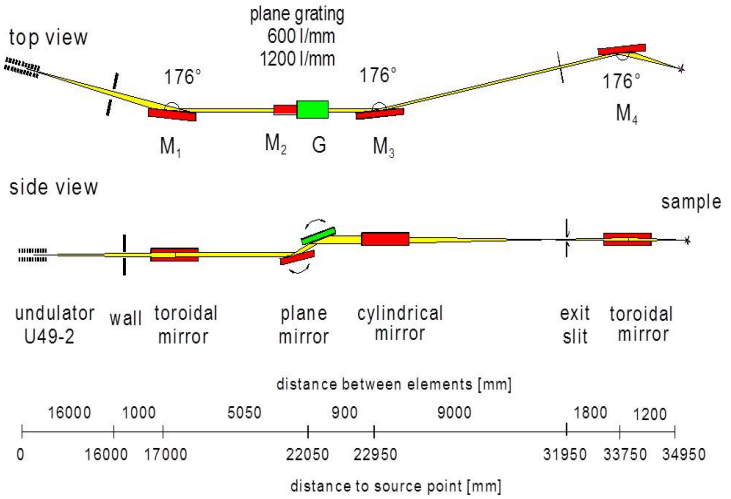

Figure A.2: *Schematic of the U-49 PGM 1 beamline, taken from [2]. This beamline has no fixed end station.*

A.1.2. Experimental Setups

The experimental end stations used in this work are shown in Figures A.3, A.4, A.5 and A.6. Figure A.7 also shows the construction of the electrochemical flow cell used for the *in-situ* electrochemical measurements.

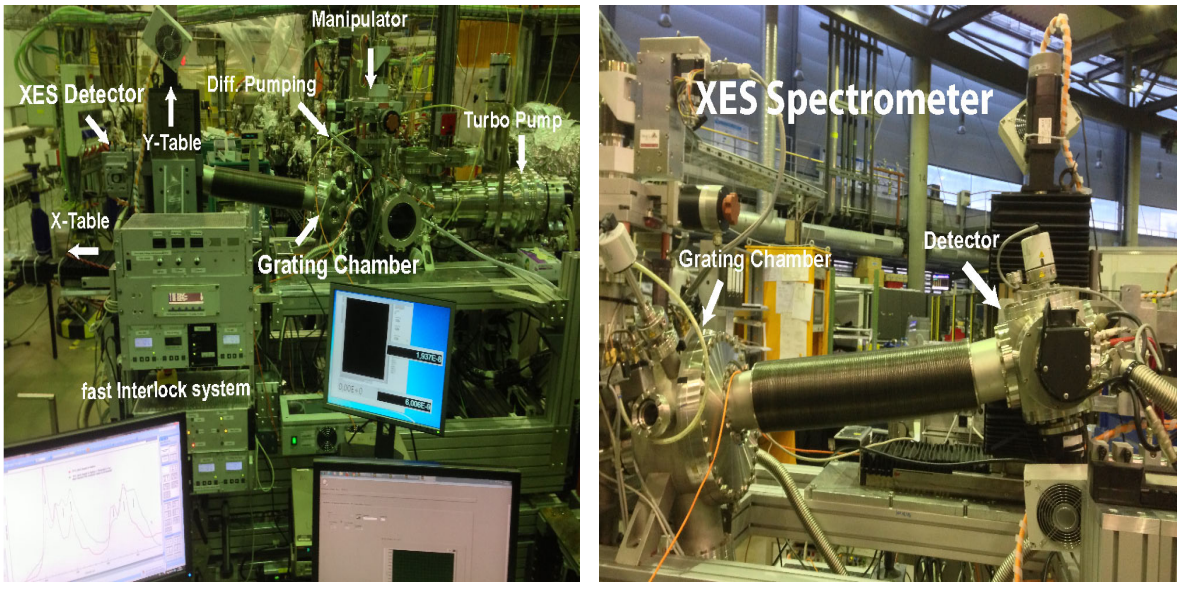

(a) (b)

Figure A.3: *Picture of Lixedrom end station for X-ray absorption and RIXS measurements on solids as well as in liquids, taken from [3].*

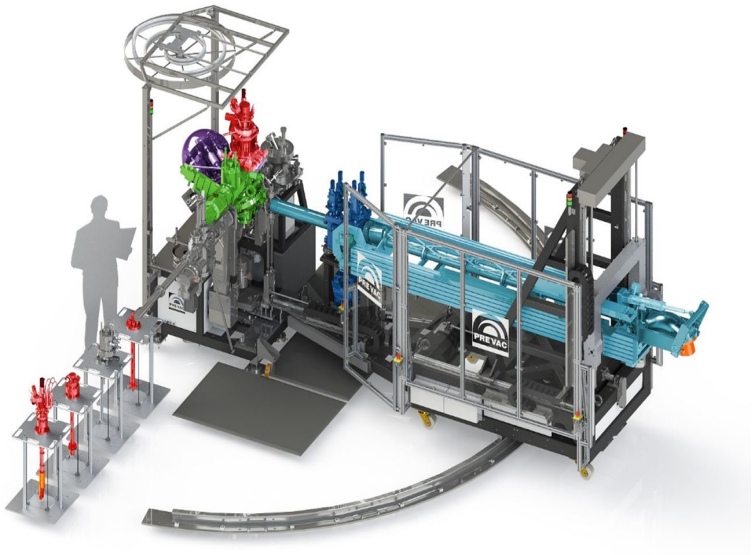

Figure A.4: *Schematic of PEAXIS end station comprising of a load lock (in grey) to transfer samples to the measurement chamber (in green), an electron analyzer for photoemission spectroscopy (in purple) and a RIXS detector with 5 m long movable arm (in blue) for angle resolved RIXS measurements, taken from [4].*

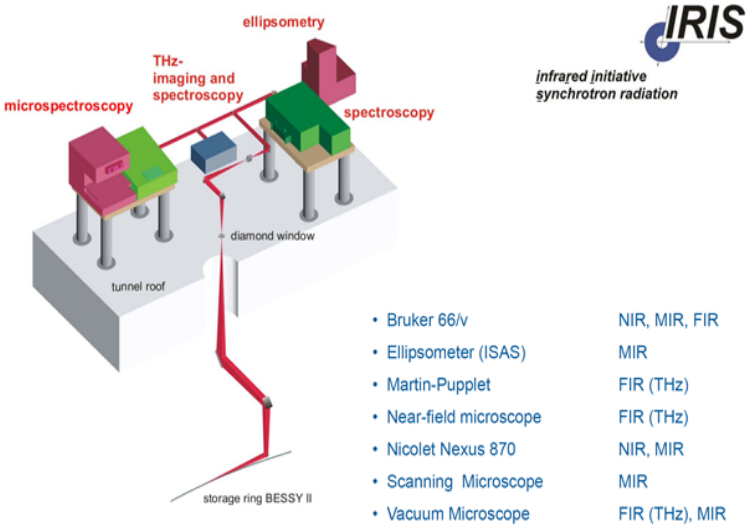

Figure A.5: *Schematic of the end stations at IRIS beamline in BESSY II. ATR-FTIR spectroscopy measurements are conducted using a Bruker 66/v spectrometer (in dark green), taken from [5].*

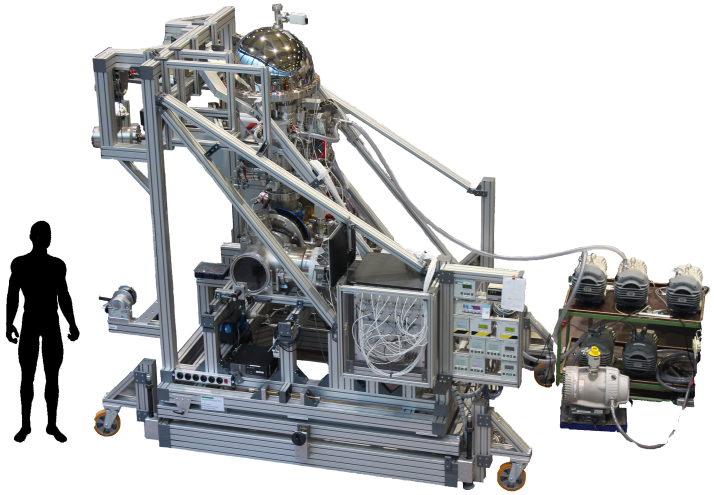

Figure A.6: *Schematic of Sol3PES end station for near ambient pressure photoemission spectroscopy experiments at BESSY II, taken from [6].*

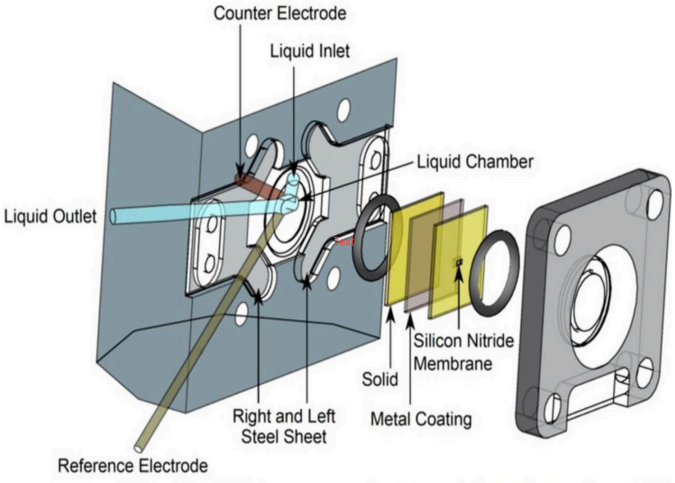

Figure A.7: *Picture of the construction of the electrochemical flow cell developed by Schwanke et al., taken from [7]. Au coated Si_3N_4 membrane acts as the working electrode and a Pt wire is used at the counter electrode. Ag/AgCl is used as the reference electrode. The liquid is flown in the liquid chamber using a syringe pump to avoid overpressures at the membrane. The O-rings ensure that the seal is well-sealed.*

A.2. Procedure for background correction

Due to high carbon contamination at the mirrors in the beamline, the raw TEY-XA spectra usually has a very strong background. This background can be corrected using the TEY-XA spectra at the C K edge measured from the beamline, shown in Figure A.8. Since the photocurrent measured from the carbon contamination at the beamline is usually higher than that measured from the sample, all TEY-XA spectra from the sample are first scaled to the first peak appearing at 280.2 eV. The background measured from the beamline is subsequently subtracted from the scaled spectrum of the sample in order to remove any contribution from the carbon contamination of the beamline. This simple background correction procedure functions well for TEY spectra measured in LiXedrom at U49-PGM1 beamline. However, since this method does not function for TEY measurements in PEAXIS, a different protocol must be established in the future.

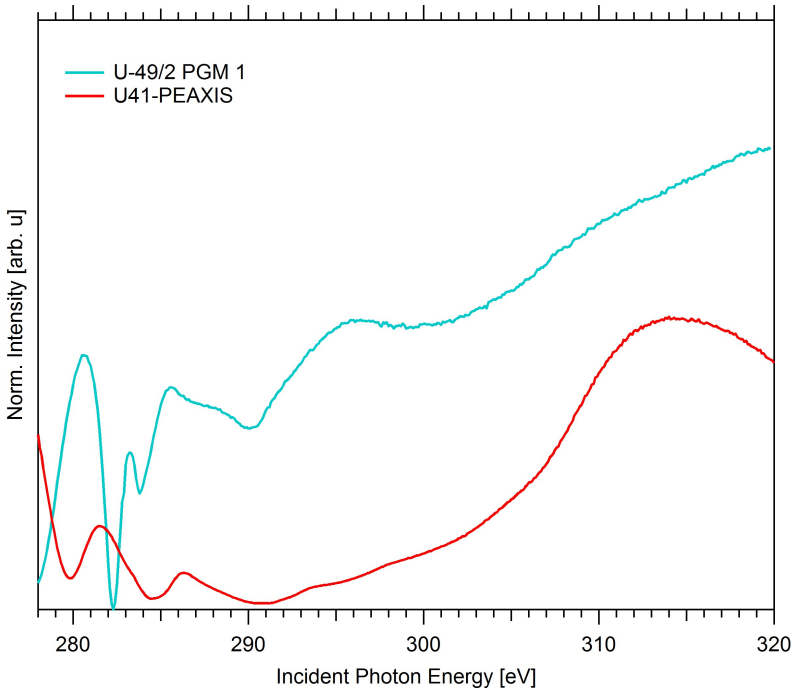

Figure A.8: *TEY-XA spectrum at C K edge measured at the U49/2-PGM1 and U41-PEAXIS beamlines for background correction.*

A

A.3. Experimental Data

A.3.1. Ru-functionalized NDs

Ru complexes were grafted on the ND surfaces using an extended tolane linker, in addition to the two linker systems presented in Chapter 4. The structure of this surface functionalized ND and a comparison of its TEY-XA spectrum at the C K edge is presented in Figure A.9.

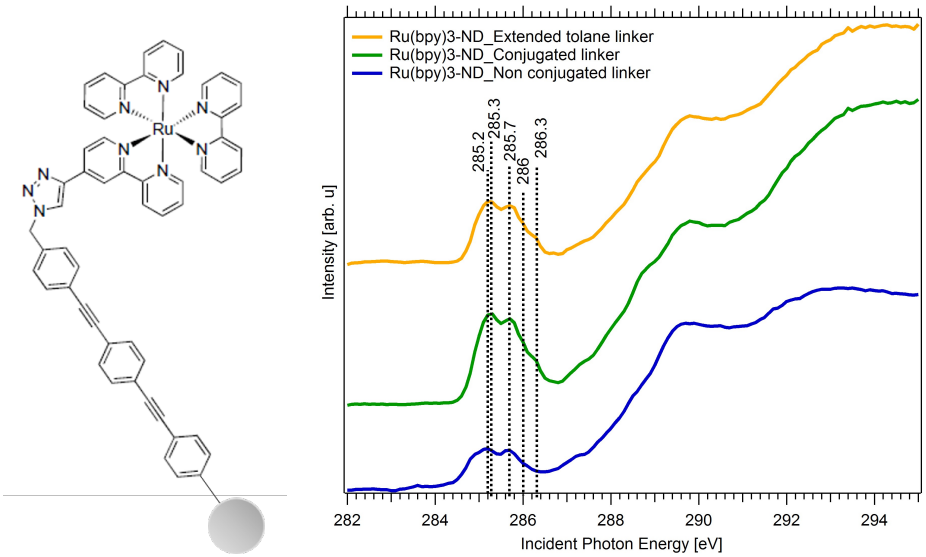

(a) (b)

Figure A.9: *(a)Structure of $Ru(bpy)_3$ attached to ND with an extended tolane linker. (b) TEY-XA spectrum at C K edge of $Ru(bpy)_3$-ND showing the electronic structure of the extended tolane linker system compared with the short conjugated and non-conjugated linker systems. The presence of extensive conjugation in the extended linker gives rise to an additional charge transfer state similar to that observed for the conjugated linker system.*

A.3.2. FTIR Spectroscopy at the diamond-water interface

NDs-H were also measured in acidic pH, the spectra for which are shown in Figure A.10. The difference spectra shown (in red and orange) show the presence of C=O groups which induce vibrations at *ca.* 1726 cm^{-1}. A broad shoulder is evidenced at *ca.* 1550 cm^{-1} which is attributed to a charge accumulation layer within the hydrophobic gap on ND-H surfaces. Additionally, Figures A.11 and A.12 present the full range FTIR spectra for **ND-OH B** and **ND-OH B+f** in acidic and basic pH in presence of D_2O. These measurements were conducted with the aim of observing differences in the spectra originating from diamond-water interactions. However, no significant changes could be observed here, besides a shift in the OH-vibrational bands.

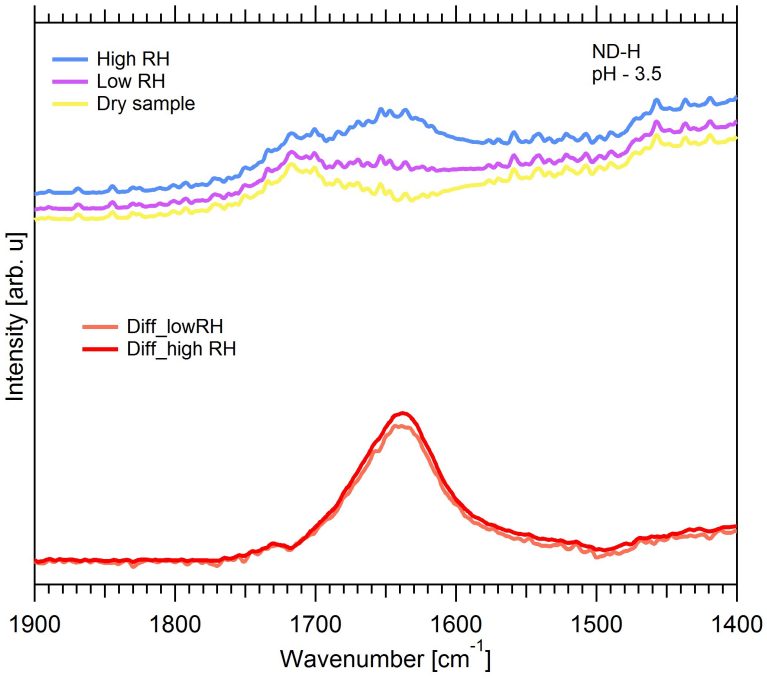

Figure A.10: *Comparison of FTIR spectra of dry ND-H (dry sample) and after exposure ot humid air with low (in pink) and high RH (in blue) under acidic pH conditions.*

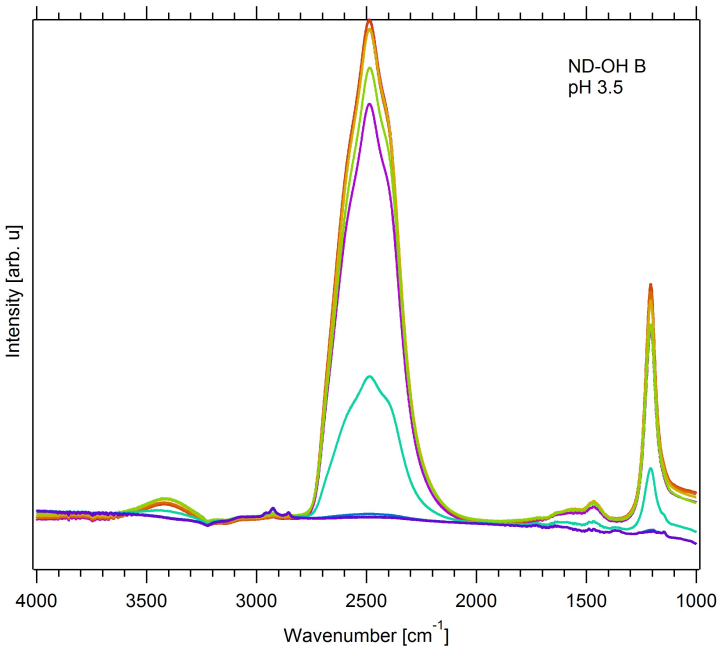

(a)

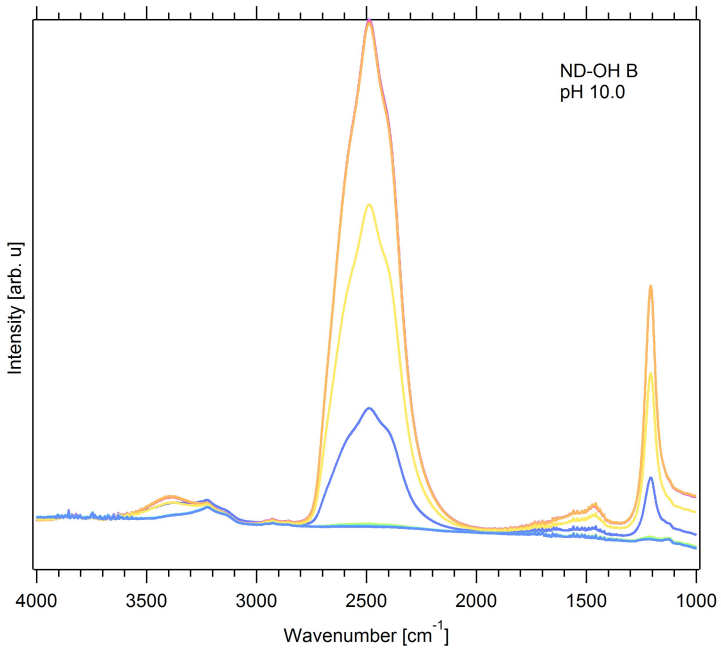

(b)

Figure A.11: *FTIR spectra of **ND-OH B** with D_2O in acidic (a) and basic (b) pH environment.*

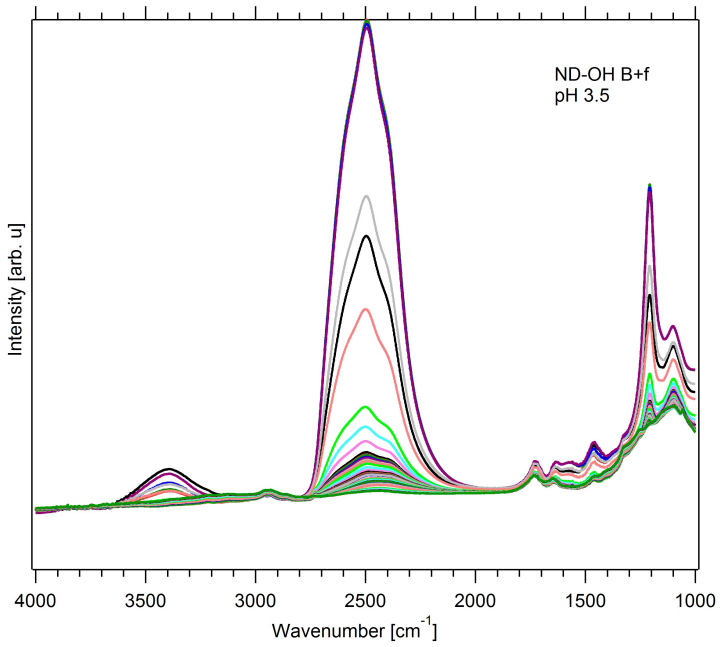

(a)

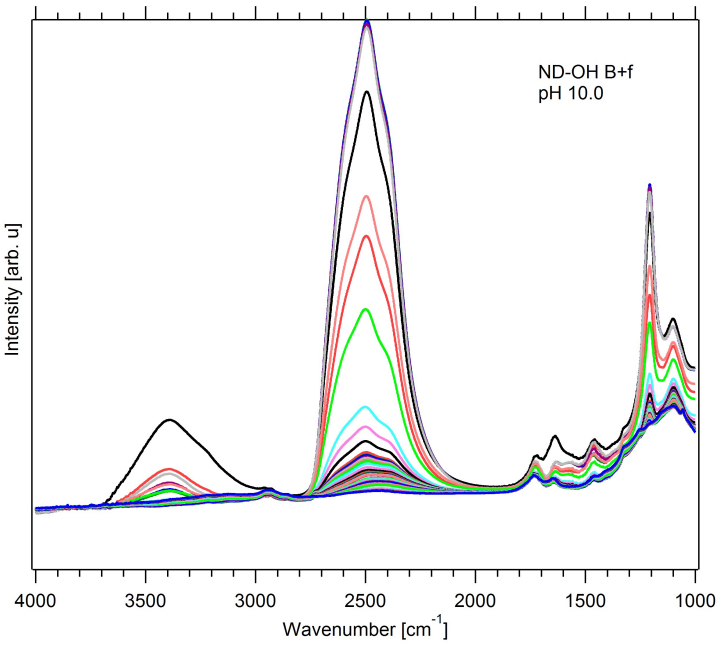

(b)

Figure A.12: *FTIR spectra of* ***ND-OH B+f*** *with* D_2O *in acidic (a) and basic (b) pH environment.*

A.3.3. Ambient-pressure PES on diamonds

The data for ambient pressure-PES measurements are presented in Figures A.13, A.14 and A.15 below. The energy scale has not been calibrated in this data. Therefore some deviation in the binding energy values for certain features in the spectrum is expected in comparison to those reported in literature. From the data presented in Figures A.13, A.14 and A.15, a peak from water can already be observed in the O 1s core level spectrum of the diamonds at *ca.* 530 eV, thereby confirming the condensation of

A

water vapour on the diamond surface. Additional data on undoped ND surfaces with different surface terminations are also presented in Figures A.16, A.17, and A.18. The shifts observed in the spectra are not real but originate primarily from change in beamline harmonics and other beamline parameters.

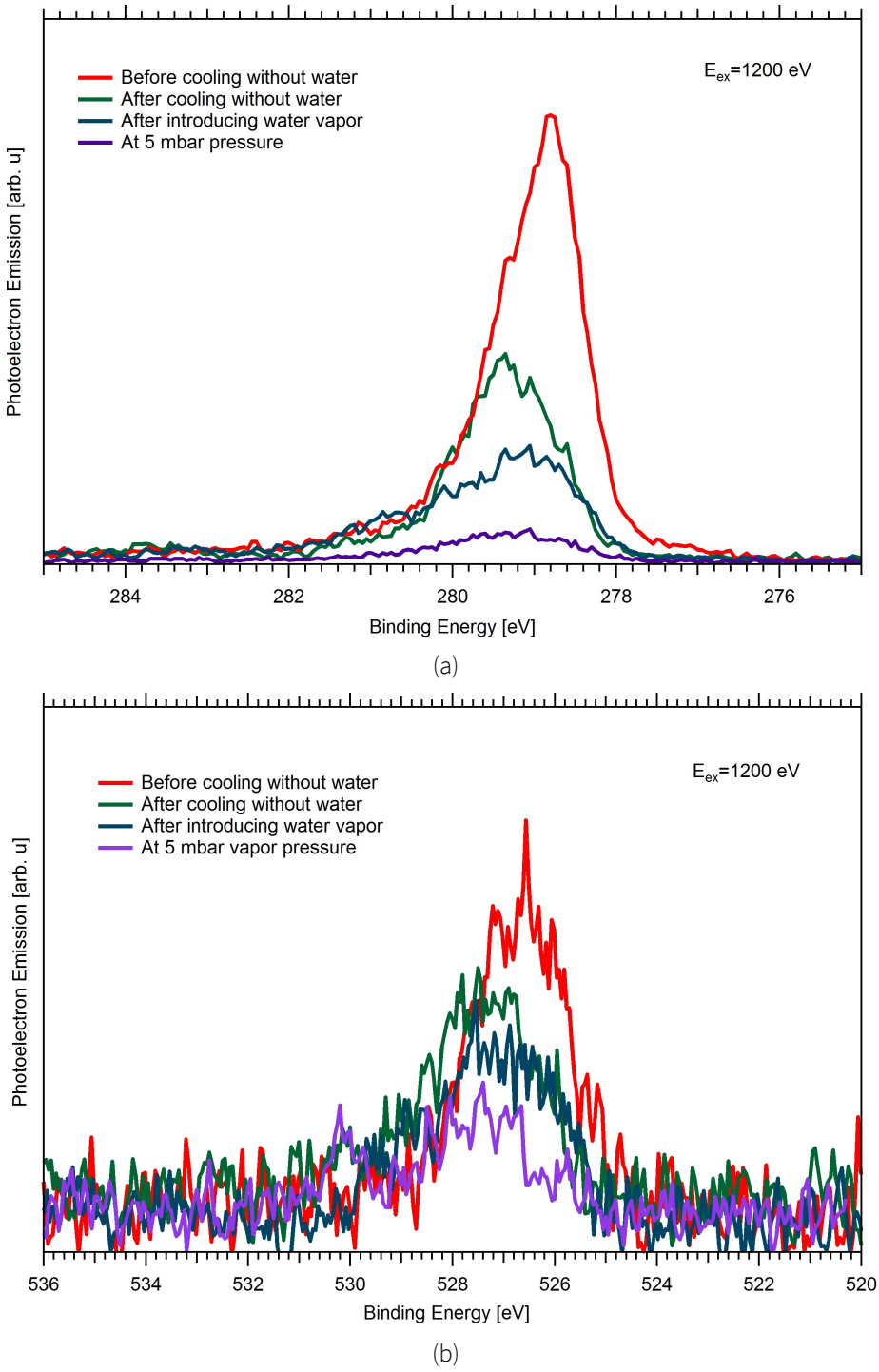

Figure A.13: *C 1s(a) and O 1s(b) core level PES spectra of OH-terminated B-doped PC diamonds. The spectra have been recorded before cooling under UHV conditions and subsequently after cooling at near ambient pressures by introducing water vapour in the interaction chamber.*

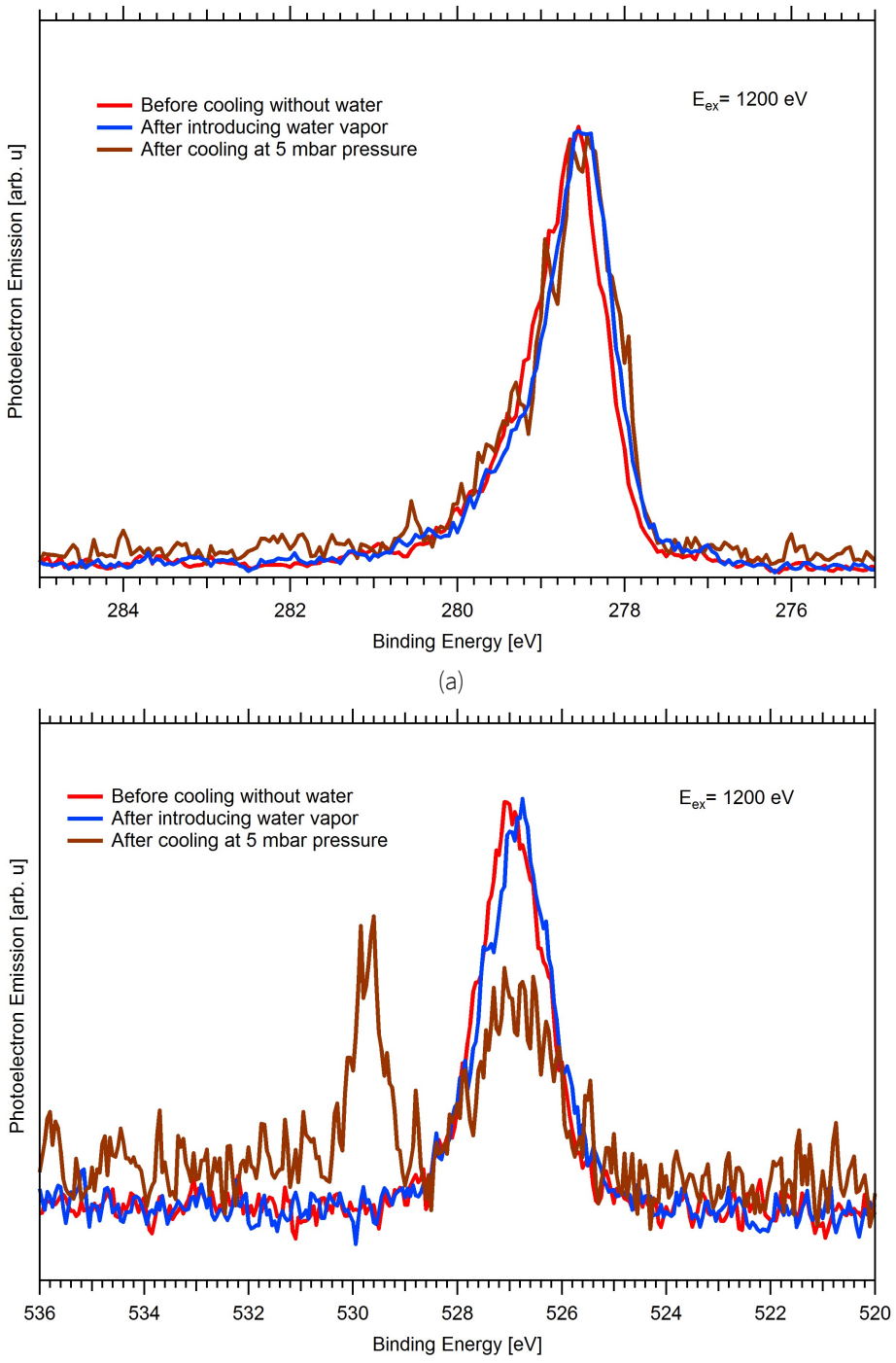

Figure A.14: *C 1s(a) and O 1s(b) core level PES spectra of H-terminated B-doped PC diamonds. The spectra have been recorded before cooling under UHV conditions and subsequently after cooling at near ambient pressures by introducing water vapour in the interaction chamber.*

A

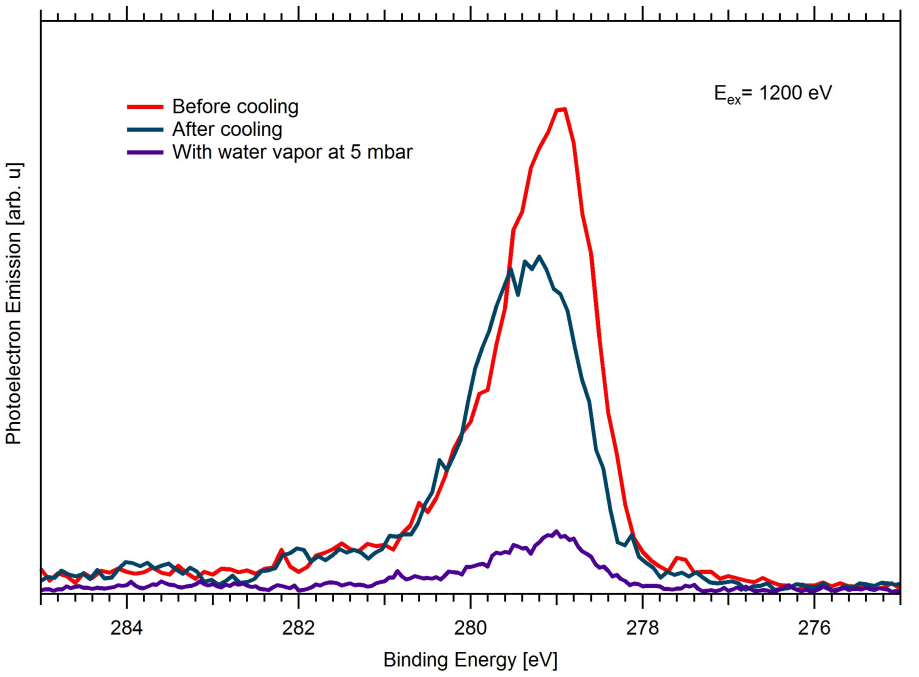

(a)

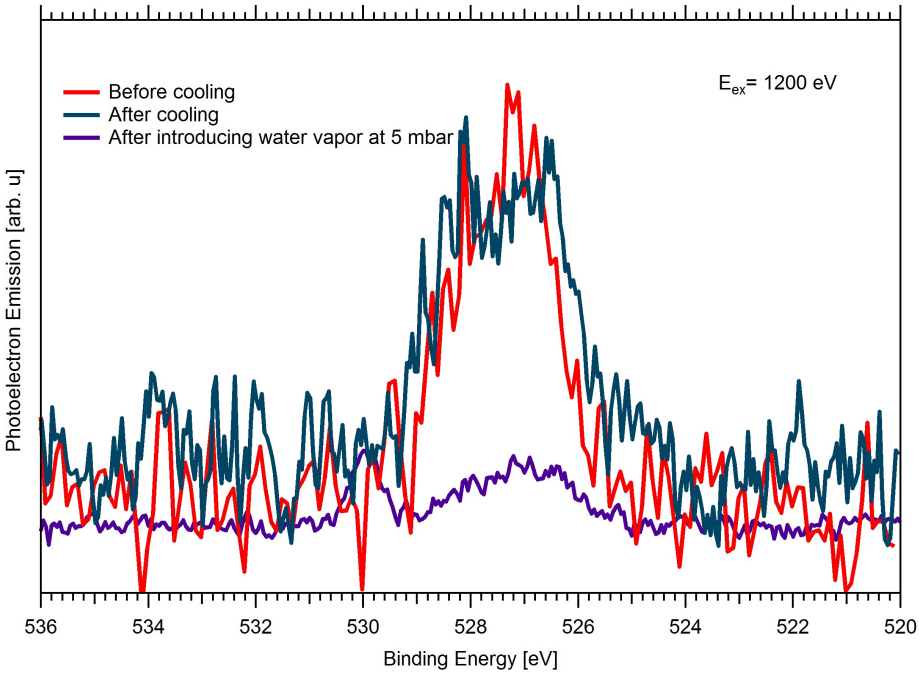

(b)

Figure A.15: *C 1s(a) and O 1s(b) core level PES spectra of F-terminated B-doped PC diamonds. The spectra have been recorded before cooling under UHV conditions and subsequently after cooling at near ambient pressures by introducing water vapour in the interaction chamber.*

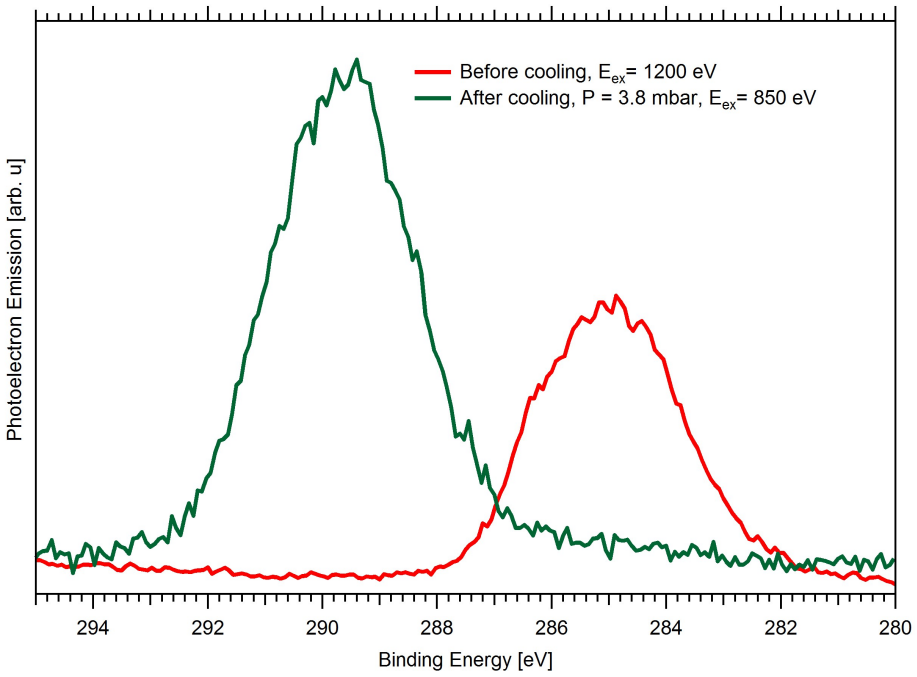

(a)

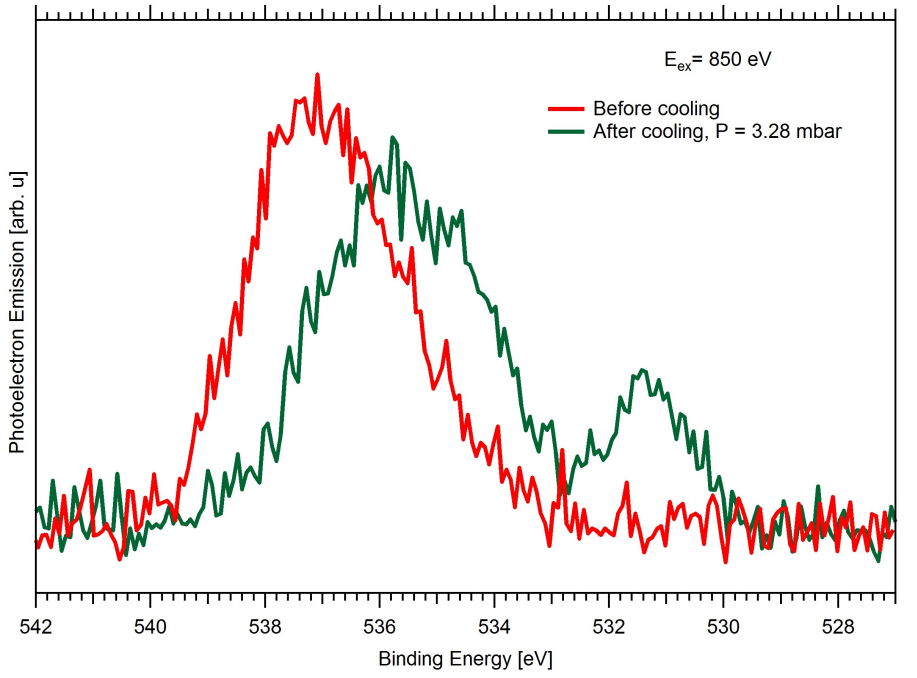

(b)

Figure A.16: *C 1s(a) and O 1s(b) core level PES spectra of OH-terminated undoped nanodiamonds. The spectra have been recorded before cooling under UHV conditions and subsequently after cooling at near ambient pressures by introducing water vapour in the interaction chamber. These spectra have not been calibrated for the energy axis.*

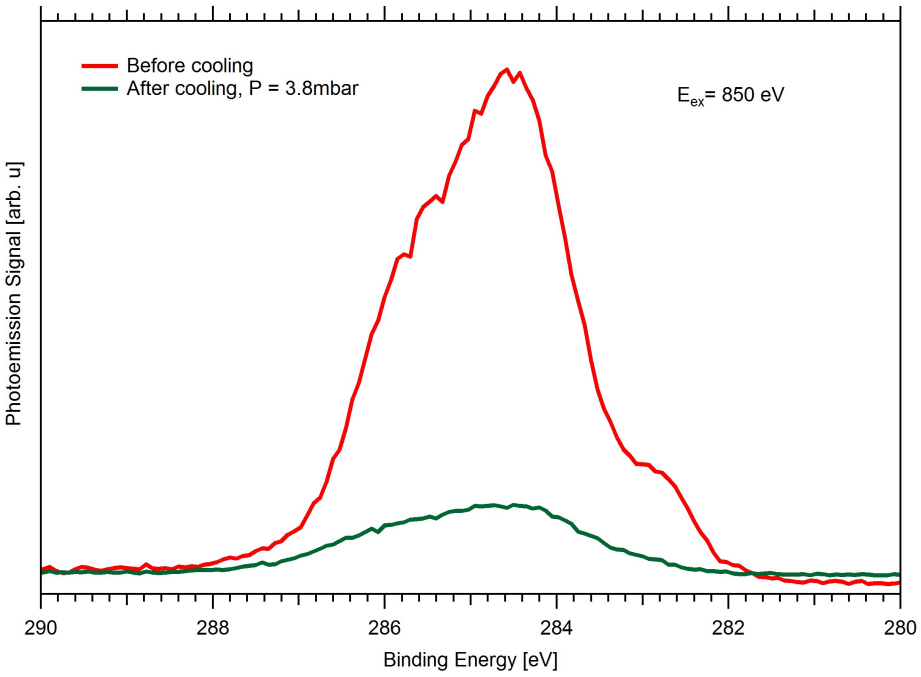

(a)

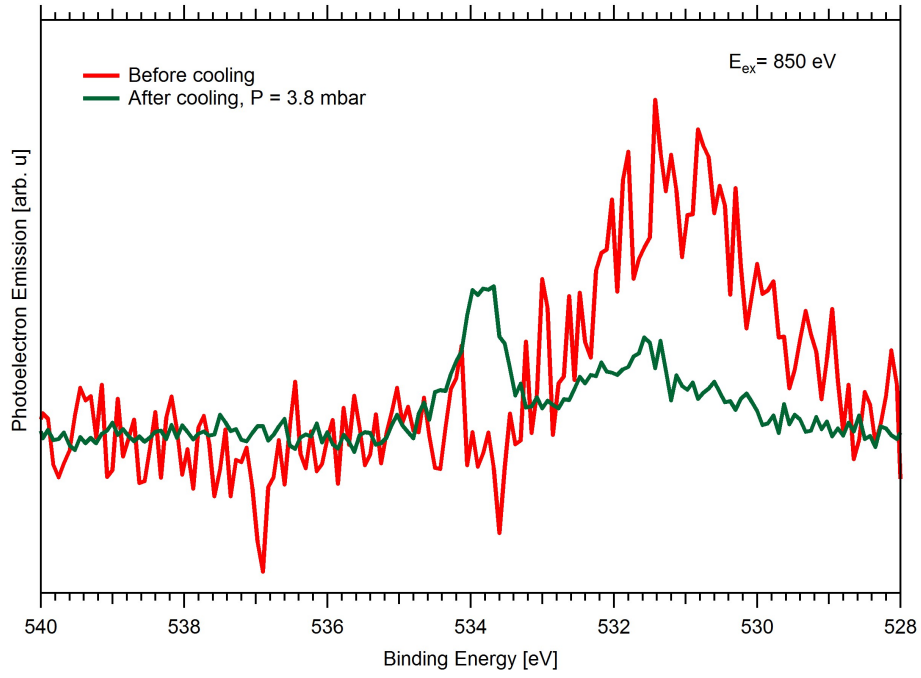

(b)

Figure A.17: *C 1s(a) and O 1s(b) core level PES spectra of H-terminated undoped nanodiamonds. The spectra have been recorded before cooling under UHV conditions and subsequently after cooling at near ambient pressures by introducing water vapour in the interaction chamber. These spectra have not been calibrated for the energy axis.*

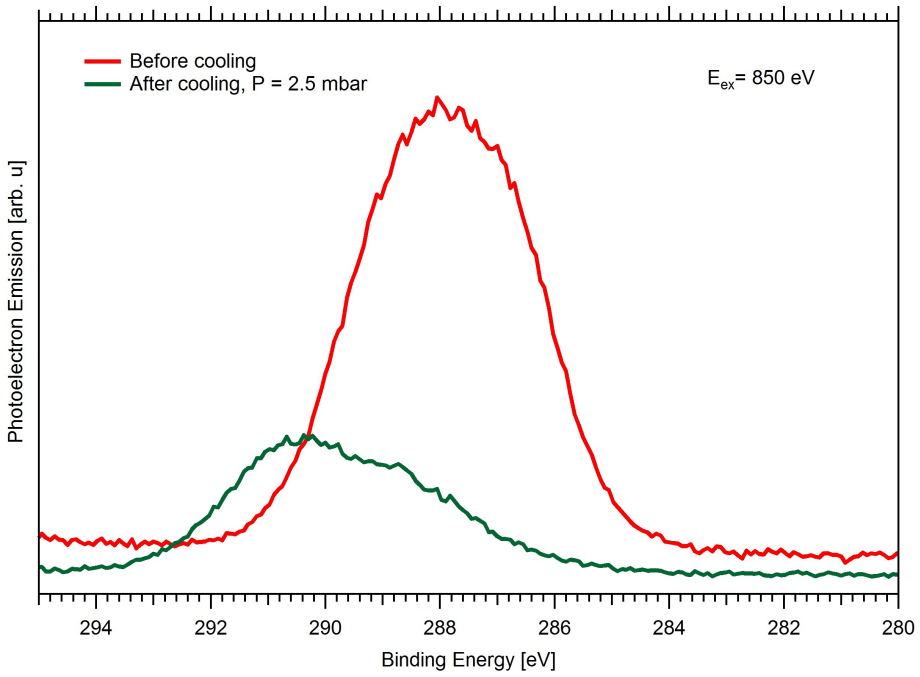

(a)

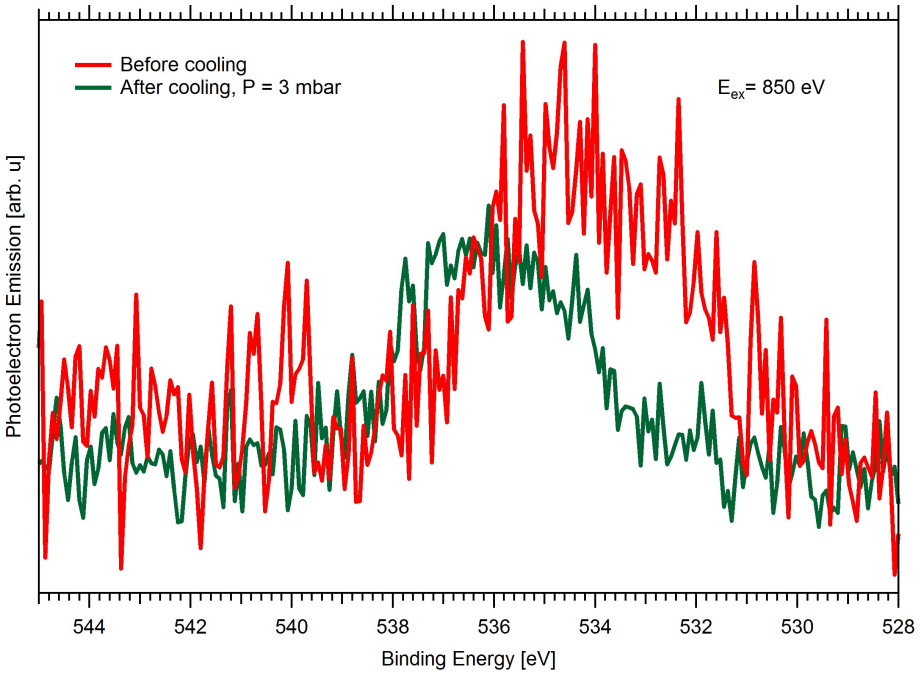

(b)

Figure A.18: *C 1s(a) and O 1s(b) core level PES spectra of F-terminated undoped nanodiamonds. The spectra have been recorded before cooling under UHV conditions and subsequently after cooling at near ambient pressures by introducing water vapour in the interaction chamber. These spectra have not been calibrated for the energy axis.*

References

[1] *U41-peaxis,* https://www.helmholtz-berlin.de/pubbin/igama_output?modus=einzel&sprache=en&gid=2126.
[2] *U49/2-pgm1 beamline schematic,* https://www.helmholtz-berlin.de/pubbin/igama_output?modus=einzel&gid=1655&sprache=en.
[3] *Lixedrom end station,* https://www.helmholtz-berlin.de/pubbin/igama_output?

modus=einzel&sprache=en&gid=1867&typoid=35517.
[4] *Fixed end station: PEAXIS,* https://www.helmholtz-berlin.de/pubbin/igama_output?modus=einzel&sprache=en&gid=2127.
[5] *IRIS beamline at BESSY II,* https://www.helmholtz-berlin.de/pubbin/igama_output?modus=einzel&gid=1605&sprache=de.
[6] R. Seidel, M. N. Pohl, H. Ali, B. Winter, and E. F. Aziz, *Advances in liquid phase soft-x-ray photoemission spectroscopy: A new experimental setup at BESSY II,* Review of Scientific Instruments **88**, 073107 (2017).
[7] C. Schwanke, R. Golnak, J. Xiao, and K. M. Lange, *Electrochemical flowcell for in-situ investigations by soft x-ray absorption and emission spectroscopy,* Review of Scientific Instruments **85**, 103120 (2014).

Curriculum Vitæ

For reasons of data protection, the curriculum vitæ is not published in the electronic version.

List of Publications

Publications from this thesis

1. **Sneha Choudhury**, Benjamin Kiendl, Jian Ren, Fang Gao, Peter Knittel, Christoph Nebel, Amélie Venerosy, Hugues Girard, Jean-Charles Arnault, Anke Krueger, Karin Larsson, Tristan Petit, *Combining nanostructuration and boron-doping to alter sub-band gap acceptor states in diamond materials*, J. Mater. Chem. A, 2018, **6**, 16645-16654.

2. Benjamin Kiendl, **Sneha Choudhury**, Amélie Venerosy, Emina Hadzifejzovic, Mailis M. Lounasvuori, Jian Ren, Kaan Atak, Tristan Petit, Hugues A. Girard, Jean-Charles Arnault, Karin Larsson, John S. Foord, Anke Krueger, *Photoelectrocatalytic conversion of CO_2 : Application of transition metal functionalised diamond nanoparticles*, in preparation

3. Tristan Petit, **Sneha Choudhury**, Peter Knittel, Nicolas Tranchant, Jean-Charles Arnault, Christoph Nebel, *Effect of diamond doping on electron emission probed by X-ray absorption spectroscopy*, in preparation

4. **Sneha Choudhury**, Benjamin Kiendl, Amélie Venerosy, Hugues A. Girard, Jean-Charles Arnault, Ljiljana Puskar, Anke Krueger and Tristan Petit, *pH effects on surface interactions of OH-terminated nanodiamonds*, in preparation

Contributed Articles

1. Tristan Petit, Ljiljana Puskar, Tatiana Dolenko, **Sneha Choudhury**, Eglof Ritter, Sergey Burikov, Kirill Laptinskiy, Quentin Brzustowski, Ulrich Schade, Hayato Yuzawa, Masanari Nagasaka, Nobuhiro Kosugi, Magdalena Kurzyp, Amélie Venerosy, Hugues Girard, Jean-Charles Arnault, Eiji Osawa, Nicholas Nunn, Olga Shenderova, and Emad F. Aziz, *Unusual Water Hydrogen Bond Network around Hydrogenated Nanodiamonds*, J. Phys. Chem. C, 2017, **121(9)**, pp 5185-5194.

2. Tristan Petit, Jian Ren, **Sneha Choudhury**, Ronny Golnak, Sreeju S. N. Lalithambika, Marc F. Tesch, Jie Xiao, Emad F. Aziz, *X-Ray Absorption Spectroscopy of TiO_2 Nanoparticles in Water Using a Holey Membrane-Based Flow Cell*, Adv. Mat. Interfaces, 2017, **4**, 1700755.

3. Jian Ren, Fabian Weber, Florian Weigert, Yajie Wang, **Sneha Choudhury**, Jie Xiao, Iver Lauermann, Ute Resch-Genger, Annika Bande, Tristan Petit, *Influence of surface chemistry on optical, chemical and electronic properties of blue luminescent carbon dots*, Nanoscale, 2019, **11**, 2056-2064.

4. Benjamin Kiendl, Solange Temgoua, Sien Drijkoningen, **Sneha Choudhury**, Tristan Petit, Ken Haenen, Julien Barjon, Anke Krueger, *Fabrication and in depth characterization of phosphorus-doped nanodiamonds*, in preparation

5. Emina Hadzifejzovic, Mailis M. Lounasvuori, Benjamin Kiendl, **Sneha Choudhury**, Tristan Petit, Anke Krueger, John S. Foord, *Photoelectrochemical investigations on Cu_2O co-promoted B-doped nanodiamond electrodes*, in preparation